DOCTORAL THESIS

RINGS DIVERSITY AROUND SMALL SOLAR SYSTEM BODIES:
DISCOVERIES AND DETECTION LIMITS

CHRYSTIAN LUCIANO PEREIRA

RIO DE JANEIRO
2024

Ministério da Ciência, Tecnologia, Inovações

Observatório Nacional

Programa de Pós-Graduação

Doctoral Thesis

RINGS DIVERSITY AROUND SMALL SOLAR SYSTEM BODIES: DISCOVERIES AND DETECTION LIMITS

by

Chrystian Luciano Pereira

Thesis submitted to the faculty of the Astronomy Ph.D program from Observatório Nacional in fulfillment of the requirements for the degree of Doctor of Philosophy in Astronomy.

Advisor: Prof. Dr. Felipe Braga Ribas

Co-advisor: Prof. Dr. Marcelo Emilio

Rio de Janeiro, RJ – Brasil

August 2024

"RINGS DIVERSITY AROUND SMALL SOLAR SYSTEM BODIES:
DISCOVERIES AND DETECTION LIMITS"

CHRYSTIAN LUCIANO PEREIRA

THESIS SUBMITTED TO THE FACULTY OF THE ASTRONOMY Ph.D. PROGRAM
FROM OBSERVATÓRIO NACIONAL IN FULLFILMENT OF THE REQUIREMENTS
FOR THE DEGREE OF DOCTOR IN ASTRONOMY.

Approved by:

_____
Prof. Dr. Felipe Braga Ribas – Observatório Nacional
& Universidade Tecnológica Federal do Paraná
(Advisor)

_____
Prof. Dr. Marcelo Emilio – Observatório Nacional &
Universidade Estadual de Ponta Grossa
(Co-advisor)

_____
Dr. Fernando Virgílio Roig – Observatório Nacional
(ON/MCTI) – Brasil

_____
Dr. Adrian Rodriguez Colucci – Observatório do
Valongo (OV/UFRJ) – Brasil

_____
Dr. Ricardo Gil-Hutton – Universidad Nacional de San
Juan (UNSJ) – Argentina

_____
Dr. Tabaré Gallardo – Universidad de la República
(UdelaR) – Uruguai

RIO DE JANEIRO, RJ – BRASIL
27 AUGUST 2024

Ata de Defesa

Doutorado em Astronomia. Processo 942/2020. Candidato **Chrystian Luciano Pereira.** No vigésimo sétimo dia do mês de agosto do ano de dois mil e vinte quatro, às 10h, na modalidade remota. Integraram a Banca Examinadora os Doutores Felipe Braga Ribas – (ON), orientador do candidato e presidente da banca; Marcelo Emilio– (ON), coorientador do candidato; Fernando Virgílio Roig – (ON), Adrian Rodriguez Colucci – (OV/UFRJ), Ricardo Gil-Hutton– Universidade Nacional de San Juan-(UNSJ), Tabaré Gallardo – (UdelaR)- Uruguai, os quais foram indicados pela Comissão de Pós-Graduação em Astronomia. O Presidente iniciou a sessão pública, tendo o candidato explanado a respeito do seu trabalho intitulado **"RINGS DIVERSITY AROUND SMALL SOLAR SYSTEM BODIES:DISCOVERIES AND DETECTION LIMITS",** sobre o qual foi sucessivamente arguido pelos membros da Banca. Após a arguição o Presidente suspendeu a sessão pública para que em sessão secreta a Banca expressasse o seu julgamento sobre o trabalho, o qual foi considerado **APROVADO**. O Presidente reabriu os trabalhos da sessão pública anunciando a decisão da Banca Examinadora. Eu, Giane do Carmo Boldrim, lavrei o presente termo que assino juntamente com os membros da Banca e o candidato.

Rio de Janeiro, 27 de agosto de 2024.

a) _____
   Felipe Braga Ribas

b) _____
   Marcelo Emilio

c) _____
   Fernando Virgílio Roig

d) _____
   Adrian Rodriguez Colucci

e) _____
   Ricardo Gil-Hutton

f) _____
   Tabaré Gallardo

g) _____
   Chrystian Luciano Pereira

h)_____
   Giane do Carmo Boldrim

Rua General José Cristino, 77 - São Cristóvão - Rio de Janeiro, RJ - Brasil
20921-400 - www.on.br - Tel.: (21) 3504 9100

Clicksign 802abbcf-24a8-4510-afe5-f2eebe203af7

Clicksign

Datas e horários em GMT -03:00 Brasilia
Log gerado em 29 de agosto de 2024. Versão v1.41.0.

Chrystian Luciano Pereira - Ata.pdf

Documento número #802abbcf-24a8-4510-afe5-f2eebe203af7

Hash do documento original (SHA256): 5260ccbcc82f26cdcc5992fb66f501bd8a33e0455d66813300b34de9b2179bed

Assinaturas

RICARDO GIL-HUTTON
Assinou em 28 ago 2024 às 07:44:52

GIANE DO CARMO BOLDRIM
CPF: 004.446.047-31
Assinou em 29 ago 2024 às 13:57:00

Fernando Virgilio Roig
CPF: 213.132.548-78
Assinou em 28 ago 2024 às 11:58:08

FELIPE BRAGA RIBAS
CPF: 040.022.789-48
Assinou em 27 ago 2024 às 17:18:35

Tabare Gallardo
Assinou em 27 ago 2024 às 19:08:58

MARCELO EMILIO
CPF: 841.053.809-15
Assinou em 27 ago 2024 às 19:21:09

CHRYSTIAN LUCIANO PEREIRA
CPF: 085.598.609-32
Assinou em 27 ago 2024 às 19:22:11

Adrián Rodriguez Colucci
Assinou em 28 ago 2024 às 10:54:02

Log

Clicksign
802abbcf-24a8-4510-afe5-f2eebe203af7
Página 1 de 3 do Log

Clicksign

Datas e horários em GMT -03:00 Brasilia
Log gerado em 29 de agosto de 2024. Versão v1.41.0.

27 ago 2024, 16:58:20   Operador com email gianeboldrim@on.br na Conta d4a6a640-21d1-4ea0-ac83-474533e86e3c criou este documento número 802abbcf-24a8-4510-afe5-f2eebe203af7. Data limite para assinatura do documento: 26 de setembro de 2024 (16:58). Finalização automática após a última assinatura: habilitada. Idioma: Português brasileiro.

27 ago 2024, 17:07:20   Operador com email gianeboldrim@on.br na Conta d4a6a640-21d1-4ea0-ac83-474533e86e3c adicionou à Lista de Assinatura:
gianeboldrim@on.br para assinar, via E-mail, com os pontos de autenticação: Token via E-mail; Nome Completo; CPF; endereço de IP. Dados informados pelo Operador para validação do signatário: nome completo GIANE DO CARMO BOLDRIM e CPF 004.446.047-31.

27 ago 2024, 17:07:20   Operador com email gianeboldrim@on.br na Conta d4a6a640-21d1-4ea0-ac83-474533e86e3c adicionou à Lista de Assinatura:
froig@on.br para assinar, via E-mail, com os pontos de autenticação: Token via E-mail; Nome Completo; CPF; endereço de IP. Dados informados pelo Operador para validação do signatário: nome completo Fernando Virgilio Roig e CPF 213.132.548-78.

27 ago 2024, 17:07:20   Operador com email gianeboldrim@on.br na Conta d4a6a640-21d1-4ea0-ac83-474533e86e3c adicionou à Lista de Assinatura:
adrian@ov.ufrj.br para assinar, via E-mail, com os pontos de autenticação: Token via E-mail; Nome Completo; endereço de IP. Dados informados pelo Operador para validação do signatário: nome completo Adrián Rodriguez Colucci.

27 ago 2024, 17:07:20   Operador com email gianeboldrim@on.br na Conta d4a6a640-21d1-4ea0-ac83-474533e86e3c adicionou à Lista de Assinatura:
ricardo.gil-hutton@conicet.gov.ar para assinar, via E-mail, com os pontos de autenticação: Token via E-mail; Nome Completo; endereço de IP. Dados informados pelo Operador para validação do signatário: nome completo RICARDO GIL-HUTTON.

27 ago 2024, 17:07:20   Operador com email gianeboldrim@on.br na Conta d4a6a640-21d1-4ea0-ac83-474533e86e3c adicionou à Lista de Assinatura:
marcelo_emilio@yahoo.com para assinar, via E-mail, com os pontos de autenticação: Token via E-mail; Nome Completo; CPF; endereço de IP. Dados informados pelo Operador para validação do signatário: nome completo MARCELO EMILIO e CPF 841.053.809-15.

27 ago 2024, 17:07:20   Operador com email gianeboldrim@on.br na Conta d4a6a640-21d1-4ea0-ac83-474533e86e3c adicionou à Lista de Assinatura:
ribas@on.br para assinar, via E-mail, com os pontos de autenticação: Token via E-mail; Nome Completo; CPF; endereço de IP. Dados informados pelo Operador para validação do signatário: nome completo FELIPE BRAGA RIBAS e CPF 040.022.789-48.

27 ago 2024, 17:07:20   Operador com email gianeboldrim@on.br na Conta d4a6a640-21d1-4ea0-ac83-474533e86e3c adicionou à Lista de Assinatura:
tabare.gallardo@fcien.edu.uy para assinar, via E-mail, com os pontos de autenticação: Token via E-mail; Nome Completo; endereço de IP. Dados informados pelo Operador para validação do signatário: nome completo Tabare Gallardo.

27 ago 2024, 17:07:20   Operador com email gianeboldrim@on.br na Conta d4a6a640-21d1-4ea0-ac83-474533e86e3c adicionou à Lista de Assinatura:
chrystianpereira@on.br para assinar, via E-mail, com os pontos de autenticação: Token via E-mail; Nome Completo; CPF; endereço de IP. Dados informados pelo Operador para validação do signatário: nome completo CHRYSTIAN LUCIANO PEREIRA e CPF 085.598.609-32.

27 ago 2024, 17:18:35   FELIPE BRAGA RIBAS assinou. Pontos de autenticação: Token via E-mail ribas@on.br. CPF informado: 040.022.789-48. IP: 177.51.202.242. Componente de assinatura versão 1.967.0 disponibilizado em https://app.clicksign.com.

Clicksign

27 ago 2024, 19:08:58   Tabare Gallardo assinou. Pontos de autenticação: Token via E-mail
tabare.gallardo@fcien.edu.uy. IP: 167.62.158.240. Localização compartilhada pelo dispositivo
eletrônico: latitude -34.8323428 e longitude -55.9513369. URL para abrir a localização no mapa:
https://app.clicksign.com/location. Componente de assinatura versão 1.967.0 disponibilizado em
https://app.clicksign.com.

27 ago 2024, 19:21:09   MARCELO EMILIO assinou. Pontos de autenticação: Token via E-mail
marcelo_emilio@yahoo.com. CPF informado: 841.053.809-15. IP: 193.19.205.199. Localização
compartilhada pelo dispositivo eletrônico: latitude -25.09887393155978 e longitude
-50.15593105138987. URL para abrir a localização no mapa: https://app.clicksign.com/location.
Componente de assinatura versão 1.967.0 disponibilizado em https://app.clicksign.com.

27 ago 2024, 19:22:11   CHRYSTIAN LUCIANO PEREIRA assinou. Pontos de autenticação: Token via E-mail
chrystianpereira@on.br. CPF informado: 085.598.609-32. IP: 168.205.194.88. Componente de
assinatura versão 1.967.0 disponibilizado em https://app.clicksign.com.

28 ago 2024, 07:44:52   RICARDO GIL-HUTTON assinou. Pontos de autenticação: Token via E-mail ricardo.gil-
hutton@conicet.gov.ar. IP: 179.63.52.95. Componente de assinatura versão 1.967.0
disponibilizado em https://app.clicksign.com.

28 ago 2024, 10:54:02   Adrián Rodriguez Colucci assinou. Pontos de autenticação: Token via E-mail adrian@ov.ufrj.br.
IP: 164.73.83.172. Componente de assinatura versão 1.968.0 disponibilizado em
https://app.clicksign.com.

28 ago 2024, 11:58:08   Fernando Virgilio Roig assinou. Pontos de autenticação: Token via E-mail froig@on.br. CPF
informado: 213.132.548-78. IP: 200.20.187.172. Localização compartilhada pelo dispositivo
eletrônico: latitude -22.9376 e longitude -43.0473216. URL para abrir a localização no mapa:
https://app.clicksign.com/location. Componente de assinatura versão 1.969.0 disponibilizado em
https://app.clicksign.com.

29 ago 2024, 13:57:00   GIANE DO CARMO BOLDRIM assinou. Pontos de autenticação: Token via E-mail
gianeboldrim@on.br. CPF informado: 004.446.047-31. IP: 200.20.187.15. Componente de
assinatura versão 1.971.0 disponibilizado em https://app.clicksign.com.

29 ago 2024, 13:57:10   Processo de assinatura finalizado automaticamente. Motivo: finalização automática após a
última assinatura habilitada. Processo de assinatura concluído para o documento número
802abbcf-24a8-4510-afe5-f2eebe203af7.

My beloved mom and dad,

Cláudia e Lauri.

x

Acknowledgments

This thesis culminates years of hard work, dedication, and perseverance. Throughout this journey, I have been fortunate to receive the support, encouragement, and guidance of many remarkable individuals. Their contributions, whether big or small, have been invaluable to my personal and professional growth, and I am deeply grateful to everyone who has supported me along the way.

Gostaria de expressar minha profunda gratidão aos meus pais, Lauri Antônio Pereira e Cláudia Mara Grande Pereira, e ao meu irmão, Luis Guilherme Pereira. Seu amor incondicional, apoio e encorajamento foram fundamentais para que eu pudesse chegar até aqui. Vocês sempre acreditaram em mim, mesmo nos momentos mais difíceis, e me deram a força necessária para seguir em frente. Este trabalho é tanto uma conquista minha quanto de vocês, que sempre estiveram ao meu lado, torcendo por mim e me incentivando a nunca desistir dos meus sonhos. A vocês, meu mais sincero e profundo agradecimento. Sou imensamente grato à minha querida, Aline Trog Ferreira, por seu constante carinho e apoio. Sua presença e incentivo foram indispensáveis durante toda esta caminhada, trazendo alegria e força nos momentos em que mais precisei. Estendo esse agradecimento à todos meus amigos e amigas.

I would like to express my profound gratitude to my advisors, Dr. Felipe Braga-Ribas and Dr. Marcelo Emilio, for their exceptional guidance, unwavering confidence, and patience throughout this research. His expertise and dedication have been crucial to my academic and professional development. Dr. Braga-Ribas has provided invaluable insights and constructive feedback and created an environment that fostered my growth as a researcher. His belief in my abilities and his support have been instrumental in overcoming challenges and achieving the goals of this thesis. I am deeply thankful for the opportunities he has afforded me and for his continuous encouragement and mentorship.

I am deeply grateful for the financial support provided by Fundação Coordenação de Aperfeiçoamento de Pessoal de Nível Superior (CAPES), Fundação Carlos Chagas Filho de Amparo à Pesquisa do Estado do Rio de Janeiro (FAPERJ), and the Laboratório Interinstitucional de e-Astronomia (LIneA). Their funding and resources have been crucial in enabling the successful completion of this research. The support from these institutions has facilitated my academic progress and allowed me to carry out this work with the necessary resources and opportunities. Their support for travel to conferences and events

"What we observe is not nature itself, but nature exposed to our method of questioning."

Werner Heisenberg

Chrystian Luciano Pereira

RINGS DIVERSITY AROUND SMALL SOLAR SYSTEM BODIES:
DISCOVERIES AND DETECTION LIMITS

ABSTRACT

The first detection of a ring system through stellar occultation, a significant milestone in the history of planetary science, occurred in 1977. Then, astronomers unexpectedly discovered Uranus's rings while studying the planet's atmosphere. This discovery was followed by a similar one in 1984 when Neptune's rings were detected as arcs using the same method. A decade ago, a ring system was identified around the Centaur object (10199) Chariklo, marking the first instance of such a feature in a small body beyond the giant planets. This discovery suggested that ring systems might be more common among small Solar System bodies than previously believed, as evidenced by subsequent findings around the dwarf planet Haumea and the indications of rings or cometary material around the Centaur (2060) Chiron.

Considering that some authors suggest cometary activity might be related to the presence of rings, we sounded the vicinity of small bodies in the outer solar system, using the stellar occultation technique to search for signs of confined material. A stellar occultation happens when an object is observed blocking a distant star's light during a certain time interval. Observing the star's light before, during, and after the occultation lets us gather detailed information about the object's astrometric position, size, shape, atmosphere, and ring systems. In terms of spatial resolution, this highly precise method can reveal fine details that are otherwise difficult to detect from ground-based observations, making it invaluable for studying distant and faint Small Solar System Objects.

The Centaurs Objects (60558) 174P/Echeclus, 29P/Schwassmann-Wachmann 1 and (2060) Chiron exhibited regular outbursts, making them ideal targets for the search for confined material. We first examined light curves from stellar occultations of the active Centaur Echeclus observed between 2019 and 2021. While no features indicative of surrounding material were detected, strong detection limits were established, and the physical properties of Echeclus were derived. We observed the first stellar occultation by 29P in December 2022 and were able to find indications of confined material symmetrically distributed around the object. Occultation observations of Chiron were conducted in 2018, 2019, and 2022 to characterize its structures over time. The 2019 event, being the first multi-chord observation of this Centaur, allowed us to constrain its tri-axial dimensions. The 2022 observations confirmed previously proposed structures and revealed significant property variations, such as width and optical depth. A recent stellar occultation of Chiron in 2023 is still under analysis, but the high-resolution data obtained at Observatório

do Pico dos Dias may solve ongoing questions about Chiron's environment.

The greatest finding came after discovering a ring beyond the Roche limit around the Trans-Neptunian Object (50000) Quaoar. We conducted an observation campaign to further characterize this ring in 2022. Our analysis revealed the presence of a second ring around Quaoar, much closer to the main body but also located beyond the Roche limit.

This thesis presents the methods developed to search for, characterize, and place upper limits on detecting confined material around Small Solar System Object. We present observational evidence that material ejections alone are not capable of forming rings. Due to the diversity of the confined structures' location in the Solar System and their properties presented here, it is clearer that the formation of rings around small bodies can only result from a combination of factors, such as (primordial) collisions or ejection processes, allied with a favorable dynamical environment around the main body. Our findings and physical properties of the studied objects are presented in association with the respective research papers.

Chrystian Luciano Pereira

DIVERSIDADE DE ANÉIS AO REDOR DE PEQUENOS CORPOS DO SISTEMA SOLAR: DESCOBERTAS E LIMITES DE DETECÇÃO

RESUMO

A primeira detecção de um sistema de anéis por meio de ocultação estelar, um marco significativo na história da ciência planetária, ocorreu em 1977. Naquela ocasião, astrônomos descobriram inesperadamente os anéis de Urano enquanto estudavam a atmosfera do planeta. Esta descoberta foi seguida por uma similar em 1984, quando os anéis de Netuno foram detectados como arcos usando o mesmo método. Há uma década, um sistema de anéis foi identificado ao redor do objeto Centauro (10199) Chariklo, marcando a primeira ocorrência de tal característica em um pequeno corpo além dos planetas gigantes. Essa descoberta sugeriu que sistemas de anéis poderiam ser mais comuns entre pequenos corpos do Sistema Solar do que se acreditava anteriormente, como evidenciado por descobertas subsequentes ao redor do planeta anão Haumea e indicações de anéis ou material cometário ao redor do Centauro (2060) Chiron.

Considerando que alguns autores sugerem que a atividade cometária pode estar relacionada à presença de anéis, investigamos a proximidade de pequenos corpos no sistema solar externo, usando a técnica de ocultação estelar para procurar sinais de material confinado.

Uma ocultação estelar ocorre quando um objeto é observado bloqueando a luz de uma estrela distante durante um certo intervalo de tempo. Observar a luz da estrela antes, durante e após a ocultação nos permite coletar informações detalhadas sobre a posição astrométrica, tamanho, forma, atmosfera e sistemas de anéis do objeto. Em termos de resolução espacial, este método altamente preciso pode revelar detalhes finos que são difíceis de detectar em observações baseadas em solo, tornando-se inestimável para estudar Objetos Pequenos do Sistema Solar distantes e fracos.

Os objetos Centauros (60558) 174P/Echeclus, 29P/Schwassmann-Wachmann 1 (29P) e (2060) Chiron exibiram erupções regulares, tornando-os alvos ideais para a busca de material confinado. Primeiramente, examinamos curvas de luz de ocultações estelares do Centauro ativo Echeclus observadas entre 2019 e 2021. Embora nenhuma característica indicativa de material circundante tenha sido detectada, limites de detecção foram estabelecidos e as propriedades físicas de Echeclus foram derivadas. Observamos a primeira ocultação estelar por 29P em dezembro de 2022 e conseguimos encontrar indicações de material confinado simetricamente distribuído ao redor do objeto. Observações de ocultação de Chiron foram conduzidas em 2018, 2019 e 2022 para caracterizar suas estruturas ao longo do tempo. O evento de 2019, sendo a primeira observação multi-cordas deste Cen-

tauro, permitiu-nos restringir suas dimensões tri-axiais. As observações de 2022 confirmaram estruturas previamente propostas e revelaram variações significativas de propriedades, como largura e profundidade óptica. Uma ocultação estelar recente de Chiron em 2023 ainda está em análise, mas os dados de alta resolução obtidos no Observatório do Pico dos Dias podem resolver questões pendentes sobre o ambiente de Chiron.

A maior descoberta veio após a detecção de um anel além do limite de Roche ao redor do Objeto Transnetuniano (50000) Quaoar. Realizamos uma campanha de observação para caracterizar melhor esse anel em 2022. Nossa análise revelou a presença de um segundo anel ao redor de Quaoar, muito mais próximo ao corpo principal, mas também localizado além do limite de Roche.

Esta tese apresenta os métodos desenvolvidos para buscar, caracterizar e estabelecer limites superiores na detecção de material confinado ao redor de pequenos corpos do Sistema Solar. Apresentamos evidências observacionais de que apenas as ejeções de material não são capazes de formar anéis. Devido à diversidade da localização das estruturas confinadas no Sistema Solar e suas propriedades apresentadas aqui, fica mais claro que a formação de anéis ao redor de pequenos corpos só pode resultar de uma combinação de fatores, como colisões (primordiais) ou processos de ejeção, aliados a um ambiente dinâmico favorável ao redor do corpo principal. Nossos achados e propriedades físicas dos objetos estudados são apresentados em associação com os respectivos artigos de pesquisa.

Contents

List of Figures

xxii

List of Tables

List of Abbreviations

29P 29P/Schwassmann-Wachmann 1.

ALMA Atacama Large Millimeter Array.

ANAN Anan Science Center, Anan, Tokushima, Japan.

au astronomical unit.

AVI Audio Video Interlave.

C/A closest approach.

CAHA Calar Alto, Spain.

CCD charge-coupled device.

CFHT Canada France Hawaii Telescope.

CHEOPS CHaracterising ExOPlanet Satellite.

CO Carbon Monoxide.

DEC Declination.

ERC European Research Council.

FITS Flexi ble mage Transport System.

FOV Field of view.

FTN Faulkes Telescope North.

FWHM Full width at half maximum.

Gaia DR3 Gaia Data Release 3.

GPS Global Positioning System.

GTC Gran Telescope Canarias.

HiPERCAM High PERformance CAMera.

HSO Herschel Space Observatory.

HST Hubble Space Telescope.

IAU International Astronomical Union.

IRAF Image Reduction and Analysis Facility.

IRTF 3-m NASA Infrared Telescope Facility.

ISAM Interactive Service for Asteroid Models.

ISU Image Stabilizing Unit.

JFC Jupiter-family comet.

JPL Jet Propulsion Laboratory.

JWST James Webb Space Telescope.

KAO Kottamia Astronomical Observatory.

KBO Kuiper Belt Object.

KFIS Kottamia Faint Imaging Spectro-Polarimeter.

LCOGT 2-m Las Cumbres Observatory Global Telescope Network.

LSST Legacy Survey of Space and Time.

LST Local Solar Time.

MBA Main Belt Asteroid.

MMR Mean Motion Resonance.

MNRAS Monthly Notices of the Royal Astronomical Society.

MPC Minor Planet Center.

MSTG Mean Sidereal Time in Greenwich.

NEA Near-Earth Asteroid.

NIMA Numerical Integration of the Motion of an Asteroid.

NTP Network Time Protocol.

NTT New Technology Telescope.

OAMR Observatorio Astronómico Municipal de Reconquista.

OES Observatorio Estrela do Sul.

OP Occultation Portal.

OPD Observatório do Pico dos Dias, Brazil.

P/A Position angle of the semi-minor axis.

PACS Photodetector Array Camera and Spectrometer.

PE160 Perkin-Elmer 1.60-meter telescope at OPD.

PRAIA Package for the Reduction of Astronomical Images Automatically.

Q1R Quaoar's first ring.

RA Right Ascension.

RECON Research and Education Collaborative Occultation Network.

ROI Region of Interest.

RUWE Renormalised Unit Weight Error.

S/N signal-to-noise ratio.

SAGE Shaping asteroid models using genetic evolution modeling algorithm.

SDO Scattered Disk Objects.

SDSS Sloan Digital Sky Survey.

SER uncompressed video format.

SG Savitzky-Golay digital filter.

SOAR SOuthern Astrophysical Research telescope.

SOR Spin-orbit resonance.

SORA Stellar Occultation Reduction and Analysis.

SPECULOOS-IO Search for habitable Planets EClipsing ULtra-cOOl Stars.

SPIRE Spectral and Photometric Imaging Receiver.

SSD Solar System Database.

SSSO Small Solar System Object.

TAOS II Transneptunian Automated Occultation Survey.

TNO Trans-Neptunian Object.

TRAPPIST-South TRAnsiting Planets and PlanetesImals Small Telescope - South.

TUHO Tohoku University Haleakala Observatory.

VTI Video Time Inserter.

WIRCam Wide-field InfraRed Camera.

List of Symbols

B Ring opening angle with the line of sight.

I Transmitted flux.

I_0 Incident flux.

L_f Fresnel scale.

T Transmittance.

W' Ring width in the sky plane.

W_r Ring width in the plane of the rings.

Δ_km Distance from the occulting object to the observer in kilometers.

Δ_au Distance between the target object and Earth.

α_obj, δ_obj Astrometric position of the object.

α_pole, δ_pole Right Ascension and Declination of the pole orientation.

χ^2_{pdf} Chi-square per degree of freedom.

ϵ' Apparent oblateness.

λ Wavelength of the observation.

$\mathrm{E_r}$ Earth's radius.

$\mathrm{H_o}$ Absolute magnitude of the object.

$\mathrm{H_\odot}$ Absolute magnitude of the Sun.

$\mathrm{R_{equiv}}$ Equivalent radius.

$\phi_\mathrm{i,model}$ Point of the modeled light curve.

$\phi_\mathrm{i,obs}$ Point of the observed light curve.

ρ Density.

$\sigma_{\mathrm{i,phot}}$ Photometric uncertainty.

σ_{model} Modeled ellipse.

τ Actual optical depth.

τ' Apparent optical depth.

τ_{N} Normal optical depth.

a Semi-major axes.

a' Apparent semi-major axis .

a_{Roche} Roche radius.

e Orbital eccentricity.

f_0, g_0 Object's center in the tangent plane.

mas Milliarcseconds.

p Actual opacity, the fractional transmission in amplitude.

p' Apparent opacity, fractional transmission in intensity.

p_{N} Normal opacity, the opacity measured in the ring plane.

r' Ring distance measured along the radius vector from the center of the main body to the center of the ring.

$r_{\star}$ Apparent star size.

t_{exp} Exposure time.

v_{N} Apparent star velocity normal to the local limb.

$v_{\perp}$ Local velocity perpendicular to the ring.

A_{τ} Equivalent depth.

E' Equivalent width as measured in the sky plane.

E_{p} Equivalent width as measured in the ring plane.

S_{r} Search radius.

Chapter 1

Introduction

It is believed that shortly after the giant planets formation, their orbits differed from what we observe today. The Nice model suggests that the four giant planets initially had nearly circular orbits around the Sun, ranging between 5.5 astronomical unit (au) and 17 au (GOMES *et al.*, 2005; LEVISON *et al.*, 2008; TSIGANIS *et al.*, 2005). In this more compact configuration, the sequence of the planets was Jupiter, Saturn, Neptune, and Uranus, which frequently exchanged positions due to their dynamic gravitational interactions, followed by a disk of planetesimals. These gravitational interactions eventually moved Saturn, Uranus, and Neptune to their current orbits. Additionally, these interactions destabilized and scattered the orbits of small bodies, forming distinct populations such as the Trojans and Kuiper Belt objects. The migration of Neptune and Uranus to the outer regions scattered the Kuiper Belt planetesimals throughout the Solar System. While newer simulations suggest variations in these scenarios, such as differences in the timing and sequence of planetary migrations (BATYGIN e BROWN, 2010; MORBIDELLI, 2010), a common point remains: the dynamic and physical evolution of small bodies in the outer Solar System is closely linked to the orbital evolution of the giant planets. Therefore, studying the physical properties of these small bodies not only enhances our understanding of their individual histories but also provides crucial insights into the broader processes of Solar System formation and evolution.

The Solar System hosts many small objects besides the planets, including asteroids, comets, dwarf planets, and distant icy bodies. These objects range from being very close to the Sun, such as the asteroid 2021 PH27 with a perihelion at 0.12 au, to having far-reaching orbits, like the dwarf planet Sedna, which reaches an aphelion distance of about 940 au. Beyond these distances, objects are found from $2,000$ au to $200,000$ au (LEVISON e DONES, 2007), in the proposed reservoir of small icy planetesimals known as the Oort Cloud, a concept first hypothesized by Jan Oort in 1950. As of July 2024, Jet Propulsion Laboratory (JPL) Solar System Database (SSD) lists $1,385,906$ Small Solar System Objects (SSSOs), including asteroids, Kuiper Belt Objects (KBOs), Trans-Neptunian

Objects (TNOs) as well as 3,956 comets (including fragments) [1]. These numbers are expected to increase to approximately 5.5 million by the end of the Legacy Survey of Space and Time (LSST), with estimates including approximately 100,000 Near-Earth Asteroids (NEAs), 5,000,000 Main Belt Asteroids (MBAs), 280,000, Jovian Trojans, 40,000 TNOs, and 10,000 Comets (VERA C. RUBIN OBSERVATORY LSST SOLAR SYSTEM SCIENCE COLLABORATION *et al.*, 2021).

SSSOs are categorized into several classes based on their characteristics, including location, composition, and orbital dynamics. The main classes include MBAs, which orbit the Sun between Mars and Jupiter; Near-Earth Asteroids NEAs, which have orbits that bring them close to Earth; and objects that share orbits with larger planets, such as Jupiter and Neptune Trojans, located at the stable Lagrangian points (L4 and L5). The Trojans constitute the second-largest reservoir of asteroids in the inner Solar System (BOTTKE *et al.*, 2002). Another class of objects, known as Centaurs, follows chaotic orbits around the Sun between Jupiter and Neptune, with perihelion distances greater than 5.2 au and semi-major axes less than 30.1 au (GLADMAN *et al.*, 2008; HORNER *et al.*, 2004). Approximately 10% of known Centaurs are active and exhibit cometary characteristics, such as comas, dust, and gas jets, despite being in asteroidal orbits (JEWITT, 2009). The exact origin of the bodies forming the Centaur class is not well-established; it is hypothesized that these bodies may evolve from Scattered Disk Objects (SDO) or other TNO populations into the Centaur region (VOLK e MALHOTRA, 2008). This evolutionary process likely involves initial migration into Neptune-crossing orbits, followed by scattering into the regions of Jupiter and Saturn (MORBIDELLI, 2008), potentially leading to their classification as short-period comets, specificallyJupiter-family comets (JFCs) (BAUER *et al.*, 2013; FERNÁNDEZ, 2009; SARID *et al.*, 2019).

In the outer regions of the Solar System, we also find dwarf planets (except Ceres, which is located in the MBA region) and TNOs. TNOs are further divided into Classical KBOs, Resonant KBOs, SDOs, and Detached Objects (DELSANTI e JEWITT, 2006). Classical KBOs, also known as Cubewanos (a term derived from the discovery of 1992 QB1 (JEWITT e LUU, 1993)), have relatively circular orbits with eccentricities (e) ranging from 0 to 0.2 and semi-major axes (a) around 42 au, reflecting the conditions of the early accretion phase of the Solar System. The inclination distribution of Classical KBOs is bimodal, dividing them into Hot Classicals (with inclinations $i > 12°$) and Cold Classicals (with inclinations $i \leqslant 4°$) (BROWN, 2001; ELLIOT *et al.*, 2005).

Cold Classicals are characterized by low orbital inclinations and eccentricities. Approximately 30% of the Cold Classicals are binary systems with similar components in size and color (FRASER *et al.*, 2017), which supports the *in situ* formation theory via the streaming instability process. This theory predicts that most planetesimals form in binary or multiple systems (NESVORNÝ *et al.*, 2019). In contrast, the Hot Classicals

---

[1] https://ssd.jpl.nasa.gov/

appear to have formed and evolved in a massive planetesimal disk characterized by a dynamically hot and collisional environment. These objects were transported to their current positions through scattering encounters with Neptune (LEVISON *et al.*, 2008). This theory is further supported by the binary characteristics observed in these objects. Unlike the Cold Classicals, most moons of Hot Classicals are significantly smaller than the primary body, suggesting they were accreted from a disk around the primary, which likely formed from the collision of two planetesimals (LEINHARDT *et al.*, 2010).

At the same time, the Resonant objects are trapped in a Mean Motion Resonance (MMR) with Neptune, such as the Plutinos, which are in a 3:2 MMR (at 39.4 au), the "Twotinos" in the 1:2 MMR (at 43.6 au), and smaller families within 3:5 MMR, 4:7 MMR, 2:5 MMR, and others. SDOs have highly inclined and elliptical orbits, with perihelia varying between approximately 30 and 40 au. Detached Objects have orbits with perihelia $q > 40$ au, far enough from Neptune to be free from its significant gravitational influence (JEWITT, 2009). Sedna is the most famous example of a Detached Object (BROWN *et al.*, 2004).

Other structures and cometary coma have been observed around some SSSO. Rings were first detected around a small body in June 2013 during a stellar occultation by the Centaur object (10199) Chariklo (BRAGA-RIBAS *et al.*, 2014). The second known object that hosts a ring system also discovered using the stellar occultation technique, is the elongated dwarf planet (136108) Haumea (ORTIZ *et al.*, 2017). Later, a remarkable ring system was discovered around the TNO (50000) Quaoar using multi-epoch stellar occultations (MORGADO *et al.*, 2023; PEREIRA *et al.*, 2023). The rings of Quaoar designated 2023 Q1R (Quaoar's first ring, Q1R for short) and 2023 Q2R (Quaoar's second ring, Q2R for short) are particularly notable for being located well beyond the classical Roche limit, assuming any realistic bulk density for the ring particles. Rings were also proposed to orbit around the Centaur (2060) Chiron (ORTIZ *et al.*, 2015, 2023; SICKAFOOSE *et al.*, 2023). However, the very nature of the secondary structures is still in debate, with some interpretations suggesting they may be cometary jets or an inner dense coma (BUS *et al.*, 1996; ELLIOT *et al.*, 1995; RUPRECHT *et al.*, 2015; SICKAFOOSE *et al.*, 2020).

Although rings' origins around these small bodies remain a topic of debate, several mechanisms have been proposed for their formation. These include the excavation of material by collisions (CANUP, 2004), the tidal disruption of an external body that crossed the planet's Roche limit (NOLL *et al.*, 2008), and the lofting of material due to cometary-like activity (BRAGA-RIBAS *et al.*, 2013). However, the most accepted hypothesis is that the rings around the Centaurs may have formed when these objects were in the KBO region, surviving their implantation in the closer region (ARAUJO *et al.*, 2018). It is suggested that particles were ejected from the parental body into an orbit within the Roche radius, possibly during the close encounters with giant planets (PAN e WU, 2016). The discovery of Quaoar's rings now challenges the Roche limit's

long-standing and widely accepted concept.

The lifetime of Centaurs is at least one order of magnitude longer (10^6 years) than the collisional spreading timescale of Chariklo's rings (10^5 years)(PAN e WU, 2016). Proposed mechanisms for ring formation, such as outbursts or excavation by collisions, are likely only to sustain pre-existing rings, thereby extending their lifetimes. Additionally, shepherd satellites can increase the rings' lifetimes by preventing them from dispersing and maintaining their structure (CHARNOZ et al., 2018), allowing them to persist until discovered by us.

The collisional (dense) rings observed around the giant planets lie within the Roche radius (a_{Roche}) of the central body, assuming the ring particles have the same bulk density (ρ) as the small inner Saturnian satellites ($\rho = 400\,\mathrm{kg\,m^{-3}}$) (ESPOSITO e DE STEFANO, 2018; THOMAS e HELFENSTEIN, 2020). This phenomenon is also observed in the rings around Haumea and Chariklo (despite uncertainties in Chariklo's mass). However, both of Quaoar's rings are located well beyond the Roche limit ($a_{\mathrm{Roche}} = 1,780$ km) when considering a realistic bulk density of $\rho = 400\,\mathrm{kg\,m^{-3}}$ for ring particles (MORGADO et al., 2023). Outside the Roche limit, particles are expected to accrete in a small satellite within a few decades (KOKUBO et al., 2000; TAKEDA e IDA, 2001) due to the energy loss during collisions, as the velocity dispersion tends to be lower than the escape velocity between two particles, resulting in accretion. To prevent accretion, a mechanism that increases the velocity dispersion is required. External factors, such as Spin-orbit resonance (SOR) between ring particles and central body, as well as MMR between Quaoar and its satellite Weywot, or the presence of an unknown shepherd satellite, may excite the ring particles, increase velocity dispersion, and preventing accretion, thereby explaining the ring confinement (e.g. MORGADO et al., 2023, and references therein). Internal factors, such as elastic collisions in ice-ice particles, can also increase the velocity dispersion and prevent the accretion of particles across a wide range of plausible bulk densities ($\rho \sim 5,000\,\mathrm{kg\,m^{-3}}$).

The rings around Chariklo, Haumea, and Quaoar (Q1R) share this common characteristic: they are located close to the 1:3 SOR with their respective central bodies. This means that a ring particle completes one orbit for every three rotations of the central body. Although the precision of the resonance locations does not allow for confirmation of an exact resonance configuration (due to uncertainties in the mass of the central body, for instance), this has led to investigations into ring behavior using N-body collisional codes under the influence of the 1:3 SOR. Initial findings suggest that a spreading ring becomes confined once the resonance is introduced (SALO et al., 2021a; SICARDY et al., 2021). However, this confinement remains not fully understood, as there are no theoretical frameworks yet developed to explain the behavior of a collisional disk under the influence of a second-order resonance like the 1:3 SOR. Therefore, the 1:3 SOR appears crucial for the ring's confinement.

Rings around Centaurs and hot Classical KBO have been observed, demonstrating a presence at vastly different heliocentric distances. This raises the question of whether rings might also be present around other classes of small bodies, including cold Classical, resonant objects, and Scattered Disk Objects. Additionally, these rings vary significantly in their physical properties, such as optical depth and radius. Further questions concern whether the origin of these rings is linked to the primordial collisional environment, significant gravitational perturbations from the giant planets, or the ejection of material through Carbon Monoxide (CO) or other volatile sublimation. Understanding these mechanisms is crucial for comprehending the formation and evolution of rings and their parent bodies in various contexts. In this study, we investigate different SSSO with the potential to host rings or other confined structures. Among them, Echeclus and 29P/Schwassmann-Wachmann 1 exhibited multiple ejection events but no clear ring signature. At the same time, Chiron increased its brightness and had several secondary detections in the occultation light curves. On the other side, our observations led to the discovery of faint and non-homogeneous rings around Quaoar, a hot Classical Kuiper Belt object located approximately 42 au from the Sun, with no evidence of activity.

This study outlines the procedures for predicting, reducing, and analyzing stellar occultation events, focusing on semi-transparent structures. We detail the methodologies employed at each stage for events involving Chiron, Echeclus, 29P, and Quaoar. Observations of Chiron's stellar occultations in 2018 and 2019 allowed us to probe its surroundings and establish detection limits for these structures. Notably, this also marks the first time that the shape of the primary body has been constrained, providing new insights into its physical characteristics. This work was published in Astronomy & Astrophysics in 2023. Furthermore, a stellar occultation by Chiron in 2022 revealed the central body and additional surrounding structures, suggesting potential temporal changes in these features. Our analysis proposes a new pole orientation for the suspected rings, also published in Astronomy & Astrophysics Letters in 2023. The most recent event by Chiron observed in 2023 is currently under analysis, and preliminary results are presented in this manuscript.

We also conducted investigations of stellar occultations by two additional active centaurs, Echeclus (three events) and 29P (one event), to explore their surrounding regions. Our objective was to identify and characterize putative structures formed by particles ejected from their surfaces during periods of cometary activity that may have been trapped in an orbit around the body. The analysis of Echeclus occultation allowed the tri-dimensional model and pole position proposed in the literature to be compared with the sky-projected body's limb. In this case, no additional material was detected around the central body within our detection limits. The results were published in Monthly Notices of the Royal Astronomical Society (MNRAS) (PEREIRA *et al.*, 2024). The stellar occultation by the Centaur 29P observed in December 2022 was the first detection of this object using this technique, resulting in a very accurate astrometric position that feeds

the ephemeris and improves the orbit. Additionally, we probe the nucleus' vicinity to search for secondary extinction features in the light curve. We found at least two points exceeding our detection limits at 3σ, besides a semi-transparent structure close to the nucleus, interpreted as a dense dust cloud above the comet's surface. These results are part of a scientific paper recently submitted to the Philosophical Transactions of the Royal Society A.

In February 2023, we reported the discovery of the Quaoar's first ring in a paper published in Nature (MORGADO *et al.*, 2023). Stellar occultations observed in June 2020 with the CHaracterising ExOPlanet Satellite (CHEOPS) space telescope, in August 2021 in Australia, and in June 2019 with Gran Telescope Canarias (GTC) revealed flux variations consistent with a ring around Quaoar. We revisited light curves from past events to search for detections compatible with this proposed ring. We calculated the ring's orbital radius and pole orientation using all events where secondary detections were identified. To better characterize this ring, we predicted new stellar occultations by Quaoar's rings. We identified a promising event on August 9, 2022, with the object's shadow passing over Hawaii, northern Mexico, and the continental United States. We obtained nine positive detections of the main body, allowing us to refine our understanding of its physical properties. The highest signal-to-noise ratio data were obtained with Canada France Hawaii Telescope (CFHT) and Gemini North telescopes, which not only confirmed the presence of the ring and its azimuthal optical depth and width variations proposed by (MORGADO *et al.*, 2023). The data also allowed another surprising discovery: a new inner ring around Quaoar. Using the light curves obtained from the 2022 stellar occultation, we detected a new structure while determining detection limits for the size and brightness of surrounding features. This structure, located approximately $2,520$ km from Quaoar's center, is consistent with a circular ring co-planar with the previously discovered ring. These results, briefly described above, are part of a Letter to the Editor published in the journal Astronomy & Astrophysics (PEREIRA *et al.*, 2023) and detailed in this work.

In this thesis, I show that rings around SSSO are found in very different environments and are presented with diverse physical characteristics and distances. I will also show that activity, feeding the object's close environment, may not be sufficient to produce a ring and that rings are found in much different environments than previously thought. During my Ph.D., I successfully applied the stellar occultation technique to study many objects, revealing details about their composition, structure, and surroundings. While focused on searching and detecting additional structures around small bodies, which resulted in six scientific papers, being the lead author of three of them. I have also collaborated on analyzing several stellar occultation events within the Lucky Star Team. This collaborative work led to eight other scientific papers, with further publications anticipated. These papers are attached in the Appendix Section.

Chapter 2

Methods

2.1 Stellar occultations by opaque bodies

2.1.1 Predictions

As previously mentioned, a stellar occultation occurs when a SSSOs passes before a distant background star, blocking its light. The timing and location of this event can be calculated using the astrometric position of the star to be occulted and the ephemeris of the occulting body. A stellar occultation is observable if the combined uncertainties of the ephemerides and star position are comparable to the radius of the occulting body. The following procedures, detailed by ASSAFIN *et al.* (2010) and GOMES-JÚNIOR *et al.* (2022), have been successfully used to predict stellar occultations by various SSSOs.

The star positions are retrieved from stellar catalogs, with Gaia Data Release 3 (Gaia DR3) (GAIA COLLABORATION *et al.*, 2016, 2023) being currently the most precise, offering positional accuracy better than one milliarcseconds (*mas*). We use the ephemeris obtained with the Numerical Integration of the Motion of an Asteroid (NIMA) method (DESMARS *et al.*, 2015) for the occulting body. This method calculates the orbit based on observations available from the Minor Planet Center (MPC) and additional observations at the OPD and Calar Alto, Spain (CAHA), along with precise astrometric positions from previous stellar occultations. In the case of the astrometric positions of the stars, the remarkable precision in their proper motion means that even when propagated to moments distant from the time of the catalog, these positions remain very precise.

The prediction of stellar occultations begins by calculating the closest approach (C/A) distance between the propagated astrometric positions of the stars and the small body. A potential stellar occultation is identified if this calculated distance is smaller than a search radius (S_r). When predicting events that project a shadow on the Earth's surface, it is necessary to account for its radius in these calculations to ensure accurate shadow
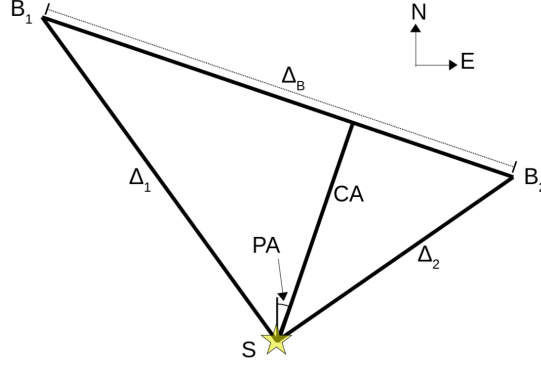
Figure 2.1: Geometric scheme of a stellar occultation. The star "S" represents the candidate star, while B_1 and B_2 denote the positions of the target body at the consecutive instants t_1 and t_2, respectively. The angular separations Δ_1, Δ_2 represent the distances between the star and the target body at B_1 and B_2, respectively. Δ_B indicates the angular separations between the star and the body's position and between the two consecutive positions of the target body. Image from GOMES-JÚNIOR *et al.* (2022).

path predictions. The search radius S_r is defined by

$$S_r = \tan^{-1}\left(\frac{E_r + T_r}{\Delta_{au}}\right), \tag{2.1}$$

where E_r is the Earth's radius, T_r is the target object's radius, and Δ_{au} is the distance between the target object and Earth. Figure 2.1 presents the geometry of a stellar occultation, where B_1 and B_1 are the ephemeris positions at two consecutive instants t_1 and t_2 with $t_2 > t_1$, and Δ_B is the difference between B_1 and B_2. Δ_1 and Δ_2 are the angular separations between the stellar astrometric position to B_1 and B_2. The distance of the C/A is then calculated with

$$C/A = \sqrt{\Delta_1^2 - \left(\frac{\Delta_1^2 - \Delta_2^2 + \Delta_B^2}{2\,\Delta_B}\right)}, \tag{2.2}$$

and the closest approach instant t_0 is obtained from

$$t_0 = t_1 + (t_2 - t_1)\sqrt{\frac{\Delta_1^2 - C/A^2}{\Delta_B^2}}. \tag{2.3}$$

The shadow velocity v_s at the Earth's surface is given by

$$v_s = \frac{\Delta \sin(C/A)}{t_2 - t_1}. \tag{2.4}$$

The next parameters to calculate in a stellar occultation are the Position angle of the semi-minor axis (P/A) and the Local Solar Time (LST) at the sub-planet point. The

P/A is defined as the angular displacement of the body relative to the star at its closest
approach and equals zero when the body is directly north of the star. It is measured in a
clockwise direction. The P/A and the C/A provide the exact location and the direction
of the shadow path over the Earth, while LST gives the solar time of the C/A, roughly
indicating whether the event will occur at night or during the day. These parameters are
given by

$$\text{LST} = t_0 + \text{long} = t_0 + \text{RA} + \text{MSTG}, \tag{2.5}$$

where RA is the Right Ascension of the body at C/A, and MSTG is the Mean Sidereal
Time in Greenwich at t_0, and

$$\text{P/A} = \tan^{-1}\left(\frac{\sin(\delta_2)\cos(\delta_1) - \cos(\delta_2)\sin(\delta_1)\cos(\Delta\alpha)}{\sin(\Delta\alpha)\cos(\delta_2)}\right) \tag{2.6}$$

Quaoar, GaiaDR3+pmGaiaDR3, NIMAv18   Offset: 0.0mas 0.0mas
updated: 2023-09-22 by Lucky Star

yyyy mm dd hh:mm:ss.s	RA_star_J2000	DE_star_J2000	C/A	P/A	vel	Delta	G*	RP*	H*
2024-08-06 01:19:54.8	18 32 48.8944	-15 03 47.384	0.073	169.27	-19.26	41.8547	16.0	15.0	99.9
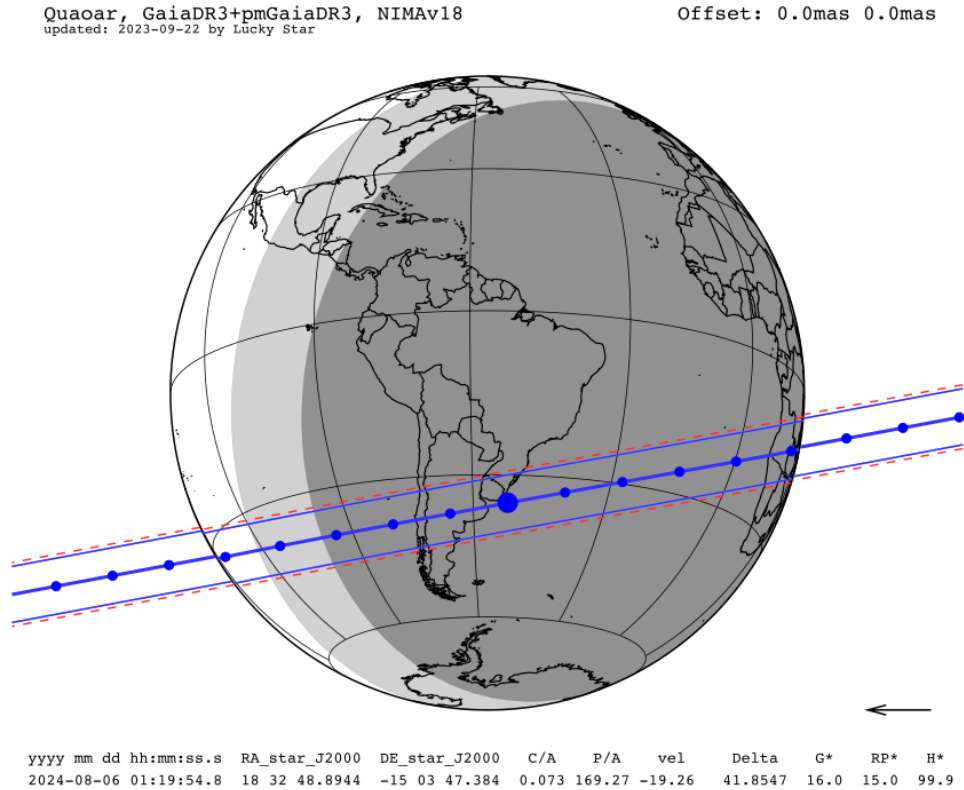
Figure 2.2: The figure shows a prediction map of a stellar occultation by Quaoar. The blue
lines indicate the boundaries of the body's shadow, while the red dashed lines represent
the 1σ uncertainty in the predicted shadow path. The large blue dot marks the point
of the closest approach, with smaller blue dots indicating one-minute intervals along the
path. The arrow on the bottom left indicates the direction of the shadow's motion. Image
from https://lesia.obspm.fr/lucky-star/occ.php?p=131362

Finally, we can generate the prediction map with this information and the conditions
to observe the event, as presented in Figure 2.2. The bottom label displays various key

parameters: the instant of closest approach (t_0), the star's Right Ascension (RA) and Declination (DEC) (J2000), the C/A, the position angle of the semi-minor axis (P/A), and the shadow velocity (where the negative signal indicate the East to West direction, also represented by the arrow). Additionally, it shows the geocentric distance (Δ_{au}) between Quaoar and Earth, and the Gaia G, RP, and H star magnitudes normalized to a body moving at $20\,km\,s^{-1}$ (indicated by the *). This stellar occultation event, like many others, was predicted under the framework of the European Research Council (ERC) Lucky Star project and is publicly accessible through the project's webpage.

In addition to ground-based predictions, our team also predicted and observed stellar occultations using space telescopes. The main advantage of using space telescopes lies in the high photometric quality obtained without interference from the Earth's atmosphere, allowing the detection of fine structures such as rings and atmosphere around target bodies. The first instance of this achievement was with ESA's CHaracterising ExOPlanet Satellite (CHEOPS, BENZ *et al.*, 2021) during an event involving the TNO (50000) Quaoar in 2020 (MORGADO *et al.*, 2022). The spacecraft detected this event, contributing to a series of observations that led to the discovery of Quaoar's first ring (Q1R) (MORGADO *et al.*, 2023). Additionally, in late 2022, a stellar occultation by the Centaur object (10199) Chariklo was predicted and observed by the James Webb Space Telescope (JWST, GARDNER *et al.*, 2023), with a positive detection specifically for the rings.

2.1.2 Observational campaigns

In the previous section, we described how a stellar occultation is predicted. Once we have the prediction maps, the next step is to organize observation campaigns. The first step is to select the most promising events, considering some factors, such as the star's brightness (typically with a magnitude of < 16), the geographic region where the shadow will pass, and the confidence level of the prediction. Additionally, we assess the scientific interest of the small body involved in the occultation. After selecting these events, we make the prediction public and invite amateur and professional astronomers to observe, aiming to optimize the distribution of observers through the shadow path. This coordination is facilitated through the Lucky Star web page and supported by tools such as Occult[1], OccultWatcher[2], and OccultWatcherCloud[3].

The increasing number of predicted and detected stellar occultations (BRAGA-RIBAS *et al.*, 2019) highlighted a need for better organization of observational information from the observers and coordinated storage of acquired data. To address this issue, the Occultation Portal (OP, KILIC *et al.*, 2022) was developed. The Occultation Portal (OP)

---

[1] http://www.lunar-occultations.com/iota/occult4.htm
[2] https://www.occultwatcher.net/
[3] https://cloud.occultwatcher.net/

is a web portal where users can select a predicted event and register their participation, providing details about their instrumental setup and observation site location. As of June 2024, the portal has registered 1,025 sites, listed 1,295 predicted events, and recorded 1,866 reports. Figure 2.3 shows a map of the registered observation sites. After an event, observers can indicate whether the event was positive and, if so, upload the acquired data to the portal. This system allows the researcher responsible for the event to access and analyze data from all observers, ensuring a comprehensive campaign analysis. The OP can be accessed at https://occultation.tug.tubitak.gov.tr/.

Map of Observation Sites Registered in OP (June 11, 2024)
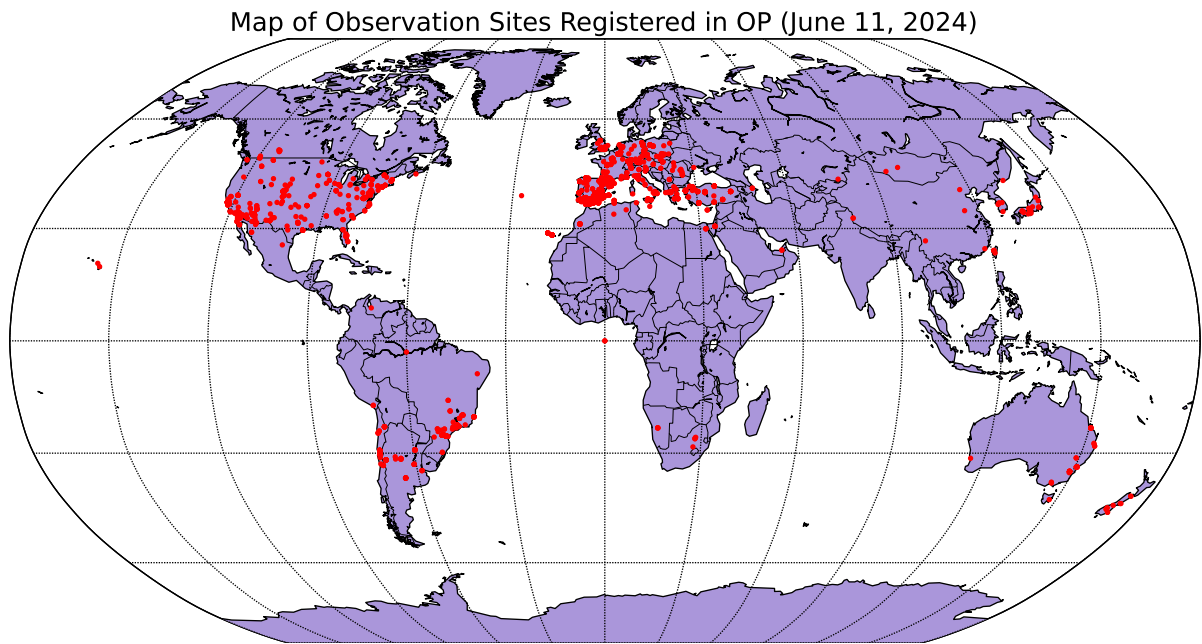
Figure 2.3: Distribution of 1,025 observation locations (marked as red dots) reported by OP observers as of June 2024, displayed on a world map. Credits: Y. Kilic/Occultation Portal.

The accuracy of object measurements depends on the quality and quantity of images acquired along the observation, meaning a high image cadence and the highest image quality (highest signal-to-noise ratio (S/N)). Some cameras experience what is known as "dead time", the period during which pixels are read and when the sensor does not record new information. Minimizing this dead time is crucial for obtaining precise measurements of the object's size and detecting narrow structures in its surroundings. Most cameras the amateur community uses exhibit negligible dead time due to using frame-transfer sensors. Other methods for sensors without this technology can reduce dead time, such as image binning or selecting a sub-frame containing the Region of Interest (ROI).

Recording the absolute time is another crucial element in achieving accurate size and shape determination for the object, with precision at the sub-kilometer level. To ensure accuracy, all observers involved in the observation campaign must adhere to a synchronized time standard. Precise synchronization, often within milliseconds, is typically achieved

using Global Positioning System (GPS) devices. This temporal data can usually be extracted directly from the image headers, whether charge-coupled device (CCD) or other formats capture the images through video cameras. Commercial cameras used by amateur astronomers, such as the QHY174M-GPS came with built-in GPS capabilities. In contrast, cameras like the Watec - 910HX video camera do not have built-in GPS and rely on an external device called a Video Time Inserter (VTI)[4], which uses a GPS signal to write timestamps onto the video frames. Additionally, when GPS is unavailable, Network Time Protocol (NTP) can be used as an alternative for time synchronization.

2.1.3 Differential aperture photometry

The variety of sensors used to acquire data from stellar occultations results in multiple data sets for the same event. Some observers record the event using the Flexi ble mage Transport System (FITS) format, while others use Audio Video Interlave (AVI) or uncompressed video format (SER)[5] formats. These video files are converted to the FITS image format using Python routines based on `astropy` (ASTROPY COLLABORATION *et al.*, 2013). The image treatment begins with standard calibration procedures, such as Bias and Flat-field corrections, if provided by the observers. These calibrations are performed using the Image Reduction and Analysis Facility (IRAF, BUTCHER e STEVENS, 1981). We can perform differential aperture photometry after correcting the scientific images for systematic effects and pixel sensibility. This process involves measuring the flux of the target star and comparing it with the flux of reference stars in the same Field of view (FOV). All these procedures are conducted using the FORTRAN based software Package for the Reduction of Astronomical Images Automatically for photometry (PRAIA, ASSAFIN, 2023). Figure 2.4 shows two frames extracted from the data set of a stellar occultation event by Quaoar observed on August 9, 2022. The procedure involves summing the counts of all pixels within the photometric aperture (red for the target star, green for the reference star in Figure 2.4) and subtracting the provisional flux by accounting for sky background contamination. The sky background contamination is calculated using the blue ring surrounding both stars, determining the sky flux per pixel. Additionally, measurements of the reference stars' flux are taken with well-distributed sampling across the field of view to mitigate low-frequency fluctuations in the stars' flux caused by variations in the sky's transparency. Finally, the flux ratio is normalized by considering regions outside the time windows that contain the central occultation or noticeable partial drops in the flux in the case of the additional structures around the main body.

A high frame rate allows for better temporal resolution in the data, crucial for detecting narrow structures and gradual flux variations in the target star's light. However, high

---

[4]https://occultations.org/observing/recommended-equipment/iota-vti/

[5]A simple image sequence format. Documentation can be found in http://www.grischa-hahn.homepage.t-online.de/astro/ser/
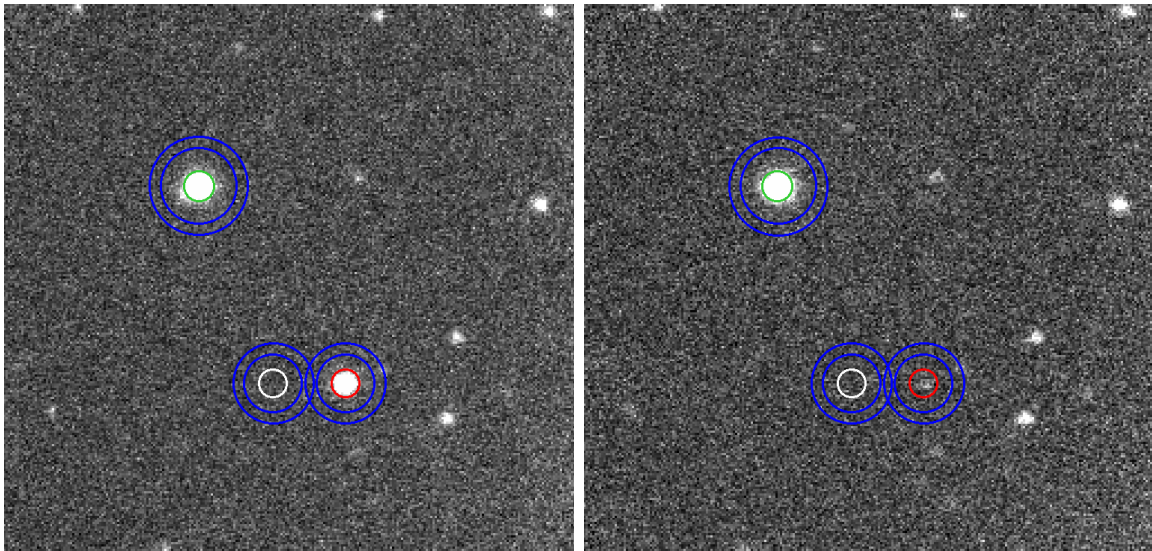
Figure 2.4: Frames from stellar occultation by Quaoar observed using the Gemini North telescope and the Alopeke' instrument (Red camera, SDSS-z' filter). The left panel shows an image before the occultation event, while the right panel shows the target star being occulted by Quaoar. The target star, reference star, and background flux (ghost) photometry aperture are marked by red, green, and white regions, respectively. The blue region indicates the sky background ring.

temporal resolution alone is insufficient; obtaining a light curve with low dispersion is also essential to accurately identify fine structures. This accuracy requires the target star's flux to be significantly higher than the background sky flux, resulting in a high S/N. Figure 2.5 shows a positive light curve obtained from the Gemini North (SDSS-r' filter) data set analysis of a stellar occultation by Quaoar on August 9, 2022. The measured fluxes of the target and reference stars show variations due to changes in sky transparency, especially after $24,000$ seconds from the reference time. When the flux ratio is calculated, these variations are mitigated, resulting in a flat light curve aside from the main body and ring events. The fluxes are plotted as a function of time relative to a reference instant, typically set at midnight on the date of the occultation.

2.1.4 Modeling a positive light curve

The moments when the star's flux disappears (ingress) and reappears (egress) behind the body's limb can be determined by modeling the positive light curve. The simplest model assumes the star is a point source blocked by an opaque body, represented geometrically without an atmosphere. However, critical physical parameters, such as Fresnel diffraction and the star's apparent diameter at the object's distance, may significantly affect the observed light curves and should be considered in the modeling process. All the procedures described in this subsection are performed using the python package Stellar Occultation
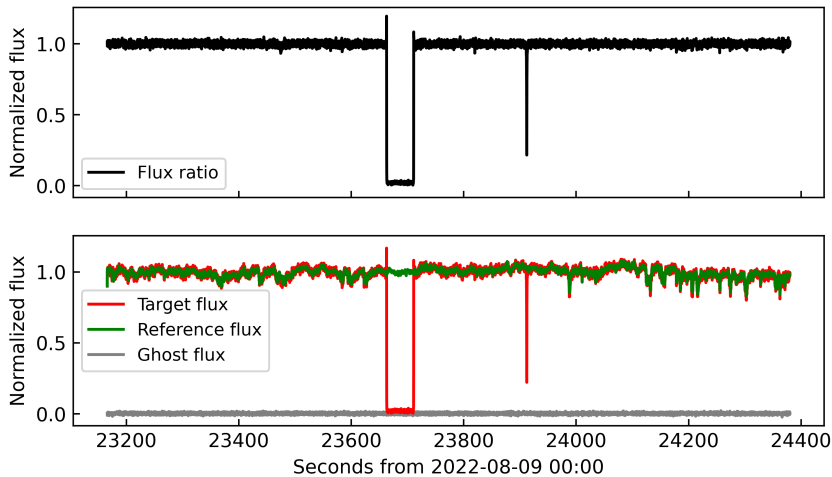
Figure 2.5: Positive light curve obtained from Gemini North telescope with the Alopeke'
instrument (Red camera, SDSS-z' filter) during the stellar occultation by Quaoar on
August 9, 2022. The black curve in the top panel shows the flux ratio. In the bottom
panel, the red curve represents the normalized flux of the target star, the green curve shows
the normalized flux of the reference star, and the grey curve displays the sky background
flux.

Reduction and Analysis[6] (SORA v0.3, GOMES-JÚNIOR *et al.*, 2022).

When an opaque body with sharp edges passes in from a point-like light source, a
diffraction effect occurs in the wavefront, known as Fresnel diffraction (Figure 2.6). This
effect smooths the light curve, making the flux drops appear more gradual. The Fres-
nel scale length can be estimated using the formula $L_f = \sqrt{\lambda\,\Delta_{km}/2}$, where λ is the
wavelength used in the observation and Δ_{km} is the distance from the occulting object to
the observer in kilometers (ROQUES *et al.*, 1987). For observations in the visible light
($\lambda \sim 550$ nm), the L_f varies from 0.45 to 1.35 km for objects between 5 and 40 au.

The apparent star size ($r_\star$) at the object distance has to be considered during the
modeling. If the star has a considerable apparent size comparable to the target's apparent
size, it will generate a penumbra at the Earth's surface. This penumbral effect occurs
because the star will not disappear instantaneously behind the body as seen by an observer
on Earth. We first need to obtain the physical stellar size to determine the $r_\star$. Since some
catalogs do not provide the stellar radius, we estimate it using empirical models, such
as those by VAN BELLE (1999) and KERVELLA *et al.* (2004), which use the stellar
apparent magnitudes in the B, V, and K bands. The key difference between these models
is that VAN BELLE (1999) estimates sizes for the main sequence, giant or super-giant
stars, while KERVELLA *et al.* (2004) focuses on dwarf stars. After estimating the angular
size of the star, we calculate its apparent size at a distance using trigonometry. Other
parameters used to create our occultation model include the apparent star velocity normal

---

[6]https://sora.readthedocs.io/latest/
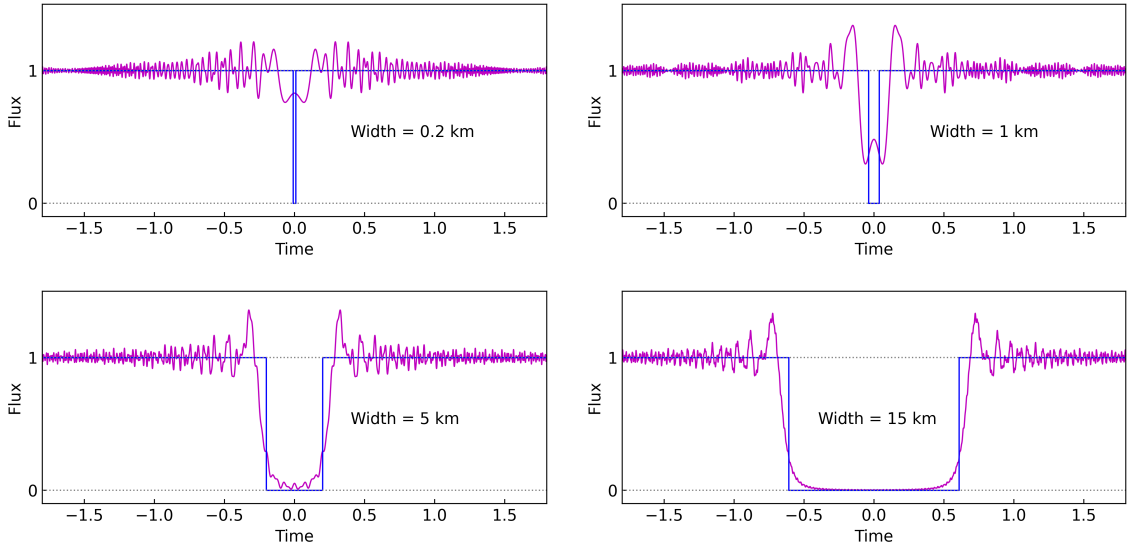
Figure 2.6: Diffraction profiles are generated by an opaque structure of varying widths occulting a point-like light source. This simulated observation assumes a Fresnel scale of $L_f = 1.27\,\mathrm{km}$, corresponding to an object located 40 au ($5.984 \times 10^9\,\mathrm{km}$) away, observed in visible wavelength light ($\lambda \sim 550\,\mathrm{nm}$).

to the local limb (v_N) and the exposure time (t_exp) of the observation. The v_N indicates the velocity at which the occultation occurs during ingress and egress; for tangential chords, this normal velocity is smaller compared to the central chord. The t_exp affects the spatial resolution of the data, calculated as a direct conversion by multiplying the shadow's nominal velocity by the exposure time. Once the projected ellipse that best fits the chords is determined, we can more precisely calculate the radial velocity of the event at each limb-chord contact point, thus enhancing our model. Finally, we can convolve the diffraction model with the observed λ and the $r_\star$, considering the star's normal velocity during ingress and egress and the duration of each exposure. This process results in a synthetic light curve. The synthetic light curve is then compared to the observed data using the χ^2 statistic to evaluate the fit quality.

$$\chi^2 = \sum_{1}^{N} \left(\frac{(\phi_{i,\mathrm{obs}} - \phi_{i,\mathrm{model}})^2}{\sigma_{i,\mathrm{phot}}^2} \right) \tag{2.7}$$

The chi-square (χ^2) statistic is used to quantify how well a model fits the observed data. A lower χ^2 value indicates a better fit. The basic equation (Equation 2.7) for χ^2 is the sum of the squared differences between the observed values ($\phi_{i,\mathrm{obs}}$) and the expected (modeled) values ($\phi_{i,\mathrm{model}}$), divided by the variance of the observed values (squared $\sigma_{i,\mathrm{phot}}$).

This process typically generates around $100,000$ models, varying the ingress and egress instants within a specific range to minimize the χ^2 value. For each model, a χ^2 value is calculated and plotted as a function of the time instant, as shown in Figure 2.7. The
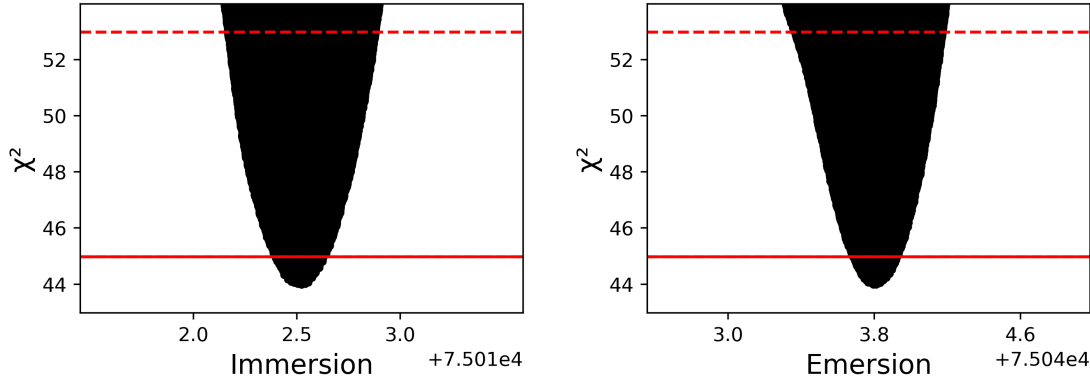
Figure 2.7: Example of a χ^2 distribution obtained from fitting a light curve to determine the instants of ingress and egress (seconds). The lowest χ^2 value gives us the best fit ($\chi^2_{\min}$). The solid red lines represent the 1σ uncertainties, while the dashed red lines indicate the 3σ uncertainties.

1σ and 3σ uncertainty intervals are determined by identifying the time instants where the χ^2 value equals $\chi^2_{\min} + 1$ (continuous red horizontal line) and $\chi^2_{\min} + 9$ (dashed red horizontal line), respectively. These intervals indicate the range of times that provide a statistically acceptable fit to the data, reflecting the confidence level in the timing of ingress and egress events.

2.1.5   Obtaining a 2D model of the occulting body

The immersion and emersion intervals are then projected onto the tangent plane, creating a positive chord where the immersion and emersion time instants define the extremities. These projections result in points that represent the relative position between the star and the object's center in the tangent plane (f_0, g_0). For a positive light curve, the immersion and emersion times indicate where the body's limb intersects the line of sight between the star and the observer. An occultation event with multiple positive detections will produce a series of these intersection points. When sufficiently close to the occulting body, negative detections are also crucial. They help refine the object's shape, size, and position and facilitate searching for secondary structures nearby.

Occasionally, observational campaigns result in fewer than three positive detections. We can only fit a circle to the two extremities with only one positive chord. If the body's equivalent diameter is known from previous observations, this fit provides two possible solutions for the object's center. If the object's diameter is unknown, the positive chord is treated as a diametrical chord, giving a lower limit for the body's radius. With two positive detections, we have four extremities to fit a circle, allowing us to estimate the astrometric position and a minimum value for the semi-major axis. An ellipse can be fitted when there are three or more detections. The five parameters needed to fit an ellipse are the center coordinates (f_0, g_0), the apparent oblateness (ϵ'), the apparent semi-major axis (a'), and

the apparent P/A, increasing from north to east. To vary all these parameters during the fitting procedure and obtain an apparent ellipse representing the object's instantaneous limb, we will need at least six chord extremities (N = 6) to fit the M = 5 parameters. This procedure is also made using the Stellar Occultation Reduction and Analysis (SORA) package (GOMES-JÚNIOR *et al.*, 2022), which generates a uniform distribution of values within a specified interval for each ellipse parameter. For each parameter set, an ellipse is generated, and the χ^2 value is calculated and recorded. The χ^2 value for the ellipse fit is using the formula:

$$\chi^2 = \sum_1^N \left(\frac{(r_{i,obs} - r_{i,calc})^2}{\sigma_i^2 + \sigma_{model}^2} \right), \qquad (2.8)$$

where $(r_{i,obs} - r_{i,calc})^2$ represents the squared difference between the observed chord extremities and the corresponding positions on the object's limb in the radial direction. The term σ_i represents the uncertainty in the chord extremity in the radial direction. The parameter σ_{model} accounts for potential body surface topographic features. Accounting for topographic features is important because, in some cases, the uncertainties in the immersion and emersion instants are small, resulting in projections on the tangent plane at a sub-kilometer scale, which can sometimes be smaller than the actual topographic variations. The σ_{model} value is determined iteratively to maintain the χ^2 per degree of freedom (χ^2_{pdf}) equals 1 (MORGADO *et al.*, 2021), indicating a good fit. The fitted apparent ellipse represents the projection of an ellipsoid onto the tangent plane, corresponding to the body's instantaneous limb. The uncertainties in the ellipse parameters are determined similarly to the light curve modeling process by using $\chi^2_{min} + 1$ for the 1σ level and $\chi^2_{min} + 9$ for the 3σ level. Notably, a negative chord close to the positive detections can constrain the possible ellipses within the uncertainty region (Figure 2.8).
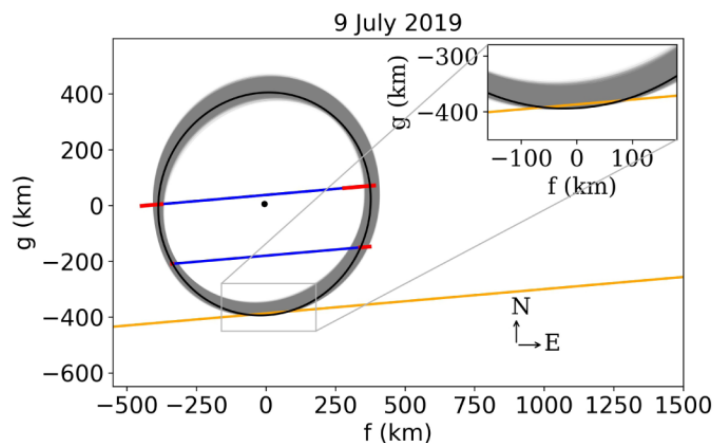
Figure 2.8: Example of an occultation with two positive chords (blue) where the possible ellipses (grey) are constrained by a nearby negative chord (orange). The best-fitting ellipse (black), which overlaps the negative chord, is determined using a σ_{model} value of 7 km, accounting for possible potential features. Image from ROMMEL *et al.* (2023).

After determining the circle or ellipse that best fits the chords, we can find its center, representing the astrometric position of the occulting object. This center indicates the difference between the object's actual position on the tangent plane and the position predicted by the ephemeris. The astrometric position at the time of occultation is obtained by adding this offset to the ephemeris position. This new astrometric position is then used to refine the object's orbit and improve future predictions of occultations. Another important outcome is the determination of the object's geometric albedo. Using the apparent ellipse (or circle) representing the body, we can calculate the equivalent radius (R_{equiv}) - the radius of a circle with the same superficial area of the fitted ellipse. The geometric albedo p_V can be calculated using the formula: $p_V = 10^{0.4(H_\odot - H_o)} \cdot (au_{km}/R_{equiv})^2$, where $H_\odot$ is absolute magnitude of the Sun, H_o is the absolute magnitude of the object, and $au_{km} = 1\,au = 1.49598 \times 10^8$ km.

2.2   Stellar occultations by rings

2.2.1   Modeling the theoretical ring profile

To date, we have confirmed rings around only four small bodies: Chariklo, Haumea, and Quaoar (besides Chiron and its changing material). Each of these objects has rings with surprisingly different characteristics. Through recurrent observations or a multi-chord detection of the ring and the central body, it is possible to determine the rings' eccentricity (e.g. MORGADO *et al.*, 2021), ascertain their inclination relative to the central body's equatorial plane, and identify azimuthal variations in their width and material density.

On the other hand, there is a need for a generic model capable of adequately representing the geometry of these rings. Therefore, we consider a circular and flat ring orbiting in the equatorial plane of the main body. The distance r of the ring is measured along the radius vector from the center of the main body to the center of the ring (Figure 2.9). We also consider the ring's radial width (W_r) limited by the inner and outer ring edges and disregarding any putative transmittance variation along the radial vector (ELLIOT *et al.*, 1984).

The occultation by the ring can be modeled as either a square-well model or a semi-transparent band with constant opacity and sharp edges. The apparent opacity (p') represents the depth of the flux drop in the light curve resulting from the band's passage in front of the star. It can be defined as $p' = 1 - \frac{I}{I_0} = 1 - T$, where I is the transmitted flux, I_0 is the incident flux, and T is the transmittance. For a fully transparent ring, $p' = 0$ or $T = 1$; for an opaque ring, $p' = 1$ or $T = 0$. The width of the band denotes the apparent width of the local ring portion, represented by W', calculated by multiplying the occultation duration Δt by the local velocity perpendicular to the ring ($v_\perp$) to the ring. These parameters are referred to as "apparent" because they depend on the ring
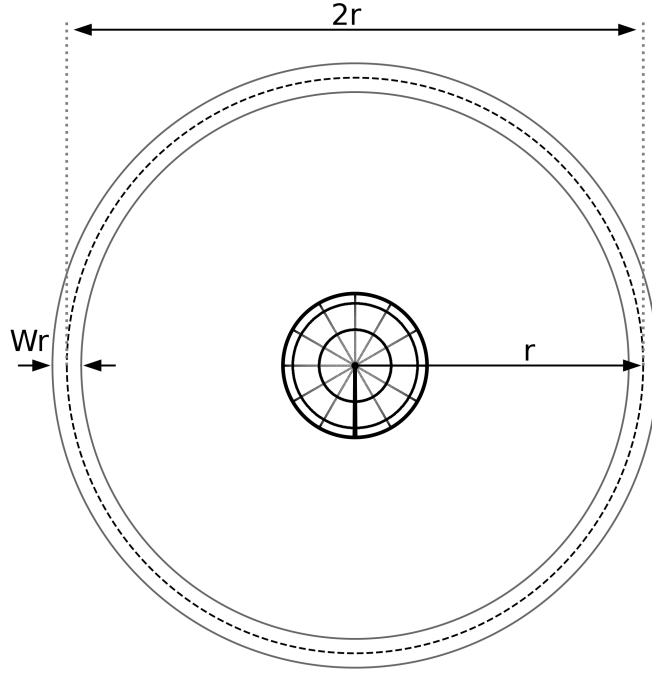
Figure 2.9: Ring geometry for a pole-on view. Our models consider the flat ring circular and concentric with the central body. W_r represents the radial ring width. The distance r is measured along the radial vector to the center of the ring.

opening angle (B) and P/A; in other words, these parameters are projected onto the tangent plane.

The derivation of the synthetic light curve profile for ring occultations closely mirrors the process of constructing a model for the occultation by an opaque body. The following procedures use algorithms based on the SORA package and follow the description presented in the literature (e.g. CUZZI, 1985; ELLIOT *et al.*, 1984; ROQUES *et al.*, 1987). Our ring model comprises a rectangular semi-transparent band with abrupt edges and a constant apparent opacity p', lasting for a duration Δt (see Figure 2.10), what we call a square-well model. We integrate the effects of Fresnel diffraction caused by the sharp edges of the ring (see Figure 2.6). We then convolve the light curve profile with the star's apparent radius at the object's distance (disregarding the limb-darkening) and the instrumental response. This process yields the synthetic profile of the ring, which can be compared to the observed light curve using χ^2 statistics. In our chi-square minimization procedure, we vary the ring's ingress and egress instants and the apparent opacity p' to achieve the best fit. These parameters and the 3σ uncertainties are stored to determine the ring's local parameters. This analysis is performed using the `lc.occ_lcfit` function from SORA v0.3 for each detection. An exception occurs in cases where the ring detections are close to each other, such as the rings of Chariklo (BRAGA-RIBAS *et al.*,
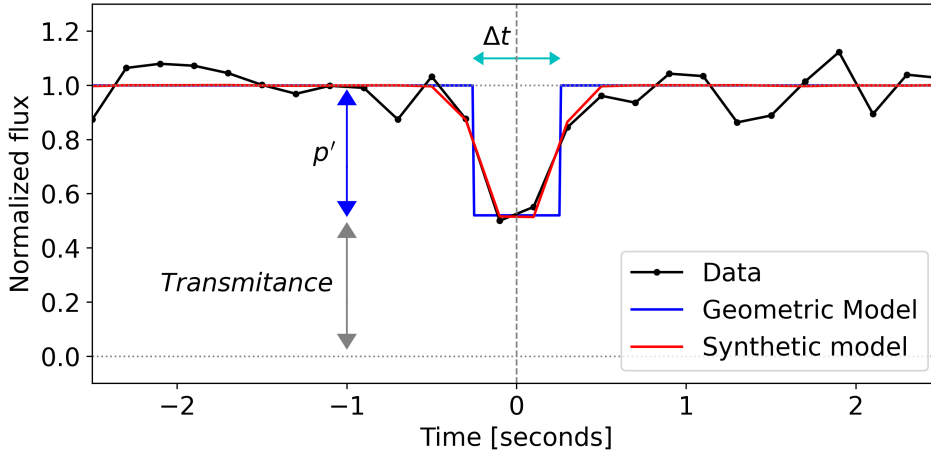
Figure 2.10: Simulated light curve depicting an occultation by a ring, with flux plotted as a function of time (black line). The blue line illustrates our geometric model, which assumes a constant apparent opacity p' for the ring and an occultation duration Δt. This model is convolved with the effects of Fresnel diffraction, the apparent radius of the star, and the exposure time, producing a synthetic curve (red line). The grey dashed line indicates the center of the ring.
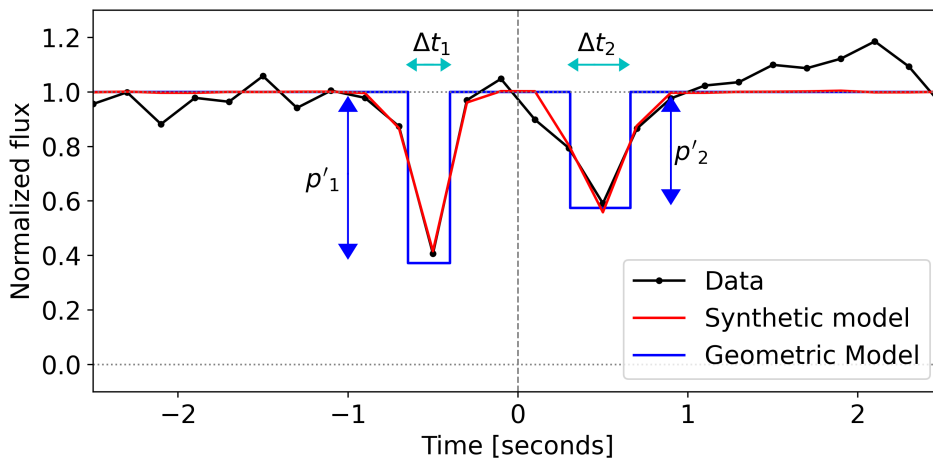
Figure 2.11: Light curve obtained on 2011 stellar occultation by Chiron (FTN data set) showing an occultation by two close structures. The normalized flux ratio is plotted as a function of time (black). The blue line presents both geometric models, and the red curve presents the synthetic model. The grey vertical line at zero indicates the center of these two structures.

2014) and the 2011 detections of structures around Chiron with the Faulkes Telescope North (FTN) (RUPRECHT *et al.*, 2015; SICKAFOOSE *et al.*, 2020). In these cases, the diffraction fringes from one ring can interfere with the profile of the nearby ring, and for accurate modeling, both rings are treated together. An external algorithm based on the same SORA function is used to achieve this. It returns the ingress and egress instants and the opacity for each ring. An example with the FTN data from 2011 Chiron occultation is presented in Figure 2.11. This plot presents the synthetic light curve obtained

considering the diffraction pattern created by the two rings. We have two geometric models with constant apparent opacity p_1' (resp. p_2') and duration $\Delta t_1 = |t_{ing1} - t_{egr1}|$ (resp. $\Delta t_2 = |t_{ing2} - t_{egr2}|$). The curve is convolved with the Fresnel diffraction generated by both rings simultaneously, along with the stellar apparent radius and exposure time, resulting in synthetic ring profiles.

In some cases, the exposure time is insufficient for resolving two closely spaced rings (e.g. Chariklo rings), and they appear as a single structure in the observed light curve. In such instances, where it is known that two rings are within the same occultation profile, we can use the same approach of fitting two square-well models (Figure 2.12). However, in this case, we fix the apparent distance between the two bands, the apparent opacity, and the apparent width of the rings as published in the literature. We then vary only the distance of these structures from the center of the main body using a modified version of the earlier code to fit two square-well models for cases with known ring parameters. In this scenario, the only free parameter is the central instant of the occultation by the structures. It is essential to mention that the values published in the literature may be the normal values of these structures, i.e., the values already converted to the orbital plane of the ring. Therefore, we need to consider the geometry of the rings for the occultation epoch and project these structures onto the tangent plane to obtain the apparent parameters that will be used during the fit procedure.
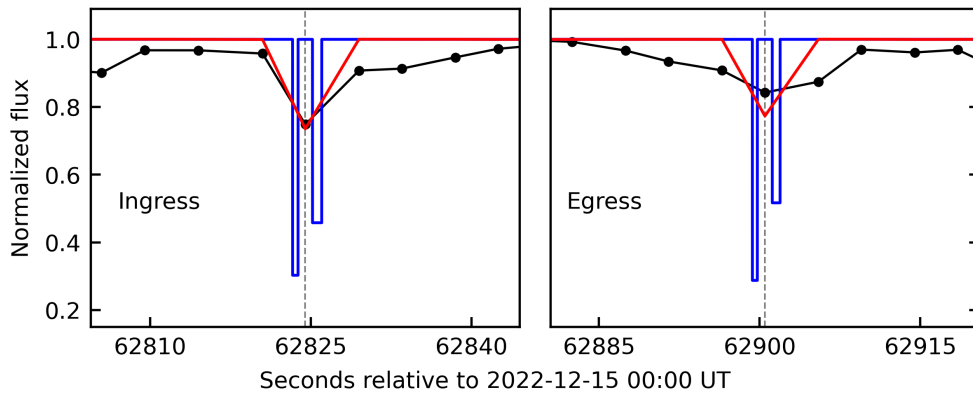
Figure 2.12: Example of an unresolved detection of the two ring-like structures around Chiron. The geometric model of the ring-like structure from the 2011 stellar occultation (blue lines) is convolved using the light curve parameters of the 2022 stellar occultation, producing the synthetic light curve (red).

2.2.2 Ring local properties

As mentioned, the ring properties obtained from fitting a theoretical profile to the light curve result in apparent properties, i.e., projected onto the tangent plane. The apparent opacity tells us how much starlight is removed by the presence of the rings. From the p', we can obtain the apparent optical depth (apparent optical thickness), denoted as τ'.

This dimensionless quantity indicates how much the medium attenuates electromagnetic radiation, such as visible light, and is defined as the negative natural logarithm of the transmittance (T) of the medium

$$\tau' = -\ln(T) = -\ln(1 - p').$$ (2.9)

A higher optical depth indicates a greater likelihood of absorption or scattering within the medium, resulting in less transmitted light. Conversely, a lower optical depth suggests a more transparent medium.

One might think that it suffices to make the projection considering the opening angle of the ring relative to the line-of-sight to convert these apparent quantities to normal values, as normal opacity (p_{N}) and normal optical depth (τ_{N}). However, despite our occultation model treating the ring as a semi-transparent band with sharp edges, it's crucial to remember that rings are, in reality, a structure composed of numerous small particles, each interacting with light individually.

When particle sizes (1-10 meters) are much smaller than the Fresnel scale (kilometers), the ring removes a fraction $(1 - p)$ of the amplitude of the wavefront and $(1 - p)^2$ of the energy, where p is the actual opacity. To relate the p' with the p, one can use $(1 - p') = (1 - p)^2$. Taking the logarithm on both sides to obtain the optical depths reveals an apparent optical depth (τ') twice the ring's actual optical depth (τ), or $\tau' = 2\tau$. In other words, the ring appears twice as opaque in our light curves than it is. This effect was confirmed during the Voyager PPS occultation experiment (LANE *et al.*, 1986) where the uranian rings' optical depths appeared to be half the value obtained from Earth-based stellar occultation. The rationale behind the factor of two can be understood through the insights provided by CUZZI (1985) and ROQUES *et al.* (1987) during the analysis of the occultations by Uranus's rings. The diffracted energy is contained within the Airy disc characterized by $\theta_d = \frac{\lambda}{2\,\mathrm{r}}\Delta$, being λ the wavelength, $2\,\mathrm{r}$ the particle diameter, and Δ the observer-ring distance. Suppose an observer positions themselves sufficiently close to the ring. In that case, the projected Airy disc is not so broad, and the diffracted light is still close enough to the incident light, making it challenging to distinguish between them. Therefore, the observer will detect the total incident energy minus what has been physically removed by the ring particles. On the other hand, one observer sufficiently distant from the ring will witness a much larger diffraction cone extending beyond the width of the rings. In this case, the observer will detect the total incident energy minus the energy taken away by the diffraction and again minus what has been physically removed by the ring particles. From the geometric optics regime, we know that the amount of diffracted energy is the same amount directly removed by the physical surface of the particles, resulting in an extinction twice as large as the current value caused by the particles alone. Correctly determining these quantities is important because the optical

depths retrieve the particle filling factor used in dynamics to study the collision rate and allow estimates of the particle albedo.
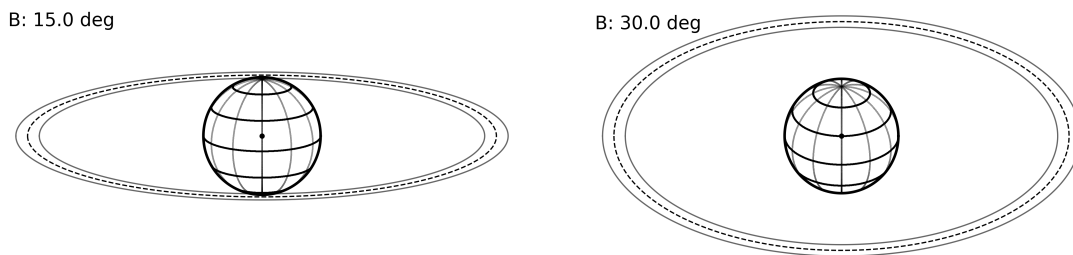
Figure 2.13: The ring geometry in the tangent plane is represented for two different aperture angles: $B = 15.0$ degrees on the left panel and $B = 30.0$ degrees on the right panel.

The diffraction-corrected quantities p and τ can now be projected to the ring plane considering the ring B during the occultation, defined by

$$B = \arcsin[-\sin(\delta_{\mathrm{pole}})\sin(\delta_{\mathrm{obj}}) + \cos(\delta_{\mathrm{pole}})\cos(\delta_{\mathrm{obj}})\cos(\alpha_{\mathrm{pole}} - \alpha_{\mathrm{obj}})] \tag{2.10}$$

where α_{pole} and δ_{pole} are the Right Ascension and Declination of the ring pole orientation, and $\alpha_{\mathrm{obj}}, \delta_{\mathrm{obj}}$ are the Right Ascension and Declination of the main body. This aperture angle is measured relative to the observer's line-of-sight, as illustrated in Figure 2.13.

For cases where the orientation of the ring's pole is still undetermined, a method similar to the ellipse fitting described in Section 2.1.5 can be employed. In this case, we consider the ring to be circular. So, we can evaluate the ring aspect angle from the projected ellipse semi-minor axis. Each ring detection is represented by a segment projected onto the sky plane, from which we calculate its midpoint, thus determining the central point of the detection. The uncertainties at the extremities of these segments, which intersect the ring, are propagated to the detection center. Fitting an ellipse to a range of potential pole orientations and ring radii becomes feasible with five or more detections. The best fit is obtained by varying the pole orientation and the major semi-axis of the apparent ellipse within a specified range, recording the χ^2 values, and evaluating the χ^2_{min}.

Two extreme cases are considered when deriving the ring properties: a multilayer ring, where the ring's thickness is much greater than the diameter of the individual particles, and a mono-layer ring, where the thickness is on the order of the size of a single particle. In a multilayer ring, multiple layers of particles are stacked on each other, causing significant shadowing effects. In contrast, a mono-layer ring has a thickness on the order of the size of a single particle, meaning the particles are arranged in a single layer with minimal overlapping. Mono-layer rings are typically less dense and may have different light-scattering characteristics due to the lack of significant shadowing effects (ELLIOT

et al., 1984).

$$p_{\mathrm{N}} = (1 - \sqrt{(1 - p')}\,|\sin(B)| \tag{2.11}$$

to transform apparent opacity p' to normal opacity p_{N}. In the poly-layer case, the transformation from apparent to normal optical depth is made using

$$\tau_{\mathrm{N}} = \frac{\tau'}{2}\,|\sin(B)|. \tag{2.12}$$

Our approach to determining the ring W_{r} is made by projecting the ring ingress and egress instants on the tangent plane, obtaining a small segment representing the ring cut. Then, by projecting this segment onto the ring plane, we calculate the radial distance from each extremity of the ring chord to the center of the system ring-body, deducing the W_{r} from the difference between these positions (See Figure 2.9).

Other relevant properties for the study of rings are also obtained, such as the equivalent width E_p and the equivalent depth A_τ. These parameters serve as quantitative indicators of the material density (per unit length) within a radial slice of the ring. The validity of these measurements depends on whether the ring structure is mono-layer or multilayer (FRENCH *et al.*, 1991). The equivalent width E_p is defined as the width of an opaque ring that would block the same amount of starlight as a semi-transparent ring with a certain W_{r} and can be numerically calculated from the integral of the p_{N} over the radial profile in the ring plane (BÉRARD *et al.*, 2017):

$$E_p = |\sin(B)|\,v_{\mathrm{r}} \int_{\mathrm{profile}} (1 - \sqrt{(1 - p')}\,dt. \tag{2.13}$$

Similarly, the A_τ is defined by the integral of the τ_{N} over the ring profile along the ring plane (W_r):

$$A_\tau = -\frac{\sin(B)}{2}\,v_{\mathrm{r}} \int_{\mathrm{profile}} \ln(1 - p')\,dt, \tag{2.14}$$

where v_r is the radial star velocity measured in the ring plane. Suppose the ring is resolved (with two or more points within the W_r) and presents sharp edges. In that case, we can obtain these integral properties by multiplying the radial width of the ring by the normal opacity and normal optical depth obtained from the square-well fit:

$$E_p = W_{\mathrm{r}}\,p_{\mathrm{N}} \tag{2.15}$$

$$A_\tau = W_{\mathrm{r}}\,\tau_{\mathrm{N}} \tag{2.16}$$

If the ring is resolved but does not present sharp edges (such as Lorentzian profile, for instance), the integrals presented in the Equations 2.13 and 2.14 can be numerically determined. On the other hand, the ring detection can present only one data point, i.e., an unresolved detection.

When a ring is detected as an unresolved feature (only one data point), it becomes difficult to accurately determine its opacity due to its correlation with the ring width. As the opacity is poorly constrained ($0 \leqslant p \leqslant 1$), significant uncertainties in the modeled apparent opacity arise, making it challenging to evaluate the integrals without additional information. BÉRARD *et al.* (2017) addressed this problem by considering the ring's apparent equivalent width (E′) in the tangent plane, which equals the product of the ring's perpendicular width ($W_\perp$) and its apparent opacity (p'): $E' = W_\perp \, p'$. The E_p can be expressed in terms of the E' in the form

$$E_p = |\sin(B)| \left(\frac{v_r}{v_\perp} \right) \frac{E'}{2 - p}. \tag{2.17}$$

As opacity is poorly constrained ($0 \leqslant p \leqslant 1$),

$$|\sin(B)| \left(\frac{v_r}{v_\perp} \right) \frac{E'}{2} \leqslant E_p \leqslant |\sin(B)| \left(\frac{v_r}{v_\perp} \right) E'. \tag{2.18}$$

This implies an uncertainty of up to a factor of two for E_p, according to the assumed value of p. However, by fitting the synthetic profile using the square-well model, E_p can be measured, although p remains unconstrained. Consequently, unresolved profiles will exhibit greater errors than resolved profiles, though E_p is defined in both scenarios. It is important to note the equality $p' = \frac{E'}{W_\perp} = \frac{E'}{W_r} \left(\frac{v_r}{v_\perp} \right)$. As $W_\perp$ can be retrieved from the fitted synthetic profile, p' and consequently E_p can be constrained (BÉRARD *et al.*, 2017).

Some rings, like Saturn's F ring, may not exhibit sharp edges and constant opacity as we have considered in our square-well model. In the absence of sharp edges, the Fresnel diffraction does not influence the ring profile, but we still consider the diffraction by the individual particles. Indeed, as it will be shown in Section 3.1, we have encountered such structures with radially variable opacity in the data obtained from the Canada-France-Hawaii Telescope (CFHT) and the Gemini-North Telescope: the outer ring of Quaoar (Figure 2.14).

The light curves are transformed from flux to normal optical depth using $\tau_N(i) = -\ln\left[T\left(i\right)\right]^{\frac{|\sin(B)|}{2}}$, where $T(i)$ is the transmittance of the *i-th* data point, and plotted as a function of radial distance in the ring plane. A Lorentzian function is compared to the observed data using a non-linear least squares through a Python algorithm based on `scipy.optimize.curve_fit package`. The input parameters for this fitting procedure are the approximated ring center position, the function's FWHM, and the estimated area under the curve. The area under the best-modeled curve corresponds to the equivalent depth (A_τ), representing a measure of the overall opacity of the ring. The Lorentzian FWHM approximates the ring's core width (in the case of a confined ring enveloped by diffuse material). Furthermore, the position of the function's peak in the fitted Lorentzian profile reveals the mean radial distance between the ring and the main body's center.
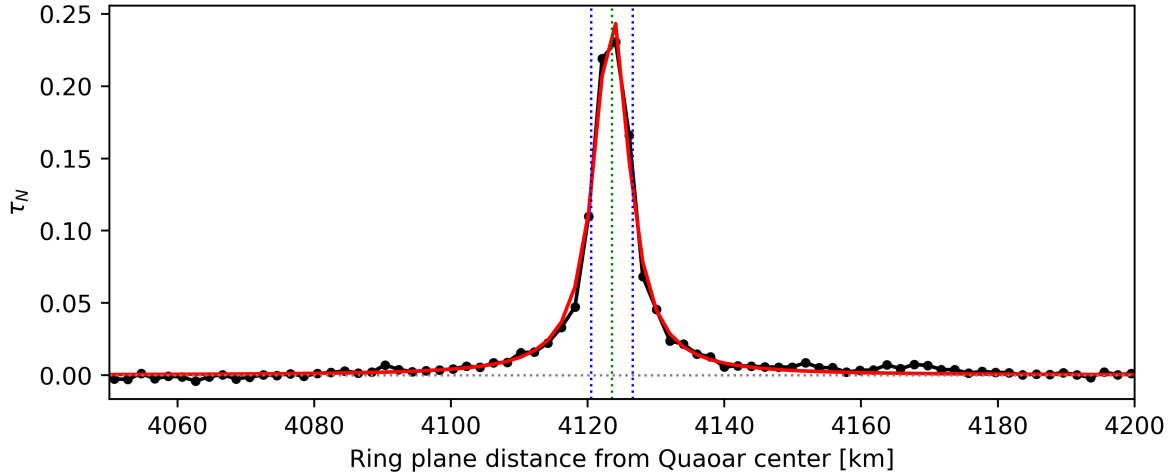
Figure 2.14: Normal opacity versus radial distance in the ring plane for the densest part of Quaoar external ring. The black curve shows the data points. The dotted green line indicates the Lorentzian center, while the blue line denotes the profile's FWHM.

Additionally, the A_τ value is extracted from the integral of the ring profile within the curve of p_N as a function of radial distance in the ring plane (r). It is important to note that the stellar apparent diameter has a negligible influence on the detailed ring profile, allowing us to focus on the intrinsic properties of the ring itself.

2.2.3   Determining detection limits

Hitherto, we saw the analysis of the additional structures defined as rings that present noticeable flux drops in the light curves. However, there are some cases where the light curves do not present signatures of the known rings, either because the standard deviation of the data is high, because there is not enough spatial resolution to reveal the structures, or due to the star's size and Fresnel scale effects smoothing the light curve. Therefore, determining the detection limits allows us to know whether the rings were not detected due to observational circumstances (insufficient temporal resolution or low S/N) or whether they possibly present spatial or temporal variations, such as longitudinal homogeneities or dynamical evolution. For instance, some light curves on Quaoar's stellar occultations present sufficient spatial resolution and S/N to detect the densest part of the Q1R (external) ring at the egress region (see section 3.1, for details). However, no flux drop was detected in the expected ring location at the ingress region. This leads us to argue that the ring presents variability in particle density number and/or radial width. For bodies with no confirmed additional structures in the surroundings, determining detection limits allows us to constrain the amount of material orbiting the body, being their satellites, rings, or cometary coma.

The equivalent width was used to determine the detection limits on additional material

in the light curves with arc detections from ground-based Neptune's stellar occultations between 1983 and 1989 (SICARDY *et al.*, 1991). BOISSEL *et al.* (2014) also used this procedure to determine the upper limits for detecting two extreme structures around Pluto: an opaque individual circular satellite (a moonlet) and semi-transparent complete rings. Limits on additional material were also placed for Chariklo by BÉRARD *et al.* (2017), using the high-quality Danish light curve obtained on June 3, 2013, and by MOR-GADO *et al.* (2021) using the July 23, 2017 event light curves obtained at the ESO's Very Large Telescope (VLT), Observatório do Pico dos Dias (OPD), and Danish telescope (La Silla). Similar approaches were used in searching for rings around the Centaurs Chiron (BRAGA-RIBAS *et al.*, 2023), Echeclus (PEREIRA *et al.*, 2024), and (95626) 2002 GZ32 (SANTOS-SANZ *et al.*, 2021).

To search for secondary detections, we plot the normalized stellar flux ϕ_i as a function of the radial distance r projected to the body's equatorial plane. Then, we determine the equivalent width value for each point $E_p(i)$ of a putative ring from

$$E_p(i) = \frac{|\sin(B)|}{2}[1 - \phi(i)]\Delta r(i), \tag{2.19}$$

where B is the ring aperture angle, $\phi(i)$ is the normalized flux, and $\Delta r(i)$ is the radial distance between two consecutive points projected in the ring plane. Since the stellar radial velocity varies with the distance from the body's center, the $\Delta r(i)$ varies accordingly, improving the light curve S/N in the regions close to the body. An example of the resulting light curve is presented in Figure 2.15, with $E_p(i)$ plotted against the radial distance in the object's equatorial plane. When the ring pole orientation is unknown, one can determine the apparent equivalent width using $E' = [1 - \phi(i)]v'\Delta t$, being v' the apparent star velocity in the tangent plane. For bodies with a ring system already been identified, we can search for additional material in the regions outside the events by using rings or the main body and the pole orientation of the known ring. The detection limits are obtained from the standard deviation of the E_p curve in the region of interest. Using the example of the stellar occultation by Quaoar and the data obtained with the Gemini North telescope in the z' filter, the 3σ detection limits for the equivalent width in the region suggest that any structure in the Q1R ring plane with $E_p \sim 12$ meters would have been detected as an individual point. Given that the average spatial resolution of this light curve in the ring plane is about 2 km, we can say that this light curve can detect structures in extreme cases: semi-transparent structures with $W_r \sim 2$ km and normal opacity $p_N = E_p/W_r \sim 0.006$ or opaque structures with radial width W_r of 12 meters, and all intermediate solutions. Individual analysis is performed on data points above the 3σ level concerning the reference star flux on a light curve to eliminate the possibility that these decreases in flux (increase in E_p) could be attributed to factors such as passing clouds or other artifacts in the image. The procedure allowed us to detect the second ring
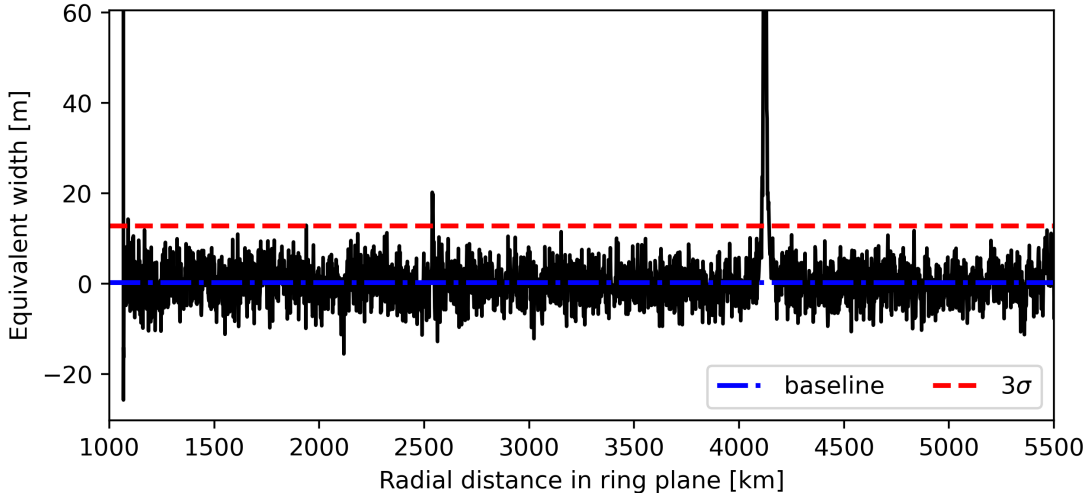
Figure 2.15: Equivalent width E_p light curve plotted as a function of the radial distance in the Quaoar's equatorial plane. Near $1,000$ km, the E_p increase is due to the Quaoar's occultation. Near $4,000$ km, the external ring (Q1R) is observed. The red dashed line represents the 3σ standard deviation, calculated using the points between the main body and the Q1R ring. The points near $2,500$ km above this 3σ indicate the presence of the Quaoar's internal ring (Q2R), identified using this method.

around Quaoar (Q2R), orbiting at $\sim 2,560$ km from the body's center (Figure 2.15).

Searching broader structures can be conducted by re-sampling light curves at lower spatial resolutions to enhance sensitivity and identify structures with specific widths. Our method involves smoothing the light curve using the Savitzky-Golay (SG) digital filter through `scipy.signal.savgol_filter` Python package. This digital filter fits a local polynomial to a small fixed-size window of data points, typically an odd number of data points that is shifted along the light curve. For each position of the window, a first-degree polynomial is fitted to the data within the window. The value at the center of the window is then replaced with the value predicted by the polynomial fit. This process is repeated for each window position, re-sampling the light curve. This process keeps the interest features while reducing noise and fluctuations, enhancing the sensitivity to detect structures with radial width W_r similar to the selected window size.

An example of the use of the SG digital filter is presented in Figure 2.16. Here, we opened a fixed-size window of about 10 km to search for narrow rings with this width, obtaining a re-sampled light curve. One can note that the individual points close to the 3σ limit in the original E_p curve are smoothed out and do not appear in the re-sampled light curve. The new 3σ upper limit is determined for the re-sampled light curve, enhancing the presence of a potential narrow ring width $W_r \sim 10$ km. It is essential to mention that with this method, it is impossible to distinguish artificial events, such as electric discharges or rapid decentering, from real ones (SICARDY *et al.*, 1991).

The search also can be done for a discrete body, such as a small satellite. This discrete
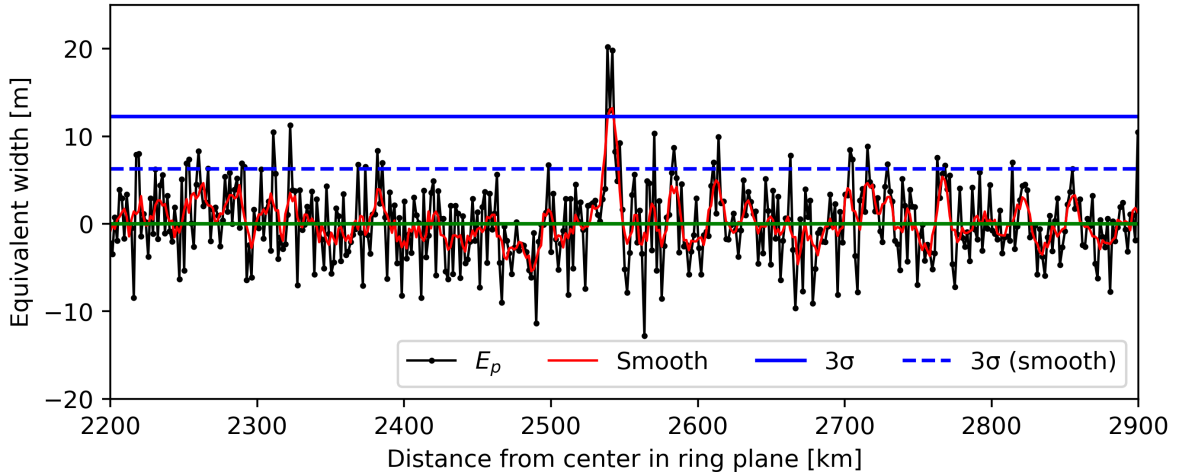
Figure 2.16: Equivalent width E_p light curve plotted as a function of the radial distance in the Quaoar's equatorial plane (black points), with the respective 3σ upper limit indicated by the continuous blue horizontal line. The smooth light curve obtained using the SG digital filter is plotted in red, with the 3σ upper limit indicated by the blue dashed horizontal line. The green continuous horizontal line indicates the zero point for E_p.

body has a spherical shape, with an angular diameter larger than the star's apparent diameter, causing a total stellar flux block. In this circumstance, the detection limits can be performed considering the 3σ uncertainty in flux as the apparent opacity p', the star radial velocity in the sky plane $v_\perp$, and the duration of the occultation Δt, so the limits for a chord length is obtained from $l = p'\, v_\perp\, \Delta t$. As we can see, the chord length equals the apparent equivalent depth $E' = W_\perp\, p'$. The average chord length for a circular projection can be obtained through the Pythagorean theorem, where a square is drawn within a circle with radius (r), with the square side (l) being the circle's chord $l^2 = r^2 + r^2$, or $l = \sqrt{2}\, r$. In other words, if the upper limit for the chord length is 100 meters, on average, this can correspond to a circular body with a minimum radius of $r = 70$ meters occulting the star.

Chapter 3

Results

This thesis presents the culmination of a comprehensive study focused on the search and characterization of rings around Small Solar System Objects, shedding light on their complexity and ubiquity. The stellar occultation technique provided a unique opportunity to probe these bodies' physical properties and surrounding structures, such as rings and atmospheres. Significant effort was made to analyze occultation data to understand the characteristics and behaviors of Small Solar System Object (SSSO) and their rings, contributing to the scientific literature with some published works that delve into specific aspects of stellar occultations by rings around small objects. These publications are detailed in the subsequent sections and available in the Appendix chapter.

3.1   The Trans-Neptunian Object (50000) Quaoar

The TNO (50000) Quaoar received the provisory designation 2002 LM_{60} when it was discovered by astronomers Brown and Trujillo in June 2002 on images taken with the 1.2-meter Samuel Oschin Schmidt telescope at Palomar observatory, but with precovery images dated back to 1954. Initially, its diameter was estimated at $1,260 \pm 190$ km based on direct imaging using the Hubble Space Telescope (HST) (BROWN e TRUJILLO, 2004). However, subsequent observations with the Spitzer Space Telescope and newer HST data yielded a smaller diameter range of about 850–890 km (FRASER e BROWN, 2010; STANSBERRY *et al.*, 2008). FORNASIER *et al.* (2013) estimated a diameter of D = $1,073.6 \pm 37.9$ km and a density of $\rho = 2.18^{+0.43}_{-0.36}\,\mathrm{g\,cm^{-3}}$ using combined observations from Herschel Photodetector Array Camera and Spectrometer (PACS) and Spectral and Photometric Imaging Receiver (SPIRE). Quaoar has a short-term variability on the rotational light curve explained by a rotational period of P = 8.8394 ± 0.0002 hours. However, the light curve seems to be double-peaked, so a rotational period of P = 17.6788 ± 0.0004 hours is likely (ORTIZ *et al.*, 2003).

The first observation of a stellar occultation by Quaoar was a single-chord observed on 2011 February 11 (PERSON *et al.*, 2011), allowing determining a lower limit on Quaoar's size. The first multi-chord event was observed on 2011 May 4, with six positive chords and close negatives. The 2012 February 17 event was a double-chord, and the 2012 October 15 was a single-chord. These events yield an equivalent radius R_{equiv} = 555 ± 2.5 km, a geometric albedo $p_V = 0.109 \pm 0.007$, true oblateness $\epsilon = 0.087^{+0.0268}_{-0.0175}$, an equatorial radius R_{equat} = 569^{+24}_{-17} km, and a density of $\rho = 1.99 \pm 0.46\,\mathrm{g\,cm^{-3}}$ (assuming a Mclaurin spheroid) (BRAGA-RIBAS *et al.*, 2013). A recent stellar occultation event was observed on 2022 August 9, allowing determining an apparent semi-major axis of $a' = 579.5 \pm 4.0$ km and apparent oblateness $\epsilon' = 0.12 \pm 0.01$, resulting in an area-equivalent radius of 543 ± 2 km (PEREIRA *et al.*, 2023). This makes Quaoar the fifth largest TNO after Eris, Haumea, Makemake, and Gonggong (excluding Pluto).

Quaoar's orbital characteristics classify it as a hot classical object (GLADMAN *et al.*, 2008), with a semi-major axis of 43.51 au, an orbital period of 287 years, an orbital eccentricity of 0.035, and an inclination of 7.98 degrees. In 2007, a satellite was discovered orbiting Quaoar using images from the HST (BROWN e SUER, 2007). By observing the orbital motion of Weywot, astronomers have been able to determine Quaoar's mass to M = $(1.40 \pm 0.21) \times 10^{21}$ kg (FRASER *et al.*, 2013; VACHIER *et al.*, 2012). Weywot's orbit has a semi-major axis of $13,289 \pm 189$ km, eccentricity 0.056 ± 0.093, and an orbital period of 12.4311 ± 0.0015 days (VACHIER *et al.*, 2012). Assuming the same geometric albedo for Quaoar and Weywot ($12.7 \pm 1\%$), FORNASIER *et al.* (2013) estimates the Weywot diameter as D = 81 ± 11 km. However, during an observation of an occultation by Quaoar on August 04, 2019, Weywot was also detected, yielding a chord length of

168 ± 15 km. Recent stellar occultations by Weywot reinforce the interpretation that this satellite is larger than previously assumed. This can improve the determination of Weywot's orbital parameters, leading to a more accurate estimation of Quaoar's mass (BRAGA-RIBAS *et al.*, submitted). These parameters are essential for elucidating the dynamics of the enigmatic rings situated beyond the Roche limit.

The following section summarizes the analysis and methods used to discover the two rings of (50000) Quaoar, outside the classical Roche limit. The first ring, Q1R, was published in February 2023 in Nature, entitled "A dense ring of the Trans-Neptunian object Quaoar outside its Roche limit" (MORGADO *et al.*, 2023, see Appendix E), where I contribute to the detection limits determination, discussion and writing. The second ring was discovered using data from a stellar occultation in 2022, with the results presented in a paper led by me and published in April 2023 in the Astronomy & Astrophysics Letters, entitled "The two rings of (50000) Quaoar" (PEREIRA *et al.*, 2023, in Appendix A).

3.1.1   The discovery of the Quaoar's first ring (2023 Q1R)

Several stellar occultations by Quaoar were observed between 2018 and 2021, revealing secondary events (MORGADO *et al.*, 2023). In addition to completely disappearing behind Quaoar (main occultation event), the stars had also partially and briefly dimmed before and/or after the main occultation event. Some features were observed in the data obtained with the 10.4-meter GTC with the High PERformance CAMera (HiPERCAM, DHILLON *et al.*, 2021) instrument[1]. Amateur astronomers in Australia reported the ring-like feature during an occultation on 2021 August 27. Detecting these ring-like features led us to return to old data from an occultation in 2018, where one observer in southern Africa detected a shallow and extensive flux drop at about 3, 300 km from Quaoar's center in the sky plane. Observations taken in 2021 with the CHaracterising ExOPlanet Satellite (CHEOPS, BENZ *et al.*, 2021) and an amateur astronomer in Australia resulted in three more detections of this ring-like feature (MORGADO *et al.*, 2022). The high-quality photometry from the CHEOPS data set revealed two shallow flux drops on both sides of the central body occultation. The observation from Australia did not detect Quaoar's occultation. Still, it detected a narrow flux drop corresponding to a structure with ~ 21 km and normal optical depth τ_N of about 0.03.
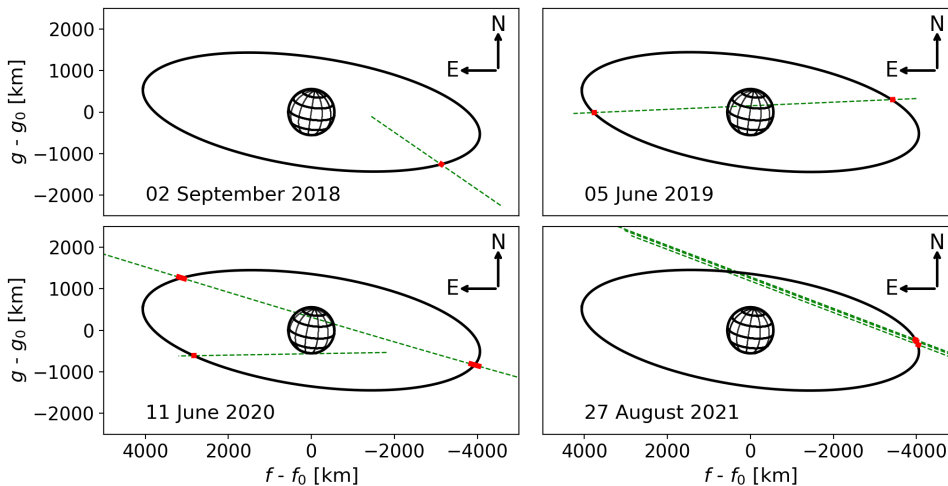
Figure 3.1: All ring detections on 2018-2021 stellar occultation events, projected in the sky-plane. Figure extracted from MORGADO *et al.* (2023).

Assuming that Quaoar's ring pole orientation does not present any variation between 2018 and 2021, we can fit a projected common ellipse for all ring detections by varying the pole orientation and the ring radius. The best-fitted ellipse is evaluated using the χ^2 statistics (Equation 2.8). The best result is a circular ring centered in Quaoar (Figure 3.1), with a radius of $\sim 4, 148.4 \pm 7.4$ km (~ 7.4 Quaoar radius), and with two mirrored solutions for the pole orientation: RA= $156°.05 \pm 0.89$; DEC= $+81°.40 \pm 0.11$, and

---

[1]This camera uses a four-band system with g_s ($0.40-0.55\,\mu m$), r_s ($0.550-0.69\,\mu m$), i_s ($0.69-0.82\,\mu m$), z_s ($0.82-1.00\,\mu m$), and u_s ($0.3-0.4\,\mu m$) bands (the occulted star could not be detected at u_s-band).
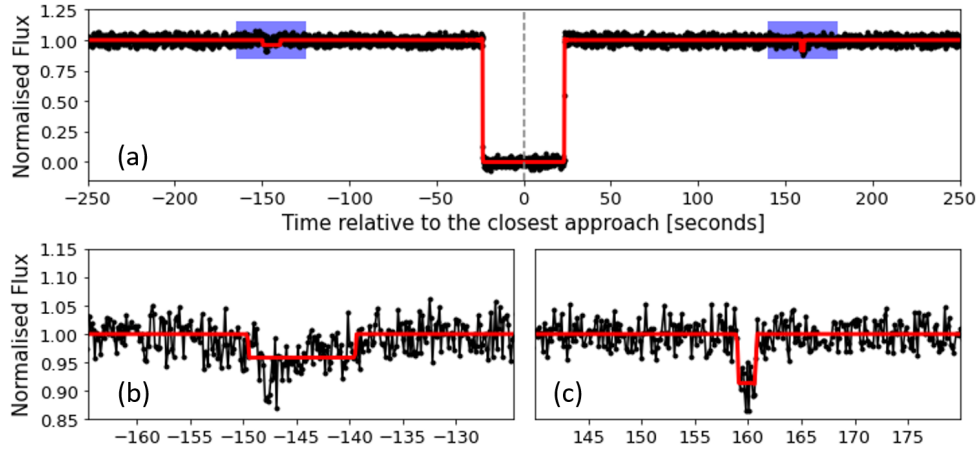
Figure 3.2: Light curve obtained with the HiPERCAM (i_S band) on the 10.4-m GTC as example of the Quaoar ring detections. The observed flux (back) is plotted as a function of the time relative to the closest approach 2019 June 05 at 03:00:31.86 UT. The red curve presents the modeled events for the Q1R before and after the main event by Quaoar. Figure extracted from MORGADO *et al.* (2023).

RA= $258°.47 \pm 0.87$; DEC= $+54°.14 \pm 0.11$. This result puts the ring close to the 1:3 SOR and inclined by $43° \pm 12°$ or $6° \pm 12$ relative to Weywot orbit, respectively. The ring also shares its position with the 6:1 MMR with Weywot's orbital period.

This ring presented two unprecedented and remarkable properties: a) its width and optical depths vary longitudinally, being narrow (< 7 km) and thick ($\tau_N = 0.77$) in some regions, while broad (> 300 km) and thin ($\tau_N = 0.005$) in others (see Figure 3.2 and Table 3.1); b) it orbits Quaoar in a region well beyond the classical Roche limit of the central body, which is at a distance of $1,780$ km, as suggested by MORGADO *et al.* (2023), when we considering realistic density values for the particles present in the ring ($\rho = 0.4\,\mathrm{g\,cm^{-3}}$, based on Saturn's rings). At that and larger distances, the ring particles should accrete into satellites and disappear in a few decades (KOKUBO *et al.*, 2000; TAKEDA e IDA, 2001). To account for the presence of Quaoar's rings at such a distance, one would have to assume that the particles are composed of a highly porous material with a bulk density of $\rho_{\mathrm{Roche}} \sim 30\,\mathrm{kg\,m^{-3}}$, which seems unrealistic (MORGADO *et al.*, 2023). Elastic collisions between ice particles can enhance velocity dispersion and inhibit the accretion of particles over a broad range of realistic bulk densities ($\rho \sim 5,000\,\mathrm{kg\,m^{-3}}$). Laboratory experiments with frosted-ice-covered particles at lower temperatures (< 123 K) indicate a much higher steady-state velocity dispersion due to the less dissipative impacts (HATZES *et al.*, 1988). However, viscous spreading caused by these impacts poses a challenge, as it must be counteracted by mechanisms such as resonances to maintain the ring's narrowness (MORGADO *et al.*, 2023). From its optical depth, Q1R qualifies as a dense ring, meaning that its particles suffer a fraction to several collisions per revolution. Consequently, its dynamics strongly depend on collisions, in contrast to some tenuous dust rings of the

giant planets with an optical depth $\leqslant 10^{-4}$ and where particles evolve independently.

Dynamically, the Q1R ring shows a common characteristic of Chariklo's and Haumea's rings. Its position is close to the region of the 1:3 SOR, reinforcing the link between this resonance and the confinement of rings. Preliminary numerical simulations show that an initially scattered colliding particle system is confined in a narrow ring under that resonance (MORGADO *et al.*, 2023; SALO *et al.*, 2021b; SICARDY *et al.*, 2021).
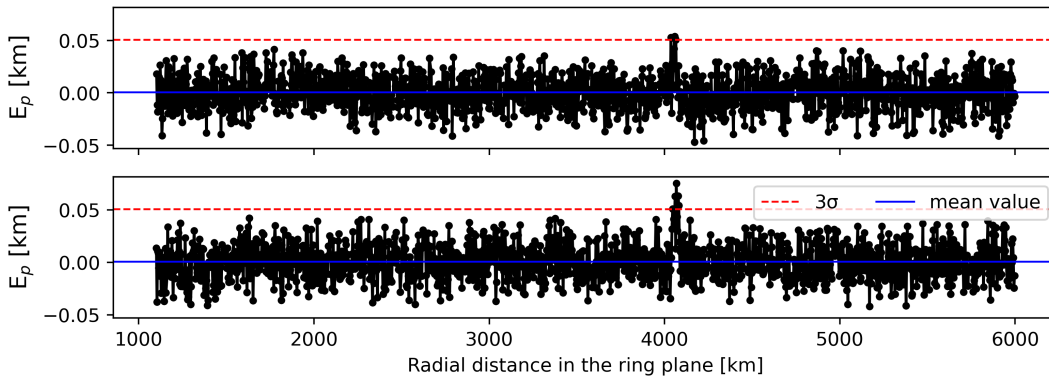
Figure 3.3: Light curve obtained with the HiPERCAM (i_S band) on the 10.4-m GTC converted to equivalent width E_p plotted as a function of the radial distance projected in the ring plane, being the top (resp. bottom) panel the region prior (resp. after) the local closest approach. The blue line indicates the mean of the distribution, and the red line is the 3σ upper limit. The Q1R detections are over this limit on both sides of the central body occultation (> 1000 km).

A search for material was performed in all light curves presented in MORGADO *et al.* (2023). The method described in Section 2.2.3 was applied, where we converted the flux versus time light curve to equivalent width as a function of the radial distance in the ring plane and searched for outliers over 3σ from the mean. For light curves with ring detections, we searched for material between rings and Quaoar; for the other light curves, the search was performed in all data points external to the main event. We resampled the light curves using windows of 300 km to increase the sensibility for detections of wider and dimmer structures. As a result, we have not found any additional flux drop consistent with narrow or broad rings in the light curve of the events observed from 2011 up to 2021. This is mainly due to the observations' lack of photometric sensitivity and/or temporal resolution. All the values obtained on detection limits are presented in Table 3.2, and an example of the graphs generated during this procedure is presented in Figure 3.3. In this example, with the HiPERCAM (i_S band) light curve on the 2019 June 05 event, we have positive detection for Quaoar and the Q1R ring on both sides of the central body. The upper limits for the equivalent depth in the region between the Q1R ring and the central body are $E_p = 0.050$ km at the 3σ level.

Table 3.1: Physical and global parameters of Quaoar Q1R ring, with 1σ error bars. Table adapted from MORGADO *et al.* (2023).

Ring global parameters[a]			
Radius [km]	Pole RA [deg] (J2000)	Pole Dec [deg]	Inclination relative to Weywot orbit[d] [deg]
Solution 1: 4,097.3 (9.5)	156.05 (0.89)	+81.40 (0.11)	43 (12)
Solution 2: 4,148.4 (7.4)	258.47 (0.87)	+54.14 (0.11)	6 (12)

Ring local parameters.			
Date and Station	Radial Width [km]	Normal optical depth	Equivalent Width [km]
02-09-2018 HESS (bef.)	22.29 (1.27)	0.032 (0.003)	0.67 (0.06)
05-06-2019 GTC g_s (bef.)	n.a[b]	n.a[b]	n.a[b]
05-06-2019 GTC r_s (bef.)	336.34 (23.81)	0.010 (0.007)	3.38 (0.82)
05-06-2019 GTC i_s (bef.)	301.38 (2.50)	0.007 (0.001)	2.08 (0.13)
05-06-2019 GTC z_s (bef.)	306.55 (2.36)	0.009 (0.002)	2.77 (0.21)
05-06-2019 GTC g_s (aft.)	109.68 (61.45)	0.017 (0.005)	1.72 (1.08)
05-06-2019 GTC r_s (aft.)	40.69 (4.83)	0.018 (0.002)	0.69 (0.04)
05-06-2019 GTC i_s (aft.)	44.09 (1.05)	0.016 (0.001)	0.70 (0.05)
05-06-2019 GTC z_s (aft.)	109.78 (63.00)	0.013 (0.002)	1.48 (0.90)
11-06-2020 CHEOPS (bef.)	n.a[c]	n.a[c]	1.10 (0.40)
11-06-2020 CHEOPS (aft.)	n.a[c]	n.a[c]	0.80 (0.41)
11-06-2020 Mount Carbine (aft.)	21.34 (3.13)	0.052 (0.016)	1.02 (0.28)
27-08-2021 Reedy Creek[d] (bef.)	$4.91^{+6.94}_{-0.43}$	$1.548^{+1.267}_{-1.290}$	$1.70^{+0.66}_{-0.53}$
27-08-2021 Algester[d] (bef.)	$6.69^{+2.56}_{-1.02}$	$1.008^{+2.215}_{-0.792}$	$2.21^{+0.35}_{-0.83}$
27-08-2021 Samford Valley[d] (bef.)	$7.09^{+0.86}_{-0.52}$	$0.235^{+0.042}_{-0.045}$	$1.21^{+0.13}_{-0.14}$

[a] For each ring's pole orientation, an opposite direction is possible depending on the particles' direction of motion. Solution 2 is preferred because it is closer to Weywot's orbital pole orientation.
[b] The light curve S/N does not allowed the detection of the ring.
[c] These values are unavailable as the ring is unresolved. Only the Equivalent Width (Radial Width × Normal opacity) can be computed.
[h] Due to the small number of points within each detection, the 1σ uncertainty has a large asymmetry.

Table 3.2: Results on detection limits determination for Quaoar multi-epoch observations. Table adapted from MORGADO *et al.* (2023).

Date	Site	Original spatial resolution		Resampled data		
		W_r [km]	$E_p(3\sigma)$ [km]	W_r [km]	$E_p(3\sigma)$ [km]	N
2018	Les Makes	0.261	0.040	299.799	0.004	1150
2019	PIRATE - Tenerife	189.005	22.663	378.010	22.663	2
2019	Artermis - Tenerife	59.064	1.188	295.321	0.862	5
2019	Liverpool - La Palma	14.175	2.110	297.677	0.744	21
2019	TRAPPIST-North	118.006	7.509	236.001	7.509	2
2021	Glenlee (AUS)	3.413	0.225	296.983	0.070	87
2021	Hawkesbury Heights (AUS)	3.402	0.230	299.374	0.071	88
2021	Hazelbrook (AUS)	3.402	0.258	299.368	0.069	88
2021	Yass (AUS)	2.658	0.166	297.707	0.050	112
2021	Murrumbateman (AUS)	1.701	0.152	299.402	0.027	176

3.1.2   The discovery of the Quaoar's second ring (2023 Q2R)

Aiming for a better understanding of the nature of this curious ring around Quaoar, new stellar occultations were predicted. An event occurred on August 9, 2022 (Figure 3.4), caught the attention as the shadow passed over Mexico, the continental United States, and the Hawaiian archipelago, sites with large professional telescopes and a significant number of amateur observatories. An observational campaign was triggered involving 24 Research and Education Collaborative Occultation Network (RECON) stations formed by citizen astronomers with portable telescopes in the continental US. The observations were also performed using the following professional telescopes: Canada France Hawaii Telescope (CFHT, 3.6-meter) and Gemini-North (8.1-meter), located in MaunaKea, Hawaii; Tohoku University Haleakala Observatory (TUHO, 0.6-meter), Haleakala, Hawaii; the Transneptunian Automated Occultation Survey (TAOS II, 1.3-meter), San Pedro Martir, Baja California, Mexico; and the Hale Telescope (5.1-meter) located at Palomar Observatory, San Diego, California. The observational circumstances of this campaign can be found in Table B.1 in PEREIRA *et al.* (2023) (Appendix A). Figure 3.5 presents the post-occultation map with all sites involved in this campaign.

The occultations by the main body and Q1R were recorded in broadband (no filters) at the Tohoku University Haleakala Observatory (TUHO) and Transneptunian Automated Occultation Survey (TAOS II). Due to the lack of S/N, only the occultation by the main body was extracted from the data acquired at the University of California in Santa Cruz (UCSC-CA, California, US), Dunrhomin Observatory (Colorado, US), Sommers-Bausch Observatory (Colorado, US), Nederland (Colorado, US) and a mobile station in Bonny Doon Eco Reserve (California, US).

The observation at CFHT was made using the Wide-field InfraRed Camera (WIRCam, PUGET *et al.*, 2004) at $2.15\mu m$ (Ks-band), and the science data were obtained from the Image Stabilizing Unit (ISU), responsible for image stabilization. The ISU is a small window with 30x30 pixels and a scale of 0.300 arcsec/pixel on each of the four detectors in the focal plane[2]. The data were provided in cubes with 1,599 images totaling 181.43 seconds, resulting in an exposure time per frame of 0.113 seconds.

The observation at Gemini North was made with the instrument 'Alopeke (SCOTT *et al.*, 2021), a component that has a dichroic splitter to separate the light beam at $674\mu m$ for two iXon Ultra 888 EX cameras, one coupled on a red filter wheel (transmitted flux) and the other on a blue filter wheel (reflected flux). The images were then acquired in the SDSS r' ($947\mu m$) and z' ($620\mu m$) filters for blue and red filter wheels, respectively, using the Wide-Field mode with a sub-array of 256×256 pixels and 1×1 bin. This configuration allowed acquisition with an exposure time of 0.100 seconds and a readout time of 1 millisecond[3].

---

[2]https://www.cfht.hawaii.edu/Instruments/Imaging/WIRCam/
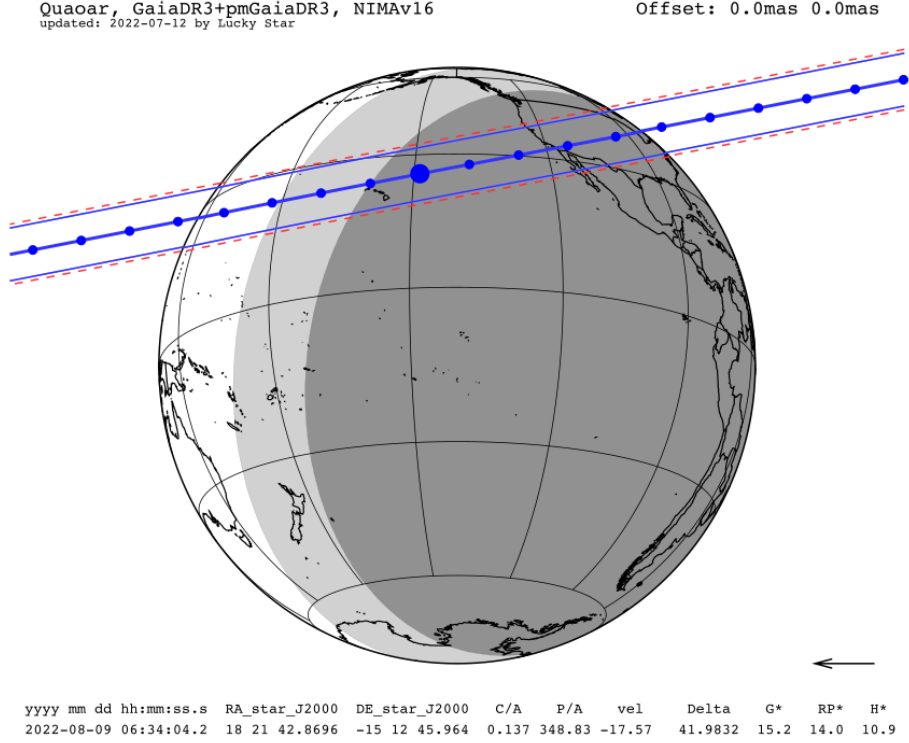[3]https://www.gemini.edu/instrumentation/alopeke-zorro

Figure 3.4: Prediction map of the occultation by Quaoar on August 9, 2022. The shadow path was predicted to pass over the continental United States, Hawaii, and Mexico. The top label shows the stellar catalog and ephemeris used in the prediction. The bottom label shows the geocentric closest approach (C/A) instant, the star position, the geocentric closest approach (C/A, in arc-seconds), the object position angle relative to the star (P/A, in degrees), the object geocentric distance (Delta, in au), the Gaia magnitudes normalized for the event velocity (G*, RP*, H*). The blue lines limit the object shadow, with the red dashed line limiting the 1σ uncertainty. The blue dots are separated by 60 seconds from each other, being the big one the geocentric closest approach instant. Map from https://lesia.obspm.fr/lucky-star/occ.php?p=105952.

All the light curves were obtained from differential aperture photometry using the PRAIA software ASSAFIN (2023). The light curve modeling was conducted through pipelines built with SORA package (GOMES-JÚNIOR *et al.*, 2022). The light curves were modeled using the expected limb velocity calculated from a preliminary ellipse fit. The limb-darkened star angular diameter was calculated by Pierre Kervella (private communication) as 44μmas, a red giant star with R = 14 R$_\odot$ and T$_{eff}$ ~4000 K - the apparent star diameter corresponds to approximately 1.3 km at Quaoar distance. The light curve dispersion was calculated separately for points before ingress and after egress. The dispersion computation does not consider the spikes for the light curves with diffraction signatures (CFHT and Gemini).

Calculating the velocities of disappearance and reappearance of the star behind Quaoar for the CFHT and Gemini North light curves requires consideration. The local values of the radial velocity obtained from a preliminary elliptical fit do not allow a good fit between
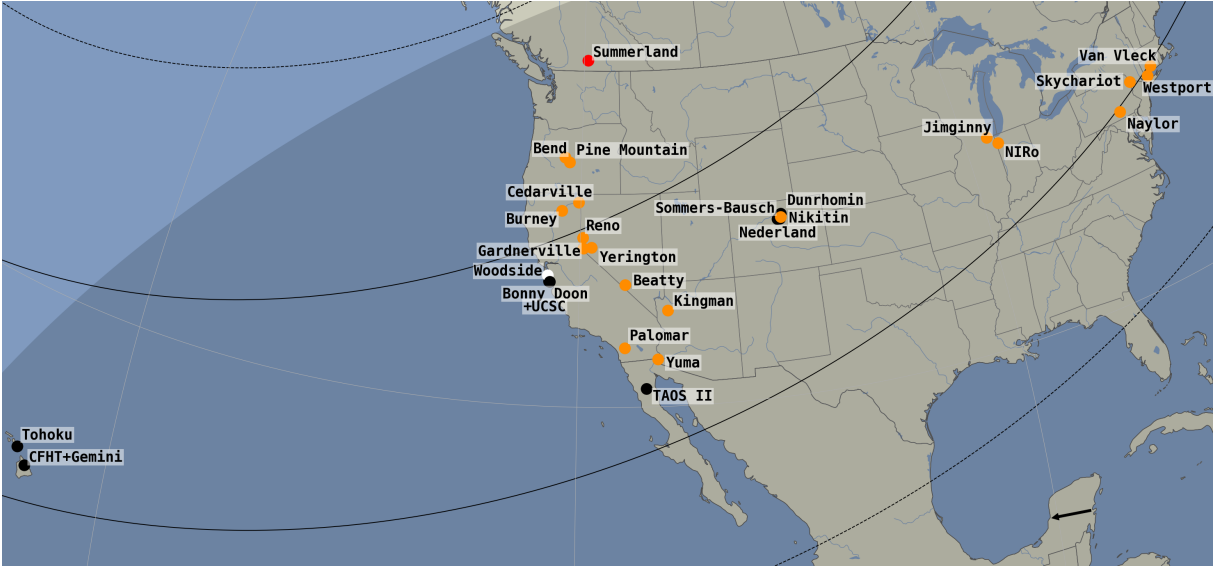
Figure 3.5: Post-event map showing positive detections of occultations (black dots) and sites reporting cloudy weather (orange dots). The white dot indicates areas with no data due to instrumental limits. A red dot represents a site with data, but no occultation was detected. Solid black lines delineate Quaoar's shadow limits, while dashed black lines mark the projections of Quaoar's ring (Q1R). A black arrow in the bottom right indicates the direction of the shadow's motion. Adapted figure from PEREIRA *et al.* (2023).

synthetic and observed curves. Thus, fixing the star's apparent diameter and considering the band-pass and FWHM, we fitted the light curve, keeping the local velocity as a free parameter. Among the curves, the one with the lowest dispersion is the observation with the z' band of the Gemini ('Alopeke Red), so we use this curve as a reference to calculate the radial velocity at the ingress and egress instants iteratively and use this velocity for the CFHT - and the observation with the r' band (Gemini Blue). Despite a clear separation between the chords obtained from the CFHT and Gemini North when projected onto the sky plane, this separation is smaller than the apparent diameter of the star, and, therefore, the velocities were considered the same at both sites – 10.19 $\mathrm{km\,s^{-1}}$ for ingress, and 16.61 $\mathrm{km\,s^{-1}}$ for egress.

Figure 3.6 presents the modeled curve plotted over the observed data from the Gemini r'-band, which shows the good fit obtained by varying the star velocity at the limb limit. The ingress and egress instants for this, and other light curves in this event, were determined using the standard procedure described in Section 2.1.4, with all the results summarized in Table 3.3. By projecting the chords obtained from the ingress and egress instants determined for each site, we search for the best-fitted ellipse by allowing the values of center, apparent oblateness, apparent semi-major axis, and apparent position angle to vary over a wide range. Additionally, a 5 km topography was considered for the fit (σ_{model} in Equation 2.8). By generating $500,000$ ellipses in the phase space, we found an ellipse that best fits the chord extremities and their correspondent 1σ marginal error
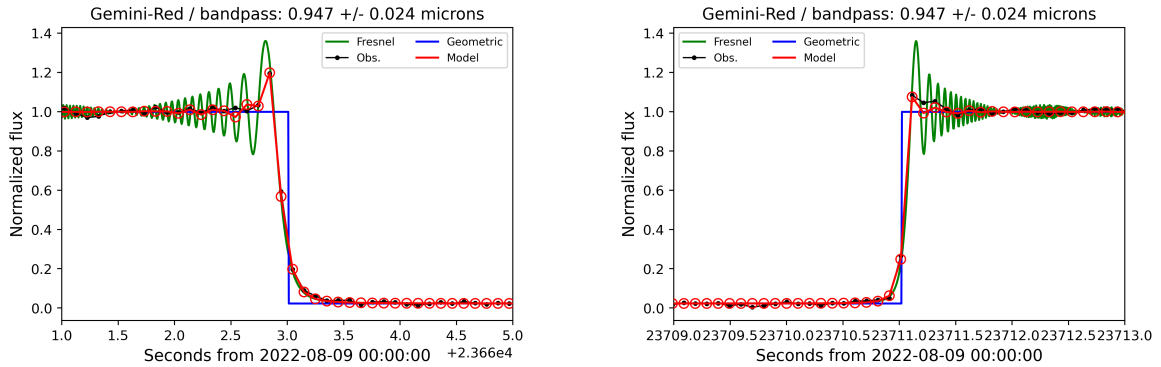
Figure 3.6: Synthetic light curve (red) plotted over the observed data (black) from the Gemini z' data set. In green is the Fresnel diffraction effect, and in blue is the geometric model representing the opaque body occulting the star.

Table 3.3: Ingress and egress times for Quaoar's main body on August 9, 2022. The times are given in UT, and the uncertainties in the 1σ level are given in seconds. Table from PEREIRA *et al.* (2023).

Site	Ingress (hh:mm:ss.s)	Egress (hh:mm:ss.s)
CFHT (Ks)	06:34:23.34 (0.02)	06:35:11.42 (0.01)
Gemini North (z')	06:34:23.29 (0.01)	06:35:11.29 (0.01)
Gemini North (r')	06:34:23.27 (0.03)	06:35:11.28 (0.02)
TUHO	06:34:23.5 (0.2)	06:35:18.1 (0.2)
TAOS II	06:30:38.3 (0.2)	06:31:35.1 (0.1)
Dunrhomin	06:30:03.3 (0.4)	06:31:02.8 (0.9)
Sommers-Bausch	06:30:02.6 (0.2)	06:31:03.8 (0.5)
UCSC	06:31:20.3 (0.1)	06:32:00.9 (0.1)
Nederland	06:30:03.4 (0.5)	06:31:04.4 (0.8)
Bonny Doon	06:31:20.7 (0.4)	06:32:01.3 (0.4)

bar. The best-fitted ellipse parameters and the geocentric astrometric position of Quaoar on the stellar occultation epoch are presented in Table 3.4 and represented in Figure 3.7.

The Q1R ring was detected on both sides of the central body occultation in the Gemini North and CFHT light curves, while only in the region after the central body occultation in the TAOS II and TUHO light curves, with their physical characteristics determined as detailed in Section 2.2.1. The findings of the denser part of the Q1R in the Gemini North and CFHT light curves suggest the existence of diffuse material with about 50 km width with variable optical depth enveloping a more confined (FWHM $\sim$ 5.7 km) and densest ($\tau_{\max} = 0.3$) structure, resembling Saturn's F ring (MURRAY e FRENCH, 2018). The quality of the TAOS II and TUHO light curves only allows for detecting a ring with sharp edges but consistent width and optical depths in the CFHT and Gemini detections when considering the complete structure (confined nucleus plus envelope wings). The average distance of these five detections is $4,122$ km. Due to the low optical depth of
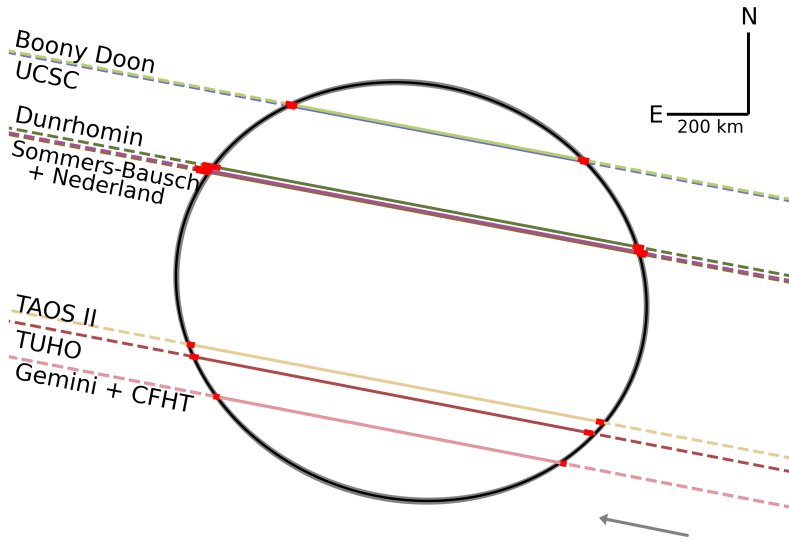
Figure 3.7: Representation of the best elliptical fit (black ellipse) and the uncertainties within the 1σ region (grey) (see Table 3.4). The red segments represent the uncertainties in instants determination (see Table 3.3). Note that both Gemini North and the CFHT chords have an uncertainty that is too small to be seen in the projection, represented by a red square bigger than their actual error bar size. Image from PEREIRA *et al.* (2023).

the Q1R segment intercepted before the closest approach, only the light curves obtained at Gemini and CFHT have adequate S/N for detection. The Gemini detection in the r'-band appears more sharply defined than its counterpart in the z'-band, but this effect remains marginal considering the S/N. The CFHT light curve shows simultaneous flux drops with the Gemini's. Still, it may be influenced by a sky's deterioration that prevents an accurate determination of the ring width (see Figure 3.8). Nonetheless, the central times and widths of the Gemini and CFHT detections are consistent at the 1σ level. The average width of the broader ring detected in the 2022 event is 90 km, with a normal optical depth of about $\tau_{\mathrm{N}} = 0.006$, and distant $\sim 3,995$ km from the Quaoar's center. It is important to note that these properties are different than the values retrieved in past detections by this ring, where the Q1R ring width was > 300 km, indicating again the variable nature of this structure. These observations confirm the interpretation that the Q1R ring presents longitudinal variations in the optical depth and radial width. The ring properties were determined using the method presented in Section 2.2.1 for all the detections, with the results provided in Table 3.5, and the modeled and observed curves for the ring detections are presented in Figure 3.8.

The data sets obtained with the CFHT and Gemini telescopes allowed probing for new secondary detections in the light curves in regions between the main body and the Q1R ring. These data sets reveal additional secondary events symmetrically located about 2,500 km from the Quaoar's center. Two such events are simultaneously detected in the

Table 3.4: Results obtained from the ellipse fit for Quaoar event on August 9, 2022, for the geocentric closest approach instant 06:34:03.560 UT. The marginal error bars are in the 1σ region. The error bar for the geocentric position is given in *mas*. Table from PEREIRA *et al.* (2023).

Parameter	Value
Apparent semi-major axis [km]	$a' = 579.5\,(4.0)$
Apparent oblateness	$\epsilon' = 0.12\,(0.01)$
Equivalent radius [km]	$R_{\mathrm{equiv}} = 543\,(2)$
Ephemeris offset [km]	$f_0 = -24.7\,(2.0)$
	$g_0 = -13.9\,(2.1)$
Position angle [deg]	$P = 345.2\,(1.2)$
χ^2 per degree of freedom	0.986
Geocentric astrometric position (ICRS)	$\alpha = 18^{\mathrm{h}}\,21^{\mathrm{m}}\,42^{\mathrm{s}}.8677703\,(0.289)$
	$\delta = -15^{\mathrm{o}}\,12'\,45''.829691\,(0.230)$

Gemini z'-band and CFHT Ks-band light curves before the closest approach, with detections reaching around 5.5σ and 5.2σ, respectively. Conversely, the light curves show simultaneous events after the closest approach with significant detections of 5.7σ, 3.7σ, and 4.7σ in the Gemini z' and r' and CFHT, respectively. When projecting these detections onto the sky plane, we could fit a projected ellipse with the same opening angle B and position angle P as the Q1R ring, i.e., a circular ring concentric and co-planar with the Q1R, with a radius of 2,520 km. Assuming the light curves follow a normal distribution, the probability of individual points with equivalent width $E_p(3\sigma) > 12$ km occurring randomly in each light curve is $p \approx 1.4 \times 10^{-3}$, with p approaching zero for larger values of E_p. While the two light curves from the Gemini instrument may be correlated, as they were taken at the same telescope, the Gemini and CFHT data are independent regarding fast-seeing fluctuations. Using Poisson statistics, we estimate that the probability of the simultaneous events in the Gemini and CFHT data occurring randomly due to seeing fluctuations is very low, with $p \approx 10^{-6}$.

Regarding the local properties of Quaoar's second ring (2023 Q2R), the radial width in the ring plane varies from 7 to 10 km, while the normal optical depth τ_{N} varies between from 0.003 to 0.01. This indicates that the Q2R ring may not present azimuthal variations like the Q1R. We can compare the quantity of material presented in the ring cuts using the equivalent width values. We can see that the densest part of the Q1R has about 20-35 times more material than the Q2R ring. All the ring properties obtained from the 2022 event are presented in Table 3.5. Considering the double-peaked rotation period of P = 17.6788 ± 0.0004 hours ORTIZ *et al.* (2003) and the Quaoar's mass of M = 1.20 (0.05) $\times 10^{21}$ kg, we derive the 5:7 SOR location at $2,525 \pm 35$ km. This implies that the Q2R ring, with radius $2,520 \pm 20$ km falls into the resonance region within the 1σ uncertainties. As with the 1:3 SOR, the 5:7 SOR is a second-order resonance and may be the key in the ring confinement. However, more detections of Q2R and its orbit

refinement, besides the Quaoar's shape determination, are required to understand better the ring's local and global properties and how the ring relates to the resonances.

Table 3.5: Physical parameters of rings Q1R and Q2R obtained from August 9th, 2022 stellar occultation. The normal opacity, p_{N}, and normal optical depth, τ_{N}, were calculated from the ring opening angle, B, and position angle, P, derived from the orientation of the body. The other parameters are r, the radial distance from Quaoar's center in kilometers; W_{r}, the radial width in kilometers; E_p the equivalent width in kilometers. The terms "ing" and "egr" stand for ingress and egress, respectively, and refer to the fact that the detection occurred before and after the occultation by Quaoar's main body, respectively. The error bars in parentheses are at the 1σ level. Table adapted from PEREIRA *et al.* (2023).

Ring	Detection	r (km)	W_{r} (km)	p_{N}	τ_{N}	E_p (km)
Q1R$_{ing}$	CFHT	3,994.5 (2.0)	105.6 (4.4)	0.0059 (0.0004)	0.0060 (0.0004)	0.6 (0.2)
	GN (z')	3,995.5 (0.4)	76.5 (0.9)	0.0051 (0.0002)	0.0052 (0.0002)	0.4 (0.1)
	GN (r')	3,995.9 (0.6)	85.5 (1.4)	0.0066 (0.0006)	0.0066 (0.0006)	0.6 (0.2)
Q1R$_{egr}$	CFHT[a]	4,123.69 (0.05)	6.09 (0.11)	0.17 (0.02)	0.2 (0.1)	2.01 (0.03)
	GN (z')[a]	4,122.88 (0.02)	5.29 (0.06)	0.18 (0.02)	0.26 (0.06)	1.87 (0.02)
	GN (r')[a]	4,122.62 (0.04)	5.1 (0.1)	0.17 (0.03)	0.2 (0.1)	1.74 (0.03)
	TUHO	4,113.6 (7.7)	78 (18)	0.06 (0.02)	0.07 (0.03)	4.6 (3.5)
	TAOS II	4,131.4 (4.5)	35 (16)	0.09 (0.04)	0.12 (0.06)	3.3 (3.1)
Q2R$_{ing}$	CFHT	2,490.6 (1.5)	16.1 (3.3)	0.0045 (0.0008)	0.0045 (0.0008)	0.07 (0.04)
	GN (z')	2,493.9 (0.6)	11.3 (1.1)	0.0065 (0.0009)	0.0065 (0.0009)	0.07 (0.04)
	GN (r')	n.d.[b]	n.d.[b]	n.d.[b]	n.d.[b]	n.d.[b]
Q2R$_{egr}$	CFHT	2,540.8 (0.3)	11.2 (0.4)	0.0090 (0.0009)	0.0092 (0.0009)	0.10 (0.04)
	GN (z')	2,540.4 (0.3)	6.8 (0.8)	0.009 (0.001)	0.010 (0.001)	0.06 (0.03)
	GN (r')	2,537.7 (1.3)	9.4 (2.9)	0.006 (0.002)	0.007 (0.002)	0.06 (0.05)

[a]From Lorentzian fit. The width W_{r} is defined as the FWHM of the τ_{N} profile. [b]Not detected. GN, Gemini North.

We combined the data from this study with previous observations published by MORGADO *et al.* (2023) to refine the Q1R orbital parameters, assuming a fixed ring pole orientation between 2018 and 2022. We explored a range of pole orientations and ring radii using a χ^2 statistic, resulting in two complementary solutions. The preferred solution has a χ^2 per degree of freedom (χ^2_{pdf}) of 1.6 and demonstrates better agreement with observations than the mirror solution with $\chi^2_{pdf} = 4.1$. Moreover, the preferred solution is co-planar with Weywot's orbit to within 5 ± 7 degrees, as expected from a primordial disk surrounding Quaoar that evolved into a ring and formed its satellite. The mirrored solution is inclined by 45 ± 7 degrees to Weywot's orbit. The position angles of Quaoar's projected limb (345.2 ± 1.2 degrees) and Q1R (350.2 ± 0.2 degrees) are misaligned by approximately 5 degrees. Therefore, our findings suggest that Q1R orbits close to Quaoar's equatorial plane, assuming Quaoar is an oblate spheroid. Some of this misalignment may arise from Quaoar's shape being a triaxial ellipsoid or a body with a more complex shape,

meaning the position angle of Quaoar's limb may not align with the position angle of Quaoar's pole.
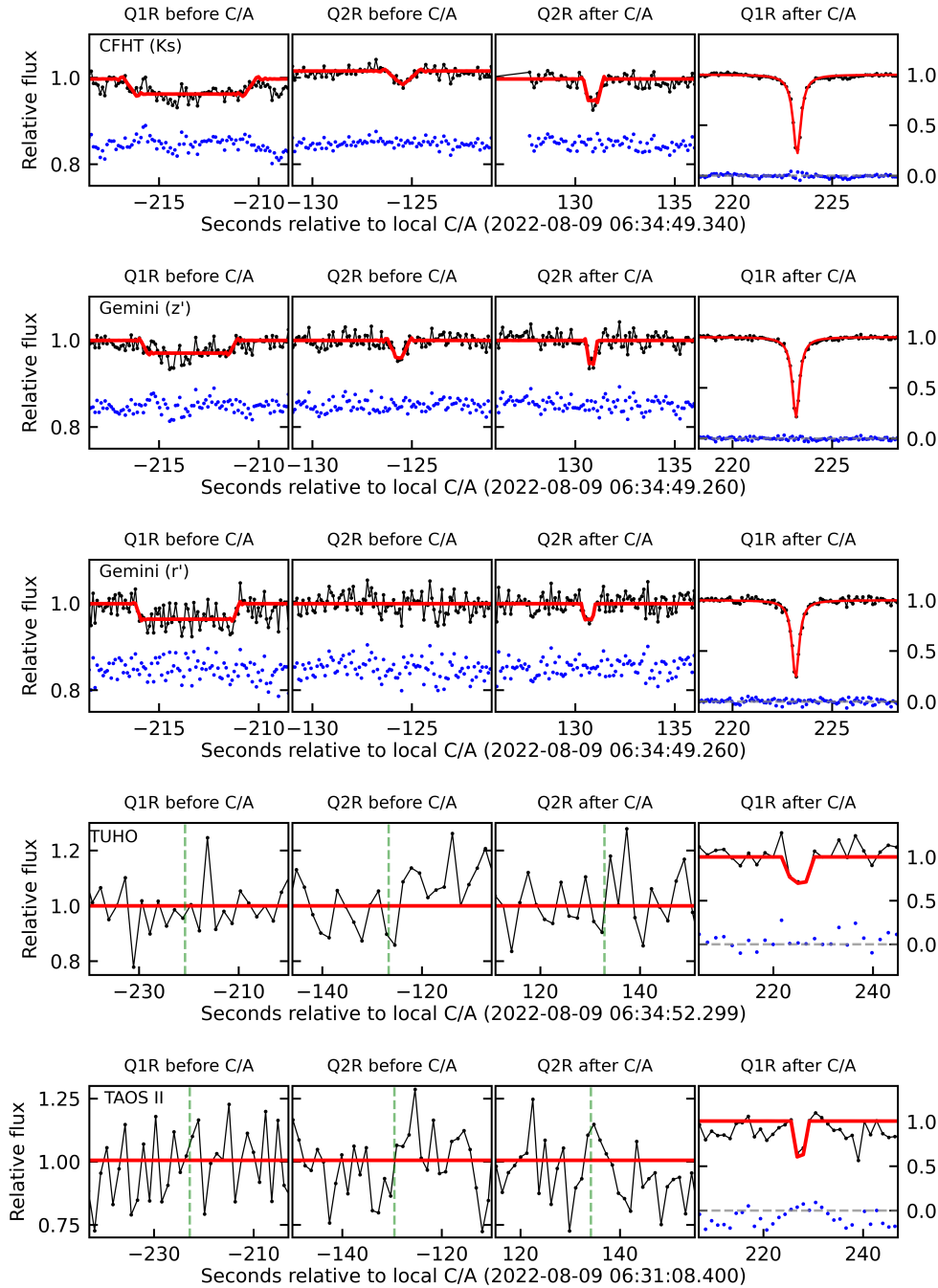
Figure 3.8: Fitted light curves for all five data sets from August 9th, 2022 Quaoar stellar occultation. The top three are the light curves with enough S/N to detect the Q2R and the tenuous part of the Q1R ring (CFHT Ks band and Gemini North at z' and r' bands). The last two panels present the light curves from TUHO and TAOS II observatories, with S/N sufficient only for detecting the densest region of the Q1R at the egress region. These light curves are plotted as a function of the time in seconds relative to the local closest approach (C/A), with a different y-axis scale in the rightmost panel in each row (dense part of Q1R). The green vertical dashed lines in the TUHO e TAOS II light curves represent the theoretical times for the Q1R and Q2R rings. Image from PEREIRA *et al.* (2023).

3.2 (2060) 95P/Chiron

Discovered by Charles Kowal at Palomar Observatory on November 1st, 1977 (KOWAL *et al.*, 1979), the Centaur (2060) Chiron was the first to be observed on this class of small objects – the earliest recovery date is registered to April 24th, 1895. To be classified as a Centaur, the body needs to have an orbit with the perihelion q and semi-major axis a between the semi-major axis of Jupiter and Neptune ($a_J = 5.2$ au and $a_N = 30.0$ au, respectively), besides the absence of 1:1 resonance with giant Planets (JEWITT, 2009). Chiron has an orbital semi-major axis $a = 13.709$ au, with perihelion at $q = 8.543$ au, aphelion at $Q = 18.876$ au, inclination $i = 6.917°$, and eccentricity $e = 0.376$ (Solar System Database/JPL156). Also denominated as 1977 UB, Chiron is the second largest object in the Centaurs class with different diameters presented in the literature obtained using various techniques: the first estimates for the Chiron's size were published by LEBOFSKY *et al.* (1984) using five-color ($\lambda = 0.36 - 0.85$ μm) and thermal infrared ($\lambda = 22.5$ μm) photometric observations, giving an upper limit for the diameter of 180^{+40}_{-50} km ($\leqslant 250$ km at the 2σ level). The absence of detections at 60 μm and 800 μm set upper limits for the diameter of 372 km and 300 km, respectively (JEWITT e LUU, 1992; SYKES e WALKER, 1991). Using multi-year thermal infrared observations, CAMPINS *et al.* (1994) estimates a diameter between 148 ± 22 km and 208 ± 20 km. Observations with the Hershel Space Telescope suggest a diameter of 218 ± 20 km (FORNASIER *et al.*, 2013), while more recent observations using the Atacama Large Millimeter Array (ALMA) suggest a diameter of 210 ± 10 km (LELLOUCH *et al.*, 2017). Also, results from the November 7th, 1993 single chord occultation suggest a lower limit for diameter of approximately 166 km (BUIE *et al.*, 1993). Using a multi-chord stellar occultation, we determined, for the first time, the triaxial dimensions for Chiron based on the true rotational light curve and assuming the equivalent radius from the literature. From our determination, we obtain a volume-equivalent diameter of $D_{vol} = 196 \pm 34$ km (BRAGA-RIBAS *et al.*, 2023).

The Centaur Chiron has presented cometary behavior since its discovery, with an increase in the absolute magnitude occurring in 1978 when Chiron was at 17.5 au from the Sun (HARTMANN *et al.*, 1990). Compared with the absolute magnitudes obtained in 1980 and 1983, an increase of 0.6 mag at the beginning of 1988 and 1.0 mag by the end of the same year was observed (HARTMANN *et al.*, 1990). A cometary coma was indirectly observed in 1988 when a decrease in the amplitude of the rotational light curve was observed, with Chiron at a heliocentric distance of about 12 au (BUS *et al.*, 1989; HARTMANN *et al.*, 1990). Two independent observers detected the cometary coma directly when Chiron was at 11.8 au in 1988, extending for about eight arc-seconds (MEECH e BELTON, 1990). All these characteristics gave Chiron the periodic comet designation 29P/Chiron.

The inner coma of Chiron was first probed using stellar occultations in November 1993

(BUS *et al.*, 1996) and in March 1994 (ELLIOT *et al.*, 1995). The 1993 event presents features in five light curves interpreted as narrow collimated dust jets. The 1994 event also presented dense and narrow features, with occultation depth of about 70%, that were also interpreted as jet-like features. The nature of these secondary structures around Chiron remained a mystery until November 2011, when a stellar occultation was detected using the 3-m NASA Infrared Telescope Facility (IRTF) and the 2-m Las Cumbres Observatory Global Telescope Network (LCOGT) FTN, both in Hawaii (RUPRECHT *et al.*, 2015). The symmetrical features were detected in the two light curves, but the high cadence of the IRTF observations revealed a structure similar to Chariklo's rings. Using the 2011 detections plus the jet-like features detected in the '90s, ORTIZ *et al.* (2015) proposed that a circular ring with a radius of about 324 km could explain the secondary flux drops and the long-term variability in the light curves for preferential pole orientation of $\lambda \sim 144°$, $\beta \sim 24°$.

The sections below present the analysis of Chiron's most recent stellar occultations, part of which was already published in two papers in 2023 and part analyzed in this work in preparation for a future paper. The first paper was published in Astronomy & Astrophysics with the title "Constraints on (2060) Chiron's size, shape, and surrounding material from the November 2018 and September 2019 stellar occultations" (BRAGA-RIBAS *et al.*, 2023, see Appendix E). Secondary flux drops were not detected in the 2018 and 2019 stellar occultations. Still, the analysis of the positive chords by Chiron allowed us to determine the body's triaxial dimensions and the detection limits for confined or broad structures in the surroundings. The results presented in this paper are a follow-up to my Master's thesis, assigning me as the second author of this paper. The second paper uses data from a stellar occultation detected in 2022 that was observed using big telescopes, which allowed the detection of secondary structures around Chiron. It was published in Astronomy & Astrophysics Letters with the title "Changing material around (2060) Chiron revealed by an occultation on December 15, 2022" (ORTIZ *et al.*, 2023, see Appendix E). The joint analysis of these structures and those observed in 2011 resulted in the determination of a new pole orientation for the proposed rings around Chiron. Besides the previously proposed ring, at $\sim$ 324 km, we observe new structures at $\sim$ 423 km and $\sim$ 580 km. My direct engagement in data analysis, combining analysis of former detections for pole determination and writing part of the paper, resulted in me being the second author of this work.

The latest stellar occultation was detected on September 10, 2023, with at least ten positive detections for Chiron and the most detailed cover of its surrounding environment. The analysis of this event is presented in 3.2.2.

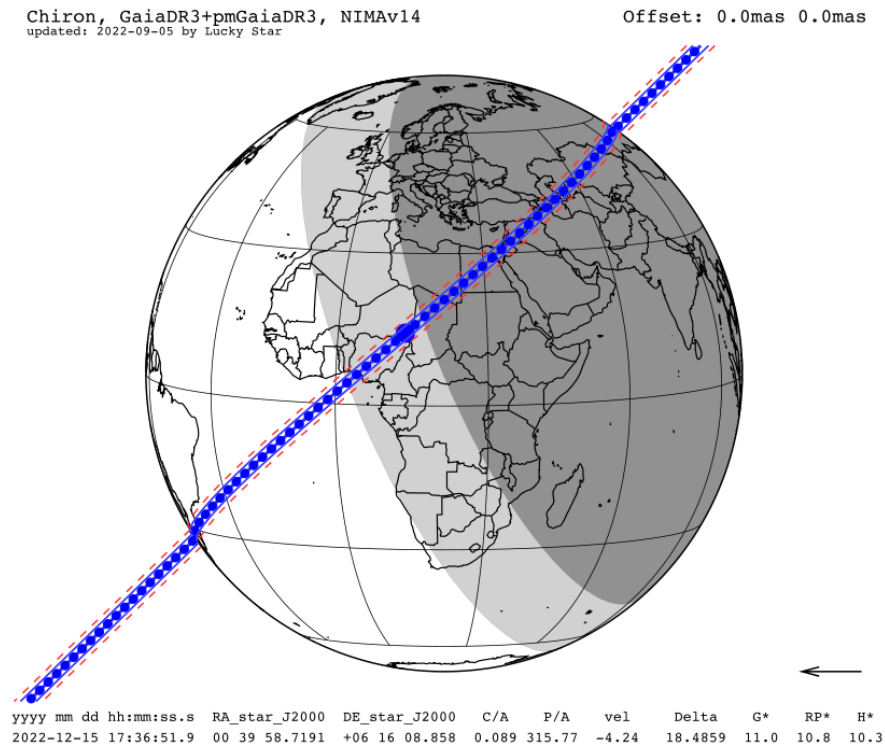### 3.2.1 Stellar occultation on December 15, 2022

Figure 3.9: Prediction map of the occultation by Chiron on December 15, 2022. The shadow path was predicted to pass over North Africa, the Middle East, and East Asia. The top label shows the stellar catalog and ephemeris used in the prediction. The bottom label shows the geocentric closest approach (C/A) instant, the star position, the geocentric closest approach (C/A, in arc-seconds), the object position angle relative to the star (P/A, in degrees), the object geocentric distance (Delta, in au), the magnitude normalized for the event velocity (G*). The blue lines limit the object shadow, with the red dashed line limiting the 1σ uncertainty. The blue dots are separated by 60 seconds from each other, being the big one the geocentric closest approach instant. Map from https://lesia.obspm.fr/lucky-star/occ.php?p=108185.

A stellar occultation by the Centaur object Chiron was predicted and successfully observed on December 15th, 2022, 17:36:52 UT, involving a bright star with magnitude G = 12.7 (G* = 11.0, the star magnitude normalized to a body moving at $20\,\mathrm{km\,s^{-1}}$). The shadow path was predicted to pass over North Africa, the Middle East, and East Asia (Figure 3.12. This event was particularly interesting given the low relative velocity of the shadow over the Earth's surface of about $4.2\,\mathrm{km\,s^{-1}}$, allowing a high spatial resolution even with longer exposure times. Acquisitions were made under a clear sky using two telescopes: one in Egypt and the other in Israel. The observations in Egypt used the 1.88-meter telescope at the Kottamia Astronomical Observatory (KAO) (AZZAM *et al.*, 2010) equipped with the Kottamia Faint Imaging Spectro-Polarimeter (KFIS) (AZZAM *et al.*, 2022). The acquisitions were made using imaging mode with 4x4 binning to re-

duce readout time and using a SDSS g-band filter. The exposure time of the observation was 3 seconds, with a readout time of about 1.5 seconds. The total cycle time of 4.5 seconds gives us a spatial resolution in the sky plane of about 19 km. In Israel, the data were taken using a CCD camera with a Kodak KAF-8300 sensor coupled to a 0.45-meter telescope at the Wise Observatory. The exposure time of the acquisitions was 3 seconds, with a readout time of about 4.5 seconds. Here, the total cycle time of about 7.5 seconds results in a spatial resolution of about 32 km. Other observatories participating in this observational campaign were Neot Smadar Observatory (NSO) in Israel (technical problems), TÜBITAK National Observatory in Turkey (negative), and a second telescope in the Wise Observatory (technical problems). The observational campaign was managed through the Occultation Portal (KILIC *et al.*, 2022), where the data sets were also uploaded by observers and stored.

The light curves from both data sets were obtained through differential aperture photometry after the bias subtraction and flat field corrections, in a procedure already explained in Section 2.1.3. From the analysis of the light curves, we identified that the KAO site did not detect the occultation by the Chiron, being a negative chord. The Wise light curve shows a flux drop that reaches zero for at least 12 seconds, indicating a positive detection of Chiron itself. Although it does not indicate a drop in flux due to the Chiron's occultation, the KAO light curve showed fractional flux drops with a depth with a peak value of about 25%. Besides Chiron's absence of an occultation, these secondary features appear symmetrical to the KAO theoretical closest approach. Note that the Wise light curve begins during the secondary structure's occultation before the closest approach, preventing earlier detection of the counterpart structure.

Our analysis of these secondary detections starts by generating a synthetic light curve built using a geometric model representing the rings observed in the 2011 stellar occultation. The ring local properties were obtained by re-analyzing the IRTF light curve published by RUPRECHT *et al.* (2015) and SICKAFOOSE *et al.* (2020) using our methods, presented in Section 2.2.1. We use the same feature nomenclature used by SICKAFOOSE *et al.* (2020), where the main detections are labeled as A1 and A2 (resp. A3 and A4) for the region before (resp. after) the local closest approach, increasing in time see Figure 3.10. With a cycle time of 4.5 seconds resulting in a spatial resolution of about 19 km, the KAO light curve allows the detection of a more detailed cut of the observed structure. We identified three structures with their counterparts, totaling six flux drops varying in apparent opacity from about $0.25 \leqslant p' \leqslant 0.1$. We labeled these features using the numbers 1, 2, and 3, from the innermost to the outermost. When projected to the proposed ring plane, considering the pole orientation from ORTIZ *et al.* (2015) ($\lambda_{\mathrm{pole}} = 144°, \beta_{\mathrm{pole}} = 24°$), we identified these structures with extinction peak localized at a radial distance relative to Chiron's center of about 320 ± 16 km (feature 1), 445 ± 11 km (feature 2), and extending up to ~ 585 km (feature 3). Since feature 1 falls inside the expected position of the rings
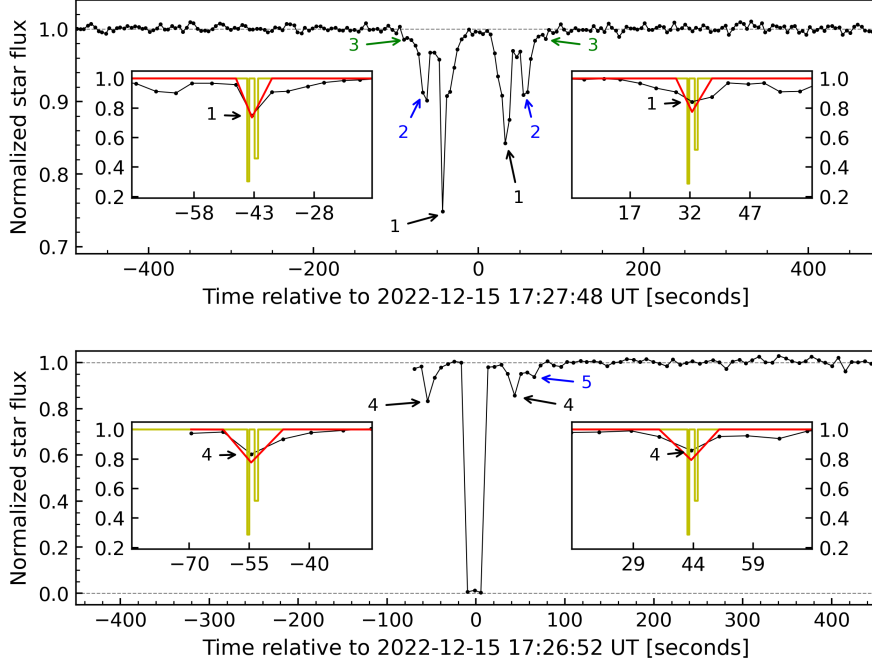
Figure 3.10: Comparison between the structures detected around Chiron in 2011 and the detections in the 2022 light curves from KAO (top panel) and Wise (bottom panel) observatories. The observed data points are in black. The synthetic light curve (red) was built using the geometric model representing the 2011 IRTF detections (gold), convolved with Fresnel diffraction, instrumental response, and apparent star diameter effects from 2022 stellar occultation. Note the difference in the y-scale in both images. Adapted figure from ORTIZ *et al.* (2023).

proposed by ORTIZ *et al.* (2015), we fit the synthetic light curve obtained using the 2011 detections to the observed data. For the detection before the local closest approach, the extinction in flux in the KAO light curve can be explained by the 2011 ring's presence. For the region after the local closest approach, the observed flux extinction fits the synthetic curve within 3σ confidence level. The plausible interpretation is that the structure observed in 2011 is still in the same place and will have similar optical depth in 2022.

On the other hand, the light curve clearly shows that more material is dispersed (or even confined) in Chiron's surroundings. If co-planar and concentric with the proposed rings, the shallow and broad extinction feature enveloping the confined structures suggests the presence of a thin disc with a normal optical depth of $\tau_N \sim 0.006$ extending from 225 km to 640 km. SICKAFOOSE *et al.* (2020) also shows a structure (labeled as A5, Figure 1 in their paper) located ~ 432 km from Chiron's center that coincides in distance with the features identified in KAO light curve (label 2 and 5, Figure 3.10) in both sides of the local closest approach. Despite the lower spatial resolution (~ 32 km), the Wise light curve detected these same structures. The additional features reported by SICKAFOOSE *et al.* (2020) (A6-A13) were not detected in the KAO or Wise light curves.

The secondary structures detected around Chiron in the 2011 and 2022 stellar occul-

tations can be analyzed together to determine better the pole orientation and radii of the proposed rings. We put the detections, labeled as 1 in both light curves of the 2022 event (ORTIZ *et al.*, 2023) and the features labeled as A1 and A2 in RUPRECHT *et al.* (2015) and SICKAFOOSE *et al.* (2020), onto the sky plane considering the correct projection of each event. Thus, these structures are better explained by a circular ring with radius $r = 325 \pm 16$ km and a preferential pole orientation $\lambda_{\mathrm{pole}} = 151° \pm 8°$ and $\beta_{\mathrm{pole}} = 18° \pm 11°$. The best fit of this joint analysis is presented in Figure 3.11.
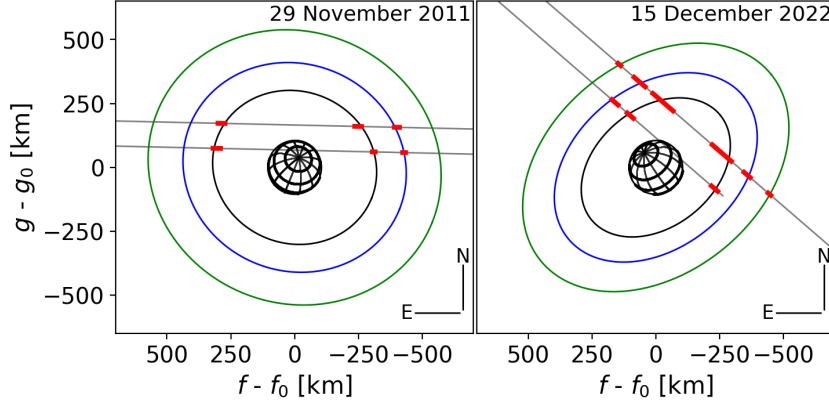

Figure 3.11: Sky plane plots displaying the structures that can match the occultation features from 2011 (left panel) and 2022 (right panel). The red segments represent the complete range of the extinction features, while the grey straight lines correspond to the chords observed at KAO and Wise observatories. Figure from ORTIZ *et al.* (2023).

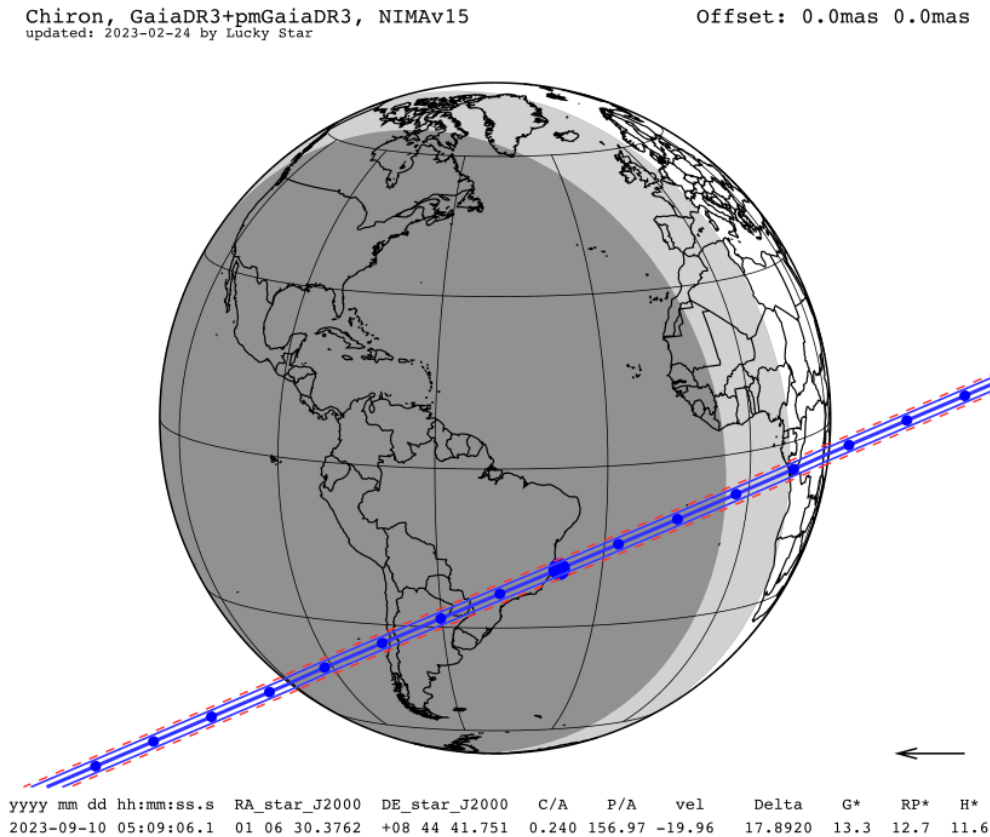### 3.2.2 Stellar occultation on September 10, 2023

Figure 3.12: Prediction map of the occultation by Chiron on September 10, 2023. The shadow path was predicted to pass over Chile, Argentina, and Brazil. The top label shows the stellar catalog and ephemeris used in the prediction. The bottom label shows the geocentric closest approach (C/A) instant, the star position, the geocentric closest approach (C/A, in arc-seconds), the object position angle relative to the star (P/A, in degrees), the object geocentric distance (Delta, in au), the magnitude normalized for the event velocity (G*). The blue lines limit the object shadow, with the red dashed line limiting the 1σ uncertainty. The blue dots are separated by 60 seconds from each other, being the big one the geocentric closest approach instant. Map from https://lesia.obspm.fr/lucky-star/occ.php?p=123202.

The most recent stellar occultation by the Centaur (2060) Chiron at the time of this thesis was predicted and successfully observed on September 10th, 2023, at 05:09:06 UT using professional and small telescopes located at Chile, Argentina, and Brazil. The nominal velocity of the shadow is about $20\,\mathrm{km\,s^{-1}}$. The total number of stations participating in this observational campaign managed with OP[4] was twenty-four, most of these with observations prevented by weather. Of these, at least eleven telescopes were located under the shadow of Chiron over the Earth's surface, with seven confirmed detections. The observational circumstances of all the observatories are presented in Table 3.6.

---

[4]https://occultation.tug.tubitak.gov.tr/chords/1144

Table 3.6: Observational circumstances of the September 10, 2023, stellar occultation by Chiron.

Site	Latitude Longitude Altitude (m)	Telescope (mm) Camera Filter	Exposure (s) Cycle (s)	Status	Observers
OPD Brazópolis Brazil	-22 32 07.748 -45 34 57.540 1810.67	1600 IXon Clear	0.120 0.133	Positive	G. Benedetti-Rossi T. Laidler
OPD Brazópolis Brazil	-22 32 07.748 -45 34 57.540 1810.67	600 IXon filter	0.670 0.683	Positive	L. Liberato H. Dutra
OAMR Reconquista Argentina	-29 09 17.809 -59 38 45.762 50.00	254 Player One Ceres-M Clear	0.800 2.000	Positive	T. Speranza
Reconquista Argentina	-29 08 25.183 -59 38 36.609 50.00	305 QHY174GPS Clear	0.600 0.560	Positive	A. Stechina
OES Sarandi Brazil	-23 30 49.164 -51 51 33.270 469.00 m	200 Raptor Clear	0.600 0.600	Positive	F. Braga-Ribas C. A. Domingues

OAMR: Observatorio Astronómico Municipal de Reconquista;
OES: Observatorio Estrela do Sul;
OPD: Observatorio do Pico dos Dias

When possible, we applied the appropriate Bias and Flat field corrections to the observed data. Each available data set was analyzed using differential aperture photometry, utilizing one or more stars in the field as a reference (except for the PE160 light curve due to the small FOV). After normalizing the light curve, we derived the ingress and egress times of the occultation using the SORA package. The radial velocities were calculated individually for the chord-limb contact points after an initial run of the ellipse fit. Then, we used these new velocities to re-run the light curve modeling and obtain more precise occultation instants, with the values presented in Table 3.7.

Table 3.7: Immersion and emersion instants, and the respective 1σ uncertainties, in seconds from September 10, 2023, at 00:00 UT.

Site	Immersion			Emersion		
	Instant [seconds]	Velocity [km s^{-1}]	χ^2_{pdf}	Instant [seconds]	Velocity [km s^{-1}]	χ^2_{pdf}
OPD (PE160)	$18{,}589.788 \pm 0.001$	10.76	0.903	$18{,}596.320 \pm 0.006$	13.05	0.695
OPD (IAG60)	$18{,}589.862 \pm 0.009$	10.72	13.234	$18{,}596.440 \pm 0.005$	13.23	8.798
OAMR	$18{,}664.341 \pm 0.579$	8.90	5.077	$18{,}670.424 \pm 0.649$	10.47	5.923
Reconquista	$18{,}665.015 \pm 0.017$	8.90	3.742	$18{,}670.818 \pm 0.021$	9.86	4.428
OES	$18{,}621.206 \pm 0.054$	2.21	2.167	$18{,}623.468 \pm 0.029$	3.94	1.102

By projecting the chords onto the sky plane, we notice that the chords are misaligned. To align the chords, an offset of +0.06 seconds was applied to the PE160 chord (equivalent to half an exposure time) and -0.6 seconds to the Reconquista chord (representing one exposure). Finally, we can fit a projected ellipse representing the object limb at the

occultation instant. Due to the long cycle time and large error bars, we disregarded the chord obtained from Observatorio Astronómico Municipal de Reconquista (OAMR) observations for the elliptical fit. Thus, we had only three effective chords for our fit: PE160, Reconquista, and Observatorio Estrela do Sul (OES). There are also two possible positive chords between OPD and OES, but the observers have not yet made these data sets available. By generating 500,000 ellipses varying the apparent oblateness, position angle, center, and semi-major axis, we found the best solution for an ellipse representing Chiron's shape at the occultation instant. The best-fitted ellipse is plotted over the chords in Figure 3.13 with the best parameters presented in Table 3.9. Table 3.8 presents the χ^2 results from this fit, with the χ^2 maps displayed in Figure 3.14.

Table 3.8: χ^2 results from the ellipse fitted to the September 10, 2023 chords.

Parameter	Value
$\chi^2_{\min}$	8.820
Fitted points	6
Fitted parameters	5
χ^2_{pdf}	8.820

Table 3.9: Best ellipse parameters in the 1σ and 3σ levels for the ellipses fitted to the September 10, 2023 chords.

	f_0	g_0	a'	ϵ'	P/A
1σ	15.568 ± 0.667	-26.767 ± 0.521	111.525 ± 0.783	0.310 ± 0.009	41.665 ± 0.841
3σ	15.510 ± 2.158	-26.820 ± 1.736	111.456 ± 2.544	0.309 ± 0.031	41.534 ± 2.924

On September 5, 6, 20, and 21, we utilized the SOuthern Astrophysical Research telescope (SOAR) telescope equipped with the Goodman Spectrograph (CLEMENS *et al.*, 2004) in image mode to gather data for determining the rotational phase during the occultation (more information about this proposal for SOAR observations are in Appendix D). This campaign aimed to capture high-quality images and derive the target object's precise rotation light curve. Unfortunately, adverse weather conditions prevented observations on the first night. Data were successfully acquired on September 20, covering almost one rotational cycle. On September 21, weather conditions again hindered observations for half the night, and strong winds caused the few images obtained to be blurry. We used the Red Camera with SDSS$-r'$ filter to acquire the images. The exposure time was 300 seconds. This setup was chosen to maximize the signal-to-noise ratio and minimize atmospheric interference. The rotation light curve was obtained using Package for the Reduction of Astronomical Images Automatically (PRAIA) photometry in mode 2 (varying aperture photometry, manual object indication) (ASSAFIN, 2023). Although various stars were considered in the photometry process, the relative magnitude light curve (Figure 3.15 was constructed using only one calibration star.
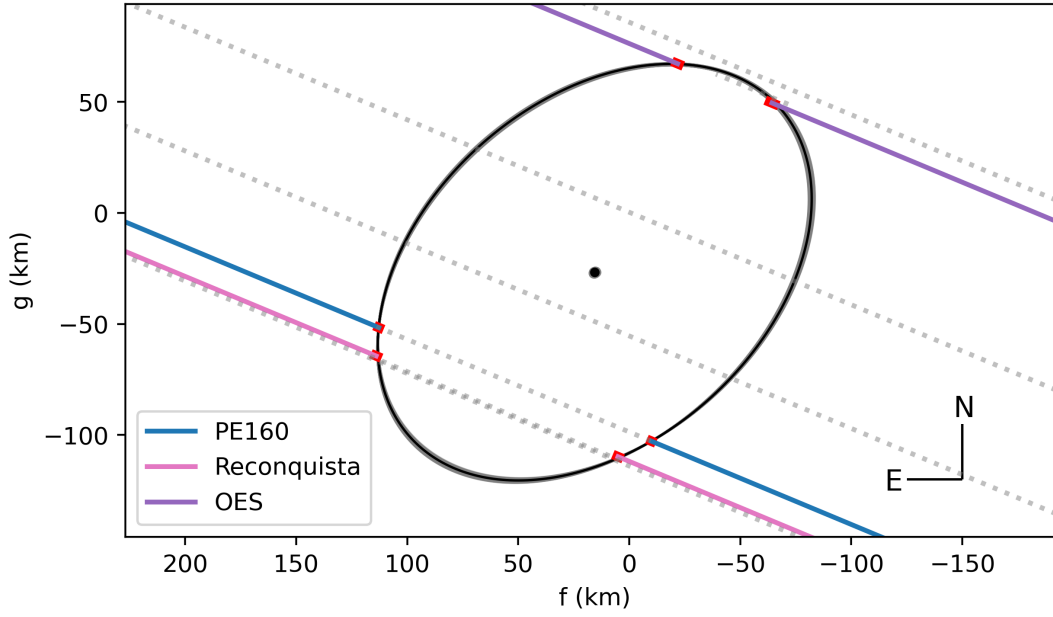
Figure 3.13: Best ellipse (black) fitted to the chord extremities. The grey dotted lines represent the chords that were deactivated for the fit (larger uncertainties), are negative, or are not provided by observers. All the ellipses within the 1σ uncertainty level are in grey. The red segments present the chord's uncertainties. The black dot is in the ellipse center with respective uncertainty.
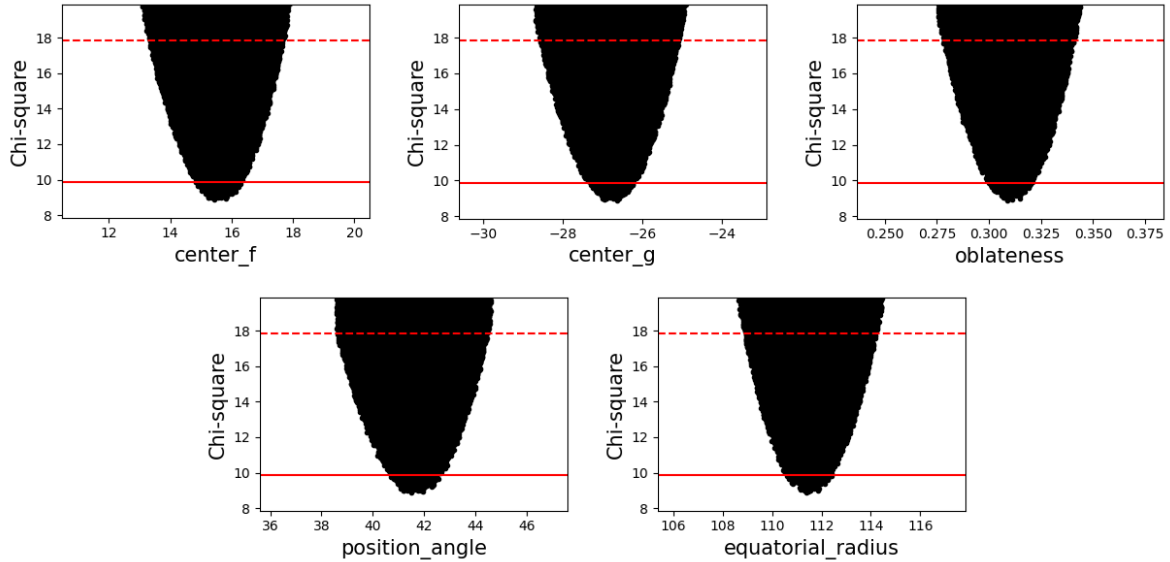

Figure 3.14: χ^2 maps from the ellipse fit procedure applied to the extremities of the September 10, 2023, stellar occultation. The red lines delimit the 1σ (continuous) and 3σ (dashed) uncertainties.

The relative magnitudes were calculated as:

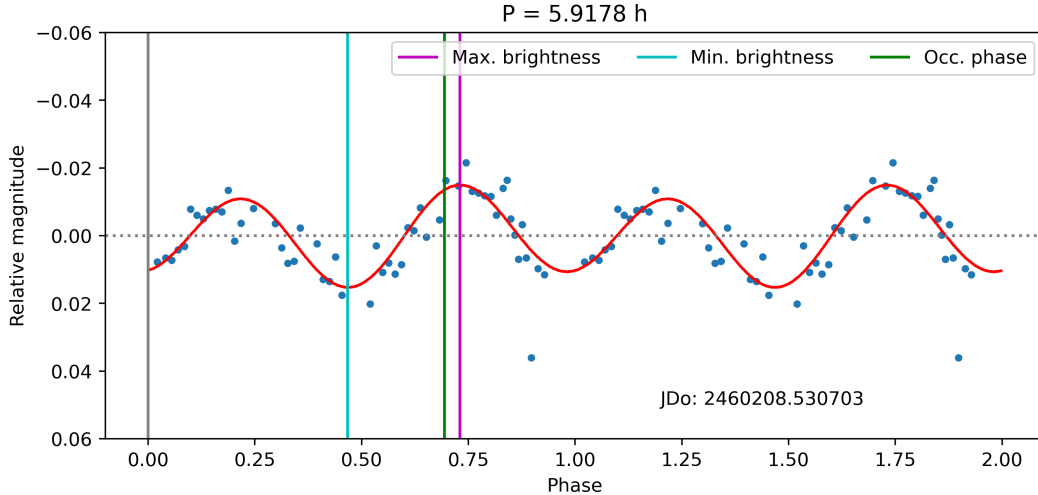$$m_{\mathrm{rel}} = -2.5 \log \left(\frac{\mathrm{F_{obj}}}{\mathrm{F_{star}}} \right) \tag{3.1}$$

Figure 3.15: Chiron's rotational light curve obtained at SOAR. The data were folded using a rotational period of P = 5.917813 hours, being the zero rotational phase the instant of the first frame corrected by the light time (2460208.530703 JD).

Figure 3.15 displays only the data from September 21, as it is of higher quality. Using the `astropy.timeseries` Python package (Lomb-Scargle), we fixed the rotation period of Chiron as P = 5.917813 hours, based on MARCIALIS e BURATTI (1993). This allowed us to estimate the rotational phases and the moments of maximum (2460208.7108833 JD) and minimum brightness (2460208.64596902 JD). Starting from the reference instant for phase zero (2460208.530703 JD), we propagated the 3D shape proposed in (BRAGA-RIBAS et al., 2023) to the time of the occultation, thereby determining the rotational phase of Chiron at that moment. All instants obtained in this section have already been corrected for light time.

We projected the ellipsoid onto the tangent plane for maximum and minimum brightness. We used the nominal values for Chiron's semi-axes obtained by BRAGA-RIBAS et al. (2023): $a = 126 \pm 22$ km, $b = 109 \pm 19$ km, $c = 68 \pm 13$ km. The pole coordinates were taken from ORTIZ et al. (2023), with ecliptic coordinates $\lambda_{\mathrm{pole}} = 151°$, $\beta_{\mathrm{pole}} = 18°$. The propagation was performed using the ARCHINAL et al. (2018) formalism, with the reference instant being the moment of maximum brightness in the rotational light curve. For this instant, we set the prime meridian at the reference epoch $W_0 = 0°$. Figure 3.16 shows the propagated ellipsoids for the maximum and minimum brightness instants.

The first test was to propagate the ellipsoid to the occultation epoch and compare it with the projected chords, using the same center obtained from the apparent ellipse fit as a seed, searching for the best values while keeping the scale equal to 1, i.e., keeping the ellipsoid semi-axes the same as the nominal values obtained by BRAGA-RIBAS et al. (2023). As shown in the left panel of Figure 3.17, the ellipsoid is larger than the fitted apparent ellipse. Therefore, we allowed the scale to change to see if the result could be
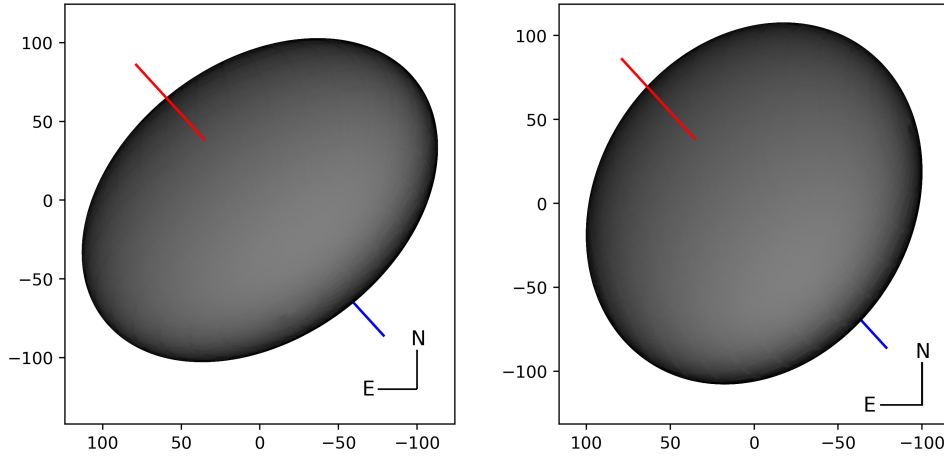
Figure 3.16: Ellipsoids generated using Chiron's semi-axes (BRAGA-RIBAS *et al.*, 2023) propagated for the maximum (left) and minimum (right) brightness instants.

improved. The result improved, yielding a scale value of 0.898 ± 0.003, indicating that the ellipsoid may be 11% smaller than the published values but still within the uncertainties.
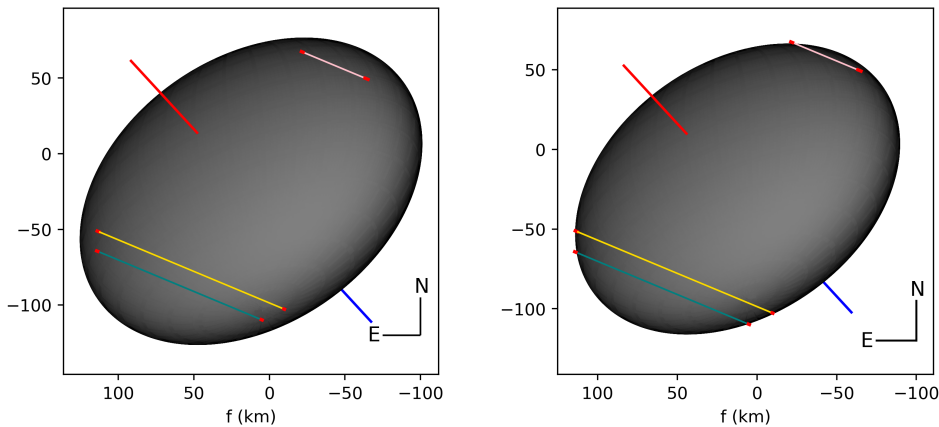

Figure 3.17: Ellipsoids propagated to the occultation epoch and limb-fitted to the chords extremities. Left: fit procedure made varying the f_0, g_0 center position; Right: fit procedure varying the f_0, g_0 center position and the scale.

The stellar occultation by Chiron observed in September 2023 was unique not only in the number of chords (the highest number of detections for this object in a single event to date) but also in providing a survey of the surroundings of the main body through light curves with high signal-to-noise ratio and data acquisition cadence. The best light curve in these terms was obtained in the PE160 site and is only comparable in quality with the FTN light curve (RUPRECHT *et al.*, 2015) and SICKAFOOSE *et al.* (2020). The exposure time of 0.120 seconds, with a readout time of ~ 0.013 seconds, allows an exposure cover of about 2.4 km in the sky plane. Despite the absence of calibrations stars due to the small FOV, the curve's standard deviation reaches 0.033, as the sky

remains very stable during the observation. The total cover of this light curve is about 25,000 km onto the sky plane and about 37,000 km when projected to the equatorial plane, considering the ring geometry obtained from pole orientation proposed by ORTIZ *et al.* (2023).
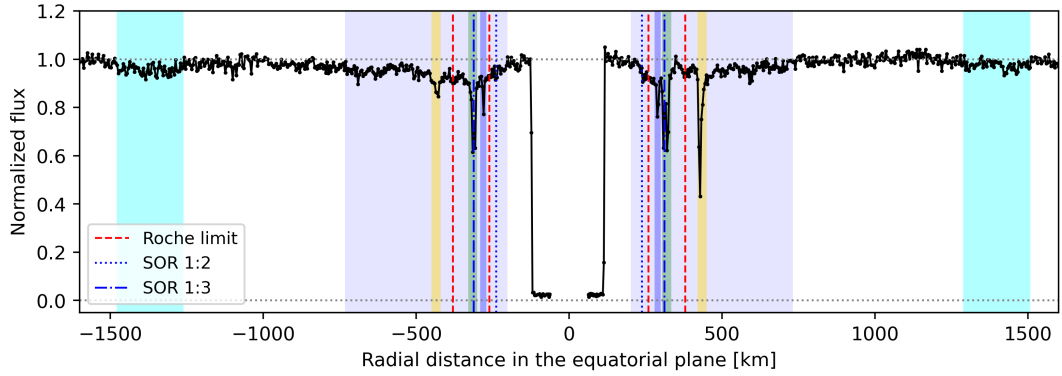

Figure 3.18: PE160 light curve obtained in OPD site in 2023 Chiron's event showing the detected features color-coded (see text). The light curve was projected to the equatorial plane considering the pole orientation proposed by ORTIZ *et al.* (2023).
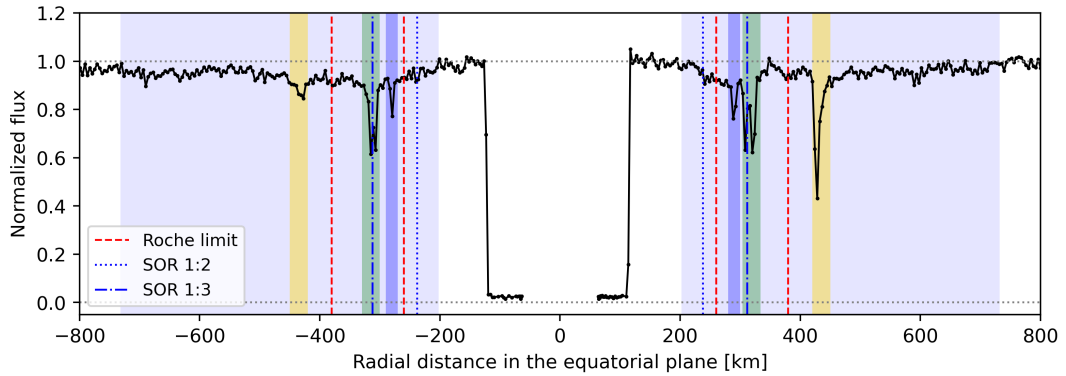

Figure 3.19: Zoomed view of the PE160 light curve obtained in OPD site in 2023 Chiron's event showing the detected features color-coded (see text), with the Roche limit and SOR regions. The light curve was projected to the equatorial plane considering the pole orientation proposed by ORTIZ *et al.* (2023).

Several secondary extinction features were identified in the PE160 light curve, with some detections matching the structures observed in past events (ORTIZ *et al.*, 2023; RUPRECHT *et al.*, 2015; SICKAFOOSE *et al.*, 2020, 2023). This light curve also reveals some new structures around the central body that may not have been detected before due to the light curve quality or because they have evolved recently. Figure 3.19 presents the PE160 light curve with the secondary features identified by colored patches in the 2023 stellar occultation. The outermost symmetrical feature (cyan) is located at an average distance of about 1,383 km, extending for at least 220 km. We identified a broad and

thin feature extending from ~ 200 km to ~ 730 km on both sides of the main body (light purple regions). The yellow regions show a symmetrical and possible variable structure similar to Quaoar's Q1R ring, which is thin before the closest approach but narrow and dense after the closest approach. The distance of these two features is ~ 450 km. The region marked in green indicates the features located at an average distance of 332 km from Chiron's center and matches the structures detected in the 2011 stellar occultation. Very close to this one, another structure was observed for the first time (blue narrow region) at a distance of about 295 km. The red dashed line marks the expected Roche limit region, spanning from 260 km for Chiron's mass of $M = 4.8 \pm 2.3 \times 10^{18}$ kg (BRAGA-RIBAS $et\ al.$, 2023) and considering the particles' density of $1,000$ kg m^{-3} (water-ice), to about 380 km when considering the largest mass within uncertainties and realistic Saturnian ring particles' density of 450 kg m^{-3} (THOMAS e HELFENSTEIN, 2020, as cited in SICKAFOOSE $et\ al.$, 2023). The dotted and dash-dotted blue lines indicate the
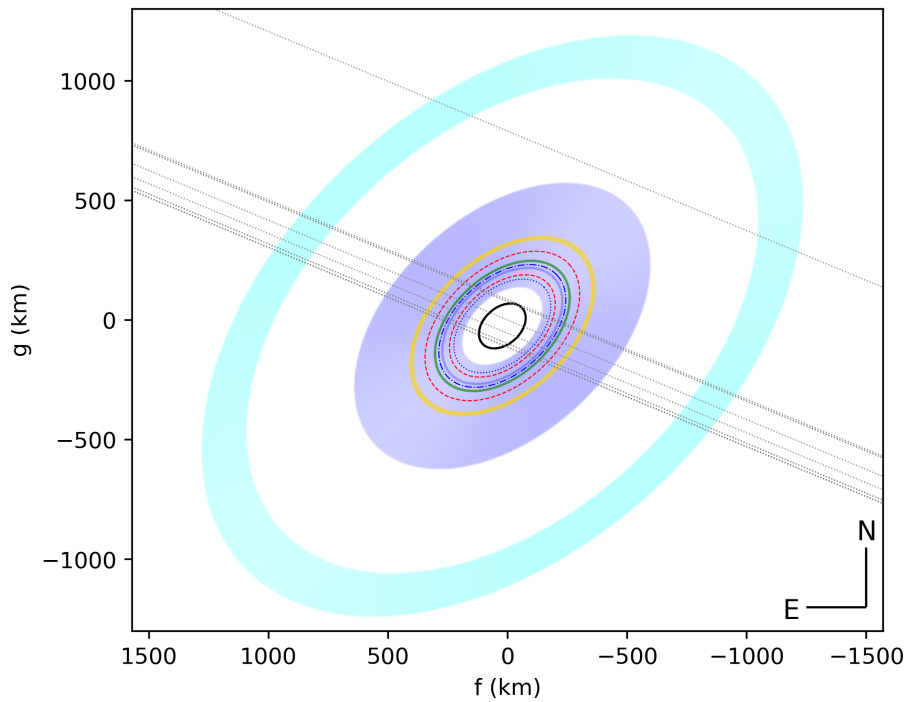

Figure 3.20: Features detected around Chiron on 2023 event projected into sky plane, assuming they are co-planar and share the same pole. The color-coded ellipses follow the same scheme as in Figure 3.19. The central black ellipse shows the best ellipse fitted to the positive chords. The grey dotted straight lines present the occultation chords.

1:2 and 1:3 SOR, respectively ~ 238 km and ~ 312 km. These values were estimated considering the Chiron's density $\rho = 1,119 \pm 4$ kg m^{-3} (BRAGA-RIBAS $et\ al.$, 2023), the volume equivalent radius R$_{\text{vol}}$ = 98 ± 19 km (BRAGA-RIBAS $et\ al.$, 2023), rotational period P = 5.917813 ± 0.000007 hours (MARCIALIS e BURATTI, 1993). The structure

highlighted by the green region in Figure 3.19 lies in the 1:3 SOR location, a common characteristic between the Chariklo, Haumea, and the outermost Quaoar rings. Also, some structures are possible beyond Chiron's classical Roche limit, particularly the structure at ∼ 330 km (green region) that was detected over the years (2011, 2022, and 2023).

Other observatories, in addition to PE160, detected additional features around Chiron, even with small spatial resolution and signal-to-noise ratio. Figure 3.21 shows all the features detected in this event. When projected in the sky plane, assuming they are planar, sharing the same pole, these symmetrical features produce the ellipses presented in Figure 3.20. The radial profiles were plotted considering the normal optical depth τ_N as a function of the radial distance projected in the sky plane. This plot allows a direct comparison of the location of the detected structures. Still, unfortunately, the differences in the quality of the data sets prevent a direct comparison between the normal optical depths. When
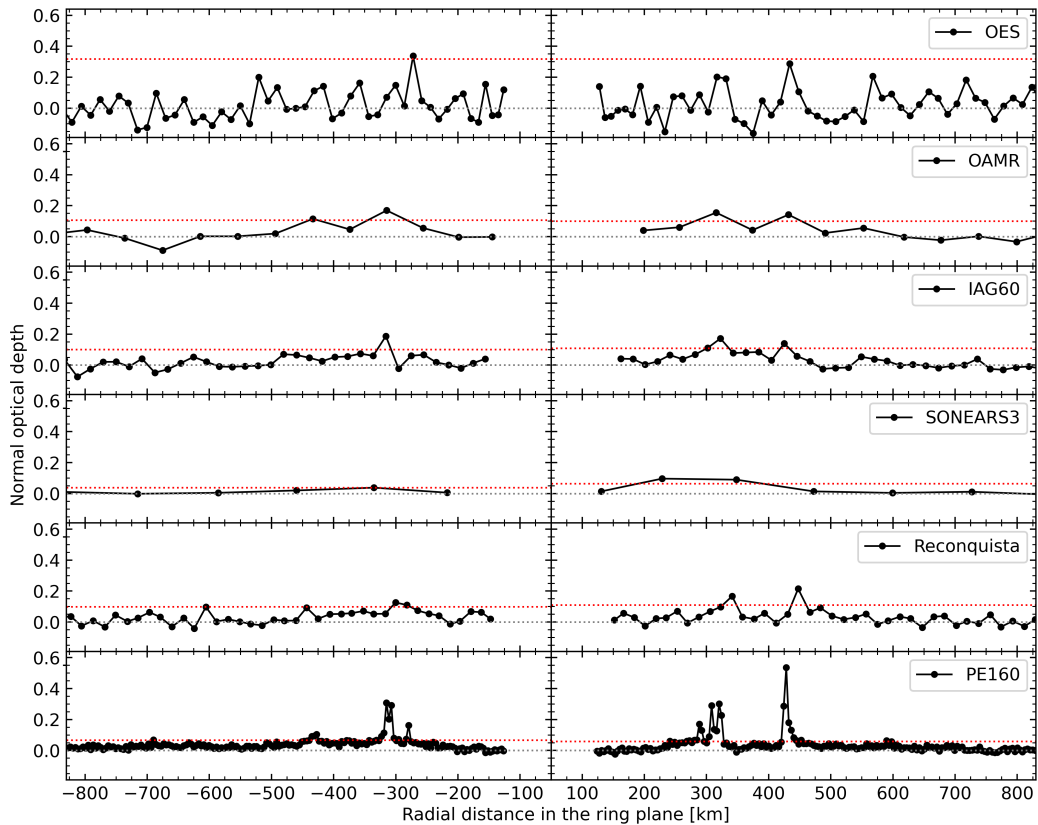

Figure 3.21: Radial profiles of the detected structures around Chiron from 2023 stellar occultation, with the normal optical depth plotted as a function of the radial distance in the ring plane considering the pole orientation proposed by ORTIZ *et al.* (2023). The dotted lines mark the mean (grey) and the 3σ standard deviation (red) of the normal optical depth distribution.

comparing the structures observed over the years around Chiron, we notice a certain variability in the amount of material in the environment around the main body. We can use the light curve from FTN from 2011 and compare it with those obtained in 2022 (KAO)

and 2023 (OPD). Figure 3.22 presents the multi-epoch detections of the structures around Chiron. The projection was made considering the event geometry for each occultation epoch and considering the most recent pole orientation solution $\lambda_{\text{pole}}, \beta_{\text{pole}} = 151°, 18°$ (ORTIZ *et al.*, 2023).

At first glance, it is possible to note that the 2011 detection does not coincide in position when compared with the 2022 and 2023 events. This is probably due to pole orientation uncertainties, the fact that the structures have a pole variation in time, or that the structures do not share the same pole orientation. As we see before, the depth of the extinction features observed in the 2022 event can be explained by the two close structures observed by FTN in 2011. Still, we can see more material diffuse surrounding the structures, mainly when we compare the 2011 and 2023 events, suggesting that these structures evolved significantly over the years. These profile differences can be explained by variations in width and opacity in different longitudes, i.e., an inhomogeneous structure. An increase in Chiron's brightness was observed on February 8, 2021, lasting until June 18 of the same year (DOBSON *et al.*, 2021) and does not return to the pre-2021 brightness. This suggests a hypothesis that more dust and/or ice are present in the body's vicinity, explaining the apparent increase in material in Chiron's environment. This increase in brightness is consistent with the previous ones, either caused by a cometary activity (e.g., BUS *et al.*, 1989; DOBSON *et al.*, 2024; MEECH e BELTON, 1990) or an impact-triggered activation by a swarm of particles (GIL-HUTTON, 2024; ORTIZ *et al.*, 2023). In both cases, a significant amount of dust or ice particles is expected to remain in orbit. Since this is a work in progress, the results may change as the analysis evolves. The
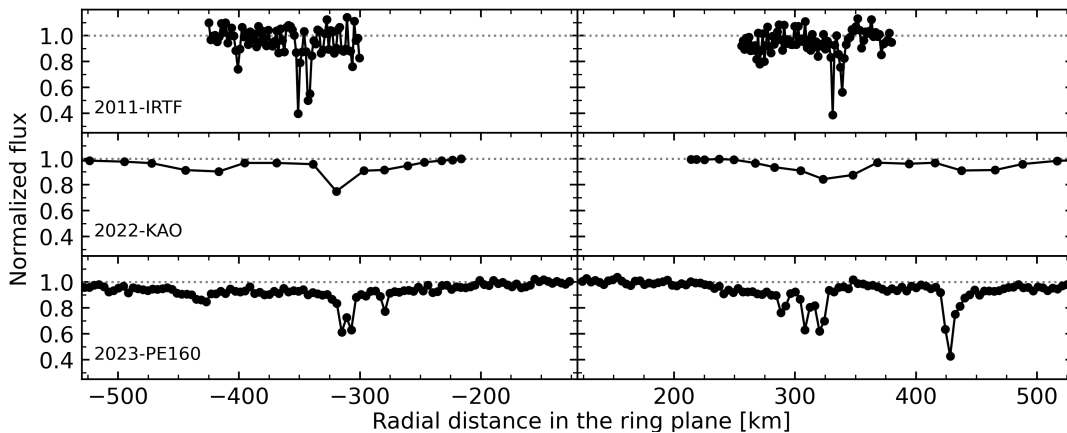

Figure 3.22: Radial profiles of the structures detected around Chiron in 2011, 2022, and 2023 stellar occultation events.

next steps include a joint analysis of all detections to determine a new orientation for the rings' pole that better explains the distribution of the features. Additionally, individual analysis of each structure observed in 2023 and its convolution for the 2022 event will be performed to understand if these structures remained constant between these two events.

3.3 (60558) 174P/Echeclus

The Centaur (60558) Echeclus, previously designated 2000 EC98, was discovered by Terry Bressi of Spacewatch on March 3, 2000 (MARSDEN, 2000). Echeclus has a highly eccentric orbit, characteristic of Centaurs, with a semi-major axis of approximately $a = 10.75$ au, which places it between the orbits of Saturn and Uranus. Its perihelion distance is about $q = 5.85$ au, while its aphelion distance is around $Q = 15.54$ au. The orbital eccentricity is $e = 0.456$, indicating a significantly elongated orbit. Echeclus has an orbital inclination of $i = 4.3°$ relative to the ecliptic plane, which is relatively low. The orbital period is approximately 35.27 years. These orbital elements are retrieved from JPL115[5]. From thermal observations using the *Spitzer Space Telescope*, STANSBERRY *et al.* (2008) calculated a diameter of 83.6 ± 15 km and a geometric albedo of $0.0383^{+0.0189}_{-0.0108}$. BAUER *et al.* (2013) derived an equivalent diameter of 59 ± 4 km and an albedo of 0.08 ± 0.02 from thermal infrared observations using the *Wide-field Infrared Survey Explorer*. DUFFARD *et al.* (2014), using the PACS instrument on the Herschel Space Observatory (HSO), obtained an equivalent diameter of 64.6 ± 1.6 km with an albedo of $0.052^{+0.007}_{-0.0071}$.

Echeclus has exhibited varying levels of cometary activity over the past few years. The most significant outburst occurred between November and December 2005 at 13 au, increasing its brightness by ~ 7 magnitudes (CHOI *et al.*, 2006b). This significant activity was noteworthy for its brightness and because the mass ejection source seemed to be about $55,000$ km from Echeclus. This behavior was attributed to a fragment detaching during the outburst, with the fragment becoming the primary source of the activity (BAUER *et al.*, 2008; CHOI *et al.*, 2006a; FERNÁNDEZ, 2009; WEISSMAN *et al.*, 2006). Alternatively, the decentralized coma might have resulted from material ejection in three different regions at different times: two short events followed by a longer-lasting ejection (ROUSSELOT *et al.*, 2016). On May 30, 2011, JAEGER *et al.* (2011) observed a new outburst as Echeclus approached perihelion at 7.5 au, with a coma extending for one arc-minute ($\sim 327,000$ km). Observations in June 2011 showed a 40 arcsec ($\sim 218,000$ km) coma and a jet-like feature six arcsec ($\sim 33,000$ km) long, accompanied by a ~ 3 magnitude brightening. The outbursts in August 2016 resulted in a ~ 3-magnitude brightening without notable coma features (MILES, 2016a). After its perihelion in April 2015, Echeclus experienced its second-largest brightness outburst, with an amplitude of about four magnitudes (JAMES, 2018). Observations using the FTN and the IRTF after the December 2017 outburst revealed an asymmetrical coma morphology in the North-South direction, supporting previous ideas about dust properties (KARETA *et al.*, 2019). Subsequent studies suggest that seasonal effects can trigger material ejections, and variations in the color index as a function of distance from the nucleus indicate that particles may have

---

[5]https://ssd.jpl.nasa.gov/tools/sbdb_lookup.html#/?sstr=2060558

different sizes or compositions (ROUSSELOT *et al.*, 2021). Using a large number of photometric observations, ROUSSELOT *et al.* (2021) compute a shape model for Echeclus with the Shaping asteroid models using genetic evolution modeling algorithm (SAGE) method (BARTCZAK e DUDZIŃSKI, 2018) and obtained a sidereal rotational period of P = 26.785278 ± 10⁻⁶ hours. Also, six equally probable pole solutions were determined. Given Echeclus's history of material ejections (ROUSSELOT *et al.*, 2021, and references therein) and the possibility that the material ejected during cometary outbursts can remain in orbit (BRAGA-RIBAS *et al.*, 2014), the question arose about the presence of rings or confined material around it. With this in mind, we monitored stellar occultations, searching for secondary events that might indicate the existence of such structures around Echeclus.

In this section, I present the results from the paper I led and published in the MNRAS, named "Physical properties of Centaur (60558) 174P/Echeclus from stellar occultations" (PEREIRA *et al.*, 2024, Appendix B). The findings are from a double-chord stellar occultation observed in January 2020, a single-chord detection in January 2021, and a close appulse in August 2019. The 2020 occultation event provided valuable data that constrained the size and shape of Echeclus. Using this data, along with the 3D model and pole coordinates proposed in the literature, we could determine the size and volume of Echeclus. Furthermore, data from all three stellar occultation events were analyzed to search for evidence of secondary structures around Echeclus.

3.3.1   Appulse on October 29, 2019


```
              Object        Diam   Tmax   dots <> ra_offset_dec
              60558 Echeclus  59 km   4.6s   60 s <>  +0.0   +0.0
```

```
     year-m-d        h:m:s UT     ra__dec__J2000__candidate    C/A    P/A    vel   Delta   G*   long
     2019-10-29  08:40:50.100  05 16 34.3901 +18 22 21.328  0.764  168.08 -12.78   8.40  13.7  272
```
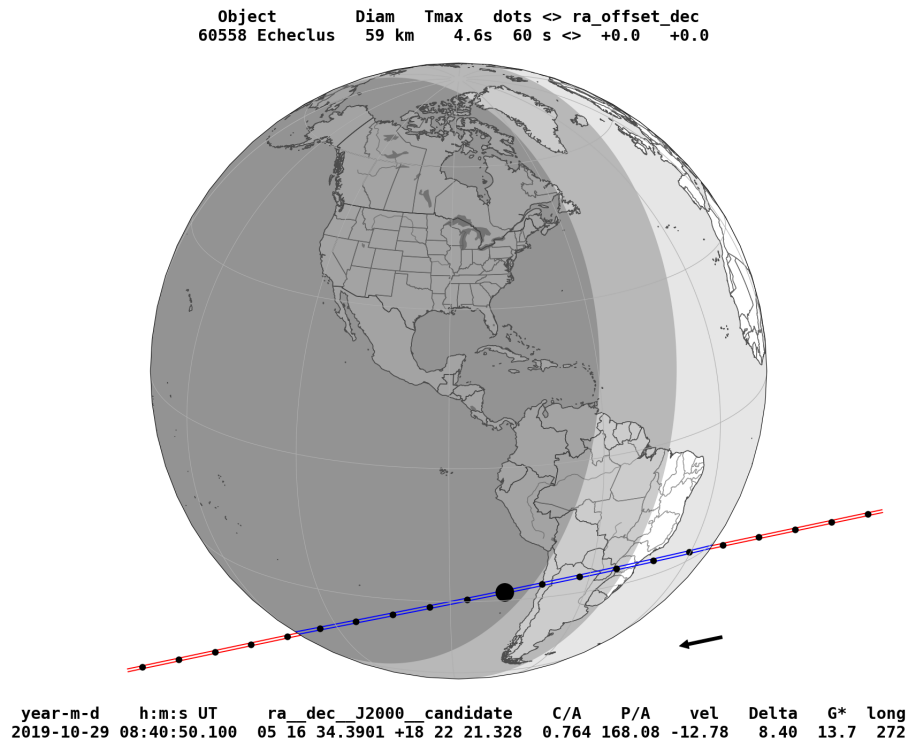
Figure 3.23: Prediction map of the occultation by Echeclus on October 29, 2019. The shadow path was predicted to pass over Chile, northern Argentina, Paraguay, and southern Brazil. The top label shows the stellar catalog and ephemeris used in the prediction. The bottom label shows the geocentric closest approach (C/A) instant, the star position, the geocentric closest approach (C/A, in arc-seconds), the object position angle relative to the star (P/A, in degrees), the object geocentric distance (Delta, in au), the magnitude normalized for the event velocity (G*). The blue lines limit the object shadow. The blue dots are separated by 60 seconds from each other, being the big one the geocentric closest approach instant.

The star involved in the 2019 appulse was the Gaia DR3 3395392378744301696, with a G magnitude of 14.199. The occultation prediction was made using the NIMAv6 ephemeris, supported by astrometric observations conducted a few days before the predicted date. The prediction indicated that the object's shadow would pass over northern Chile, Argentina, Paraguay, and southern Brazil. The geocentric closest approach was at 2019-10-29 08:40:50.2 UT, with an estimated shadow velocity of 12.8 km s^{-1}, resulting in a maximum expected occultation duration of 6.8 seconds. More details on this stellar occultation are presented in the labels of Figure 3.25.

The observational campaign for this event included observations from the Chilean telescopes SOAR at Cerro Pachón, TRAnsiting Planets and PlanetesImals Small Telescope - South (TRAPPIST-South) and NTT at La Silla Observatory, Search for habitable Planets EClipsing ULtra-cOOl Stars (SPECULOOS-IO) at Cerro Paranal, and San Pedro de

Atacama observatories. All the obtained light curves for this appulse are presented in PEREIRA *et al.* (2024, Figure D1. See appendix B). Unfortunately, the sites that observed this event did not detect the occultation by Echeclus, as they were not located under the object's shadow. However, we used the successfully recorded occultations from 2020 and 2021 to update the Echeclus ephemeris and calculate where the 2019 shadow should have passed. Additionally, we checked the Renormalised Unit Weight Error (RUWE) of the target star in the Gaia DR3 Catalogue, which was 0.948. The RUWE indicates the quality of the single-star model fit to the observations, with values close to 1 being ideal. Values greater than 1.4 may suggest that the source is not a single star or that there are issues with the astrometric solution (c.f., GOMES-JÚNIOR *et al.* (2022) and references therein). This procedure ensured the accuracy of the star position and allowed us to estimate the detection limits of material around the main body. We could then determine the distance between the chords and the object's center by considering the ephemeris as perfect.
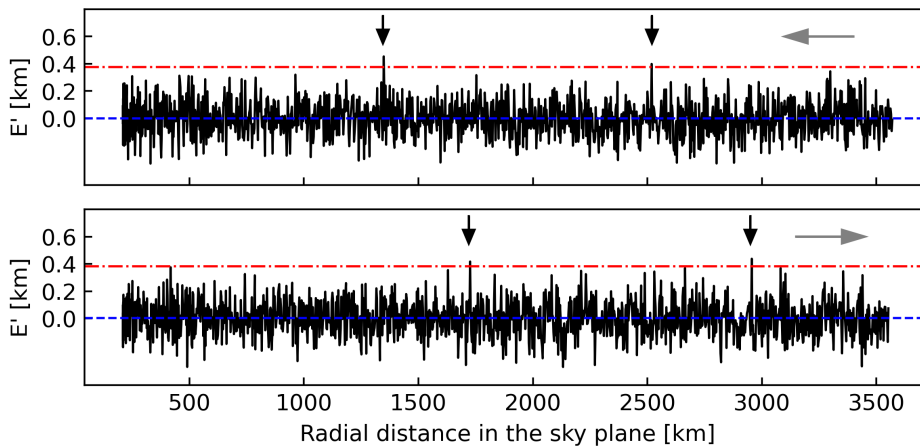

Figure 3.24: Apparent equivalent width (E′) curve plotted as a function of the radial distance in the sky plane for the NTT data set. The blue dashed line indicates the mean of the E′, and the red dashed-dotted line indicates the 3σ standard deviation of E′. The black arrows identify the data points that exceed the 3σ regions. The grey arrows indicate the direction of the time increase.

We searched for significant flux drops in the stellar occultation light curves to identify any sparse or confined material around Echeclus. For this analysis, we considered the standard deviation at the 3σ level as the upper limit for the apparent opacity (p') on the sky plane, thus estimating the upper limits for the actual optical depth (τ). In 2019, the most reliable data set was obtained in NTT and provided an optical depth limit of $\tau = 0.07$, based on structures with a radial width of 2.6 km in the sky plane. We estimated limits on apparent optical depth for the smoothed light curve as $\tau' = 0.01$. For opaque structures, this implies that small satellites with a diameter greater than 380 meters would be detectable in the regions probed by the chords. The NTT observation

covers about 7,123 km radially. We identified four data points in the NTT data set with apparent equivalent width (E') that exceeds our 3σ observational limits (Figure 3.24). When analyzing these points individually, we identify variations in the target and reference stars, implying that sky fluctuations may cause these extinctions in flux. All the results in the detection limits can be found in PEREIRA *et al.* (2024, Table C1. See appendix B).

3.3.2   Stellar occultation on January 22, 2020

Object	Diam	Tmax	dots <> ra_offset_dec
	59 km	5.3s	60 s <> +0.0 +0.0

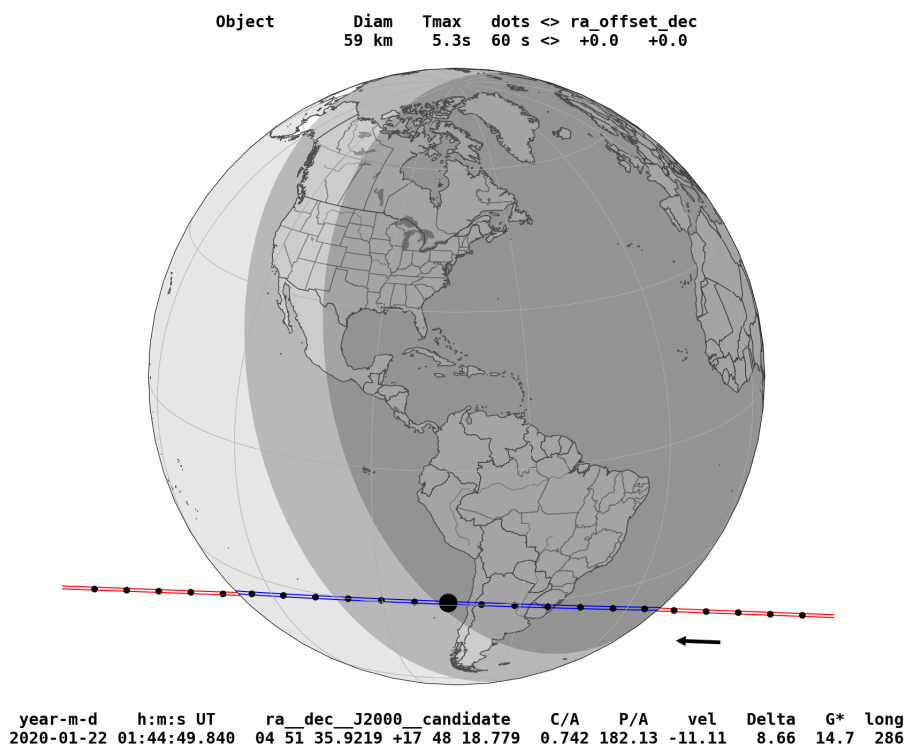| year-m-d	h:m:s UT	ra__dec_J2000__candidate	C/A	P/A	vel	Delta	G*	long
2020-01-22	01:44:49.840	04 51 35.9219 +17 48 18.779	0.742	182.13	-11.11	8.66	14.7	286

Figure 3.25: Prediction map of the occultation by Echeclus on January 22, 2020. The shadow path was predicted to pass over Chile, northern Argentina, Paraguay, and southern Brazil. The top label shows the stellar catalog and ephemeris used in the prediction. The bottom label shows the geocentric closest approach (C/A) instant, the star position, the geocentric closest approach (C/A, in arc-seconds), the object position angle relative to the star (P/A, in degrees), the object geocentric distance (Delta, in au), the magnitude normalized for the event velocity (G*). The blue lines limit the object shadow. The blue dots are separated by 60 seconds from each other, being the big one the geocentric closest approach instant.

The January 22, 2020, event crossed central Chile, Argentina, and Uruguay with a shadow velocity of $11.1\,\mathrm{km\,s^{-1}}$ and a maximum duration of 7.8 seconds. We obtained two positive and four negative detections from nine observations, with three other sites experiencing technical problems or overcast conditions. This marked the first double-chord

occultation for Echeclus. Data was acquired at SOAR using the Raptor Merlin camera with GPS as the time source. In La Canelilla, Chile, data was collected using a ZWO ASI1600MM video camera with AVI video format and NTP monitor as the reference time. All the observational circumstances are presented in PEREIRA *et al.* (2024, Table B1. See appendix B). With the Fresnel scale $L_f = \sqrt{\lambda D/2} = 0.67$ km and the apparent star diameter at 8.66 au equal to 0.11 km, the light curves are dominated by the instrumental response, considering exposure times of 0.25 seconds (2.77 km) for SOAR and 0.3 seconds (3.33 km) for La Canelilla, Chile. These two positive light curves and their respective models are presented in Figure 3.26.
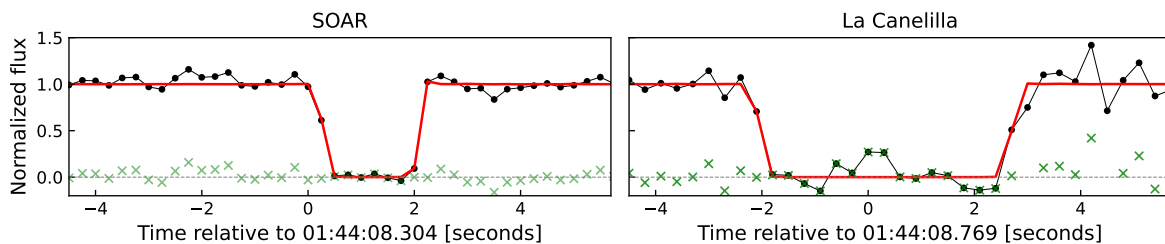

Figure 3.26: Modeled light curves for 2020 stellar occultation by Echeclus. The black curve represents the data, and the red curve is the modeled light curve. The green markers represent the residuals. The zero instant in the graph is the local closest approach on January 22, 2020. Adapted figure from PEREIRA *et al.* (2024).

ROUSSELOT *et al.* (2021) derived a tri-dimensional model for Echeclus by analyzing twenty-seven rotational light curves obtained between 2011 and 2019. They used the SAGE modeling technique (BARTCZAK e DUDZIŃSKI, 2018) to obtain the sidereal period of P $= 26.785178 \pm 10^{-6}$ hours and an axial ratio of $a/b = 1.32$ and $b/c \sim 1.1$. The rotational elements and the 3D model were accessed via Interactive Service for Asteroid Models (ISAM) service[6]. The pole orientation furnished in the ISAM is $\lambda_{\text{pole}} = 115.2°$ and $\beta_{\text{pole}} = 21.5°$, with $\gamma_0 = 80°$ for the reference epoch $t_{\text{ref}} = 2455437.367$ JD. We transform these coordinates from the Kaasalainen formalism (KAASALAINEN *et al.*, 2001) to the International Astronomical Union (IAU) recommendations (ARCHINAL *et al.*, 2018) using the appropriated rotation matrices, obtaining the pole coordinates RA $= 122° \, 18' \, 05.8''$, DEC $= 42° \, 09' \, 16.6''$, and the prime meridian $W_0 = 336.793618°$ for the reference epoch t_{ref}. By propagating the Echeclus tri-axial shape from the t_{ref} to the occultation epoch, we obtain the projected limb of the body. This limb can be compared with the occultation chords by varying the center (f_0, g_0) and model scale. This comparison involves the χ^2 minimization using

$$\chi^2 = \sum_{i=1}^{N} \frac{\phi_{(i,obs)} - \phi_{(i,cal)}}{\sigma_i^2},$$

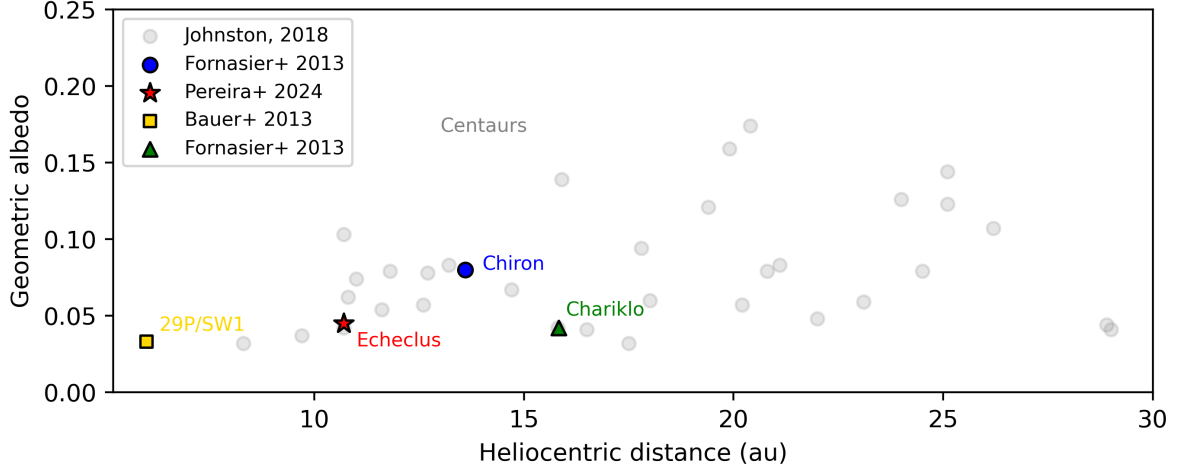[6] http://isam.astro.amu.edu.pl/

Figure 3.27: Geometric albedo versus heliocentric distance for Centaurs (grey) from the Johnstons Archive[9]. The geometric albedo for 29P (BAUER *et al.*, 2013), Echeclus (PEREIRA *et al.*, 2023), Chiron (FORNASIER *et al.*, 2013), and Chariklo (FORNASIER *et al.*, 2013) are present in colored markers.

where $\phi_{(i,obs)} - \phi_{(i,cal)}$ is the difference between the chord extremities and the projected limb and σ_i the uncertainty in the chord extremity. The 3D model plotted against the 2020 occultation chords is presented in Figure 3.28. The best-fitted center is $f_0 = 17.6 \pm 0.2$ km and $g_0 = -83.6 \pm 0.5$ km, with the scale factor of 30.7 ± 0.5. From this, we retrieve the dimensions of Echeclus' semi-axis as $a = 38.6 \pm 0.6$ km, $b = 29.6 \pm 0.5$ km, and $c = 26.0 \pm 0.4$ km, resulting in a projected equivalent radius in area of $R_{equiv} = 31.16 \pm 0.51$. Thus, we can now determine the geometric albedo for Echeclus using the $p_V = 10^{0.4(H_{\odot,V} - H_V)}(au_{km}/R_{equiv})^2$, where $au_{km} = 1\,au = 1.49598 \times 10^8$ km, $H_{\odot,v} = -26.74$ is the Sun absolute magnitude in V-band, $H_V = 9.971 \pm 0.31$ is the Echeclus instantaneous absolute magnitude in V-band at the rotational phase, and $R_{equiv} = 31.16 \pm 0.51$ km is the area-equivalent radius of projected Echeclus' limb at the occultation epoch. The absolute magnitude was determined using the tool and procedures by MORALES *et al.* (2022) and based on 438 multi-epoch observations from Gaia SSO release (TANGA *et al.*, 2023). Taking the light curve amplitude of $\Delta m = 0.068$ as the uncertainty in the absolute magnitude to account for the rotational phase, we calculated the geometric albedo of Echeclus at the time of the occultation as $p_V = 0.0450 \pm 0.0043$. This albedo, despite being consistent with published values for Echeclus, is lower than the average albedo for Centaurs, estimated at 0.073[7] (see Figure 3.27).

We search for additional features in the light curves obtained in this event by determining the detection limits in opacity and apparent equivalent width. The limits were calculated for all the light curves (PEREIRA *et al.*, 2024, Figure D2. See appendix B), but the one obtained in SOAR was the best in signal-to-noise ratio and spatial resolution.

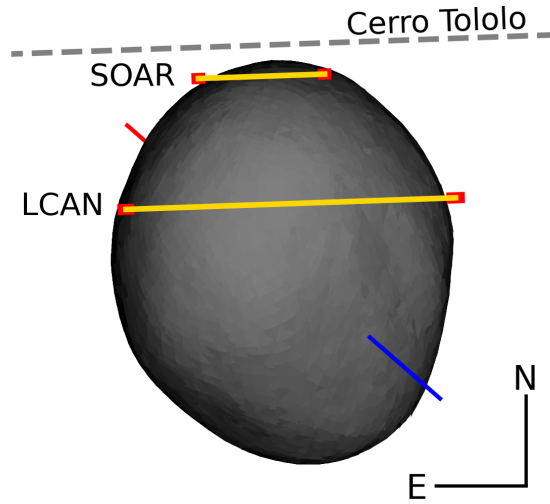[7]https://www.johnstonsarchive.net/astro/tnodiam.html

Figure 3.28: Plane-of-sky view of Echeclus 3D model for the January 22, 2020, stellar occultation.

The calculated limits for apparent optical depth and apparent equivalent width in the full-resolution light curve (averaging 2.9 km per data point) are $\tau = 0.15$ and $E_p \sim 800$ m. For the resampled light curve, with a spatial resolution of 97.8 km, the 3σ limit for apparent optical depth is $\tau' = 0.04$. The radial coverage of the SOAR observation in the sky plane is approximately $14,000$ km. All the results in the detection limits can be found in PEREIRA *et al.* (2024, Table C1. See appendix B).
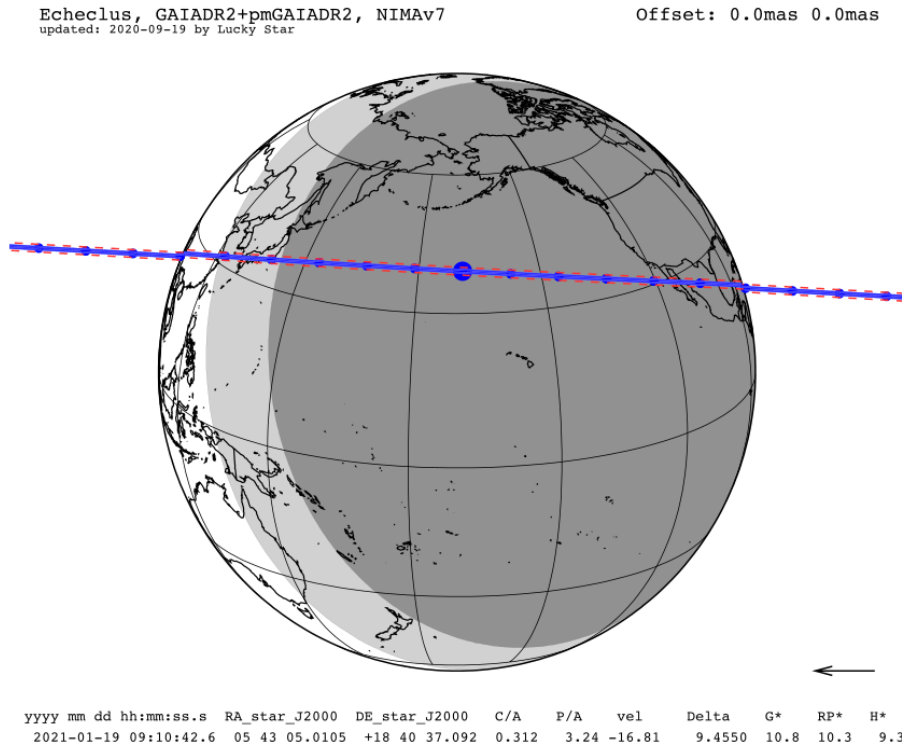
3.3.3 Stellar occultation on January 19, 2021

Figure 3.29: Prediction map of the occultation by Echeclus on January 19, 2021. The shadow path was predicted to pass over Japan and Mexico. The top label shows the stellar catalog and ephemeris used in the prediction. The bottom label shows the geocentric closest approach (C/A) instant, the star position, the geocentric closest approach (C/A, in arc-seconds), the object position angle relative to the star (P/A, in degrees), the object geocentric distance (Delta, in au), the magnitude normalized for the event velocity (G*). The blue lines limit the object shadow, and the dashed red indicates the 1σ uncertainty in the shadow path. The blue dots are separated by 60 seconds from each other, being the big one the geocentric closest approach instant.

An occultation by Echeclus was predicted to occur on January 19, 2021, with the closest approach occurring at 09:10:22.620 UTC and the shadow's path passing over Japan. The occulted star was the Gaia DR3 3399123330937092224 with G magnitude 10.990. The maximum duration for this event is 3.8 seconds, considering the geocentric shadow velocity of 16.81 $\mathrm{km\,s^{-1}}$. An observation campaign was organized in Japan.

Unfortunately, the object's shadow was shifted about a radius to the south, reaching the 1σ uncertainty limit of the prediction and leaving most of the telescopes involved in this observational campaign outside the shadow-path region. The circumstances of this event can be found in PEREIRA *et al.* (2024, Table B1. Appendix B). The event was successfully observed through thin clouds at ANAN. The instants of ingress and egress were determined from the light curve obtained by differential aperture photometry. For this event, the Fresnel Scale is $L_f = \sqrt{\lambda D/2} = 0.70$ km, and the apparent star diameter

at Echeclus distance was estimated to be 0.39 km. The best-fitted model that fits the observed data is presented in Figure 3.30.
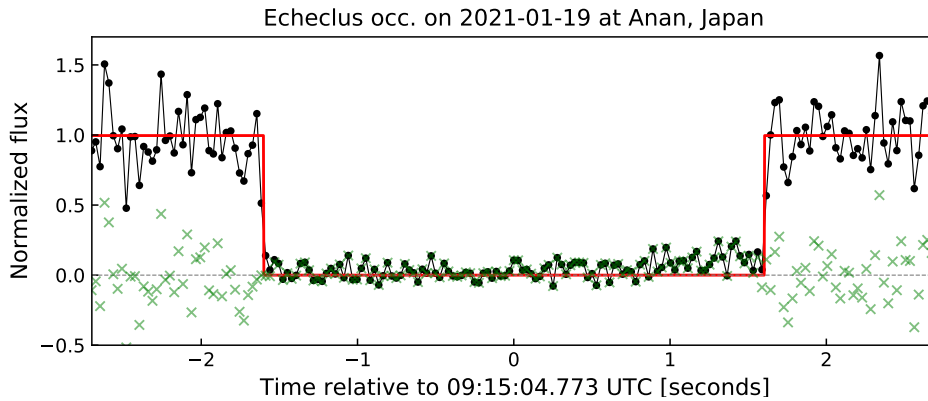

Figure 3.30: Modeled light curves for 2021 stellar occultation by Echeclus acquired in ANAN site. The black curve represents the data, and the red curve is the modeled light curve. The green markers represent the residuals. The zero instant in the graph is the local closest approach on January 19, 2021. Adapted figure from PEREIRA *et al.* (2024).

A procedure similar to that in the 2020 event was employed to compare the positive chord from the 2021 stellar occultation with the proposed 3D model and pole. In this case, the best match between the chord extremities and the projected limb was achieved by adjusting the center position while maintaining the same scale as determined from the 2020 occultation. The resulting projection of the 3D model at the occultation epoch and the positive chord is presented in Figure 3.31.
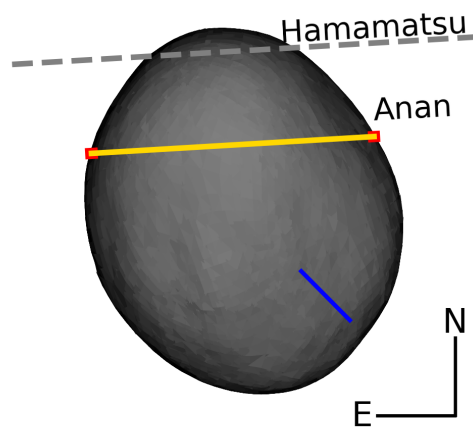

Figure 3.31: Plane-of-sky view of Echeclus 3D model for the January 19, 2021, stellar occultation. Figure from PEREIRA *et al.* (2024).

Since the star involved in the 2021 stellar occultation is bright, some telescopes could

use a high acquisition rate. Regarding signal-to-noise ratio and spatial resolution, the best light curve was obtained at Okazaki, Japan, with a resolution of 1.2 km and a standard deviation of 0.10 at the 1σ level (Figure 3.32). The full-resolution light curve provides a lower limit for the apparent optical depth of $\tau = 0.16$, with an apparent equivalent width upper limit of $E' \sim 370$ m. When the light curve is resampled over a 99.4 km window to search for broader features, the detection limit improves to $\tau = 0.02$. The chord passed 25 km from Echeclus's center and covered a distance of $9,600$ km in the sky plane. All the results in the detection limits can be found in PEREIRA *et al.* (2024, Table C1. See appendix B)).
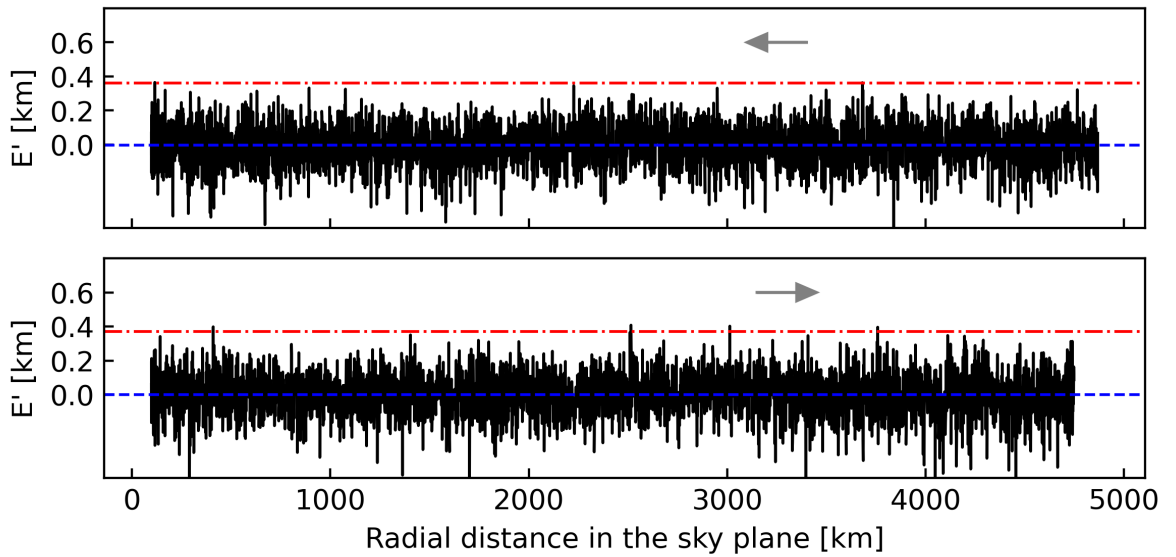

Figure 3.32: Apparent equivalent width (E') curve plotted as a function of the radial distance in the sky plane for the Okazaki data set. The blue dashed line indicates the mean of the E', and the red dashed-dotted line indicates the 3σ standard deviation of E'. The black arrows identify the data points that exceed the 3σ regions. The grey arrows indicate the direction of the time increase.

Driven by the quest to identify confined material around this Centaur exhibiting significant activity, we detected two stellar occultations that enabled precise measurements of its size and albedo. Our observations demonstrate that no surrounding opaque structure with a width greater than 162 meters (or semi-transparent with width 1.2 km and $p' = 0.26$) exists, indicating that Echeclus lacks confined structures similar to those observed around Chariklo or Chiron.

3.4   29P/Schwassmann-Wachmann 1

Comet 29P is a notable comet known for its frequent and unpredictable outbursts. Discovered while active on November 15, 1927, by German astronomers Arnold Schwassmann and Arno Arthur Wachmann at the Hamburg Observatory, 29P has been a subject of interest due to its unique characteristics. 29P orbits the Sun in the outer Solar System, with its semi-major axis placing it in the Centaur population. Its orbital elements from JPL K192/80[10] are semi-major axis $a = 6.04$ au, eccentricity $e = 0.044$, perihelion and aphelion $q = 5.77$ au, and $Q = 6.31$ au, and inclination $i = 9.36°$. Its orbital period is 14.87 years. These elements indicate a nearly circular orbit with a low inclination relative to the ecliptic plane. More precisely, this object lies in a region called "Gateway" - where the objects are transitioning from Centaurs to the JFC (SARID et $al.$, 2019). Regarding size, CRUIKSHANK e BROWN (1983) provides a value of 40 ± 5 km for 29P diameter based on thermal measurements. Observations using $Spitzer$ suggest a diameter of 54 ± 10 km (STANSBERRY et $al.$, 2004), while WISE measurements suggest 46 ± 13 km (BAUER et $al.$, 2013) and SCHAMBEAU et $al.$ (2015) estimate a diameter of D $= 60.4^{+7.4}_{-5.8}$ km. The stellar occultation technique can be the key to accessing the nucleus hidden underneath the cometary coma and obtaining more precise measurements of nucleus size.

One of the most intriguing features of 29P is its frequent outbursts, where it suddenly brightens by several magnitudes. This gives the title of the most active comets to 29P. These outbursts can increase the comet's brightness by several magnitudes within a short period, sometimes within just a few hours. These brightness increases are typically between 1 and 5 magnitudes. Still, they can occasionally be even more dramatic[11]. The exact cause of these outbursts is not completely understood. But, they are generally attributed to the sublimation of volatile materials trapped beneath the comet's surface. As 29P lies in a region too cold for water-ice sublimation, its outbursts appear to be associated with releasing carbon monoxide (CROVISIER et $al.$, 1995). Using extensive observational data, these outbursts' periodicity could indicate the cometary nucleus's rotational period as 57.09 ± 0.06 days (MILES, 2016b). The rotational period for this comet remains a mystery since different authors reported a wide range of possible periods, such as 14 or 32 hours (MEECH et $al.$, 1993), six days (JEWITT, 1990), and 60 days (STANSBERRY et $al.$, 2004).

In this section, I present the results obtained from the first-ever stellar occultation by the active Centaur 29P while the object was active. We applied an image treatment to mitigate the coma contribution and improve the occultation light curve. The single chord, obtained using the SOAR telescope, results in a circular fit representing the nucleus on the

---

[10]https://ssd.jpl.nasa.gov/tools/sbdb_lookup.html#/?sstr=29P&view=OPDCA

[11]https://britastro.org/section_information_/comet-section-overview/mission-29p-2

sky plane, retrieving an accurate astrometric position for 29P. This allowed the ephemeris to improve, significantly improving the precision of future stellar occultation predictions. Also, we detected a semi-transparent structure very close to the nucleus, interpreted as a dense dust cloud over the surface. We also determined detection limits for additional material around 29P, where we found possible extinction features. All these results are presented in a paper I led that was already submitted to the Philosophical Transactions of the Royal Society A, entitled "Centaur 29P/Schwassmann-Wachmann 1 and its near-nucleus environment from a stellar occultation" (see appendix C).

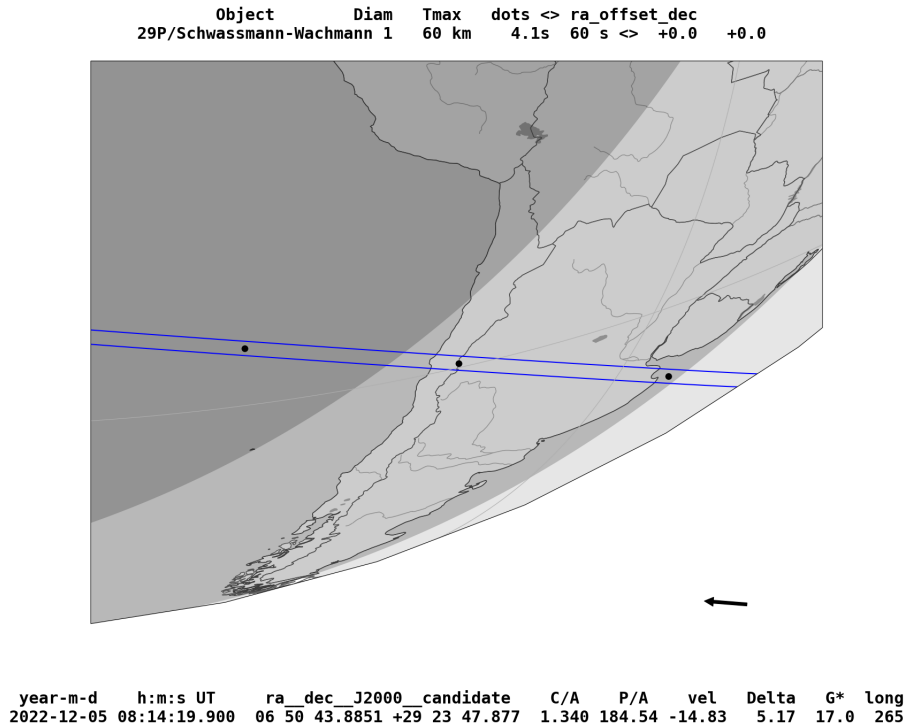### 3.4.1   Stellar occultation on December 05, 2022

Figure 3.33: Prediction map of the occultation by 29P on December 05, 2022. The shadow path was predicted to pass over Chile and Argentina. The top label shows the stellar catalog and ephemeris used in the prediction. The bottom label shows the geocentric closest approach (C/A) instant, the star position, the geocentric closest approach (C/A, in arc-seconds), the object position angle relative to the star (P/A, in degrees), the object geocentric distance (Delta, in au), the magnitude normalized for the event velocity (G*). The blue lines limit the object shadow, and the dashed red indicates the 1σ uncertainty in the shadow path. The blue dots are separated by 60 seconds from each other, being the big one the geocentric closest approach instant.

This event was predicted using the NIMAv2 ephemeris based on 559 Earth-based direct observations with the Gaia DR3 sources. The C/A was predicted to be December 05, 2022, at 08:14:19 UT, with a shadow path passing over the central regions of Chile and Argentina. The target star is the Gaia DR3 888441442906065536 source, with magnitude G = 16.9 and RUWE 1.027 (false flag for duplicity). Considering the apparent motion of the comet projected in the sky plane, the geocentric velocity was determined to be $14.8\ \mathrm{km\,s^{-1}}$ and the maximum duration of 4.1 seconds for the centrality of the occultation. More details on the prediction can be found in the labels of Figure 3.33 and the appendix C as well.

The data analysis starts with the classical corrections by flat and bias frames, with posterior differential aperture photometric extraction of the target and reference stars fluxes (Section 2.1.3). As the nucleus was active during the occultation, we detected

significant interference from the scattered light of the coma entering the photometric aperture. To eliminate this contamination, we process each data set image individually. First, we performed an initial photometry to obtain the x and y positions of the fixed sources (stars) in the image. This allows isolate the motion of the comet in the FOV, that facilitating a focused analysis on the comet behavior. Assuming that this motion is in a straight line, we can fit a first-degree polynomial to obtain the theoretical positions of the moving object frame to frame. Using these theoretical positions, we build a composite frame by stacking all the frames of the data set using the median, resulting in a clear representation of the cometary coma. The last step was subtracting this comet-stacked frame from each frame, thus eliminating the coma contamination. Figure 3.34 exemplified this procedure.
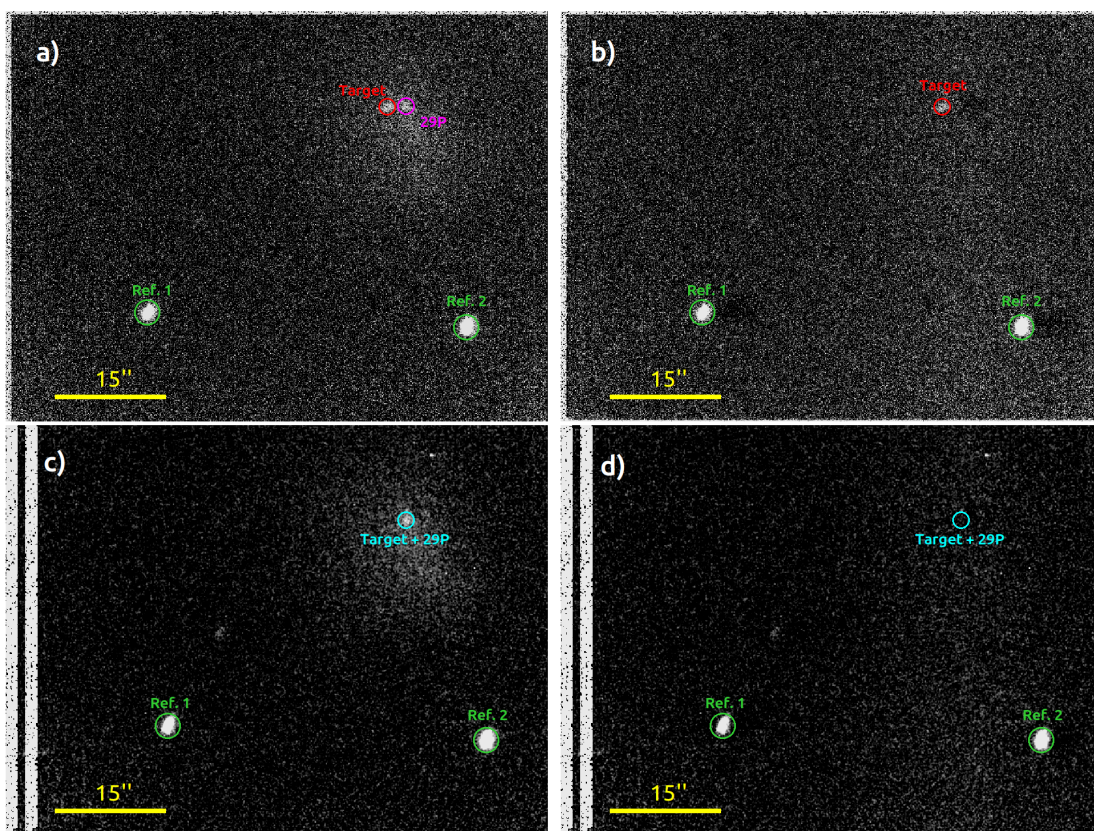

Figure 3.34: Elimination of the contamination from the cometary coma. First frame of the data set before (a) and after (b) the coma removal process. The frames c and d are in the central instant for the occultation, before and after the coma removal process, respectively. The red circle indicates the target star separated from the occulting body (magenta region). The cyan regions show the target star plus occulting body flux. The green regions indicate the reference stars used during the differential aperture photometry. Each frame has a field of view (FOV) of $\sim 1.2' \times 0.9'$. Figure from PEREIRA *et al.* (submitted).

We can now perform the definitive photometry with the corrected frames to obtain the occultation light curve. We use two stars as a reference to mitigate the sky flux

variations. Figure 3.35 presents the light curves obtained a) before the cometary coma removal, b) after the coma removal, and c) after the detrending process to eliminate systematic flux variations. The detrend was made by smoothing the light curve using the Savitzky-Golay digital filter (SG) in windows of 135 seconds (about $1,000$ km in the sky plane) for data points external to the occultation. Subsequently, we interpolated the region within the occultation using a polynomial function. Then, we divide the definitive photometric light curve by the smoothed one to eliminate the low-frequency variations in flux. This correction was based on the approach used by BOUFLEUR *et al.* (2018) to reduce the systematic variations in exo-planet transit light curves. It is important to remember that this approach may eliminate possible real extinctions in the stellar flux caused by broad and shallow structures.
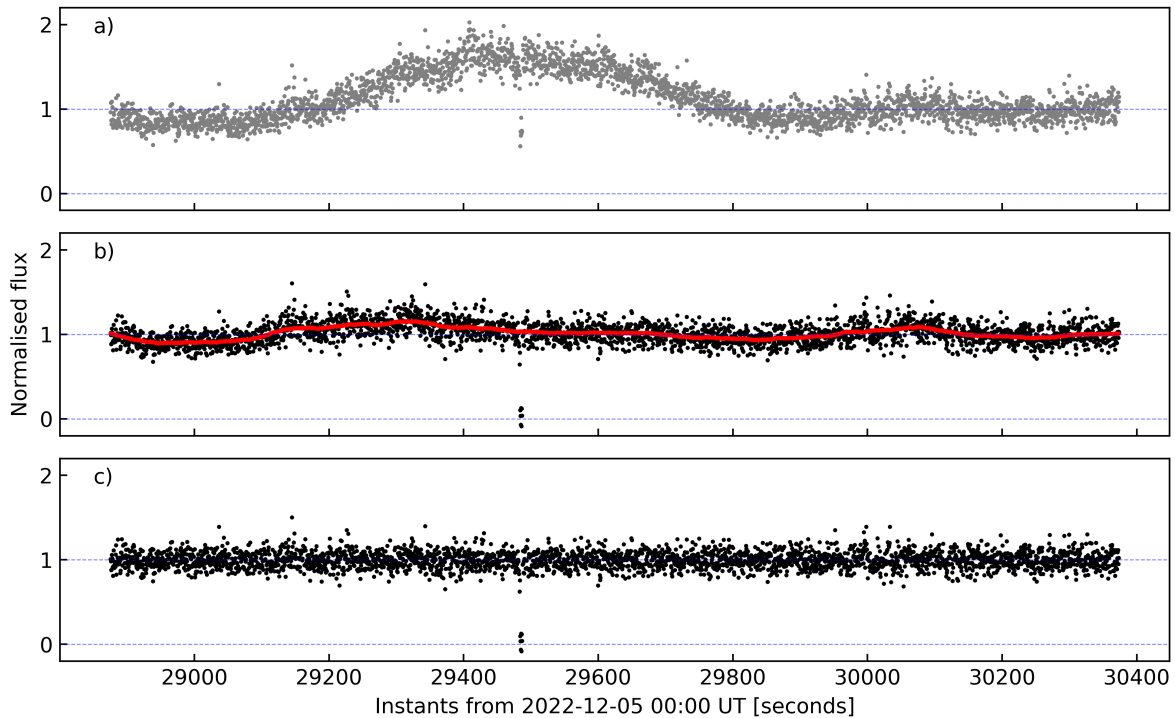

Figure 3.35: Light curves obtained from the 29P stellar occultation on December 05, 2022. a) the light curve obtained from the original data set, corrected from bias and flats only; b) the light curve obtained from the coma-removal correction applied frame-to-frame (black dots), and the smoothed light curve obtained using the SG filter with 135-second window size; c) final light curve obtained after all the corrections. Figure from PEREIRA *et al.* (submitted).

The ingress and egress instants of the star being occulted by 29P can now be determined. We do this using SORA using the procedure explained in Section 2.1.4. These instants are 08:11:23.00 $\pm$ 0.06 UT and 08:11:26.64 $\pm$ 0.07 UT for ingress and egress, respectively. With a duration of 3.65 ± 0.05 seconds and a shadow velocity of $14.8\,\mathrm{km\,s}$, the chord length was estimated to be 54.0 ± 1.5 km. The best-fitted model is plotted over

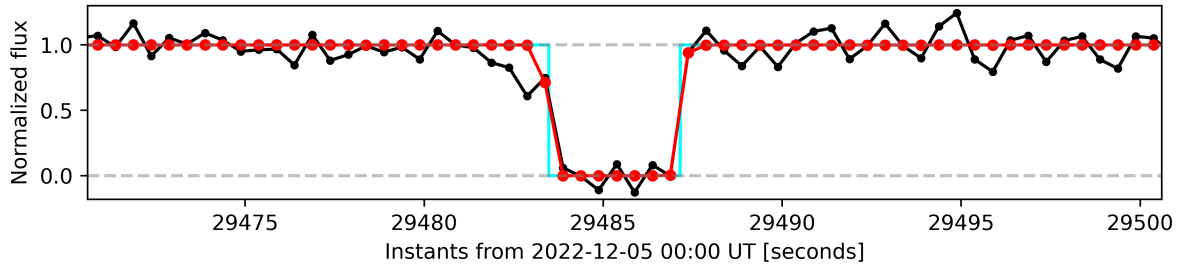the observed data in Figure 3.36.

Figure 3.36: Modeled light curve for the December 5, 2022, stellar occultation by 29P. The curve represents the synthetic curve that best fits the observed data (black). In cyan, the geometric model.

As we have a single chord, we can only fit a circle to the extremities. Therefore, we obtained two solutions for the 29P center. The difference between these two solutions is ~ 6 mas. The astrometric solutions are presented in PEREIRA *et al.* (submitted, Table 1. See appendix C).

We notice a slight decrease in flux as the star moves behind the nucleus during ingress, which is not present during egress. This phenomenon can be explained by either 1) the star being gradually occulted by an opaque object, exposing a topographic feature along the limb, or 2) a thick dust cloud near the nucleus that partially obstructs the stellar flux. This partial flux drop was fitted using a step-wise model that considers all the physical effects used in the square-well model. The gradual dimming is modeled by varying the opacity of the "step" in the ingress region.

The optimal synthetic light curve was derived using χ^2 statistics, comparing $100,000$ generated models with the observed light curve. The 1σ marginal error bar was determined by the $\chi^2_{\min} + 1$ interval. The fitted semi-transparent box suggests a dust cloud at a height of ~ 23.4 km from the nucleus limb, with an optical depth $\tau = 0.18 \pm 0.02$ (this optical depth accounts for Airy diffraction). It is noteworthy that the nucleus occultation (segment BC in Figure 3.37) shows a slightly shorter chord length (~ 51.7 km) compared to the previous fit, which did not consider the gradual flux variation. However, this difference is not significant for the astrometric position.

When analyzing the full-resolution light curve, we identify single data point flux drops corresponding to possible structures with apparent equivalent widths of $E' = 2.8$ km and $E' = 2.4$ km in the regions before and after the closest approach (black arrows in Figure 3.38), respectively. These structures are localized at an average distance of $1,737$ km from the cometary nucleus in the sky plane. This corresponds to a semi-transparent structure with a width of approximately 7.4 km and apparent opacities of $p' = 0.368$ for ingress and $p' = 0.316$ for egress. This distance is close to the co-rotational region (approximately $1,757$ km), calculated considering the nucleus's rotational period of 57
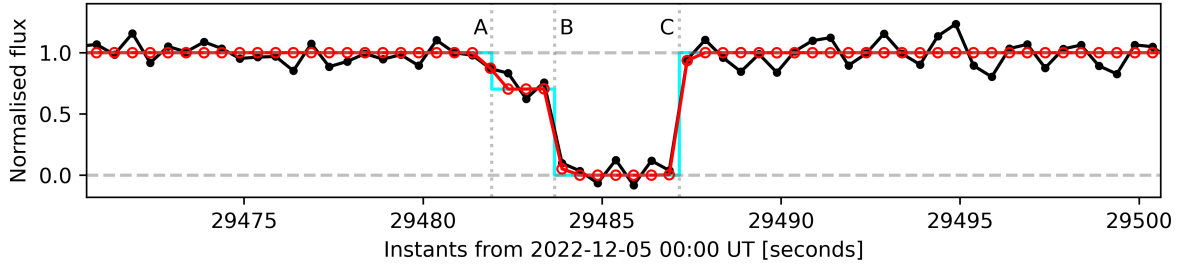
Figure 3.37: Modeled light curve (red) that best fits the observed data (black). The cyan curve represents the step-wise model for the semi-transparent screen blocking the stellar flux (segment A to B) just before the occultation by the nucleus (B to C). Figure from PEREIRA *et al.* (submitted).

days (estimated from the periodicity of the outbursts), a radius of 30.2 km, and a density of $\rho = 1,119 \text{ kg m}^{-3}$ (based on estimates of another active Centaur Chiron).
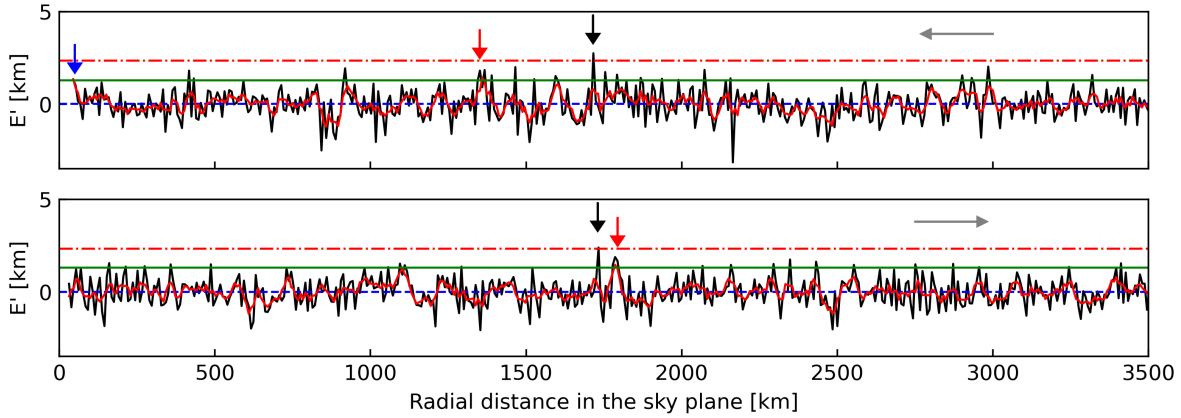

Figure 3.38: Apparent equivalent width as a function of radial distance for the regions before (top panel) and after (bottom panel) the closest approach, covering a total of $7,000$ km in the sky plane. The grey horizontal arrows indicate the time evolution. The blue dashed line represents the mean of the E' distribution, and the red dot-dashed line shows the 3σ upper limit of E'. The green horizontal line marks the 3σ upper limit for the 25 km-resampled curve (red). The arrows indicate the identified features above the upper limits for the full-resolution (black) and resampled (red) curves. The dust cloud (Section 5) is also visible in the 25 km-resampled curve (blue arrow). Figure from PEREIRA *et al.* (submitted).

The 25 km resampled light curve shows flux variations above the 3σ upper limit: at $1,352.3 \pm 1.0$ km from the nucleus center in the pre-closest approach region (red arrow, top panel in Figure 3.38); the feature has a width $W_\perp = 29.4 \pm 2.2$ km and an opacity $p = 0.10 \pm 0.03$. After the closest approach, the feature has a width $W_\perp = 28.0 \pm 5.0$ km and an opacity $p = 0.12 \pm 0.05$ (red arrow, bottom panel in Figure 3.38). Despite the

low significance of these features, their symmetry for the body's center is noteworthy. While unlikely, these features might suggest a localized accumulation of material ejected by the nucleus, forming a debris region or other confined narrow structures in the internal cometary coma.

Chapter 4

Conclusion

Small Solar System Object (SSSO) are remnants from the early Solar System. By studying their composition, structure, and distribution, we gain valuable insights into the conditions and processes of the Solar System's formation and evolution. The scattering of these bodies due to planetary migrations reveals how the planets arrived at their current orbits, enhancing our understanding of the dynamic processes that shape the Solar System, including forming moons, rings, and impact craters. Stellar occultations are crucial in this study because they offer exceptional precision in studying small and distant objects and their environments. By meticulously analyzing the timing and characteristics of these occultations, we can obtain valuable information about the size and shape of the occulting body. This technique also enables the detection and study of atmospheres or sets limits on their presence. Additionally, stellar occultations have facilitated the discovery and analysis of rings around SSSO.

Rings have been observed around Centaurs and hot Classical KBO objects at various heliocentric distances, prompting questions about their presence around cold Classical and resonant objects. Key questions include whether their origin is tied to the primordial collisional environment, gravitational perturbations from giant planets, or material ejection due to CO or other volatile sublimation. To address this, we studied the stellar occultation by Chiron, Echeclus, and 29P/Schwassmann-Wachmann 1, some of the most active centaurs, making significant contributions to understanding the physical characteristics of the parent body and its surrounding environment, either by detecting confined material around Chiron or by placing detection limits.

An effective confinement mechanism is necessary to keep these structures confined; otherwise, they should have either been dispersed or accreted by the central body (SICARDY et al., 2021). A critical factor in this confinement seems to be the resonances, as the rings found around Chariklo, Haumea, and Quaoar are located close to the 1:3 SOR (also 5:7 SOR for the Quaoar's Q2R ring), or even the MMR with the known or/and unknown satellites (RODRÍGUEZ et al., 2023). Future works may search for shepherd satellites that could confine these rings by testing various masses, radii, and orbital configurations

that explain the ring's local and global properties (e.g. SICKAFOOSE e LEWIS, 2024). The similarities and differences of the confirmed rings around the small bodies are presented in Table 4.1. The need to investigate the mechanisms responsible for sustaining ring structures over time is evident.

Table 4.1: Summary of the physical properties of the known rings around Chariklo, Haumea, and Quaoar.

	Chariklo inner / outer ring	Haumea	Quaoar inner / outer ring
Body radius, R [km]	~ 125	~ 712	~ 543
Classical Roche limit, a_{Roche} [km]	< 400	$\sim 2{,}420$	$\sim 1{,}780$
3:1 resonance [km]	408 ± 20	$2{,}285\pm8$	$4{,}200\pm60$
Ring radius, r [km]	$385.9 \pm 0.4\ (\sim3.1\text{R})$ $399.8 \pm 0.6\ (\sim3.2\text{R})$	$2{,}287^{+75}_{-45}(\sim3.2\text{R})$	$2{,}520\pm20(\sim4.6\text{R})$ $4{,}057\pm6\ (\sim7.5\text{R})$
Gap [km]	~14	-	$\sim1{,}537$
Ring width [km]	$4.8 \leqslant W_{\text{r}} \leqslant 9.1$ $3.3 \leqslant W_{\text{r}} \leqslant 5.0$	~70	$7 \leqslant W_{\text{r}} \leqslant 16$ $5 \leqslant W_{\text{r}} \leqslant 336$
Optical depth	$0.45 \leqslant \tau_{\text{N}} \leqslant 0.32$ $0.05 \leqslant \tau_{\text{N}} \leqslant 0.07$	~0.1	$0.003 \leqslant \tau_{\text{N}} \leqslant 0.01$ $0.004 \leqslant \tau_{\text{N}} \leqslant 0.2$
Equivalent width (E_p) [km]	~ 2.0 ~ 0.2	~5.6	$0.06 \leqslant E_p \leqslant 0.1$ $0.3 \leqslant E_p \leqslant 2.0$

In this study, we discovered an unexpected second ring around Quaoar and provided a detailed analysis and results from the stellar occultation of August 2022. During this event, we gathered nine positive chords for the main body, which allowed us to accurately determine Quaoar's size, projected shape, and astrometric position. The elliptical fitting of these chords provided the following results: an apparent semi-major axis of roughly 579 ± 4 km, an apparent flattening of 0.12 ± 0.01, and an area-equivalent radius of about 543 ± 2 km. We also refined the orbital radius of the Q1R ring to approximately $4{,}057 \pm 6$ km, and its pole orientation, resulting in $\alpha_{\text{pole}} = 17^{\text{h}}\,19^{\text{m}}\,16^{\text{s}}.8 \pm 55^{\text{s}}.2$ and $\delta_{\text{pole}} = +53°\,27' \pm 18'$. The excellent quality of the Gemini North and CFHT light curves revealed details about the Q1R ring, confirming its non-homogeneous nature. The radial opacity profile of this ring was found to be Lorentzian in shape, extending about 60 km, with a full width at half maximum (FWHM) of around 5 km and a peak optical depth of approximately 0.275. Alongside expected secondary events related to the known ring, new secondary events were observed, indicating the presence of an additional ring around Quaoar. The new ring has an estimated radius of about $2{,}520 \pm 20$ km if concentric and co-planar to the Q1R ring, a typical width of around 10 km, and a normal optical depth of about 0.007. Like the Q1R ring, this new ring is also situated beyond the classical Roche limit of $1{,}780$ km.

Our investigations into Chiron's occultations in 2018 and 2019 provided the first reliable constraints on the shape and dimensions of its primary body. These observations were pivotal in establishing detection limits for surrounding structures. The occultation in 2022 revealed not only the central body but also additional structures. These structures

were consistent in location with those detected through stellar occultations in the 1990s and 2011, though they differed in optical depth, suggesting potential temporal variations in these features. This analysis also proposed a revised pole orientation for the previously proposed rings. Through a stellar occultation, we found that Chiron is surrounded by a tenuous disk ~ 580 km in radius, with dense ring-like concentrations at 325 ± 16 km and 423 ± 11 km (these two already detected in the 2011 stellar occultation (RUPRECHT *et al.*, 2015; SICKAFOOSE *et al.*, 2020)). These features are enhanced in 2022 data, likely due to Chiron's 2021 brightness outburst. The connection between the outburst and the rings remains unclear. However, 2021 Chiron's brightness is near its 1970s peak (cometary activity), consistent with its 50-year orbital period , suggesting some link between orbital location and brightness. The rapid increase in brightness eliminated proposed explanations, such as high-albedo surface features or changes in ring geometry over time. The most plausible cause seems to be an episodic cometary activity (DOBSON *et al.*, 2024, and references therein). The latest observed occultation by Chiron was in September 2023 and is currently under analysis. The initial findings suggest a growing amount of material scattered between the proposed rings, which could provide further insights into the formation and evolution of these rings. The subsequent phase of this analysis entails employing the three-dimensional model for Chiron and projecting it to the observation dates to determine a new center for the system. Assuming the rings are circular and concentric with Chiron, we can refine their pole orientation. By modeling the structures revealed in our most accurate light curve in 2023 stellar occultation, we can compare them with those detected in previous events and trace the temporal evolution of the proposed ring's properties.

Our study on the Centaur Echeclus included three stellar occultation events aimed at exploring its surrounding regions. Events were predicted and observed in 2019 and 2020 in South America and 2021, with the shadow passing over Japan. Observations in 2019 only allowed for the study of the surroundings of the object, as there was no detection of the occultation by the main body. In 2020, the first detection with more than one chord occurred, making it possible to determine the body's limb at the event's moment. The 2021 event, with only one positive detection, allowed for the adjustment of the body's center and, consequently, a refinement of its ephemeris and limiting the presence of material in its surroundings. By adjusting the extremities of the 2020 event's chords to possible ellipses and limiting the equivalent diameter to 64 km as presented in the literature, we found, at the 1σ level, an equatorial radius of 40 km and a flattening of 0.362. We use the 3D model and pole orientation ($\lambda_{\text{pole}}, \beta_{\text{pole}} = 115.2°, 21.5°$) for Echeclus from the ISAM service, along with its rotational period (P $= 26.785178 \pm 10^{-6}$ hours) as proposed by ROUSSELOT *et al.* (2021), to fit the projected limb to the stellar occultation chords. Given that the 2020 event provided two positive chords, we propagate Echeclus' rotation from the model's reference epoch to the occultation epoch. By adjusting the

limb center and scale, we determine the semi-axes of Echeclus to be: $a = 37.0 \pm 0.6$ km, $b = 28.4 \pm 0.5$ km, and $c = 24.9 \pm 0.4$ km, resulting in an area-equivalent radius of 30.0 ± 0.5 km. We calculate the instantaneous geometric albedo as $p_{\mathrm{v}} = 0.050 \pm 0.004$ from the projected limb's area and the absolute magnitude. The best light curves in terms of spatial coverage and S/N of the observed stellar occultations were La Silla/NTT in 2019, which covered about $7,000$ km in the sky plane; SOAR in 2020, covering $14,000$ km in the sky plane; and Okazaki/Japan in 2021, which covered about $9,000$ km in the sky plane. With these data, we determined lower limits for detecting apparent opacity at the 3σ level as $p' = 0.135$, $p' = 0.189$, and $p' = 0.258$, respectively. Equivalent width limits were also determined for these three data sets, with 166 meters for La Silla, 331 meters for SOAR, and 162 meters for Okazaki.

The stellar occultation by 29P/Schwassmann-Wachmann1 in December 2022 represented a significant advancement, as this technique was the first detection of this object. The accurate astrometric position obtained from this event refined the ephemeris. It improved the orbit of 29P to an unprecedented level, as the coma prevents the nucleus' astrometric position from being accurately determined using other techniques. In this study, we applied a method that effectively removes contamination from the coma, enabling the extraction of an uncontaminated stellar occultation light curve. Our analysis revealed a gradual dimming of the star during ingress. The lack of similar dimming on egress is inconsistent with the presence of a shell of material close to the nucleus during this intense outburst activity. Slow-moving material in this region would be expected to fall back under the nucleus's gravitational influence. Therefore, we attribute the dimming to localized dust and gas emission from an area on the nucleus near the morning terminator, where solar radiation heats the region and triggers activity. This behavior was interpreted as a potential dense dust cloud near the nucleus, extending to more than 23 km above the surface, with an optical depth of $\tau = 0.18 \pm 0.02$. In analyzing the full-resolution light curve, we observed single data point flux drops that suggest the presence of structures with apparent equivalent widths of $E' = 2.8$ km and $\mathrm{E}' = 2.4$ km, occurring in the regions before and after the closest approach, respectively. These structures are localized at an average distance of $1,737$ km from the cometary nucleus in the sky plane. The 25 km resampled light curve reveals flux variations exceeding the 3σ upper limit: in the pre-closest approach region, the feature has a width of $W' = 29.4 \pm 2.2$ km and opacity of $p = 0.10 \pm 0.03$, while in the post-closest approach region, the feature has a width of $W' = 28.0 \pm 5.0$ km and opacity of $p = 0.12 \pm 0.05$. Although the significance of these features is low, their symmetry around the body's center is notable. While unlikely, these features could indicate a localized accumulation of material ejected by the nucleus, potentially forming a debris envelope or other confined narrow structures.

Investigating SSSO, including Centaurs and Classical KBO, reveals diverse structures and phenomena, particularly in the context of ring systems. Our study highlights that

rings around Centaurs and hot Classical KBO have been observed, demonstrating their presence across a broad range of heliocentric distances. These observations raise intriguing questions about the potential for rings around other small body classes, such as cold Classical and resonant objects, and the mechanisms underlying their formation. The origins of these rings remain a subject of debate, with hypotheses ranging from primordial collisional environments and gravitational perturbations by giant planets to material ejection through volatile sublimation.

Our findings suggest that the rings' origins around SSSO can be diverse. We observe that the rings of Quaoar and Haumea may have formed from primordial collisions. These collisions, occurring in the early stages of the Solar System, could have created stable ring structures around these objects that survive during the planetary migration, since that close encounters with giant planets (ARAUJO *et al.*, 2018; WOOD *et al.*, 2017) or other small bodies (IKEYA e HIRATA, 2024) capable of significantly damaging or destroying these ring structure are extremely rare. On the other hand, in Chiron, we identify a confinement of material that possibly originates from the ejections. During stellar occultations, we detected structures that may be related to Chiron's cometary activity, where the materials are ejected and confined in disks or rings. If not forming, these material ejections must be at least feeding pre-existing structures since we observe a temporal evolution in their physical properties. Both Centaurs 29P and Echeclus also display recurring cometary activity. However, unlike Chiron, additional structures around these bodies are not observed. This is observational evidence that material ejections alone cannot form rings, as the particles tend to fall back into the central body or be ejected from the system. In summary, our studies indicate that the formation of confined structures around SSSO can result from a combination of primordial collisions, ejections processes, and the dynamical environment in the main body surroundings.

Understanding these mechanisms is essential for comprehending rings' formation, evolution, and confinement around small Solar System bodies. Utilizing the stellar occultation technique has proven instrumental in our efforts to explore these distant and faint objects. This method has detected and characterized ring systems around Quaoar and other small bodies, providing valuable insights into their physical properties and structural characteristics. Our study's results contribute to the broader understanding of ring dynamics and highlight the effectiveness of stellar occultations in revealing details that are challenging to capture through direct imaging. Discoveries so far suggest that ring systems could be more common that previously thought. Although it is challenging to estimate how many more SSSO may possess rings, it is reasonable to expect that, as observational techniques continue to improve and more occultations are observed, the number of known ringed small bodies could increase significantly. This is especially likely with the expansion of global professional-amateur collaborations and increasing use of space-based telescopes (e.g., JWST, CHEOPS).

As we continue to explore these intriguing phenomena, future observations and analyses will be crucial for addressing outstanding questions about ring formation and the diverse characteristics of SSSO. A significant aspect of this research is collaboration between professional and amateur astronomers. Their contributions have been invaluable in extending the observational reach and improving the accuracy of our results. This collaborative effort underscores the vital role that diverse astronomical communities play in advancing our understanding of the Solar System and achieving scientific discoveries. Our research demonstrates the importance of continued exploration in this field and the potential for groundbreaking findings that could fundamentally alter our knowledge of the outer Solar System.

Bibliography

ARAUJO, R. A. N., WINTER, O. C., SFAIR, R., 2018, "Rings under close encounters with the giant planets: Chariklo versus Chiron", Mon. Not, Roy. Astron. Soc., v. 479, n. 4 (out.), pp. 4770–4777. doi: 10.1093/mnras/sty1770.

ARCHINAL, B. A., ACTON, C. H., A'HEARN, M. F., et al., 2018, "Report of the IAU Working Group on Cartographic Coordinates and Rotational Elements: 2015", *Celestial Mechanics and Dynamical Astronomy*, 130(3):22. doi: 10.1007/s10569-017-9805-5.

ASSAFIN, M., 2023, "Differential aperture photometry and digital coronagraphy with PRAIA", Planet. Space Sci., 239:105816. doi: 10.1016/j.pss.2023.105816.

ASSAFIN, M., CAMARGO, J. I. B., VIEIRA MARTINS, R., et al., 2010, "Precise predictions of stellar occultations by Pluto, Charon, Nix, and Hydra for 2008-2015", Astron. Astrophys., 515:A32. doi: 10.1051/0004-6361/200913690.

ASTROPY COLLABORATION, ROBITAILLE, T. P., TOLLERUD, E. J., et al., 2013, "Astropy: A community Python package for astronomy", Astron. Astrophys., 558:A33. doi: 10.1051/0004-6361/201322068.

AZZAM, Y. A., ALI, G. B., ISMAIL, H. A., et al., 2010, "Current and Future Capabilities of the 74-inch Telescope of Kottamia Astronomical Observatory in Egypt". In: *Third UN/ESA/NASA Workshop on the International Heliophysical Year 2007 and Basic Space Science*, v. 20, *Astrophysics and Space Science Proceedings*, pp. 175–187, jan. doi: 10.1007/978-3-642-03325-4_16.

AZZAM, Y. A., ELNAGAHY, F. I. Y., ALI, G. B., et al., 2022, "Kottamia Faint Imaging Spectro-Polarimeter (KFISP): opto-mechanical design, software control and performance analysis", *Experimental Astronomy*, v. 53, n. 1 (fev.), pp. 45–70. doi: 10.1007/s10686-021-09802-z.

BARTCZAK, P., DUDZIŃSKI, G., 2018, "Shaping asteroid models using genetic evolution (SAGE)", Mon. Not, Roy. Astron. Soc., v. 473, n. 4 (fev.), pp. 5050–5065. doi: 10.1093/mnras/stx2535.

BATYGIN, K., BROWN, M. E., 2010, "Early Dynamical Evolution of the Solar System: Pinning Down the Initial Conditions of the Nice Model", *The Astrophysical Journal*, v. 716, n. 2 (jun.), pp. 1323–1331. doi: 10.1088/0004-637X/716/2/1323.

BAUER, J. M., CHOI, Y.-J., WEISSMAN, P. R., et al., 2008, "The Large-Grained Dust Coma of 174P/Echeclus", Publ. Astron. Soc. Pacific, v. 120, n. 866 (abr.), pp. 393. doi: 10.1086/587552.

BAUER, J. M., GRAV, T., BLAUVELT, E., et al., 2013, "Centaurs and Scattered Disk Objects in the Thermal Infrared: Analysis of WISE/NEOWISE Observations", Astrophys. J., 773(1):22. doi: 10.1088/0004-637X/773/1/22.

BENZ, W., BROEG, C., FORTIER, A., et al., 2021, "The CHEOPS mission", *Experimental Astronomy*, v. 51, n. 1 (fev.), pp. 109–151. doi: 10.1007/s10686-020-09679-4.

BÉRARD, D., SICARDY, B., CAMARGO, J. I. B., et al., 2017, "The Structure of Chariklo's Rings from Stellar Occultations", Astron. J., 154(4):144. doi: 10.3847/1538-3881/aa830d.

BOISSEL, Y., SICARDY, B., ROQUES, F., et al., 2014, "An exploration of Pluto's environment through stellar occultations", Astron. Astrophys., 561:A144. doi: 10.1051/0004-6361/201321836.

BOTTKE, W. F., J., CELLINO, A., PAOLICCHI, P., et al., 2002, "An Overview of the Asteroids: The Asteroids III Perspective". In: *Asteroids III*, pp. 3–15.

BOUFLEUR, R. C., EMILIO, M., JANOT-PACHECO, E., et al., 2018, "A modified CoRoT detrend algorithm and the discovery of a new planetary companion", Mon. Not, Roy. Astron. Soc., v. 473, n. 1 (jan.), pp. 710–720. doi: 10.1093/mnras/stx2187.

BRAGA-RIBAS, F., SICARDY, B., ORTIZ, J. L., et al., 2013, "The Size, Shape, Albedo, Density, and Atmospheric Limit of Transneptunian Object (50000) Quaoar from Multi-chord Stellar Occultations", Astrophys. J., 773(1):26. doi: 10.1088/0004-637X/773/1/26.

BRAGA-RIBAS, F., SICARDY, B., ORTIZ, J. L., et al., 2014, "A ring system detected around the Centaur (10199) Chariklo", Nature, v. 508, n. 7494 (abr.), pp. 72–75. doi: 10.1038/nature13155.

BRAGA-RIBAS, F., CRISPIM, A., VIEIRA-MARTINS, R., et al., 2019, "Database on detected stellar occultations by small outer Solar System objects". In: *Journal*

of Physics Conference Series, v. 1365, *Journal of Physics Conference Series*, p. 012024, out. doi: 10.1088/1742-6596/1365/1/012024.

BRAGA-RIBAS, F., PEREIRA, C. L., SICARDY, B., et al., 2023, "Constraints on (2060) Chiron's size, shape, and surrounding material from the November 2018 and September 2019 stellar occultations", Astron. Astrophys., 676:A72. doi: 10.1051/0004-6361/202346749.

BRAGA-RIBAS, F., VACHIER, F., DESMARS, J., et al., submitted, "Present and Future of Stellar Occultation by Transneptunian Satellites: first detections and orbits of Vanth, Hi'iaka, and Weywot", *Philosophical Transactions of the Royal Society A*, (july).

BROWN, M. E., SUER, T. A., 2007, "Satellites of 2003 AZ_84, (50000), (55637), and (90482)", IAU Circ., v. 8812 (fev.), pp. 1.

BROWN, M. E., 2001, "The Inclination Distribution of the Kuiper Belt", *The Astronomical Journal*, v. 121, n. 5 (may), pp. 2804. doi: 10.1086/320391. Disponível em: <https://dx.doi.org/10.1086/320391>.

BROWN, M. E., TRUJILLO, C. A., 2004, "Direct Measurement of the Size of the Large Kuiper Belt Object (50000) Quaoar", Astron. J., v. 127, n. 4 (abr.), pp. 2413–2417. doi: 10.1086/382513.

BROWN, M. E., TRUJILLO, C., RABINOWITZ, D., 2004, "Discovery of a Candidate Inner Oort Cloud Planetoid", Astrophys. J., v. 617, n. 1 (dez.), pp. 645–649. doi: 10.1086/422095.

BUIE, M. W., OLKIN, C., MCDONALD, S., et al., 1993, "(2060) Chiron", IAU Circ., v. 5898 (nov.), pp. 1.

BUS, S. J., BOWELL, E., HARRIS, A. W., et al., 1989, "2060 Chiron: CCD and electronographic photometry", Icarus, v. 77, n. 2 (fev.), pp. 223–238. doi: 10.1016/0019-1035(89)90087-0.

BUS, S. J., BUIE, M. W., SCHLEICHER, D. G., et al., 1996, "Stellar Occultation by 2060 Chiron", *Icarus*, v. 123, n. 2 (out.), pp. 478–490. doi: 10.1006/icar.1996.0173.

BUTCHER, H., STEVENS, R., 1981, "Image Reduction and Analysis Facility Development", *Kitt Peak National Observatory Newsletter*, v. 16 (jan.), pp. 6.

CAMPINS, H., TELESCO, C. M., OSIP, D. J., et al., 1994, "The Color Temperature of (2060) Chiron: A Warm and Small Nucleus", Astron. J., v. 108 (dez.), pp. 2318. doi: 10.1086/117244.

CANUP, R. M., 2004, "Simulations of a late lunar-forming impact", Icarus, v. 168, n. 2 (abr.), pp. 433–456. doi: 10.1016/j.icarus.2003.09.028.

CHARNOZ, S., CANUP, R. M., CRIDA, A., et al., 2018, "The Origin of Planetary Ring Systems". In: Tiscareno, M. S., Murray, C. D. (Eds.), *Planetary Ring Systems. Properties, Structure, and Evolution*, pp. 517–538. doi: 10.1017/9781316286791.018.

CHOI, Y. J., WEISSMAN, P., CHESLEY, S., et al., 2006a, "Comet 174P/Echeclus", *Central Bureau Electronic Telegrams*, v. 563 (jun.), pp. 1.

CHOI, Y. J., WEISSMAN, P. R., POLISHOOK, D., 2006b, "(60558) 2000 EC98", *Central Bureau Electronic Telegrams*, v. 355 (jan.), pp. 1.

CLEMENS, J. C., CRAIN, J. A., ANDERSON, R., 2004, "The Goodman spectrograph". In: Moorwood, A. F. M., Iye, M. (Eds.), *Ground-based Instrumentation for Astronomy*, v. 5492, *Society of Photo-Optical Instrumentation Engineers (SPIE) Conference Series*, pp. 331–340, set. doi: 10.1117/12.550069.

CROVISIER, J., BIVER, N., BOCKELEE-MORVAN, D., et al., 1995, "Carbon monoxide outgassing from Comet P solarSchwassmann-Wachmann 1", Icarus, v. 115, n. 1 (maio), pp. 213–216. doi: 10.1006/icar.1995.1091.

CRUIKSHANK, D. P., BROWN, R. H., 1983, "The nucleus of comet P/Schwassmann-Wachmann 1", Icarus, v. 56, n. 3 (dez.), pp. 377–380. doi: 10.1016/0019-1035(83)90158-6.

CUZZI, J. N., 1985, "Rings of Uranus: Not so thick, not so black", *Icarus*, v. 63, n. 2 (ago.), pp. 312–316. doi: 10.1016/0019-1035(85)90014-4.

DELSANTI, A., JEWITT, D., 2006, "The Solar System Beyond The Planets". In: Blondel, P., Mason, J. W. (Eds.), *Solar System Update*, p. 267. doi: 10.1007/3-540-37683-6 11.

DESMARS, J., CAMARGO, J. I. B., BRAGA-RIBAS, F., et al., 2015, "Orbit determination of trans-Neptunian objects and Centaurs for the prediction of stellar occultations", Astron. Astrophys., 584:A96. doi: 10.1051/0004-6361/201526498.

DHILLON, V. S., BEZAWADA, N., BLACK, M., et al., 2021, "HiPERCAM: a quintuple-beam, high-speed optical imager on the 10.4-m Gran Telescopio Canarias", Mon. Not, Roy. Astron. Soc., v. 507, n. 1 (out.), pp. 350–366. doi: 10.1093/mnras/stab2130.

DOBSON, M., SCHWAMB, M., FITZSIMMONS, A., et al., 2021, "New or Increased Cometary Activity in (2060) 95P/Chiron", *Research Notes of the AAS*, v. 5, n. 9 (set.). ISSN: 2515-5172. doi: 10.3847/2515-5172/ac26c9.

DOBSON, M. M., SCHWAMB, M. E., FITZSIMMONS, A., et al., 2024, "The Discovery and Evolution of a Possible New Epoch of Cometary Activity by the Centaur (2060) Chiron", , 5(7):165. doi: 10.3847/PSJ/ad543c.

DUFFARD, R., PINILLA-ALONSO, N., SANTOS-SANZ, P., et al., 2014, ""TNOs are Cool": A survey of the trans-Neptunian region. XI. A Herschel-PACS view of 16 Centaurs", Astron. Astrophys., 564:A92. doi: 10.1051/0004-6361/201322377.

ELLIOT, J. L., FRENCH, R. G., MEECH, K. J., et al., 1984, "Structure of the Uranian rings. I - Square-well model and particle-size constraints", Astron. J., v. 89 (out.), pp. 1587–1603. doi: 10.1086/113662.

ELLIOT, J. L., OLKIN, C. B., DUNHAM, E. W., et al., 1995, "Jet-like features near the nucleus of Chiron", *Nature*, v. 373, n. 6509 (jan.), pp. 46–49. doi: 10.1038/373046a0.

ELLIOT, J. L., KERN, S. D., CLANCY, K. B., et al., 2005, "The Deep Ecliptic Survey: A Search for Kuiper Belt Objects and Centaurs. II. Dynamical Classification, the Kuiper Belt Plane, and the Core Population", Astron. J., v. 129, n. 2 (fev.), pp. 1117–1162. doi: 10.1086/427395.

ESPOSITO, L. W., DE STEFANO, M., 2018, *Planetary Ring Systems: Properties, Structure, and Evolution*. Cambridge Planetary Science. Cambridge, Cambridge University Press.

FERNÁNDEZ, Y. R., 2009, "That's the way the comet crumbles: Splitting Jupiter-family comets", Planet. Space Sci., v. 57, n. 10 (ago.), pp. 1218–1227. doi: 10.1016/j.pss.2009.01.003.

FORNASIER, S., LELLOUCH, E., MÜLLER, T., et al., 2013, "TNOs are Cool: A survey of the trans-Neptunian region. VIII. Combined Herschel PACS and SPIRE observations of nine bright targets at 70-500 μm", Astron. Astrophys., 555:A15. doi: 10.1051/0004-6361/201321329.

FRASER, W. C., BROWN, M. E., 2010, "Quaoar: A Rock in the Kuiper Belt", Astrophys. J., v. 714, n. 2 (maio), pp. 1547–1550. doi: 10.1088/0004-637X/714/2/1547.

FRASER, W. C., BATYGIN, K., BROWN, M. E., et al., 2013, "The mass, orbit, and tidal evolution of the Quaoar-Weywot system", Icarus, v. 222, n. 1 (jan.), pp. 357–363. doi: 10.1016/j.icarus.2012.11.004.

FRASER, W. C., BANNISTER, M. T., PIKE, R. E., et al., 2017, "All planetesimals born near the Kuiper belt formed as binaries", *Nature Astronomy*, 1:0088. doi: 10.1038/s41550-017-0088.

FRENCH, R. G., NICHOLSON, P. D., PORCO, C. C., et al., 1991, "Dynamics and structure of the Uranian rings." In: Bergstralh, J. T., Miner, E. D., Matthews, M. S. (Eds.), *Uranus*, pp. 327–409.

GAIA COLLABORATION, PRUSTI, T., DE BRUIJNE, J. H. J., et al., 2016, "The Gaia mission", Astron. Astrophys., 595:A1. doi: 10.1051/0004-6361/201629272.

GAIA COLLABORATION, VALLENARI, A., BROWN, A. G. A., et al., 2023, "Gaia Data Release 3. Summary of the content and survey properties", Astron. Astrophys., 674:A1. doi: 10.1051/0004-6361/202243940.

GARDNER, J. P., MATHER, J. C., ABBOTT, R., et al., 2023, "The James Webb Space Telescope Mission", Publ. Astron. Soc. Pacific, 135(1048):068001. doi: 10.1088/1538-3873/acd1b5.

GIL-HUTTON, R., 2024, "Impact-triggered activation of (2060) Chiron during its 1972 and 2021 outbursts", *Icarus*, v. 420, pp. 116209. ISSN: 0019-1035. doi: https://doi.org/10.1016/j.icarus.2024.116209. Disponível em: <https://www.sciencedirect.com/science/article/pii/S0019103524002690>.

GLADMAN, B., MARSDEN, B. G., VANLAERHOVEN, C., 2008, "Nomenclature in the Outer Solar System". In: Barucci, M. A., Boehnhardt, H., Cruikshank, D. P., et al. (Eds.), *The Solar System Beyond Neptune*, pp. 43–57.

GOMES, R., LEVISON, H. F., TSIGANIS, K., et al., 2005, "Origin of the cataclysmic Late Heavy Bombardment period of the terrestrial planets", *Nature*, v. 435, n. 7041 (maio), pp. 466–469. doi: 10.1038/nature03676.

GOMES-JÚNIOR, A. R., MORGADO, B. E., BENEDETTI-ROSSI, G., et al., 2022, "SORA: Stellar Occultation Reduction and Analysis", Mon. Not, Roy. Astron. Soc., (jan.). doi: 10.1093/mnras/stac032.

HARTMANN, W. K., THOLEN, D. J., MEECH, K. J., et al., 1990, "2060 Chiron: Colorimetry and cometary behavior", Icarus, v. 83, n. 1 (jan.), pp. 1–15. doi: 10.1016/0019-1035(90)90002-Q.

HATZES, A. P., BRIDGES, F. G., LIN, D. N. C., 1988, "Collisional properties of ice spheres at low impact velocities", Mon. Not, Roy. Astron. Soc., v. 231 (abr.), pp. 1091–1115. doi: 10.1093/mnras/231.4.1091.

HORNER, J., EVANS, N. W., BAILEY, M. E., 2004, "Simulations of the population of Centaurs – I. The bulk statistics", *Monthly Notices of the Royal Astronomical Society*, v. 354, n. 3 (11), pp. 798–810. ISSN: 0035-8711. doi: 10.1111/j.1365-2966.2004.08240.x. Disponível em: <https://doi.org/10.1111/j.1365-2966.2004.08240.x>.

IKEYA, R., HIRATA, N., 2024, "Gravitational disturbance on asteroidal ring systems by close encounter with a small object", *Icarus*, v. 418, pp. 116153. ISSN: 0019-1035. doi: https://doi.org/10.1016/j.icarus.2024.116153. Disponível em: <https://www.sciencedirect.com/science/article/pii/S0019103524002136>.

JAEGER, M., PROSPERI, E., VOLLMANN, W., et al., 2011, "Comet 174P/Echeclus = (60558) Echeclus", IAU Circ., v. 9213 (jun.), pp. 2.

JAMES, N. D., 2018, "Outburst of comet 174P/Echeclus", *Journal of the British Astronomical Association*, v. 128 (fev.), pp. 51.

JEWITT, D., 1990, "The Persistent Coma of Comet P/Schwassmann-Wachmann 1", Astrophys. J., v. 351 (mar.), pp. 277. doi: 10.1086/168463.

JEWITT, D., LUU, J., 1993, "Discovery of the candidate Kuiper belt object 1992 QB_1", Nature, v. 362, n. 6422 (abr.), pp. 730–732. doi: 10.1038/362730a0.

JEWITT, D., 2009, "THE ACTIVE CENTAURS", *The Astronomical Journal*, v. 137, n. 5 (apr), pp. 4296. doi: 10.1088/0004-6256/137/5/4296. Disponível em: <https://dx.doi.org/10.1088/0004-6256/137/5/4296>.

JEWITT, D., LUU, J., 1992, "Submillimeter Continuum Observations of 2060 Chiron", Astron. J., v. 104 (jul.), pp. 398. doi: 10.1086/116247.

KAASALAINEN, M., TORPPA, J., MUINONEN, K., 2001, "Optimization Methods for Asteroid Lightcurve Inversion. II. The Complete Inverse Problem", Icarus, v. 153, n. 1 (set.), pp. 37–51. doi: 10.1006/icar.2001.6674.

KARETA, T., SHARKEY, B., NOONAN, J., et al., 2019, "Physical Characterization of the 2017 December Outburst of the Centaur 174P/Echeclus", Astron. J., 158 (6):255. doi: 10.3847/1538-3881/ab505f.

KERVELLA, P., THÉVENIN, F., DI FOLCO, E., et al., 2004, "The angular sizes of dwarf stars and subgiants. Surface brightness relations calibrated by interferometry", Astron. Astrophys., v. 426 (out.), pp. 297–307. doi: 10.1051/0004-6361: 20035930.

KILIC, Y., BRAGA-RIBAS, F., KAPLAN, M., et al., 2022, "Occultation portal: A web-based platform for data collection and analysis of stellar occultations", Mon. Not, Roy. Astron. Soc., v. 515, n. 1 (set.), pp. 1346–1357. doi: 10.1093/mnras/ stac1595.

KOKUBO, E., IDA, S., MAKINO, J., 2000, "Evolution of a Circumterrestrial Disk and Formation of a Single Moon", *Icarus*, v. 148, n. 2, pp. 419–436. ISSN: 0019-1035. doi: https://doi.org/10.1006/icar.2000.6496. Disponível em: <https: //www.sciencedirect.com/science/article/pii/S0019103500964960>.

KOWAL, C. T., LILLER, W., MARSDEN, B. G., 1979, "The Discovery and Orbit of (2060) Chiron". In: Duncombe, R. L. (Ed.), *Dynamics of the Solar System*, v. 81, p. 245, jan.

LANE, A., LANE, L., WEST, R., et al., 1986, "Photometry from Voyager 2: Initial results from the uranian atmosphere, satellites and rings", *Science*, v. 233 (jan.), pp. 1450–1454.

LEBOFSKY, L. A., THOLEN, D. J., RIEKE, G. H., et al., 1984, "2060 Chiron: Visual and thermal infrared observations", Icarus, v. 60, n. 3 (dez.), pp. 532–537. doi: 10.1016/0019-1035(84)90160-X.

LEINHARDT, Z. M., MARCUS, R. A., STEWART, S. T., 2010, "THE FORMATION OF THE COLLISIONAL FAMILY AROUND THE DWARF PLANET HAUMEA", *The Astrophysical Journal*, v. 714, n. 2 (apr), pp. 1789. doi: 10.1088/0004-637X/714/2/1789. Disponível em: <https://dx.doi.org/10. 1088/0004-637X/714/2/1789>.

LELLOUCH, E., MORENO, R., MÜLLER, T., et al., 2017, "The thermal emission of Centaurs and trans-Neptunian objects at millimeter wavelengths from ALMA observations", Astron. Astrophys., 608:A45. doi: 10.1051/0004-6361/ 201731676.

LEVISON, H. F., DONES, L., 2007, "Comet Populations and Cometary Dynamics". In: McFadden, L. A. A., Weissman, P. R., Johnson, T. V. (Eds.), *Encyclopedia of the Solar System*, pp. 575–588. doi: 10.1016/B978-012088589-3/50035-9.

LEVISON, H. F., MORBIDELLI, A., VANLAERHOVEN, C., et al., 2008, "Origin of the structure of the Kuiper belt during a dynamical instability in the orbits of Uranus and Neptune", *Icarus*, v. 196, n. 1, pp. 258 – 273. ISSN: 0019-1035. doi: https://doi.org/10.1016/j.icarus.2007.11.035.

MARCIALIS, R. L., BURATTI, B. J., 1993, "CCD Photometry of 2060 Chiron in 1985 and 1991", *Icarus*, v. 104, n. 2, pp. 234–243. ISSN: 0019-1035. doi: https://doi.org/10.1006/icar.1993.1098. Disponível em: <https://www.sciencedirect.com/science/article/pii/S0019103583710985>.

MARSDEN, B., 2000, "Eight TNOs and Centaurs." *MPEC 2000-E64*.

MEECH, K. J., BELTON, M. J. S., 1990, "The Atmosphere of 2060 Chiron", Astron. J., v. 100 (out.), pp. 1323. doi: 10.1086/115600.

MEECH, K. J., BELTON, M. J. S., MUELLER, B. E. A., et al., 1993, "Nucleus Properties of P/Schwassmann-Wachmann 1", Astron. J., v. 106 (set.), pp. 1222. doi: 10.1086/116721.

MILES, R., 2016a, "Comet 174P/Echeclus = (60558) Echeclus", *CBET*, v. 4313 (set.).

MILES, R., 2016b, "Discrete sources of cryovolcanism on the nucleus of Comet 29P/Schwassmann-Wachmann and their origin", Icarus, v. 272 (jul.), pp. 387–413. doi: 10.1016/j.icarus.2015.11.011.

MORALES, R., MORALES, N., DUFFARD, R., et al., 2022, "Cataloguing astronomical ground-based images of asteroids and TNOs". In: *European Planetary Science Congress*, pp. EPSC2022–652, set. doi: 10.5194/epsc2022-652.

MORBIDELLI, A., 2008, "Comets and Their Reservoirs: Current Dynamics and Primordial Evolution". In: *Saas-Fee Advanced Course 35: Trans-Neptunian Objects and Comets*, Berlin: Springer-Verlag, p. 132.

MORBIDELLI, A., 2010, "A coherent and comprehensive model of the evolution of the outer Solar System", *Comptes Rendus Physique*, v. 11 (nov.), pp. 651–659. doi: 10.1016/j.crhy.2010.11.001.

MORGADO, B. E., SICARDY, B., BRAGA-RIBAS, F., et al., 2021, "Refined physical parameters for Chariklo's body and rings from stellar occultations observed between 2013 and 2020", Astron. Astrophys., 652:A141. doi: 10.1051/0004-6361/202141543.

MORGADO, B. E., BRUNO, G., GOMES-JÚNIOR, A. R., et al., 2022, "A stellar occultation by the transneptunian object (50000) Quaoar observed by CHEOPS", Astron. Astrophys., 664:L15. doi: 10.1051/0004-6361/202244221.

MORGADO, B. E., SICARDY, B., BRAGA-RIBAS, F., et al., 2023, "A dense ring of the trans-Neptunian object Quaoar outside its Roche limit", Nature, v. 614, n. 7947 (fev.), pp. 239–243. doi: 10.1038/s41586-022-05629-6.

MURRAY, C. D., FRENCH, R. S., 2018, "The F Ring of Saturn". In: Tiscareno, M. S., Murray, C. D. (Eds.), *Planetary Ring Systems: Properties, Structure, and Evolution*, p. 338–362, Cambridge University Press.

NESVORNÝ, D., LI, R., YOUDIN, A. N., et al., 2019, "Trans-Neptunian binaries as evidence for planetesimal formation by the streaming instability", *Nature Astronomy*, v. 3 (jun.), pp. 808–812. doi: 10.1038/s41550-019-0806-z.

NOLL, K. S., GRUNDY, W. M., CHIANG, E. I., et al., 2008, "Binaries in the Kuiper Belt". In: Barucci, M. A., Boehnhardt, H., Cruikshank, D. P., et al. (Eds.), *The Solar System Beyond Neptune*, pp. 345–363. doi: 10.48550/arXiv.astro-ph/ 0703134.

ORTIZ, J. L., GUTIÉRREZ, P. J., SOTA, A., et al., 2003, "Rotational brightness variations in Trans-Neptunian Object 50000 Quaoar", Astron. Astrophys., v. 409 (out.), pp. L13–L16. doi: 10.1051/0004-6361:20031253.

ORTIZ, J. L., DUFFARD, R., PINILLA-ALONSO, N., et al., 2015, "Possible ring material around centaur (2060) Chiron", Astron. Astrophys., 576:A18. doi: 10.1051/0004-6361/201424461.

ORTIZ, J. L., SANTOS-SANZ, P., SICARDY, B., et al., 2017, "The size, shape, density and ring of the dwarf planet Haumea from a stellar occultation", Nature, v. 550, n. 7675 (out.), pp. 219–223. doi: 10.1038/nature24051.

ORTIZ, J. L., PEREIRA, C. L., SICARDY, B., et al., 2023, "Changing material around (2060) Chiron revealed by an occultation on December 15, 2022", Astron. Astrophys., 676:L12. doi: 10.1051/0004-6361/202347025.

PAN, M., WU, Y., 2016, "On the Mass and Origin of Chariklo's Rings", Astrophys. J., 821(1):18. doi: 10.3847/0004-637X/821/1/18.

PEREIRA, C. L., SICARDY, B., MORGADO, B. E., et al., 2023, "The two rings of (50000) Quaoar", Astron. Astrophys., 673:L4. doi: 10.1051/0004-6361/ 202346365.

PEREIRA, C. L., BRAGA-RIBAS, F., SICARDY, B., et al., 2024, "Physical properties of Centaur (60558) 174P/Echeclus from stellar occultations", *Monthly Notices*

of the Royal Astronomical Society, v. 527, n. 2 (10), pp. 3624–3638. ISSN: 0035-8711. doi: 10.1093/mnras/stad3318. Disponível em: <https://doi.org/10.1093/mnras/stad3318>.

PEREIRA, C. L., BRAGA-RIBAS, F., SICARDY, B., et al., submitted, "Centaur 29P/Schwassmann-Wachmann 1 and its near-nucleus environment from a stellar occultation", *Philosophical Transactions of the Royal Society A*, (july).

PERSON, M. J., ELLIOT, J. L., BOSH, A. S., et al., 2011, "Constraints On The Size Of KBO (50000) Quaoar From A Single-chord Stellar Occultation". In: *American Astronomical Society Meeting Abstracts #218*, v. 218, *American Astronomical Society Meeting Abstracts*, p. 224.12, maio.

PUGET, P., STADLER, E., DOYON, R., et al., 2004, "WIRCam: the infrared wide-field camera for the Canada-France-Hawaii Telescope". In: Moorwood, A. F. M., Iye, M. (Eds.), *Ground-based Instrumentation for Astronomy*, v. 5492, *Society of Photo-Optical Instrumentation Engineers (SPIE) Conference Series*, pp. 978–987, set. doi: 10.1117/12.551097.

RODRÍGUEZ, A., MORGADO, B. E., CALLEGARI JR., N., 2023, "Dynamical characterization of the 6/1 mean motion resonance between Quaoar's ring and Weywot", *Monthly Notices of the Royal Astronomical Society*, v. 525, n. 3 (08), pp. 3376–3383. ISSN: 0035-8711. doi: 10.1093/mnras/stad2413. Disponível em: <https://doi.org/10.1093/mnras/stad2413>.

ROMMEL, F. L., BRAGA-RIBAS, F., ORTIZ, J. L., et al., 2023, "A large topographic feature on the surface of the trans-Neptunian object (307261) 2002 MS$_4$ measured from stellar occultations", Astron. Astrophys., 678:A167. doi: 10.1051/0004-6361/202346892.

ROQUES, F., MONCUQUET, M., SICARDY, B., 1987, "Stellar occultations by small bodies - Diffraction effects", Astron. J., v. 93 (jun.), pp. 1549–1558. doi: 10.1086/114438.

ROUSSELOT, P., KORSUN, P. P., KULYK, I., et al., 2016, "A long-term follow up of 174P/Echeclus", Mon. Not, Roy. Astron. Soc., v. 462 (nov.), pp. S432–S442. doi: 10.1093/mnras/stw3054.

ROUSSELOT, P., KRYSZCZYŃSKA, A., BARTCZAK, P., et al., 2021, "New constraints on the physical properties and dynamical history of Centaur 174P/Echeclus", Mon. Not, Roy. Astron. Soc., v. 507, n. 3 (nov.), pp. 3444–3460. doi: 10.1093/mnras/stab2379.

RUPRECHT, J. D., BOSH, A. S., PERSON, M. J., et al., 2015, "29 November 2011 stellar occultation by 2060 Chiron: Symmetric jet-like features", *Icarus*, v. 252, pp. 271–276. doi: 10.1016/j.icarus.2015.01.015.

SALO, H., SICARDY, B., MONDINO-LLERMANOS, A., et al., 2021a, "Resonance confinement of collisional particle rings". In: *European Planetary Science Congress*, pp. EPSC2021–338, set.a. doi: 10.5194/epsc2021-338.

SALO, H., SICARDY, B., MONDINO-LLERMANOS, A., et al., 2021b, "Resonance confinement of collisional particle rings". In: *European Planetary Science Congress*, pp. EPSC2021–338, set.b. doi: 10.5194/epsc2021-338.

SANTOS-SANZ, P., ORTIZ, J. L., SICARDY, B., et al., 2021, "The 2017 May 20 stellar occultation by the elongated centaur (95626) 2002 GZ_{32}", Mon. Not, Roy. Astron. Soc., v. 501, n. 4 (mar.), pp. 6062–6075. doi: 10.1093/mnras/staa3881.

SARID, G., VOLK, K., STECKLOFF, J. K., et al., 2019, "29P/Schwassmann–Wachmann 1, A Centaur in the Gateway to the Jupiter-family Comets", *The Astrophysical Journal Letters*, v. 883, n. 1 (sep), pp. L25. doi: 10.3847/2041-8213/ab3fb3. Disponível em: <https://dx.doi.org/10.3847/2041-8213/ab3fb3>.

SCHAMBEAU, C. A., FERNÁNDEZ, Y. R., LISSE, C. M., et al., 2015, "A new analysis of Spitzer observations of Comet 29P/Schwassmann-Wachmann 1", Icarus, v. 260 (nov.), pp. 60–72. doi: 10.1016/j.icarus.2015.06.038.

SCOTT, N. J., HOWELL, S. B., GNILKA, C. L., et al., 2021, "Twin High-resolution, High-speed Imagers for the Gemini Telescopes: Instrument description and science verification results", *Frontiers in Astronomy and Space Sciences*, 8:138. doi: 10.3389/fspas.2021.716560.

SICARDY, B., ROQUES, F., BRAHIC, A., 1991, "Neptune's rings, 1983-1989: Ground-based stellar occultation observations I. Ring-like arc detections", Icarus, v. 89, n. 2 (fev.), pp. 220–243. doi: 10.1016/0019-1035(91)90175-S.

SICARDY, B., SALO, H., SOUAMI, D., et al., 2021, "Rings around small bodies: the 1/3 resonance is key". In: *European Planetary Science Congress*, pp. EPSC2021–91, set. doi: 10.5194/epsc2021-91.

SICKAFOOSE, A. A., BOSH, A. S., EMERY, J. P., et al., 2020, "Characterization of material around the centaur (2060) Chiron from a visible and near-infrared stellar occultation in 2011", *MNRAS*, v. 491, n. 3 (jan.), pp. 3643–3654. doi: 10.1093/mnras/stz3079.

SICKAFOOSE, A. A., LEWIS, M. C., 2024, "Numerical Simulations of (10199) Chariklo's Rings with a Resonant Perturber", *The Planetary Science Journal*, v. 5, n. 2 (feb), pp. 32. doi: 10.3847/PSJ/ad151c. Disponível em: <https://dx.doi.org/10.3847/PSJ/ad151c>.

SICKAFOOSE, A. A., LEVINE, S. E., BOSH, A. S., et al., 2023, "Material Around the Centaur (2060) Chiron from the 2018 November 28 UT Stellar Occultation", *arXiv e-prints*, art. arXiv:2310.16205. doi: 10.48550/arXiv.2310.16205.

STANSBERRY, J., GRUNDY, W., BROWN, M., et al., 2008, "Physical Properties of Kuiper Belt and Centaur Objects: Constraints from the Spitzer Space Telescope". In: Barucci, M. A., Boehnhardt, H., Cruikshank, D. P., et al. (Eds.), *The Solar System Beyond Neptune*, pp. 161–179. doi: 10.48550/arXiv.astro-ph/0702538.

STANSBERRY, J. A., VAN CLEVE, J., REACH, W. T., et al., 2004, "Spitzer Observations of the Dust Coma and Nucleus of 29P/Schwassmann-Wachmann 1", Astrophys. J. Suppl., v. 154, n. 1 (set.), pp. 463–468. doi: 10.1086/422473.

SYKES, M. V., WALKER, R. G., 1991, "Constraints on the Diameter and Albedo of 2060 Chiron", *Science*, v. 251, n. 4995 (fev.), pp. 777–780. doi: 10.1126/science.251.4995.777.

TAKEDA, T., IDA, S., 2001, "Angular Momentum Transfer in a Protolunar Disk", *The Astrophysical Journal*, v. 560, n. 1 (oct), pp. 514. doi: 10.1086/322406. Disponível em: <https://dx.doi.org/10.1086/322406>.

TANGA, P., PAUWELS, T., MIGNARD, F., et al., 2023, "Gaia Data Release 3. The Solar System survey", Astron. Astrophys., 674:A12. doi: 10.1051/0004-6361/202243796.

THOMAS, P., HELFENSTEIN, P., 2020, "The small inner satellites of Saturn: Shapes, structures and some implications", Icarus, 344:113355. doi: 10.1016/j.icarus.2019.06.016.

TSIGANIS, K., GOMES, R., MORBIDELLI, A., et al., 2005, "Origin of the orbital architecture of the giant planets of the Solar System", *Nature*, v. 435, n. 7041 (maio), pp. 459–461. doi: 10.1038/nature03539.

VACHIER, F., BERTHIER, J., MARCHIS, F., 2012, "Determination of binary asteroid orbits with a genetic-based algorithm", Astron. Astrophys., 543:A68. doi: 10.1051/0004-6361/201118408.

VAN BELLE, G. T., 1999, "Predicting Stellar Angular Sizes", Publ. Astron. Soc. Pacific, v. 111, n. 766 (dez.), pp. 1515–1523. doi: 10.1086/316462.

VERA C. RUBIN OBSERVATORY LSST SOLAR SYSTEM SCIENCE COLLABORATION, JONES, R. L., BANNISTER, M. T., et al., 2021, "The Scientific Impact of the Vera C. Rubin Observatory's Legacy Survey of Space and Time (LSST) for Solar System Science". In: *Bulletin of the American Astronomical Society*, v. 53, p. 236, maio. doi: 10.3847/25c2cfeb.d8909f28.

VOLK, K., MALHOTRA, R., 2008, "The Scattered Disk as the Source of the Jupiter Family Comets", *The Astrophysical Journal*, v. 687, n. 1 (nov), pp. 714. doi: 10.1086/591839. Disponível em: <https://dx.doi.org/10.1086/591839>.

WEISSMAN, P. R., CHESLEY, S. R., CHOI, Y. J., et al., 2006, "Motion of the Activity Source Associated with Active Centaur 174P/Echeclus (60558)". In: *AAS/Division for Planetary Sciences Meeting Abstracts #38*, v. 38, *AAS/Division for Planetary Sciences Meeting Abstracts*, p. 37.06, set.

WOOD, J., HORNER, J., HINSE, T. C., et al., 2017, "The Dynamical History of 2060 Chiron and Its Proposed Ring System", *The Astronomical Journal*, v. 155, n. 1 (dec), pp. 2. doi: 10.3847/1538-3881/aa9930. Disponível em: <https://dx.doi.org/10.3847/1538-3881/aa9930>.

Appendix A

The two rings of (50000) Quaoar

Astronomy & Astrophysics

The two rings of (50000) Quaoar

C. L. Pereira[1,2], B. Sicardy[3], B. E. Morgado[4,1,2], F. Braga-Ribas[5,1,2], E. Fernández-Valenzuela[6,7],
D. Souami[3,8,9,10,★], B. J. Holler[11], R. C. Boufleur[1,2], G. Margoti[5], M. Assafin[4,2], J. L. Ortiz[7],
P. Santos-Sanz[7], B. Epinat[12,13], P. Kervella[3], J. Desmars[14,15], R. Vieira-Martins[1,2], Y. Kilic[16,17],
A. R. Gomes Júnior[18,19,2], J. I. B. Camargo[1,2], M. Emilio[20,1,5], M. Vara-Lubiano[7], M. Kretlow[7,21,22],
L. Albert[23,24], C. Alcock[25], J. G. Ball[26], K. Bender[27], M. W. Buie[28], K. Butterfield[29], M. Camarca[30],
J. H. Castro-Chacón[31], R. Dunford[29], R. S. Fisher[32], D. Gamble[29,33], J. C. Geary[25], C. L. Gnilka[34],
K. D. Green[35], Z. D. Hartman[26], C.-K. Huang[36], H. Januszewski[13], J. Johnston[37], M. Kagitani[38], R. Kamin[29],
J. J. Kavelaars[39], J. M. Keller[37], K. R. de Kleer[30], M. J. Lehner[36], A. Luken[32], F. Marchis[40,41], T. Marlin[30],
K. McGregor[42], V. Nikitin[29,43], R. Nolthenius[27], C. Patrick[29], S. Redfield[42], A. W. Rengstorf[44],
M. Reyes-Ruiz[31], T. Seccull[26], M. F. Skrutskie[45], A. B. Smith[26], M. Sproul[46], A. W. Stephens[26],
A. Szentgyorgyi[25], S. Sánchez-Sanjuán[31], E. Tatsumi[47,48], A. Verbiscer[45], S.-Y. Wang[36], F. Yoshida[49,50],
R. Young[51], and Z.-W. Zhang[36]

(Affiliations can be found after the references)

Received 9 March 2023 / Accepted 17 April 2023

ABSTRACT

Context. Quaoar is a classical trans-Neptunian object (TNO) with an area-equivalent diameter of 1100 km and an orbital semi-major axis of 43.3 astronomical units. Based on stellar occultations observed between 2018 and 2021, an inhomogeneous ring (Q1R, i.e., Quaoar's first ring) has been detected around this body.

Aims. A new stellar occultation by Quaoar was observed on August 9, 2022, with the aim of improving Quaoar's shape models and the physical parameters of Q1R, while searching for additional material around the body.

Methods. The occultation provided nine effective chords across Quaoar, pinning down its size, shape, and astrometric position. Large facilities, such as Gemini North and the Canada-France-Hawaii Telescope (CFHT), were used to obtain high acquisition rates and signal-to-noise ratios. The light curves were also used to characterize the Q1R ring (radial profiles and orbital elements).

Results. Quaoar's elliptical fit to the occultation chords yields the limb with an apparent semi-major axis of 579.5 ± 4.0 km, apparent oblateness of 0.12 ± 0.01, and area-equivalent radius of 543 ± 2 km. Quaoar's limb orientation is consistent with Q1R and Weywot orbiting in Quaoar's equatorial plane. The orbital radius of Q1R is refined to a value of 4057 ± 6 km. The radial opacity profile of the more opaque ring profile follows a Lorentzian shape that extends over 60 km, with a full width at half maximum (FWHM) of $\sim$5 km and a peak normal optical depth of 0.4. Besides the secondary events related to the already reported rings, new secondary events detected during the August 2022 occultation in three different data sets are consistent with another ring around Quaoar with a radius of 2520 ± 20 km, assuming the ring is circular and co-planar with Q1R. This new ring has a typical width of 10 km and a normal optical depth of $\sim$0.004. Just as Q1R, it also lies outside Quaoar's classical Roche limit.

Key words. methods: data analysis – methods: observational – techniques: photometric – Kuiper belt objects: individual: Quaoar – planets and satellites: rings

1. Introduction

In the last decade, three ring systems have been discovered around minor bodies in the outer Solar System: the Centaur Chariklo (Braga-Ribas et al. 2014), the dwarf planet Haumea (Ortiz et al. 2017), and the trans-Neptunian object (TNO) (50000) Quaoar (Morgado et al. 2023). Dense material has also been detected around the Centaur Chiron (Ruprecht et al. 2015; Ortiz et al. 2015; Sickafoose et al. 2020). However, the nature of this material, namely, whether it is a permanent or transient ring or a dust shell, is still a matter of debate.

Quaoar's ring, referred to as Q1R hereafter, was detected during several stellar occultations observed between 2018 and

2021 (Morgado et al. 2023). Q1R has a radius of about 4100 km with significant azimuthal variations in the optical depth, ranging between 0.004 and 0.1–0.7, and in width, ranging from 5 km to 300 km. Like Chariklo's and Haumea's rings, Quaoar's Q1R ring orbits close to the 1/3 spin-orbit resonance (SOR) with the central body, suggesting a link between this resonance and the ring (Salo et al. 2021; Sicardy et al. 2021; Morgado et al. 2023). Meanwhile, a unique property of Q1R is its location, which is far outside Quaoar's classical Roche limit. This limit is estimated to be at 1780 km from the body center, assuming particles with a bulk density of $\rho = 0.4 \, \mathrm{g\,cm^{-3}}$. Outside the Roche limit, rings should accrete into satellites over timescales of less than 100 years (Kokubo et al. 2000; Takeda & Ida 2001). However, collisions more elastic than previously considered for Saturn's ring may maintain a ring unaccreted at distances greater than the Roche limit (Morgado et al. 2023). The 6/1

mean-motion resonance (MMR) with Quaoar's satellite, Weywot, may contribute to the confinement of the ring since the satellite's eccentricity creates an equilibrium region capable of concentrating ring material in an arc over a longitude interval (Morgado et al. 2023). The confinement of the rings may also be due to the presence of putative "shepherd" satellites.

This Letter presents observations of a stellar occultation by Quaoar that occurred on August 9, 2022. This event was observed in Hawaii, the continental US, and Mexico. The high image acquisition rate and high signal-to-noise-ratios (S/Ns) obtained at Mauna Kea with the Alopeke camera at the Gemini North 8.1-m telescope and Wide-field InfraRed Camera (WIRCam) at the Canada-France-Hawaii 3.6-m Telescope (CFHT) allowed the dense part of Q1R to be radially resolved and its optical depth to be probed in the r', z' and Ks bands. Furthermore, this event revealed a new ring around Quaoar, hereafter called the Q2R (Quaoar's second ring).

2. Prediction and observation

The occultation of August 9, 2022 was predicted within the framework of the European Research Council (ERC) Lucky Star project[1]. The campaign was managed by the Occultation Portal website[2] described in Kilic et al. (2022). The occultation shadow crossed the continental United States, Mexico, and the Hawaiian archipelago with a geocentric shadow velocity of 17.6 km s^{-1}. The shadow path and the sites involved in the observation campaign are shown in Appendix C.1. More details on the occulted star and Quaoar are provided in Table 1.

Table B.1 summarizes the observational circumstances. Among the stations, CFHT was equipped with the WIRCam (Puget et al. 2004) at $2.15 \,\mu\text{m}$ (Ks-band) with an 8.8 Hz acquisition rate. The nearby Gemini North telescope used the Alopeke instrument (Scott et al. 2021) to simultaneously record the event with the z'(947 nm) and r'(620 nm) bands at a 10 Hz cadence. The images at the Tohoku University Haleakala Observatory (TUHO) in Hawaii and at the Transneptunian Automated Occultation Survey (TAOS II) in Baja California (Mexico) were taken with no filter to maximize the S/N. Q2R was not detected in these observations, likely due to insufficient S/N values. At the University of California, Santa Cruz (UCSC – California, US), the Dunrhomin Observatory (Colorado, US), Sommers-Bausch Observatory (Colorado, US), Nederland (Colorado, US), and a mobile station in Bonny Doon Eco Reserve (California, US), only the main body was recorded due to a low S/N.

3. Data analysis

The data sets were analyzed using the standard photometry procedures of the Platform for Reduction of Astronomical Images Automatically (PRAIA, Assafin et al. 2011). The flux of the occulted star was corrected by the flux of nearby reference stars to account for sky transparency variations and was normalized to the total star+Quaoar flux outside the occultation.

The Stellar Occultation Reduction and Analysis package (SORA, Gomes-Júnior et al. 2022) was used to derive the ingress and egress instants of the occultation by the main body, assuming an opaque body without atmosphere. More details are presented in Appendix A. The extremities of the resulting chords were finally used to fit an elliptical model to Quaoar's limb at the moment of the occultation.

---

[1] https://lesia.obspm.fr/lucky-star
[2] https://occultation.tug.tubitak.gov.tr

Table 1. More details about the occulted star and Quaoar.

Occulted star	
Epoch	2022-08-09 06:34:04 UTC
Source ID	*Gaia* DR3 4098214367441486592
Star position	$\alpha_\star = 18^\text{h}21^\text{m}42^\text{s}86965 \pm 0.2404$ mas
at epoch [1]	$\delta_\star = -15°12'45''9639 \pm 0.2191$ mas
Magnitudes [2]	$G = 15.3$; $RP = 14.1$; $BP = 16.8$;
	$J = 12.0$; $H = 11.0$; $K = 10.7$
Apparent diameter [3]	0.44 mas/1.33 km
RUWE [4]	0.959
(50000) Quaoar	
Ephemeris version	NIMAv16 [5]
Geocentric distance	41.983157 au
Apparent magnitude	$V = 18.8$
Mass [6]	$(1.2 \pm 0.05) \times 10^{21}$ kg
Rotation period [7]	17.6788 ± 0.0004 h
Weywot's orbital pole [6]	
RA	$17^\text{h}44^\text{m} \pm 40^\text{m}$
Dec	$+50° \pm 6°$

Notes. [1]The star position was taken from the *Gaia* Data Release 3 (GDR3) star catalog (Gaia Collaboration 2023) and is propagated to the event epoch using the formalism of Butkevich & Lindegren (2014) applied with SORA (Gomes-Júnior et al. 2022). [2]*J*, *H*, and *K* from the NOMAD catalog (Zacharias et al. 2004). [3]Limb-darkened angular diameter estimated using a fit of the spectral energy distribution of the star with Castelli & Kurucz (2003) atmosphere models, with the reddening definition of Fitzpatrick (1999). [4]Renormalized unit weight error (Lindegren et al. 2021). [5]Obtained from the Numerical Integration of the Motion of an Asteroid (NIMA, Desmars et al. 2015), based on astrometric positions derived from previous stellar occultations and the Minor Planet Center (MPC) database, available at https://lesia.obspm.fr/lucky-star/obj.php?p=958 [6]Obtained from the method of Vachier et al. (2012). [7]Assuming the double-peaked light curve from Ortiz et al. (2003).

In the case of rings, the events were fitted using the square box model described in Appendix E and pipelines based on the SORA package. This provides the radial width of the ring W_r (assuming a circular ring), its normal opacity, p_N, and normal optical depth, τ_N, from which the equivalent width, $E_p = W_r p_N$, and equivalent depth, $A_\tau = W_r \tau_N$, are derived.

In the case of the CFHT and Gemini data, the acquisition rate and S/N were high enough to provide resolved profiles of the dense part of Q1R. Then, E_p and A_τ can be obtained directly from the numerical calculations of the integrals $A_\tau = \int_{W_r} (v_r \tau_N) dt$ and $E_p = \int_{W_r} (v_r p_N) dt$ (i.e., without using the square model described above), v_r is the star velocity perpendicular to the ring, measured in the ring plane.

The dense part of Q1R has a radial profile reminiscent of the Saturnian F-ring core (Bosh et al. 2002). More precisely, it is consistent with a Lorentzian shape used here to provide the full width at half maximum (FWHM) of the profile and the event's timing, from which its location relative to Quaoar is obtained.

4. Results

4.1. Main body

The event on August 9, 2022 provided ten chords across Quaoar's main body. However, Gemini used a dual camera at two wavelengths, resulting in nine effective chords across the

Table 2. Retrieved parameters of Quaoar's body and its rings.

Quaoar's limb fitting	
Apparent semi-major axis	$a' = 579.5 \pm 4.0$ km
Apparent oblateness	$\epsilon' = 0.12 \pm 0.01$
Position angle	$P = 345.2 \pm 1.2$ deg
Ephemeris offset	$f_c = -24.7 \pm 2.0$ km
	$g_c = -13.9 \pm 2.1$ km
R_{equiv}	543 ± 2 km
χ^2 per degree of freedom	0.986
Quaoar's geocentric position (ICRS)	$\alpha = 18^{\text{h}}21^{\text{m}}42\overset{\text{s}}{.}8677703 \pm 0.249$ mas
	$\delta = -15°12'45''.829691 \pm 0.230$ mas
Q1R's preferred pole position (ICRS) [1]	$\alpha_P = 17^{\text{h}}19^{\text{m}}16\overset{\text{s}}{.}8 \pm 55\overset{\text{s}}{.}2$
	$\delta_P = +53°27' \pm 18'$
Q1R's geometry	
Radius	$4,057 \pm 6$ km
Opening angle	$B = -20.0 \pm 0.3$ deg
Position angle	$P = 350.2 \pm 0.2$ deg
χ^2 per degree of freedom	1.633
Q2R's geometry [2]	
Radius	2520 ± 20 km

Notes. Quaoar's limb, Quaoar's geocentric position, and Q1R's geometry are given at epoch August 9th, 2022, 06:34:03.560 UTC. The fits use the star position and the NIMAv16 ephemeris for Quaoar (Table 1). [1]The preferred solution is co-planar with Quaoar's equatorial plane and Weywot's orbit within 5 ± 7 deg. The complementary position $\alpha_P = 10^{\text{h}}00^{\text{m}} \pm 05^{\text{m}}$ and $\delta_P = +79°21' \pm 08'$, is not considered here as it provides a less satisfactory fit to the Q1R detections and yields an inclination of 45 deg with respect to Weywot's orbit, see Sect. 4.2 [2]Assuming a circular ring co-planar with Q1R. The error bar for the Q2R ring radius may be underestimated since we only have two effective detections, and several parameters were assumed.

body, that is, $N = 18$ chord extremities with the timings listed in Table A.1.

We used the SORA package to fit an ellipse to those extremities projected in the sky plane. This ellipse is defined by $M = 5$ parameters and the fit has $N - M = 13$ degrees of freedom. The fitted parameters are the ephemeris offsets f_c and g_c to apply to Quaoar's center in right ascension and declination, respectively, the apparent semi-major axis a' of the limb, its apparent oblateness $\epsilon' = (a' - b')/a'$, where b' is the apparent semi-minor axis of the limb, and P is the position angle of b'. The elliptical fit also considers a σ_{model}, which is the uncertainty of the ellipse associated with the existence of putative topographic features on the surface of Quaoar. From the methodology presented by (Johnson & McGetchin 1973), we estimated that Quaoar might support topographic features of about 5 km, given Quaoar's density $\rho = 1.99\,\text{g cm}^{-3}$ and strength $S = 0.0303 \times 10^9$ dynes cm^{-2}, consistent with an ice-rich composition. The standard deviation of the observed radial residuals is ~ 8 km, providing an upper limit for topographic features consistent with this prediction. Considering the equivalent radius in area as 542 km, this corresponds to 1.5%. The fit results are listed in Table 2. The chords and the best-fitting elliptical limb are plotted in Fig. 1, with more details given in Fig. A.2.

4.2. Ring Q1R

The Q1R ring was detected on both sides of the main body in the Gemini and CFHT light curves, and their physical properties
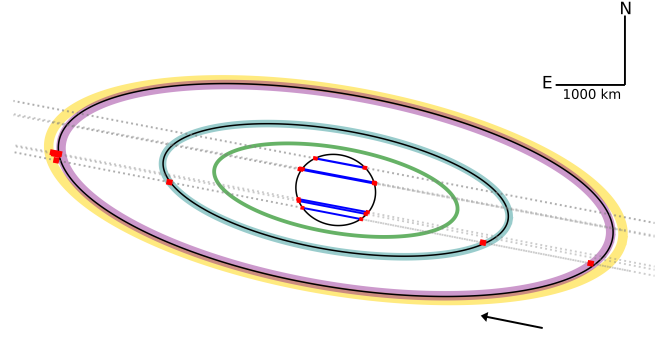
Fig. 1. Representation of our results on Quaoar's shape (center) and the detection of the two rings Q1R (outer ring) and Q2R (inner ring). The red segments correspond to the 1-σ error bars on the particular events. The orbit of Q1R is determined from a simultaneous fit using the present work and previous detections of 2018, 2019, 2020, and 2021 reported by Morgado et al. (2023) (see Sect. 4.2). The solution for the orbit of the new Q2R ring assumes that this ring is co-planar and concentric with Q1R. The central part of the plot (occultation by the solid body) is enlarged in Fig. A.2. In yellow, we show the 1/3 SOR resonance with Quaoar, and in teal is the 5/7 SOR resonance (considering the double-peaked rotation period). The purple ellipse represents 6/1 MMR with Weywot, and the green ellipse presents the expected Roche limit, considering particles with a bulk density of $\rho = 0.4\,\text{g cm}^{-3}$. The arrow shows the star's motion relative to Quaoar. Note: the orbital radius of Weywot is about three times larger than that of Q1R, and thus it is not shown in this representation.

were determined as described in Sect. 3. Although the detections of the dense part of the Q1R in the Gemini and CFHT light curves indicate the presence of diffuse material around the ring, the quality of the TAOS II and TUHO light curves only allows for the narrow and dense part of the ring to be detected. Therefore, the parameters E_p and A_τ were determined by the square box model for these data.

Due to the low optical depth of the Q1R segment intercepted before the closest approach, only the light curves obtained at Gemini and CFHT have sufficient S/N for detection (see an example in Fig. 2 and more details in Figs. 3, D.1, E.1, and E.2). The Gemini detection in the r' bandpass seems more sharply defined than its counterpart in z', but this effect remains marginal considering the S/N. The CFHT light curve shows a drop simultaneously, but it may be affected by a seeing deterioration that compromises an accurate determination of the ring boundaries. Even so, the central times of the Gemini and CFHT detections are all consistent at the 1-σ level. The parameters of Q1R for all the detections are presented in Table E.1.

We have combined the data from this work and the previous observations to improve the Q1R orbital parameters, assuming a fixed ring pole orientation between 2018 and 2022, as per Morgado et al. (2023). We tested a range of pole orientations and ring radii using a χ^2 statistic, resulting in two complementary solutions presented in Table 2. The preferred solution has a χ^2 per degree of freedom $\chi^2_{\text{pdf}} = 1.6$ and shows a better agreement with observations than the mirror solution with $\chi^2_{\text{pdf}} = 4.1$. Moreover, the preferred solution is co-planar with Weywot's orbit to within 5 ± 7 deg, as expected from a primordial disk surrounding Quaoar that evolved into a ring and formed its satellite, while the mirror solution is inclined by 45 ± 7 deg with respect to Weywot's orbit.

The position angles of Quaoar's projected pole (345.2 ± 1.2 deg) and Q1R (350.2 ± 0.2 deg) are misaligned by ~ 5 deg (Table 2). Thus, our results are consistent with Q1R orbiting
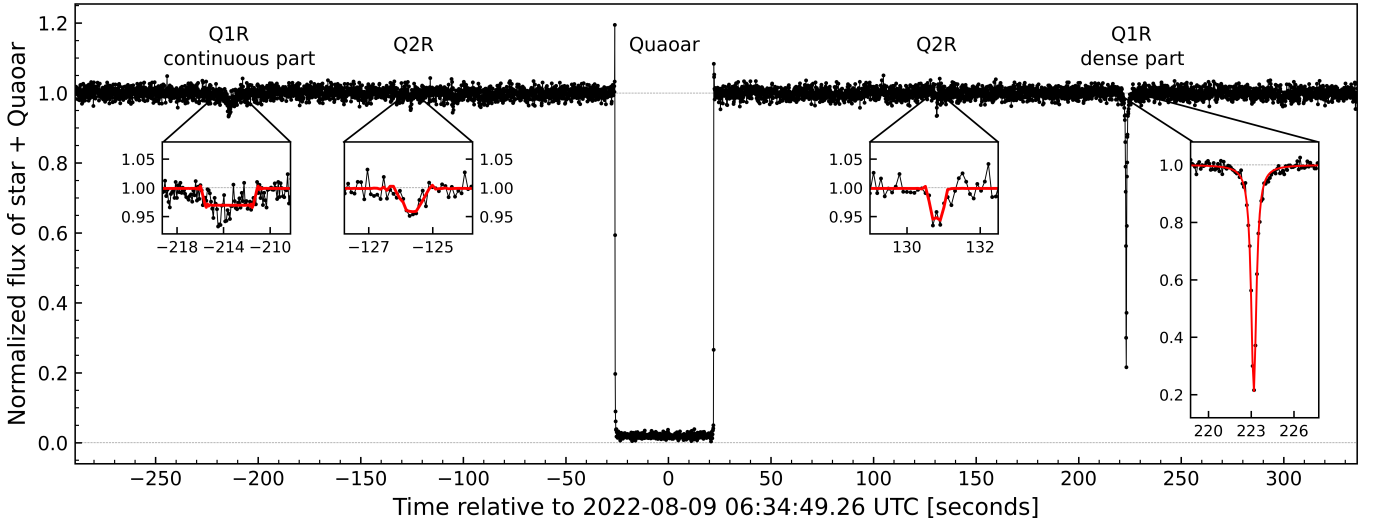
Fig. 2. Detection of Q1R, Q2R, and the main body in the Gemini (z') light curve. The normalized flux is plotted in black vs. time (UTC), while the best-fitting models are over-plotted in red. The shallow events caused by Q1R (ingress) and Q2R (ingress and egress) are fitted by a square model. A Lorentzian function fits the dense part of Q1R at egress; see Sect. 3. The spikes observed during the disappearance and the re-appearance of the star behind Quaoar stem from the diffraction by the sharp opaque limb of the body. Note: there is a variation in the flux close to −110 and 290 s, caused by sudden variations in the seeing, and they can be neglected. More detailed views of Q1R and Q2R obtained at other telescopes are displayed in Figs. 3, D.1, E.1, and E.2.

close to Quaoar's equatorial plane, assuming that the body is an oblate spheroid. Part of this misalignment could stem from the fact that Quaoar is a triaxial ellipsoid (or a body with a more complex shape). Hence, the position angle of Quaoar's limb does not necessarily coincide with the position angle of Quaoar's pole.

4.3. The discovery of a new ring around Quaoar

The unique photometric quality of the Gemini and CFHT data allowed for the detection of additional material around Quaoar (Fig. 2). These data sets reveal additional secondary events symmetrically located with respect to Quaoar (Fig. 3). Two such events are simultaneously detected in the Gemini z'-band and CFHT Ks-band light curves before the closest approach, with detections reaching around 5.5σ and 5.2σ, respectively. Conversely, the light curves display simultaneous events after the closest approach with significant detections, standing at 5.7σ, 3.7σ, and 4.7σ for the Gemini z', Gemini r', and CFHT data sets, respectively. Assuming that the light curves have a normal distribution, the probability that individual points of equivalent width $E_p(3\sigma) > 12$ km occur randomly in each light curve is $p \approx 1.4 \times 10^{-3}$, with p approaching zero for values larger than E_p. While the two light curves of the Gemini instrument may be correlated as they were taken at the same telescope, the Gemini and CFHT data are independent in terms of fast-seeing fluctuations. Using Poisson statistics, we estimate that the probability that the simultaneous events in the Gemini and CFHT data occur randomly due to the seeing fluctuations is very low, with $p \approx 10^{-6}$.

Some dips in flux were observed in the vicinity of Q2R detection in the region after the closest approach (Fig. 3). These detections are at the detection limit of our data, so we cannot say whether these are due to seeing variations or additional structures. Furthermore, we do not observe counterparts of these dips in the region before the closest approach.

All these detections are consistent with a new circular ring (Q2R) co-planar and concentric with Q1R, orbiting at 2520 ±
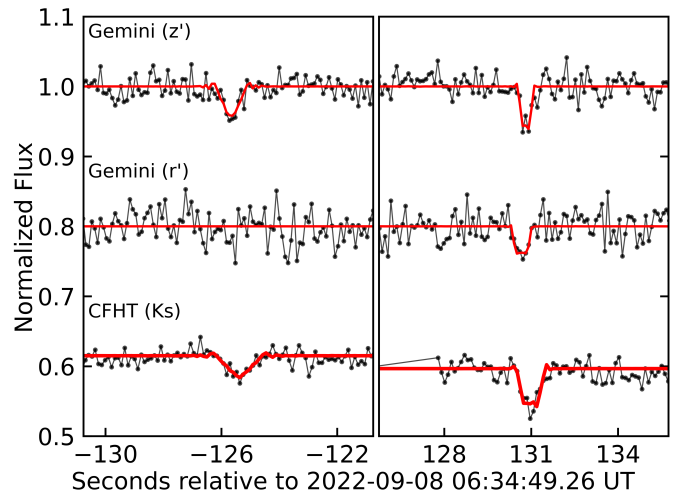
Fig. 3. Detection of the Q2R ring in the Gemini and CFHT light curves. The data points are plotted in black, and the red lines are the square box model fits derived from the quantities listed in Table E.1. An arbitrary offset was applied in the vertical direction for clarity. The time axis is relative to August 9, 2022 at 06:34:49.26 UTC, the time of the closest approach of Mauna Kea to Quaoar's shadow center.

20 km from Quaoar (Table 2). The radial width, optical depth, equivalent width, and equivalent depth of Q2R are listed in Table E.1. They were obtained as described in Appendix E.

5. Discussion and conclusions

The stellar occultation of August 9th, 2022 provided nine effective occultation chords obtained in Hawaii, Mexico, and the continental United States. They constrained Quaoar's shape, providing an apparent semi-major axis of $a' = 579.5 \pm 4.0$ km, an apparent oblateness $\epsilon' = 0.12 \pm 0.01$, and an area-equivalent radius of $R_{equiv} = a'\sqrt{1-\epsilon'} = 543 \pm 2$ km. Using an absolute magnitude of $H_V = 2.73 \pm 0.06$ (Fornasier et al. 2013), this yields

a geometric albedo of $p_V = 0.124 \pm 0.006$. Our value of R_{equiv} differs from that of Braga-Ribas et al. (2013), 555.0 ± 2.5 km, by about 12 km, that is, at the 4-σ level. This difference could be evidence that Quaoar is not an oblate spheroid, but rather a triaxial ellipsoid or a body with a more complex shape; alternatively, it may be caused by a change in the aspect-angle since 2011, as observed from Earth.

The continuous region and the dense part of Q1R were detected during this event. The dense part was radially resolved and showed a Lorentzian profile reminiscent of Saturn's F ring (Bosh et al. 2002) or Neptune's ring arcs (Nicholson et al. 1990; Sicardy et al. 1991). This contrasts with the sharp edges observed for Chariklo's main ring C1R (Bérard et al. 2017; Morgado et al. 2021). The dense part of Q1R is detected over a radial width of ~60 km with a peak optical depth of $\tau_N \approx 0.4$, an FWHM Lorentzian width of 5 km and an equivalent width E_p of around 2 km (see Table E.1). The values presented here are more precise than (but consistent with) those published by Morgado et al. (2023).

The detections of the dense part of Q1R in 2021 imply a minimum arc length of 365 km, corresponding to an azimuthal extension of about 5.1 deg (Morgado et al. 2023). The detections from CFHT, Gemini, TUHO, and TAOS II in 2022 (Figs. E.1, E.2) suggest a minimum arc-length of 226 km or ~3.2 deg. Since 2011, we have obtained 19 cuts of the Q1R with a sufficient S/N to detect the densest region. The limited azimuthal extent of the two detections of the dense regions means that they could both be parts of the same arc-like structure. If this structure was detected two times among the 19 cuts, then its extent can be estimated using Poisson statistics. This analysis yields an arc length with a 70% chance of falling between 18 and 72 deg. In this case, all of the detections in either 2021 or 2022 would each be correlated samples of one part of this arc.

The more tenuous component of Q1R is radially resolved and shows no marked structures, being consistent with a square model within our S/N limits. The best light curves (Gemini and CFHT) provide a typical width of 80–100 km and a typical normal optical depth of 0.003 (and, thus, an equivalent width of ~0.3 km) for that component at the longitude where it was detected (Table E.1).

Our detections, combined with those reported by Morgado et al. (2023), improved the orbital elements of Q1R. They are consistent with a circular ring of radius 4057.2 ± 5.8 km (Table 2) corresponding to about $7.5 \times$ Quaoar's area-equivalent radius R_{equiv}. This value coincides with the 6/1 MMR with Weywot (4020 ± 60 km) and within 3-σ of the 1/3 SOR with Quaoar (4200 ± 60 km), considering the double-peaked rotation period of 17.6788 ± 0.0004 h (Ortiz et al. 2003).

Our preferred solution for Q1R's orbital pole is consistent with this ring being co-planar with Weywot's orbit. Moreover, the apparent semi-major axes of Quaoar's limb and Q1R's orbit are aligned at the 4-σ level, suggesting that Q1R lies in Quaoar's equatorial plane, as expected from a colliding ring system (Kokubo et al. 2000).

Our data reveal a new ring (Q2R) around Quaoar. The detections are consistent with a circular ring of radius 2520 ± 20 km coplanar with Q1R (Table 2, Figs. 3 and 1). It has a typical width of 10 km, an optical depth of about 0.004, and an equivalent depth of about 0.04 km (see accurate values in Table E.1). Although closer to Quaoar than Q1R, Q2R is at $4.6 \times$ Quaoar's radius, also outside Quaoar's Roche limit, which is estimated to be around 1780 km, assuming the ring particle density as $\rho = 0.4$ g cm^{-3} (Morgado et al. 2023).

Using previously determined values for Quaoar's mass and rotation period (Table 1), we derived a 5/7 SOR radius of 2525 ± 35 km. This coincides with Q2R's radius, 2520 ± 20 km, to within the 1-σ error bars. Like the 1/3 SOR, the 5/7 SOR is a second-order resonance and, as such, may play an essential role in the confinement of Q2R. However, more solid determinations of Q2R's orbit and Quaoar's shape are required.

Table E.1 shows that differences in the equivalent widths of Q1R and Q2R are observed between the z', r', and Ks filters. The significance and interpretation of these differences require more analysis and will be discussed in a forthcoming publication. Moreover, the high S/N obtained at Gemini and CFHT will be used to detect or put a stringent upper limit on a putative atmosphere. Finally, the comparison of past (and possibly future) results derived from multi-chord occultations by Quaoar's main body will be used to constrain its shape better. This will be important for better understanding the dynamics of Quaoar's ring system, particularly under the effect of spin-orbit resonances with the body.

(SO2019A-003) and the Pico dos Dias Observatory (OP2019A-004) to improve the accuracy of the ephemeris NIMAv16.

References

Assafin, M., Vieira Martins, R., Camargo, J. I. B., et al. 2011, Gaia Follow-up Network for Solar System Objects, 85

Bérard, D., Sicardy, B., Camargo, J. I. B., et al. 2017, AJ, 154, 144

Bosh, A. S., Olkin, C. B., French, R. G., & Nicholson, P. D. 2002, Icarus, 157, 57

Braga-Ribas, F., Sicardy, B., Ortiz, J. L., et al. 2013, ApJ, 773, 26

Braga-Ribas, F., Sicardy, B., Ortiz, J. L., et al. 2014, Nature, 508, 72

Butkevich, A. G., & Lindegren, L. 2014, A&A, 570, A62

Castelli, F., & Kurucz, R. L. 2003, in Modelling of Stellar Atmospheres, eds. N. Piskunov, W. W. Weiss, & D. F. Gray, 210, A20

Cuzzi, J. N. 1985, Icarus, 63, 312

Desmars, J., Camargo, J. I. B., Braga-Ribas, F., et al. 2015, A&A, 584, A96

Elliot, J. L., French, R. G., Meech, K. J., & Elias, J. H. 1984, AJ, 89, 1587

Fitzpatrick, E. L. 1999, PASP, 111, 63

Fornasier, S., Lellouch, E., Müller, T., et al. 2013, A&A, 555, A15

Gaia Collaboration (Vallenari, A., et al.) 2023, https://doi.org/10.1051/0004-6361/202243940

Gomes-Júnior, A. R., Morgado, B. E., Benedetti-Rossi, G., et al. 2022, MNRAS, 511, 1167

Johnson, T., & McGetchin, T. 1973, Icarus, 18, 612

Kilic, Y., Braga-Ribas, F., Kaplan, M., et al. 2022, MNRAS, 515, 1346

Kokubo, E., Ida, S., & Makino, J. 2000, Icarus, 148, 419

Lindegren, L., Klioner, S. A., Hernández, J., et al. 2021, A&A, 649, A2

Morgado, B., Benedetti-Rossi, G., Gomes-Júnior, A. R., et al. 2019, A&A, 626, L4

Morgado, B. E., Sicardy, B., Braga-Ribas, F., et al. 2021, A&A, 652, A141

Morgado, B. E., Sicardy, B., Braga-Ribas, F., et al. 2023, Nature, 614, 239

Nicholson, P. D., Cooke, M. L., Matthews, K., Elias, J. H., & Gilmore, G. 1990, Icarus, 87, 1

Ortiz, J. L., Gutiérrez, P. J., Sota, A., Casanova, V., & Teixeira, V. R. 2003, A&A, 409, L13

Ortiz, J. L., Duffard, R., Pinilla-Alonso, N., et al. 2015, A&A, 576, A18

Ortiz, J. L., Santos-Sanz, P., Sicardy, B., et al. 2017, Nature, 550, 219

Puget, P., Stadler, E., Doyon, R., et al. 2004, in Ground-based Instrumentation for Astronomy, eds. A. F. M. Moorwood, & M. Iye, SPIE Conf. Ser., 5492, 978

Roques, F., Moncuquet, M., & Sicardy, B. 1987, AJ, 93, 1549

Ruprecht, J. D., Bosh, A. S., Person, M. J., et al. 2015, Icarus, 252, 271

Salo, H., Sicardy, B., Mondino-Llermanos, A., et al. 2021, European Planetary Science Congress, EPSC2021-338

Scott, N. J., Howell, S. B., Gnilka, C. L., et al. 2021, Front. Astron. Space Sci., 8, 138

Sicardy, B., Roques, F., & Brahic, A. 1991, Icarus, 89, 220

Sicardy, B., Salo, H., Souami, D., et al. 2021, European Planetary Science Congress, EPSC2021-91

Sickafoose, A. A., Bosh, A. S., Emery, J. P., et al. 2020, MNRAS, 491, 3643

Takeda, T., & Ida, S. 2001, ApJ, 560, 514

Vachier, F., Berthier, J., & Marchis, F. 2012, A&A, 543, A68

Zacharias, N., Monet, D. G., Levine, S. E., et al. 2004, Am. Astron. Soc. Meet. Abstr., 205, 48.15

[1] Observatório Nacional/MCTI, R. General José Cristino 77, CEP 20921-400 Rio de Janeiro, RJ, Brazil
e-mail: chrystianpereira@on.br

[2] Laboratório Interinstitucional de e-Astronomia – LIneA, Rio de Janeiro, RJ, Brazil

[3] LESIA, Observatoire de Paris, Université PSL, Sorbonne Université, Université de Paris, CNRS, 92190 Meudon, France

[4] Universidade Federal do Rio de Janeiro – Observatório do Valongo, Ladeira Pedro Antônio 43, CEP 20.080-090 Rio de Janeiro, RJ, Brazil

[5] Federal University of Technology – Paraná (UTFPR-Curitiba), Rua Sete de Setembro, 3165, CEP 80230-901 Curitiba, PR, Brazil

[6] Florida Space Institute, UCF, 12354 Research Parkway, Partnership 1 Building, Room 211, Orlando, FL, USA

[7] Instituto de Astrofísica de Andalucía – Consejo Superior de Investigaciones Científicas, Glorieta de la Astronomía S/N, 18008 Granada, Spain

[8] Departments of Astronomy, and of Earth and Planetary Science, 501, Campbell Hall, University of California, Berkeley, CA 94720, USA

[9] naXys, Department of Mathematics, University of Namur, Rue de Bruxelles 61, 5000 Namur, Belgium

[10] Université Côte d'Azur, Observatoire de la Côte d'Azur, CNRS, Laboratoire Lagrange, Bd de l'Observatoire, CS 34229, 06304 Nice Cedex 4, France

[11] Space Telescope Science Institute, Baltimore, MD, USA

[12] Aix Marseille Université, CNRS, CNES, LAM (Laboratoire d'Astrophysique de Marseille) UMR 7326, 13388 Marseille, France

[13] Canada-France-Hawaii Telescope, 65-1238 Mamalahoa Highway, Kamuela, HI 96743, USA

[14] Institut Polytechnique des Sciences Avancées IPSA, 63 boulevard de Brandebourg, 94200 Ivry-sur-Seine, France

[15] Institut de Mécanique Céleste et de Calcul des Éphémérides, IMCCE, Observatoire de Paris, PSL Research University, CNRS, Sorbonne Universités, UPMC Univ Paris 06, Univ. Lille, France

[16] Akdeniz University, Faculty of Sciences, Department of Space Sciences and Technologies, 07058 Antalya, Turkey

[17] TÜBİTAK National Observatory, Akdeniz University Campus, 07058 Antalya, Turkey

[18] Institute of Physics, Federal University of Uberlândia, Uberlândia-MG, Brazil

[19] UNESP – São Paulo State University, Grupo de Dinâmica Orbital e Planetologia, CEP 12516-410, Guaratinguetá, SP, Brazil

[20] Universidade Estadual de Ponta Grossa, O.A. – DEGEO, Ponta Grossa, PR, Brazil

[21] Internationale Amateursternwarte (IAS) e. V., Mittelstr. 6, 15749 Mittenwalde, Germany

[22] International Occultation Timing Association – European Section (IOTA/ES), Am Brombeerhag 13, 30459 Hannover, Germany

[23] Département de Physique and Observatoire du Mont-Mégantic, Université de Montréal, C.P. 6128, Succ. Centre-ville, Montréal, H3C 3J7 Québec, Canada

[24] Institut Trottier de Recherche sur les exoplanètes, Université de Montréal, Montreal, Canada

[25] Harvard-Smithsonian Center for Astrophysics, 60 Garden Street, Cambridge, MA 02138, USA

[26] Gemini Observatory/NSF's NOIRLab, Hilo, HI, USA

[27] Cabrillo College Astronomy, Aptos, CA, USA

[28] Southwest Research Institute, 1050 Walnut Street, Suite 300, Boulder, CO 80302, USA

[29] International Occultation Timing Association (IOTA), Topeka, KS, USA

[30] California Institute of Technology, 1200 E California Blvd, Pasadena, CA 91125, USA

[31] Universidad Nacional Autónoma de México, Instituto de Astronomía, AP 106, Ensenada 22800, BC, Mexico

[32] University of Oregon, Eugene, OR, USA

[33] CanCON – Canadian Collaborative Occultation Network, Canada

[34] NASA Ames Research Center, Moffett Field, California, USA & NASA Exoplanet Science Institute, Caltech/IPAC, Mail Code 100-22, Pasadena, CA, USA

[35] University of New Haven, Dept. of Mathematics and Physics, 300 Boston Post Road, West Haven, CT 06477, USA

[36] Academia Sinica Institute of Astronomy and Astrophysics, 11F of AS/NTU Astronomy-Mathematics Building, No.1, Sec. 4, Roosevelt Road, Taipei 10617, Taiwan, ROC

[37] University of Colorado, 2000 Colorado Avenue, Boulder, CO 80309, USA

[38] Planetary Plasma and Atmospheric Research Center, Graduate School of Science, Tohoku University, 6-3 Aramaki -aza-aoba, Aoba-ku, Sendai 980-8578, Japan

[39] Department of Physics and Astronomy, University of Victoria, Building, 3800 Finnerty Road, Victoria, BC V8P 5C2, Canada

[40] Unistellar, 5 allée Marcel Leclerc, bâtiment B, 13008 Marseille, France

[41] SETI Institute, Carl Sagan Center, Suite 200, 339 Bernardo Avenue, Mountain View, CA 94043, USA

[42] Astronomy Department and Van Vleck Observatory, Wesleyan University, Middletown, CT 06459, USA

[43] Research and Education Collaborative Occultation Network, USA

[44] Purdue University Northwest, Department of Chemistry and Physics, Hammond, IN, USA

[45] University of Virginia, Department of Astronomy, PO Box 400325, Charlottesville, VA 22904, USA

[46] Private Observatory, PA, USA

[47] Instituto de Astrofísica de Canarias, University of La Laguna, Tenerife, Spain

[48] Dept. Earth and Planetary Science, The University of Tokyo, Tokyo, Japan

[49] School of Medicine Department of Basic Sciences University of Occupational and Environmental Health, 1-1 Iseigaoka, Yahata, Kitakyusyu 807-8555, Japan

[50] Planetary Exploration Research Center, Chiba Institute of Technology, 2-17-1 Tsudanuma, Narashino, Chiba 275-0016, Japan

[51] Naylor Observatory, Lewisberry, PA, USA

Appendix A: Main body occultation and elliptical fit

The light curves obtained with the Gemini and CFHT telescopes present prominent diffraction signatures in the main body occultation mainly due to the high acquisition rate, the large wavelength, and high S/N of the light curves. During the occultation, Quaoar was at a geocentric distance of 41.983157 au, implying a Fresnel scale, $F = \sqrt{\lambda D/2}$, from 1.5 to 2.6 km, for visible to near-infrared (CFHT Ks-band) wavelengths, respectively. Considering the apparent velocity of the event as 17.57 km s^{-1} and the acquisition rate of the Gemini and CFHT instruments, we obtained a spatial resolution of these light curves of ∼1.8 km. These high-S/N light curves have a Fresnel diffraction effect on the same order of magnitude as the instrumental response (e.g., the integration time).
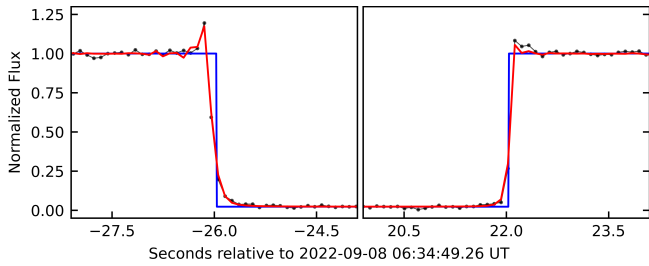
Fig. A.1. Gemini z' light curve (black dots) and the modeled light curve (red) considering the local normal star velocity, the wavelength and apparent star size. The geometric model is in blue. The normalized flux is plotted as a function of the seconds before and after the local closest approach (2022-08-09 06:34:49.26 UT).

With the limb-darkened angular diameter of the star estimated and considering the observation band pass and its FWHM, we also fit the local normal velocity ($v_\perp$). By minimizing the χ^2 statistic, we found the velocity and the ingress (egress) time that best explained the observed light curve. This was applied to the Gemini z'-band data since this was our best light curve. The radial velocities obtained are $v_\perp$ = 10.2 km s^{-1} and $v_\perp$ = 16.6 km s^{-1} for ingress and egress instants, respectively. The separation between the chords obtained from the Gemini and CFHT when projected onto the sky plane was about 160 meters, a value smaller than the star's apparent diameter. Therefore, the velocities were considered the same at both sites. This procedure resulted in an optimal fit for both diffraction spikes and the baseline occultation by the main body. Figure A.1 presents an example of this fit with the Gemini z' light curve plotted with the modeled curve.

Ingress and egress times for the main body occultation are presented in Table A.1. The instant uncertainties of the Gemini

Table A.1. Ingress and egress times for Quaoar's main body.

Site	Ingress (hh:mm:ss.s)	Egress (hh:mm:ss.s)
CFHT	06:34:23.34 (0.02)	06:35:11.42 (0.01)
Gemini (z')	06:34:23.29 (0.01)	06:35:11.29 (0.01)
Gemini (r')	06:34:23.27 (0.03)	06:35:11.28 (0.02)
TUHO	06:34:23.5 (0.2)	06:35:18.1 (0.2)
TAOS II	06:30:38.3 (0.2)	06:31:35.1 (0.1)
Dunrhomin	06:30:03.3 (0.4)	06:31:02.8 (0.9)
Sommers-Bausch	06:30:02.6 (0.2)	06:31:03.8 (0.5)
UCSC	06:31:20.3 (0.1)	06:32:00.9 (0.1)
Nederland	06:30:03.4 (0.5)	06:31:04.4 (0.8)
Bonny Doon	06:31:20.7 (0.4)	06:32:01.3 (0.4)

Notes. Times are in UT and the error bars in parentheses are in seconds and given at the 1-σ level. The significant differences in the CFHT and Gemini instants are due to the length of the chords, with the CFHT being ∼ 1 km longer than the Gemini, as expected from the limb.
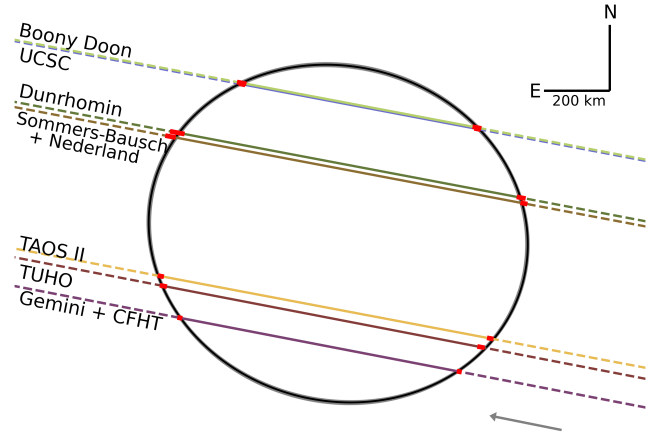

Fig. A.2. Close-up view of Fig. 1 shows the best elliptical fit (black ellipse) and ellipses within 1-σ region (grey) to the ten chords derived from the timings in Table A.1. The grey 1-σ fits differ only slightly from the black best-fit. The red segments represent the 1-σ error bars in the ingress and egress times. At this scale, the Gemini and CFHT chords are superimposed, and their error bars would be too small to be seen (i.e., they are here represented by red squares, much bigger than their actual sizes).

and CFHT light curves are limited by occultation modeling, not data quality. The elliptical fit parameters to the chord extremities are presented in Fig. A.2.

Appendix B: Observational circumstances

The observational circumstances for this occultation campaign are presented in Table B.1. We present in this work the analysis of ten data sets with positive detections for the main body, of which four are detections of the Q1R ring and three are detections of both the Q1R and Q2R rings. In addition, we have more eighteen sites that participated in the observation campaign, but reported cloudy skies. The target star was too faint for the setup in Woodside (CA, US) and Summerland BC, CA, even with 4 and 3 seconds of exposure, respectively; in addition, the Summerland data was acquired while clouds were drifting through the field.

Table B.1. Observational circumstances.

Site	Longitude [° ’ ”] Latitude [° ’ ”] Altitude [m]	Observers	Aperture (mm) Detector Filter	Exp. Time Cycle (s)	Status Light curve Dispersion
CFHT MaunaKea HI, US	-155 28 07.93 19 49 31.01 4,206.1	H. Januszewski M. Baril, B. Epinat T. Vermeulen	3,580 WIRCam Ks	0.113 0.113	Positive 0.013
Gemini-North MaunaKea HI, US	-155 28 08.6 19 49 26 4,213	T. Seccull A. Stephens	8,100 ’Alopeke r’ & z’	0.100 0.101	Positive z’: 0.012 r’: 0.022
TUHO Haleakala HI, US	-156 15 27 20 42 25.14 3,051.8	E. Tatsumi F. Yoshida M. Kagitani	600 ASI178MM None	1.500 1.634	Positive 0.098
TAOS II San Pedro Martir BC, MX	-115 27 47.88 31 02 36.26 2,824.8	J. H. Castro-Chacón S. Sánchez-Sanjuán	1,300 Andor Ixon 888 None	0.200 0.205	Positive 0.274
Dunrhomin Obs. Longmont CO, US	-105 09 46.57 40 15 08.46 1,592.8	M. Buie	280 QHY174M-GPS None	2 2	Positive 0.229
Sommers-Bausch Obs. Boulder CO, US	-105 15 47.09 40 00 13.32 1,645	J. Keller J. Johnston	508 QHY174M-GPS None	0.9 0.9	Positive 0.259
Nederland CO, US	-105 26 44.05 39 59 13.95 2,492.6	M. Skrutskie A. Verbiscer	200 QHY174M-GPS 570 nm	2 2	Positive 0.313
Bonny Doon Eco Reserve Santa Cruz CA, US	-122 08 18.62 37 03 03.12 488.4	K. Bender	203 Watec 910HX/RC None	0.260 0.260	Positive 0.538
UCSC Santa Cruz CA, US	-122 04 46.20 37 01 03.47 344.0	R. Nolthenius	203 Watec 910HX/RC None	0.500 0.534	Positive 0.556
Summerland BC, CA	-119 40 12 49 36 00 485	D. Gamble	457 QHY174M-GPS None	3 3	Negative
Woodside CA, US	-122 15 30.0 37 23 36.2 367	F. Marchis	114 eVscope/IMX347 None	4 4	Inconclusive
Naylor Obs. Harrisburg PA, US	-76 53 43.48 40 08 55.60 181.6	R. Kamin R. Young	355.6 QHY174M-GPS	0.5 0.5	Overcast
Nikitin Home Gunbarrel CO, US	-105 11 00.96 40 04 08.61 1,594	V. Nikitin	279.4 QHY174-GPS None	6 6	Overcast
Van Vleck Obs. Middletown CT, US	-72 39 33.12 41 33 18.62 68.9	K. McGregor S. Redfield	610 Apogee E2V Luminance	No data	Overcast
Skychariot Shohola PA, US	-74 58 49.28 41 21 39.94 414.6	M. Sproul	406.4 ASI1600MC None	No data	Overcast
NIRo - CAC Lowell IN, US	-87 22 31.08 41 16 15.03 195.7	A. W. Rengstorf	508 FLI PL09000 I	No data	Overcast

Table B.1. [continued.] Observational circumstances.

Site	Longitude [° ’ ”] Latitude [° ’ ”] Altitude [m]	Observers	Aperture (mm) Detector Filter	Exp. Time Cycle (s)	Status Light curve Dispersion
Jimginny Obs. Naperville IL, US	-88 07 0.00 41 45 32.40 230	R. Dunford	356 QHY174M-GPS None	No data	Overcast
Pine Mountain Obs. Bend OR, US	-120 56 28.8 43 47 30.3 1,920	S. Fisher A. Luken	610 Andor Xyla None	No data	Overcast
Palomar Obs. San Diego CA, US	-116 51 53.5 33 21 21.5 1,712	E. Fernandez-Valenzuela K.de Kleer T. Marlin, M. Camarca	5,100 CHIMERA	No data	Overcast
Westport Astronomical Obs. Westport CT, US	-73 19 39.0 41 10 16.0 87	K. D. Green	356 QHY174M-GPS None	No data	Overcast
Yerington NV, US	-119 09 39 38 59 28 1,340	M. Christensen	280 QHY174M-GPS None	No data	Overcast
Bend OR, US	-121 18 55 44 03 29 1,105	A-M. Eklund	280 QHY174M-GPS None	No data	Overcast
Yuma CA, US	-114 37 40 32 41 34 62	D. Thompson K. Conway D. Conway	280 QHY174M-GPS None	No data	Overcast
Reno NV, US	-119 49 06 39 32 42 1,387	T. Stoffel	280 QHY174M-GPS None	No data	Overcast
Cedarville CA, US	-120 10 24 41 31 45 1,420	T. Miller D. Schulz	280 QHY174M-GPS None	No data	Overcast
Kingman AZ, US	-113 51 46 35 24 43 966	C. Patrick K. Butterfield	305 QHY174M-GPS 0.5 focal reducer	No data	Overcast
Beatty CA, US	-116 45 29 36 54 04 999	J. Heller	280 QHY174M-GPS None	No data	Overcast
Burney CA, US	-121 23 56 41 02 45 1,012	M. von Schalscha	280 QHY174M-GPS None	No data	Overcast
Gardnerville NV, US	-119 44 59 38 56 29 1,449	J. Bardecker	304 Watec 910-HX None	No data	Overcast

Notes. TAOS II: The Transneptunian Automated Occultation Survey. CFHT: Canada-France-Hawaii Telescope. TUHO: Tohoku University Haleakala Observatory. UCSC: University of California, Santa Cruz. NIRo: Northwest Indiana Robotic - Calumet Astronomy Center.

Appendix C: Occultation map

Figure C.1 presents the stellar occultation map with all the sites involved in this campaign. The green dots mark the positive detections and orange dots are stations that reported cloudy weather. The white dot represents the Woodside observation with the eVscope where the event was not detected due to the low S/N of the data set. The continuous line represents the limit of the Quaoar's shadow projected over the Earth. The dashed-lines represent the Q1R and Q2R projections, as annotated in the image.
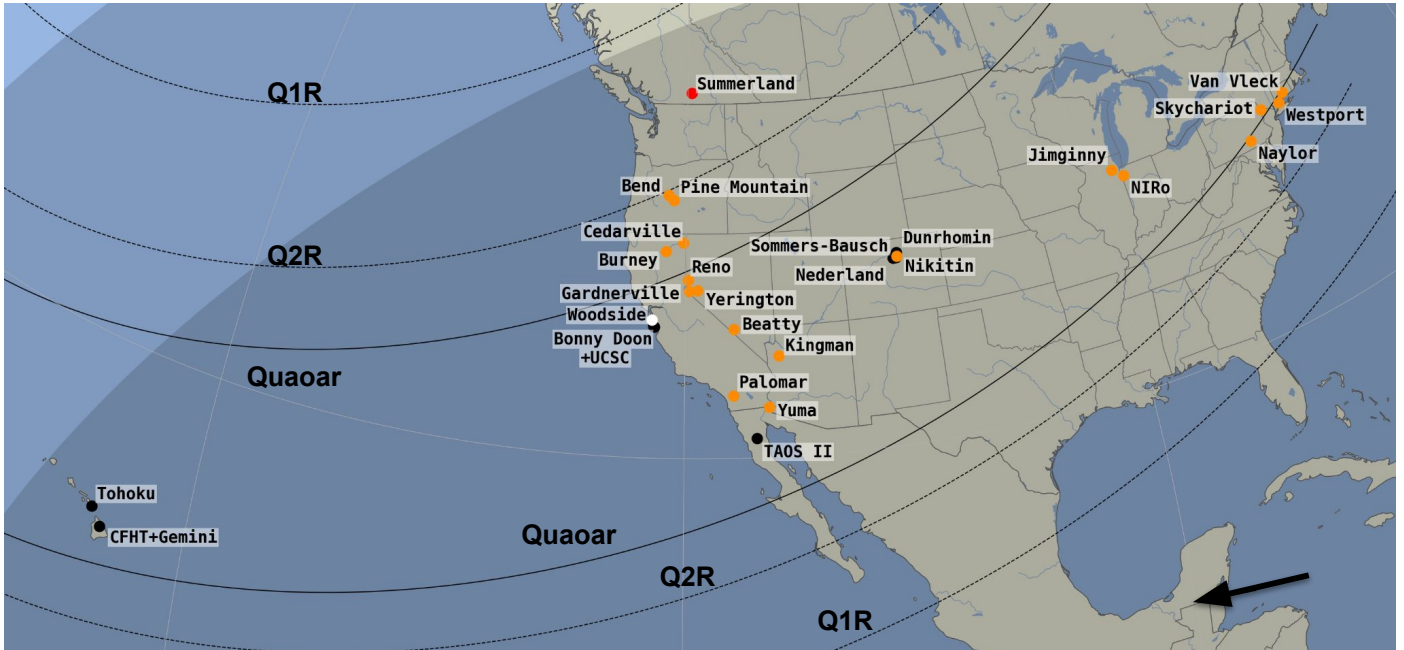
Fig. C.1. Occultation map with positive detections (black dots) and sites that reported cloudy weather (orange dots). The white dot represents no data due to the instrumental limits. In red we display a site with data but no occultation detected. The black solid lines mark Quaoar's shadow limits and the black dashed lines mark the Q1R and Q2R projections. The black arrow in the bottom right indicates the direction of motion of the shadow.

Appendix D: Light curves

Figure D.1 displays all the normalized light curves obtained during the stellar occultation by (50000) Quaoar of August 9, 2022. The stellar flux has been corrected for sky transparency fluctuations using reference stars. The time scale is relative to the closest approach time at each site. Besides the occultation by Quaoar and Q1R, the Gemini and CFHT light curves revealed the new Q2R ring. The Tohoku (TUHO) and TAOS II data allowed for the detection of the densest region of the Q1R ring. Due to the S/N limitations, the Nederland, Dunrhomin, Sommers-Bausch, UCSC, and Bonny Doon stations detected only the occultation by the main body. Some data sets presented dropped frames during the photometric process, such as the Durhomin and Nederland. This occurred due to the degradation of the sky quality shortly after the occultation of the main body, in addition to clouds crossing the field of view of the telescope.

We noticed that the Gemini and CFHT light curves were misaligned in time, probably caused by an offset in the Gemini data. As we have a reliable time source for the CFHT data, we aligned the centers of these chords by applying an offset of $+0.27$ seconds on the Gemini chord, obtaining values of $\chi^2_{\rm pdf}$ closer to 1. Although very close, this result is slightly better than applying an offset to the CFHT chord.
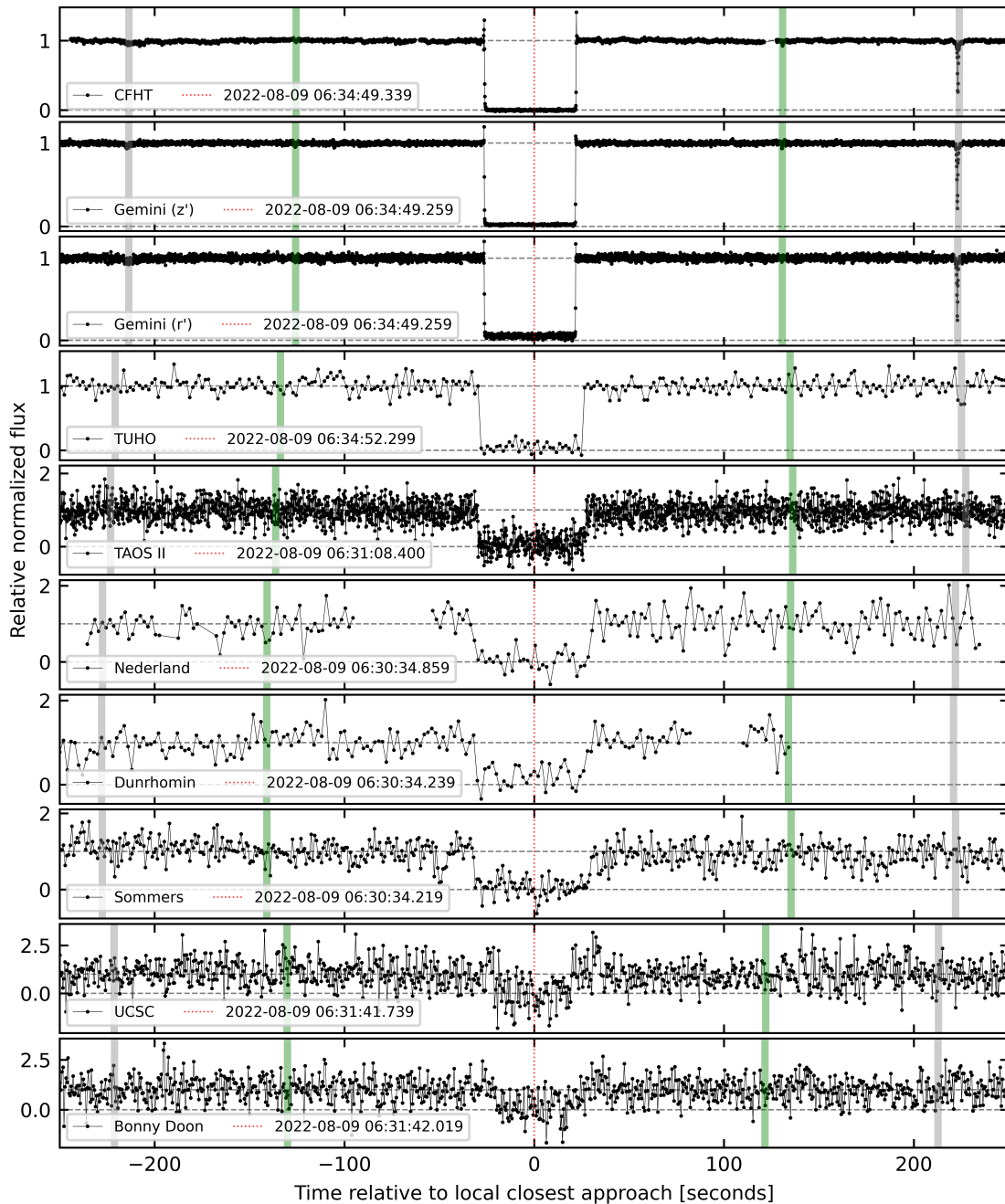
Fig. D.1. All the positive light curves obtained during the August 9, 2022 stellar occultation by Quaoar. The black dots represent the data points. These light curves are plotted as a function of the time in seconds relative to the closest approach for each site. The green and gray vertical lines stand for Q2R and Q1R, respectively. When detected, these lines stand for calculated detection times. For light curves where these secondary structures were not detected, the green and gray lines mark theoretical times expected from our best-fit solution for a circular ring. The horizontal gray dashed lines represent the baseline and minima of the stellar fluxes.

Appendix E: Modeled ring detections

The ring events were fit using the models described in Elliot et al. (1984) and Bérard et al. (2017), that is, square boxes with uniform opacity and sharp edges. As with the main body occultation modeling, the modeled curve was convolved with observation bandpass, apparent star diameter, and instrumental response, but now fitting an opacity for the square box. The outputs of a given fit are the width, W, of the event, its apparent opacity, p' (corresponding to the depth of the observed stellar flux drop), and its apparent optical depth, $\tau' = -\ln(1 - p')$. The geometry of the ring (assumed here to be circular) is defined by its opening angle, B, and the position angle, P, of its apparent semi-minor axis, counted positively from local celestial north to the celestial east direction. This provides the radial width, W_r, the normal opacity, $p_N = |\sin B| (1 - \sqrt{1 - p'})$, and the normal optical depth, $\tau_N = \tau' |\sin B|/2$, of the ring from each event. The factor of 2 in the formula for τ_N is due to the fact that Airy diffraction by individual ring particles results in a loss of light, resulting in an observed optical depth to be twice as large as would be measured at the ring level; see more details in Cuzzi (1985), Roques et al. (1987). We note that the formulae for p_N and τ_N are valid only for mono-layer and poly-layer rings, respectively. The equivalent width (respectively, depth)

$E_p = W_r p_N$ (respectively, $A_\tau = W_r \tau_N$) measures the amount of ring material that blocked the stellar rays in the mono-layer (resp. poly-layer) case.

A Lorentzian function is fitted to the dense part of the Q1R in the Gemini and CFHT light curves, converted from flux to normal optical depth as a function of radial distance in the ring plane. The area under the curve equals the equivalent width, A_τ, of the ring, and the full-width half minimum (FWHM) gives us the approximate width of the ring's core. The position of the function's valley gives us the average radial distance between the ring and Quaoar's center. The E_p value was obtained from the integral of the ring profile in the curve of the normal opacity, p_N, as a function of the radial distance in the sky plane. This modeling considers the stellar apparent diameter of 1.33 km, which has negligible influence on the ring profile.

Figs. E.1 and E.2 present all light curves in which the Q1R and Q2R rings were detected. The TAOS II light curve, used for detecting of the densest region of the Q1R ring, was obtained by applying aperture photometry to stacked images in order to increase the S/N. Stacking was performed using Python routines built from the `astropy` library as described in Morgado et al. (2019), where each new image is the average of six original images, resulting in a temporal resolution of 1.2 seconds for each stacked image.

Table E.1. Physical parameters of rings Q1R and Q2R.

Ring	Detection	Mid-time August 9th, 2022	r (km)	W_r (km)	p_N	τ_N	E_p (km)	A_τ (km)
Q1R- ing	CFHT	06:31:15.8 (0.2)	4,009.9 (1.8)	105.5 (5.6)	0.0030 (0.0003)	0.0030 (0.0003)	0.31 (0.02)	0.31 (0.02)
	Gemini (z')	06:31:15.72 (0.04)	3,995.4 (0.3)	76.4 (0.8)	0.0026 (0.0001)	0.0026 (0.0001)	0.20 (0.01)	0.20 (0.01)
	Gemini (r')	06:31:15.7 (0.1)	3,995.9 (0.8)	85.8 (1.1)	0.0032 (0.003)	0.0032 (0.0003)	0.28 (0.02)	0.28 (0.02)
Q1R- egr	CFHT[a]	06:38:32.581 (0.003)	4,123.69 (0.05)	6.1 (0.1)	0.330 (0.007)	0.395 (0.009)	2.01 (0.03)	2.41 (0.04)
	Gemini (z')[a]	06:38:32.444 (0.003)	4,123.11 (0.02)	5.3 (0.1)	0.353 (0.008)	0.417 (0.007)	1.87 (0.02)	2.21 (0.02)
	Gemini (r')[a]	06:38:32.429 (0.005)	4,122.85 (0.04)	5.1 (0.1)	0.341 (0.009)	0.398 (0.008)	1.74 (0.03)	2.03 (0.03)
	TUHO	06:38:37.4 (0.7)	4,107.2 (7.6)	71 (17)	0.03 (0.01)	0.03 (0.01)	2.3 (0.9)	2.4 (1.1))
	TAOS II	06:34:55.8 (0.5)	4,125.7 (4.4)	34 (16)	0.05 (0.02)	0.05 (0.03)	1.6 (1.1)	1.7 (1.3)
Q2R- ing	CFHT	06:32:43.9 (0.2)	2,490.4 (1.6)	16.5 (3.0)	0.0022 (0.0004)	0.0022 (0.0004)	0.036 (0.006)	0.036 (0.006)
	Gemini (z')	06:32:43.61 (0.06)	2,493.8 (0.6)	11.3 (0.8)	0.0034 (0.0005)	0.0034 (0.0005)	0.038 (0.006)	0.039 (0.006)
	Gemini (r')	n.d.[b]	n.d.[b]	n.d.[b]	n.d.[b]	n.d.[b]	n.d.[b]	n.d.[b]
Q2R- egr	CFHT	06:37:00.20 (0.01)	2,540.7 (0.1)	10.8 (0.2)	0.0049 (0.0003)	0.0049 (0.0003)	0.052 (0.001)	0.053 (0.001)
	Gemini (z')	06:37:00.09 (0.02)	2,540.45 (0.1)	6.3 (0.3)	0.0047 (0.0005)	0.0048 (0.0006)	0.030 (0.002)	0.030 (0.002)
	Gemini (r')	06:36:59.93 (0.02)	2,528.3 (1.1)	9.1 (2.5)	0.003 (0.001)	0.003 (0.001)	0.030 (0.008)	0.030 (0.008)

Notes. The normal opacity, p_N, and normal optical depth, τ_N, were calculated from the ring opening angle, B, and position angle, P, on August 9, 2022, derived from the orientation of the body obtained from the 2018-2022 data. The other parameters are: Mid-time in UT and the error bars in parentheses given in seconds; r, the radial distance from Quaoar's center in kilometers; W_r, the radial width in kilometers; E_p and A_τ, the equivalent width and equivalent depth in kilometers respectively. The terms "ing" and "egr" stand for ingress and egress, respectively, and refer to the fact that the detection occurred before and after the occultation by Quaoar's main body, respectively. The error bars in parentheses are at the 1-σ level. [a]From Lorentzian fit. The width W_r is defined as the FWHM of the τ_N profile. The E_p and A_τ values where obtained from respective integrals in the ring profile (see Sec. 3); [b]Not detected.
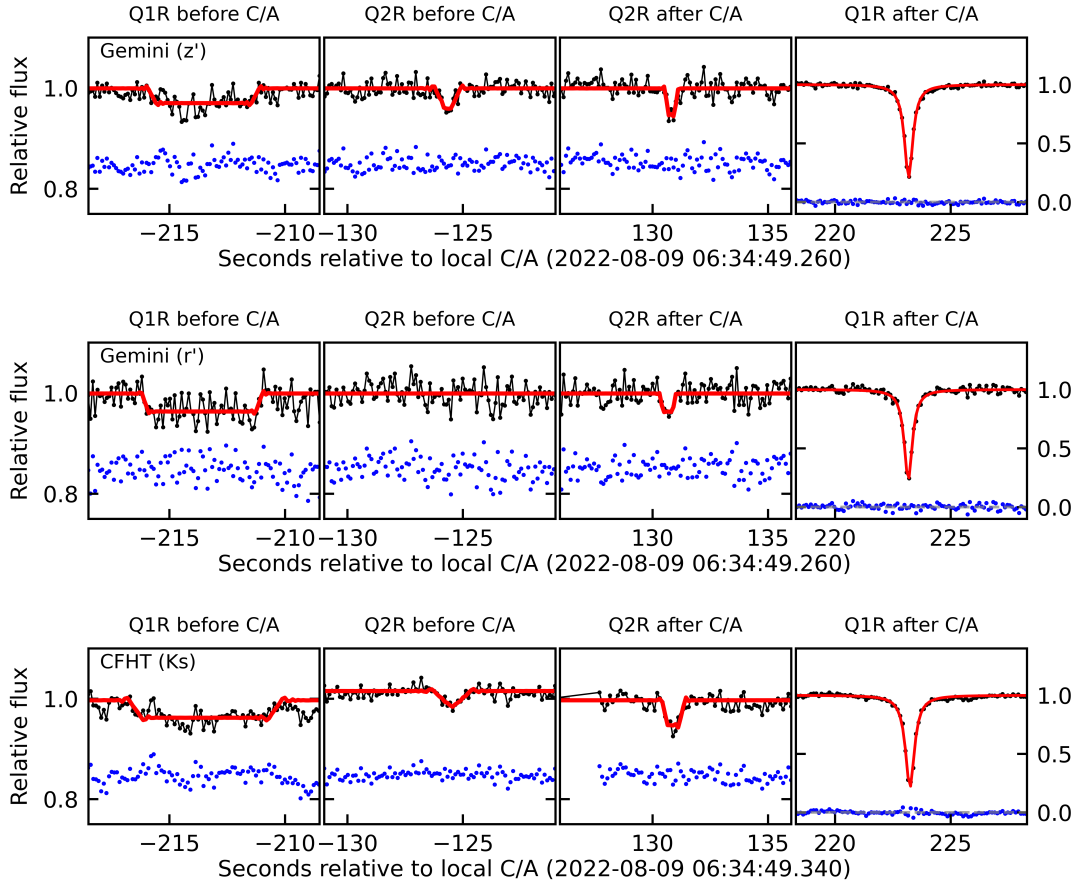
Fig. E.1. Fits to the Q1R and Q2R light curve data taken with Gemini (z'), Gemini (r'), and CFHT (Ks) (the corresponding filters are indicated in parentheses). These light curves are plotted as a function of the time in seconds relative to the local closest approach (C/A). The blue dots represent residuals with an arbitrary vertical offset for clarity. Note: the y-axis scale is different in the rightmost panel in each row (dense part of Q1R).
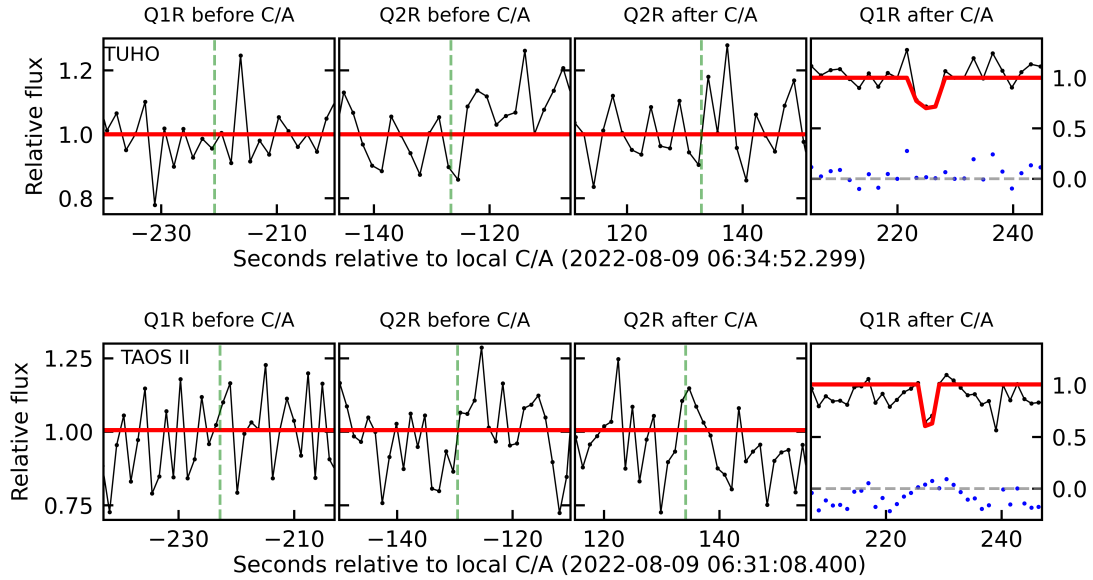

Fig. E.2. Fits to the Q1R dense ring in light curve data taken with TUHO and TAOS II telescopes, from top to bottom. TAOS II data are stacked every six images. These light curves are plotted as a function of the time in seconds relative to the local closest approach (C/A), with a different y-axis scale in the rightmost panel in each row (dense part of Q1R). The green vertical dashed lines represent the theoretical times for the Q1R and Q2R rings. Note: although marginal, the two data points that detect the Q1R ring in the TAOS II light curve are statistically significant at the 4.2-σ level.

Appendix B

Physical properties of Centaur (60558) 174P/Echeclus from stellar occultations

Physical properties of Centaur (60558) 174P/Echeclus from stellar occultations

C. L. Pereira [1,2]★ F. Braga-Ribas,[1,2,3] B. Sicardy [4] A. R. Gomes-Júnior [2,5,6] J. L. Ortiz [7]
H. C. Branco,[3,8] J. I. B. Camargo [1,2] B. E. Morgado,[1,2,9] R. Vieira-Martins,[1,2] M. Assafin [2,9]
G. Benedetti-Rossi [2,6] J. Desmars,[10,11] M. Emilio [1,3,12] R. Morales,[7] F. L. Rommel,[2,3] T. Hayamizu,[13,14]
T. Gondou,[13] E. Jehin,[15] R. A. Artola,[16] A. Asai,[13,14] C. Colazo,[17] E. Ducrot,[18] R. Duffard,[7] J. Fabrega,[19]
E. Fernandez-Valenzuela,[7,20] M. Gillon,[21] T. Horaguchi,[13,14,22] M. Ida,[13] K. Kitazaki,[13] L. A. Mammana,[23]
A. Maury,[24] M. Melita,[25,26,27] N. Morales,[7] C. Moya-Sierralta,[28] M. Owada,[13,14] J. Pollock,[29]
J. L. Sanchez,[30] P. Santos-Sanz,[7] N. Sasanuma,[13] D. Sebastian,[31] A. Triaud,[31] S. Uchiyama,[13] L. Vanzi,[32]
H. Watanabe[13] and H. Yamamura[13]

Affiliations are listed at the end of the paper

ABSTRACT

The Centaur (60558) Echeclus was discovered on 2000 March 03, orbiting between the orbits of Jupiter and Uranus. After exhibiting frequent outbursts, it also received a comet designation, 174P. If the ejected material can be a source of debris to form additional structures, studying the surroundings of an active body like Echeclus can provide clues about the formation scenarios of rings, jets, or dusty shells around small bodies. Stellar occultation is a handy technique for this kind of investigation, as it can, from Earth-based observations, detect small structures with low opacity around these objects. Stellar occultation by Echeclus was predicted and observed in 2019, 2020, and 2021. We obtain upper detection limits of rings with widths larger than 0.5 km and optical depth of $\tau = 0.02$. These values are smaller than those of Chariklo's main ring; in other words, a Chariklo-like ring would have been detected. The occultation observed in 2020 provided two positive chords used to derive the triaxial dimensions of Echeclus based on a 3D model and pole orientation available in the literature. We obtained $a = 37.0 \pm 0.6\,\mathrm{km}$, $b = 28.4 \pm 0.5\,\mathrm{km}$, and $c = 24.9 \pm 0.4\,\mathrm{km}$, resulting in an area-equivalent radius of $30.0 \pm 0.5\,\mathrm{km}$. Using the projected limb at the occultation epoch and the available absolute magnitude ($H_\mathrm{v} = 9.971 \pm 0.031$), we calculate an albedo of $p_\mathrm{v} = 0.050 \pm 0.003$. Constraints on the object's density and internal friction are also proposed.

Key words: Methods: data analysis – Methods: observational – Occultations – Minor planets, asteroids: individual: Echeclus.

1 INTRODUCTION

The Centaurs are bodies with chaotic orbits that have perihelion and the semimajor axis between the orbits of Jupiter and Neptune ($5.2\,\mathrm{au} < q < 30\,\mathrm{au}$ and $5.2\,\mathrm{au} < a < 30\,\mathrm{au}$) and not being in 1:1 mean-motion resonance with any planet (Jewitt 2009). These bodies are believed to be the primary source of Jupiter-family comets (JFC). Approximately 1/3 of Centaurs are temporarily trapped in orbits close to the Sun, and 2/3 are expected to be expelled from the Solar System (Tiscareno & Malhotra 2003). This population of small bodies is notable due to the presence of cometary activity, which has been observed in about 13 per cent of Centaurs (Bauer et al. 2008). Furthermore, the perihelion distance of the active Centaurs is systematically smaller than that of the inactive ones, leading us

to believe that thermal processes may be responsible for triggering mass loss mechanisms (Jewitt 2009).

The first Centaur object discovered was (2060) Chiron in 1977. With about 210 km in diameter, it is the second largest of its class (Lellouch et al. 2017). Chiron showed cometary activity in 1988, with coma and cometary tail detection in the following years. With this behaviour, it was designated as 95P/Chiron. Stellar occultations allowed the detection of structures analogous to collimated cometary jets (Ruprecht et al. 2015; Sickafoose et al. 2020) or rings, a hypothesis still being discussed (Ortiz et al. 2015; Braga-Ribas et al. 2023; Ortiz et al. 2023). (10199) Chariklo is the largest known Centaur, with about 250 km in diameter (Morgado et al. 2021). This object was the first small body in the Solar System where rings were confirmed (Braga-Ribas et al. 2013), followed by the dwarf planet Haumea (Ortiz et al. 2017) and the trans-Neptunian object Quaoar (Morgado et al. 2023; Pereira et al. 2023). Among the Centaurs, the object 29P/Schwassmann-Wachmann 1 (SW1) is notable. Having a quasi-circular orbit with a semimajor axis of 5.98 au, it presents

★ E-mail: chrystianpereira@on.br

Table 1. Orbital parameters and physical properties of 174P/Echeclus.

a (au)	q (au)	e	i (deg)	Hv	P (h)	D (km)	p_v
10.744	5.835	0.457	4.344	9.971 ± 0.031	26.785178 ± 0.000001	64.6 ± 1.6	$0.052^{+0.0070}_{-0.0071}$

Note. Orbital elements of 174P/Echeclus from Jet Propulsion Laboratory (JPL) Small-Body Data base Browser JPL#109: a, semimajor axis; q, perihelion distance; e, eccentricity; i, inclination; Absolute magnitude H, calculated from Gaia DR3 Solar System objects (SSO; Tanga et al. 2023) using Morales et al. (2022) method. Diameter D and albedo p_v from Duffard et al. (2014); Rotational period P from Rousselot et al. (2021).

frequent outbursts and high rates of carbon monoxide production (Senay & Jewitt 1994; Wierzchos & Womack 2020). Furthermore, SW1 is located in what we refer to as the 'Gateway', a transitional region between Centaur objects and JFC (Sarid et al. 2019).

The Centaur (60558) Echeclus, previously designated 2000 EC$_{98}$, was discovered by Terry Bressi of Spacewatch on 2000 March 03. From thermal observations using *Spitzer Space Telescope*, Stansberry et al. (2007) calculated a diameter of 83.6 ± 15 km and geometric albedo of $0.0383^{+0.0189}_{-0.0108}$. Bauer et al. (2013) derived an equivalent diameter of 59 ± 4 km and albedo 0.08 ± 0.02 from thermal infrared observations using Wide-field Infrared Survey Explorer. Duffard et al. (2014) obtained with PACS instrument on Herschel Space Observatory an equivalent diameter of 64.6 ± 1.6 km with an albedo of $0.052^{+0.007}_{-0.0071}$. Table 1 shows some of its orbital and physical properties.

Echeclus presented some cometary activity over the last few years with different intensities. The main outburst occurred between November and December 2005 at 13 au, when its brightness increased by ~ 7 magnitudes (Choi, Weissman & Polishook 2006a). Besides being the major activity recorded so far in terms of brightness, the source of the mass ejection appears to be displaced from Echeclus itself, being at $\sim 55\,000$ km from the main body. This behaviour of the coma was attributed to the detachment of a fragment during the outburst, with this fragment being the primary source (Weissman et al. 2006; Choi et al. 2006b; Bauer et al. 2008; Fernández 2009). On the other hand, the decentralized coma could result from the ejection of material in three different regions and in different occasions: two short events followed by a third longer-lasting ejection (Rousselot et al. 2016).

On 2011 May 30, Jaeger et al. (2011) reported a new outburst while Echeclus approached the perihelion at 7.5 au, with a coma extending for one arc-minute (or $\sim 327\,000$ km). Subsequent observations taken in June 2011 showed a 40 arcsec ($\sim 218\,000$ km) coma and a jet-like feature 6 arcsec ($\sim 33\,000$ km) long. During the interval of these observations, a ~ 3 visual magnitude brightening was reported. The outbursts reported in August 2016 presented a brightening amplitude of ~ 3 magnitudes, without notable features in the coma (Miles 2016). After its perihelion in April 2015, Echeclus had the second largest outburst in brightness, with an amplitude of ~ 4 magnitudes (James 2018). Observations using Faulkes North & South Telescopes and the NASA Infrared Telescope Facility just after the 2017 December outburst revealed a coma morphology asymmetric in the North–South direction that confirmed previous ideas about the dust properties (Kareta et al. 2019). Subsequent studies suggest that seasonal effects can cause material ejections. Also, the variegation of the colour index as a function of radial distance from the nucleus indicates that particles may have different sizes or compositions (Rousselot et al. 2021).

This paper presents the results of a double-chord stellar occultation observed in January 2020, a single-chord detection in January 2021, and an August 2019 close appulse. The 2020 event allowed constraining the size and shape of Echeclus. It was also used with

the 3D model and pole coordinates position proposed by Rousselot et al. (2021) to obtain its size and volume. All data sets of the three stellar occultation events were used to search for signatures that could reveal the presence of secondary structures around Echeclus, whether coma, jets, arcs, or confined rings.

2 OBSERVATIONS

The stellar occultations presented in this work were predicted by the Lucky Star project[1] using the Numerical Integration of the Motion of an Asteroid (NIMA) ephemeris (Desmars et al. 2015) and *Gaia* Data Release 2 (*Gaia* DR2) sources (Gaia Collaboration 2018). The event analysis was made using the *Gaia* Data Release 3 (*Gaia* DR3) catalogue (Gaia Collaboration 2022). The geocentric position of the target star propagated from *Gaia* DR3 catalogue to the occultation epochs is presented in Table 2, and the observational circumstances of all observatories are presented in Table B1. When available, the data sets were calibrated for bias, dark, and flat fields using the Image Reduction and Analysis Facility (IRAF) (Butcher & Stevens 1981). The light curves were obtained through differential aperture photometry using the Platform for Reduction of Astronomical Images Automatically (PRAIA) package (Assafin et al. 2011).

Finally, the ingress and egress instants were obtained from a pipeline built using the Stellar Occultation Reduction Analysis library (SORA)[2] (Gomes-Júnior et al. 2022) by modelling the light curve considering a sharp-edge model convolved with Fresnel diffraction, the apparent star diameter at Echeclus distance, and integration time (more details in Braga-Ribas et al. 2013; Souami et al. 2020).

2.1 The Echeclus appulse on 2019 October 29

The event was predicted to cross the northern region of Chile, Argentina, Paraguay, and the southern part of Brazil. The geocentric closest approach occurred on 2019 October 29, at 08:40:50.2 UT, with a shadow velocity of 12.8 km s^{-1}. The maximum expected duration for the occultation was 6.8 s.

Observations for this event were conducted at Southern Astrophysical Research Telescope (SOAR, Cerro Pachón, Chile), TRAnsiting Planets and PlanetesImals Small Telescope (TRAPPIST-South, La Silla Observatory, Chile; Jehin et al. 2011), Search for Planets EClipsing ULtra-cOOl Stars Io telescope (SPECULOOS-South Observatory, Cerro Paranal, Chile; Delrez et al. 2018; Jehin et al. 2018), New Technology Telescope (NTT, La Silla Observatory, Chile), and San Pedro de Atacama Celestial Explorations Observatory. Unfortunately, the main body shadow did not cross either of these sites, as shown in Fig. D1, and thus, the occultation by the Echeclus main body could not be detected. With the positions obtained from the stellar occultations of 2020 and 2021 and considering that the uncertainty

[1] https://lesia.obspm.fr/lucky-star/
[2] https://sora.readthedocs.io/

Table 2. Stellar parameters from *Gaia* DR3 catalogue for each observed event. The equatorial coordinates were propagated to the event epoch.

Epoch (UT)	*Gaia* DR3 Source ID	RA	Dec.	G (mag)
2019-10-29 08:40:50.1	3 395 392 378 744 301 696	$05^h16^m34.39005^s \pm 0.0614$ mas	$+18°22'21.3283'' \pm 0.0746$ mas	14.2
2020-01-22 01:44:51.8	3 406 534 520 342 323 584	$04^h51^m35.92194^s \pm 0.1405$ mas	$+17°48'18.7786'' \pm 0.1481$ mas	15.3
2021-01-19 09:10:44.6	3 399 123 330 937 092 224	$05^h43^m05.01044^s \pm 0.0609$ mas	$+18°40'37.0924'' \pm 0.0897$ mas	11.0

Table 3. Ingress and egress instants obtained from light curve modelling for 2020 January 22 and 2021 January 19 events. The 1σ error bars between parenthesis are in seconds.

Event	Site	Ingress (UT) (hh:mm:ss.s)	Egress (UT) (hh:mm:ss.s)
2020	SOAR	01:44:08.33 (0.01)	01:44:10.15 (0.01)
2020	La Canelilla	01:44:07.03 (0.04)	01:44:11.80 (0.04)
2021	Anan	09:15:03.173 (0.006)	09:15:06.378 (0.009)

in the stellar position is very small (RUWE[3] = 0.948), we were able to reconstruct the geometry of the appulse of 2019. This allows us to determine the distance between the chords and the object's centre, establishing the detection limits for additional material. Fig. F1 displays the reconstructed map showing the theoretical path of the shadow based on the updated NIMAv9 ephemeris.

2.2 Stellar occultation on 2020 January 22

The 2020 January 22 stellar occultation was predicted to cross central Chile, Argentina, and Uruguay. The shadows velocity was 11.1 km s^{-1}, resulting in a maximum duration of 7.8 s. An observation campaign was triggered over South America involving professional and amateur observatories. Two out of nine observations were positive, with four being negative and three presenting technical problems/overcast. Thus, this was the first double-chord occultation for Echeclus.

The data acquisition with SOAR was made using the visitor instrument Raptor 247 Merlin camera with GPS as a time source. In La Canelilla/Chile, the data was acquired using a 520 millimeters telescope equipped with a ZWO ASI1600MM CMOS camera in the avi video format and NTP monitor as reference time. The video was converted to fits files using Python routines based on ASTROPY (Astropy Collaboration 2013). With the Fresnel scale $L_f = \sqrt{\lambda D/2} = 0.7$ km and the apparent star diameter at 8.66 au of about 0.1 km using the models provided by van Belle (1999), the light curves are dominated by the instrumental response, considering the exposure times of 0.25 s ($\sim$2.8 km) for SOAR and 0.3 s ($\sim$3.3 km) for La Canelilla/Chile. The ingress and egress instants obtained from modeling are shown in Table 3, and the modelled light curves are presented in Fig. E1.

2.3 Stellar occultation on 2021 January 19

The shadow's path for the stellar occultation on 2021 January 19 was predicted to pass over Japan. The star's brightness allowed small

Table 4. Data used in the equilibrium analysis.

$\alpha(c/a)$	$\beta(b/a)$	Period (h)	ϕ (°)	ρ (kg m^{-3})
0.67 ± 0.02	0.77	26.785178	9	500–1,210
			10	600
			8.5–10.5	500–1,900

aperture telescopes to participate in this observational campaign. Unfortunately, the object's shadow path shifted with respect to the predicted path for about a radius to the south, reaching the 1σ uncertainty limit of the prediction. As a result, most of the telescopes involved in the observational campaign were outside the shadow-path region. The event was successfully observed through thin clouds at Anan Science Center in Anan, Tokushima, Japan. The acquisition was performed in video format using a ZWO ASI290MM camera coupled with a 254-mm telescope. An NTP monitor provided a reference time. For this event, the Fresnel Scale is calculated as $L_f = \sqrt{\lambda D/2} = 0.7$ km, and the star's apparent diameter was estimated to be 0.4 km at Echeclus distance using the models provided by van Belle (1999). With an exposure time of 0.028 s, the instrumental response is approximately 0.5 km. The instants of ingress and egress are presented in Table 3.

3 SIZE AND SHAPE

By analysing 27 light curves obtained between 2001 and 2019, Rousselot et al. (2021) reproduced a 3D model for Echeclus using the Shaping Asteroid models using Genetic Evolution (SAGE) modelling technique (Bartczak & Dudziński 2018), an algorithm based on light-curve inversion. The sidereal rotational period for Echeclus was determined to be $P = 26.785178 \pm 10^{-6}$ h. The rotational period error bar gives reasonable confidence in the orientation of the 3D shape at the time of occultation. The double-peak light curve exhibited amplitudes consistent with a triaxial body ($a > b > c$, where c is the rotation axis), with a semimajor axial ratio of $a/b = 1.32$ and $b/c \sim 1.1$ based on a comparison of the projected areas of the 3D model (Rousselot et al. 2021).

The 3D model of Echeclus can be accessed through the interactive service for asteroid models (ISAM).[4] The rotational elements of the model are $\lambda = 115.2°$, $\beta = 21.5°$, and $\gamma_0 = 80°$ for the reference epoch $t_{\text{ref}} = 2455437.367$ JD, based on Kaasalainen, Torppa & Muinonen (2001) system. To fit the occultation chords to the 3D shape model, we used SORA. To orientate the 3D shape model for the occultation epoch, SORA uses the International Astronomical Union (IAU) recommendations by Archinal et al. (2018). We transformed the ISAM parameters to the IAU formalism using appropriate rotation matrices. In the IAU formalism, pole coordinates are RA = $122° 18' 05.8''$, Dec. = $42° 09' 16.6''$, and

---

[3]Renormalized Unit Weight Error (RUWE) indicates the reliability of the single-star model based on observations, with values close to 1 being expected. Values greater than 1.4 may suggest that the source is not a single star or that there are issues with the astrometric solution (Lindegren et al. 2018).
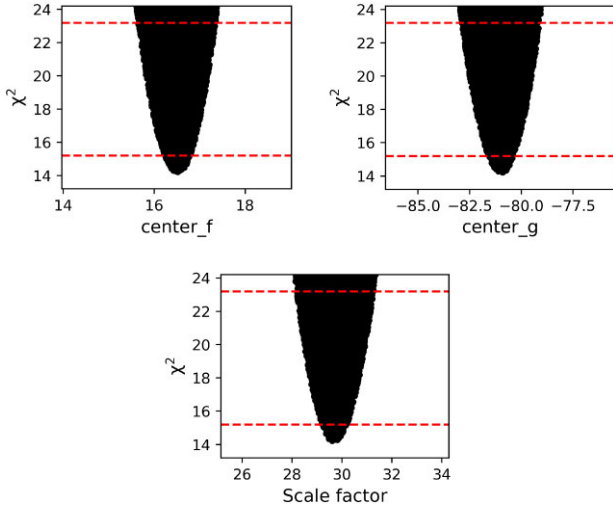
[4]http://isam.astro.amu.edu.pl/

Figure 1. χ^2 distributions obtained from shape fit for the centre positions (f and g) and scaling factor for 2021 stellar occultation. The red horizontal dashed lines delimits the 1σ (lower line) and 3σ (upper line) uncertainties.

$W_0 = 336.793618$ degrees in the reference epoch $t_{\text{ref}} = 2455437.367$ JD.

Once the apparent shape of Echeclus projected onto the sky plane at the occultation epoch is obtained, the positive chords of the 2020 event can be compared with the projected limb. This comparison involves minimizing the χ^2 function defined by

$$\chi^2 = \sum_{i=1}^{N} \frac{(\phi_{(i,obs)} - \phi_{(i,cal)})}{\sigma_i^2}, \quad (1)$$

where $\phi_{(i,obs)} - \phi_{(i,cal)}$ is the difference between the extremity of each chord and the projected shape limb and σ_i is the uncertainty of the *i*-th chord extremity. We generate numerous models by applying an offset in the body centre and re-scaling the model iteratively. This re-scaling procedure is necessary because some objects do not have a known radius, and SAGE usually scales the shape model so that the maximum radius equals 1. The obtained values are $f_c = 16.5 \pm 0.3$ km, $g_c = -80.7 \pm 0.6$ km, and a scale factor of 29.4 ± 0.5, with the correspondent χ^2 curves presented in Fig. 1. Note that there are differences between the model and the chords, but this can be accommodated by reasonable topographic features not considered in the 3D model. Checking the radial residuals between the extremities of the 2020 occultation chords and the limb, we obtain 0.3 and 0.6 km (respectively, 1.1 and 1.0 km) for the SOAR chord (respectively La Canelilla), from West to East. This is about 2.6 per cent of the estimated equivalent radius for the 3D model.

A similar procedure was applied to compare the positive chord of the 2021 stellar occultation with the proposed 3D model and pole. In this case, the better correspondence between chord extremities and projected limb is obtained by varying the center position while keeping the same scale obtained from the 2020 occultation. The results are presented in Fig. 2.

From the obtained scale, we can calculate the dimension of Echeclus' axes, being as $a = 37.0 \pm 0.6$ km, $b = 28.4 \pm 0.5$ km, and $c = 24.9 \pm 0.4$ km, giving an area-equivalent radius of $R_{\text{equiv}} = 30.0 \pm 0.5$ km. The geometric albedo was calculated using $p_v = 10^{0.4(H_{\odot,v} - H_v)} \cdot (\text{au}_{km}/R_{\text{equiv}})^2$ (Sicardy et al. 2011), where $\text{au}_{km} = 1$ au $= 1.49598 \times 10^8$ km, $H_{\odot,v} = -26.74$ is the Sun absolute magnitude in *v* band, H_v is the Echeclus instantaneous absolute magnitude in *v* band at the rotational phase, and $R_{\text{equiv}} = 30.0 \pm 0.5$ km is the
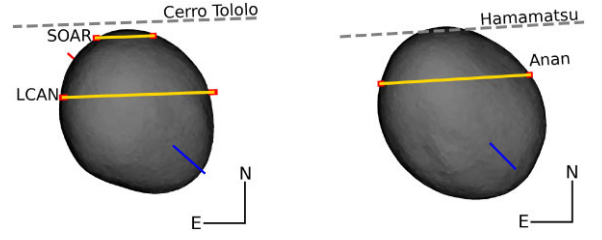
Figure 2. Plane-of-sky views of Echeclus 3D model with the observed chords, being the 2020 observed chords on the left and the 2021 observed chord on the right.

area-equivalent radius of projected Echeclus' limb at the occultation epoch. The absolute magnitude $H_v = 9.971 \pm 0.31$ is based in 438 multi-epoch observations from *Gaia* SSO release (Tanga et al. 2023) and was calculated using the tools and procedures described in Morales et al. (2022). Considering the rotational light curve and the rotational period published by Rousselot et al. (2021), we were able to determine the rotational phase and, therefore, the geometric albedo for Echeclus at 2020 stellar occultation instant as $p_v = 0.050 \pm 0.003$.

4 EQUILIBRIUM SHAPE AND DENSITY ANALYSIS

The equilibrium shape analysis method proposed by Holsapple (2001, 2004, 2007) can investigate small bodies' physical properties and internal structure of granular media characterized by an angle of friction. It correlates the object's dimensions (semi-axis *a*, *b*, and *c*), its angle of internal friction (ϕ), and the scaled spin Ω, defined by:

$$\Omega = \sqrt{\frac{4\pi}{P^2 \rho G}}, \quad (2)$$

where ρ is the mean density in kg m^{-3}, P the rotational period in hours, and G the gravitational constant. It results in rough estimates for objects with known global composition and unknown density. For objects with unknown global composition and known density, it constrains the global composition and internal structure. The angle of internal friction measures the material's response to shear stress. Higher values of ϕ imply a higher resistance to shear stress and, hence, to deformation. Materials with fluid-like behaviour have ϕ of $0°$, easily deforming, while rocks often have $\phi > 20°$. For small bodies, it can be assumed based on the object's surface composition (when known) and/or the expected characteristics of its family.

Echeclus' composition is poorly known, resulting in very loose constraints of its ϕ. An assumed range of densities was used to investigate Echeclus interior properties to obtain meaningful results. The resulting range of possible ϕ was used to (i) base general considerations regarding the object's global composition and internal structure and (ii) to indicate average global density estimates for chosen ϕ values.

For a global density between 500 and 2500 kg m^{-3}, a reasonable range of densities for Centaurs and TNOs (Sicardy et al. 2011), Echeclus must have internal friction between $8.5° > \phi > 10.5°$ (Fig. 3), compatible with what is expected for a mixture of ice and rock (Barucci, Doressoundiram & Cruikshank 2004; Yasui & Arakawa 2009). For comparison, Ortiz et al. (2017) determined a friction angle for Haumea between $10°$ and $15°$, considering the c/a $= 0.4$ ratio. Homogeneous objects behave as ideal fluids, with ϕ close or equal to $0°$, while heterogeneous bodies don't (Holsapple 2001). Hence, it is likely that Echeclus has a heterogeneous internal
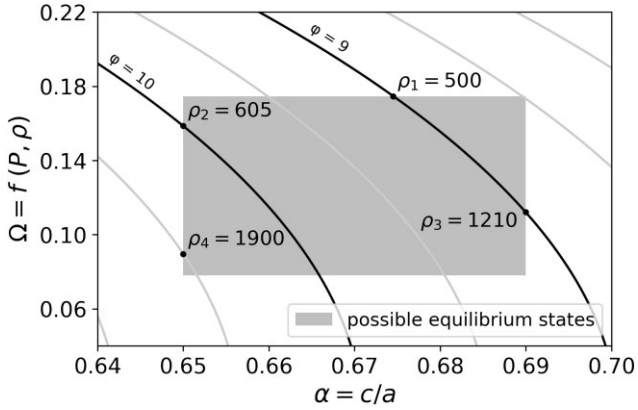
Figure 3. Ω versus α plot used for the equilibrium shape analysis. The grey lines correspond to different ϕ, spaced every $0.5°$. The black lines indicate the curves for $\phi = 9°$ and $10°$, as labelled. The grey box, limited in the x-axis by the observed c/a from the scaled 3D shape, indicates the range of possible equilibrium states for Echeclus. Its vertical size is defined by variations in the scaled spin Ω, a function of the object's period of rotation (P) and density (ρ). Letting P be constant, Ω varies with ρ. The black points indicate the corresponding ρ (in kg m^3) for the combination of Ω and α.

structure. Given its small size and the consequent unlikeliness that it had sufficient internal heat to experience any significant degree of differentiation (Shchuko et al. 2014), it is possible that it has a heterogeneous distribution of mass, a rubble-pile structure or similar, with significant internal porosity may be as high as 20–30 per cent in total volume (Yasui & Arakawa 2009).

5 LIMITS ON ADDITIONAL MATERIAL AROUND ECHECLUS

Detection limits can be calculated considering that the standard deviation of the light curve in the regions external to central body occultation is related to the minimum detectable apparent opacity p′ of any structure around a body (Braga-Ribas et al. 2023, and references therein). The search for additional material was done using light curves from the three events here reported, to determine the detection limits of apparent opacity (p′) and optical depth (τ'). We call these values *apparent* since the properties are measured in the sky plane and not perpendicular to the structures, for example, in the case of discs or rings.

The depth of the observed stellar flux drop is the apparent opacity and is defined by $p' = 1 - \frac{I}{I_0}$, where I and I_0 are the transmitted and incident stellar flux, respectively. Assuming that the white noise follows a Gaussian distribution and considering that the standard deviation of the target star flux is equivalent to p′, a single point detection will only be statistically significant if it is outside the 3σ level of the mean flux. With the apparent opacity, we can constrain the apparent optical depth from $\tau' = -ln(1 - p')$ for a possible structure around Echeclus (more details in Boissel et al. 2014 and Bérard et al. 2017).

A disc is made of particles that diffract light from the star individually. For a particle in the ring with a radius of approximately 1 m, we have a diffraction cone with an angular diameter $\phi_d = \lambda D / r$ of about 900 km, at the Echeclus distance (1.3×10^9 km) and for observations at a wavelength centered at 0.65 μm. Even for the 100 km smoothed light curve, the structure widths we seek are narrower than the diffraction cone-diameter. This implies a loss of energy both by the individual diffraction of the particles and by the flux blocked by these particles when these are much larger than the

wavelength. This is known as the extinction paradox. Thus, the rings appear twice as optically thick as they are (Cuzzi 1985). In this sense, the real optical depth in the sky plane is $\tau = \tau'/2$, or equivalently for the apparent opacity, $p = 1 - \sqrt{1 - p'}$.

Data points on a light curve above the 3σ level are analysed individually against the reference star flux to eliminate the possibility that these drops in flux could have been caused by passing clouds or other artefacts in the image. To search for wider structures, such as the broad, shallow drops in flux observed around Chiron in a 1993 stellar occultation Elliot et al. (1995), we resampled our best light curves for each event by applying a Savitzky–Golay filter with windows of ∼100 km (F3 extension from Elliot et al. 1995). The detection limit for all light curves in the three events analysed in this work is presented in Table C1.

We can also compute limits for apparent equivalent width, which will give us the minimum values for the length of a chord from a serendipitous stellar occultation and, therefore, a upper limit for the radius of the occulting body. Ignoring diffraction effects, we can obtain this limit from the equation $E'_p(i) = [1 - \phi(i)]\Delta r(i)$, where $\phi(i)$ is the normalized stellar flux and $\Delta r(i)$ is the difference between consecutive points in the sky plane, obtained from exposure time times sky plane radial velocity. The values for E'_p are presented in Table C1.

The best data set from the 2019 appulse was obtained with NTT at La Silla Observatory, with an average radial resolution of 2.6 km and a standard deviation of 0.048 (1σ). We determine the 3σ level for the optical depth as $\tau = 0.07$ and apparent equivalent width as $E'_p \sim 380$ m. For the smoothed light curve, we estimated limits on apparent optical depth as $\tau = 0.01$, covering about 7,123 km radially. As mentioned, we did not detect the main body at the observatories involved in this campaign; therefore, to determine the radial distances, we considered the object's theoretical position calculated with NIMA ephemeris, which used the astrometric positions obtained from the 2020 and 2021 detected occultations.

In the 2020 event, the best light curve was obtained with the SOAR telescope. This light curve is positive, so the standard deviation was calculated in the regions outside the main body occultation. The calculated limits for apparent optical depth and apparent equivalent width in the full resolution light curve (average 2.9 km per data point) is $\tau = 0.15$ and $E'_p \sim 800$ m. For the resampled light curve, with a spatial resolution of 97.8 km, the 3σ limit for apparent optical depth is $\tau = 0.04$. The radial sky plane cover is about 14 000 km.

Since the star involved in the 2021 stellar occultation is bright, a high acquisition rate could be used on some telescopes. The best light curve considering S/N and spatial resolution was obtained at Okazaki/JP, with $\delta_r = 1.2$ km and standard deviation at 1σ level of 0.10. The full-resolution light curve provides a lower limit for the apparent optical depth of $\tau = 0.16$. The light curve resampled over a 99.4 km window has a detection limit of $\tau = 0.02$ and $E'_p \sim 370$ m, with the chord passing distant 25 km from Echeclus center and covering a distance of 9600 km in the sky plane.

6 CONCLUSION AND DISCUSSION

Echeclus, a Centaur with cometary activity, has shown multiple outbursts and has been the subject of extensive observations. In this work, we presented the results of the two successful stellar occultations events by Echeclus in 2020 and 2021, and an appulse in 2019. These observations and recent publications with photometric studies allow us to obtain important physical properties of this Centaur. In addition, better-quality light curves made it possible to probe the surroundings of the object in search of confined or diffuse structures.

Figure 4. Echeclus stellar occultation predicted for 2023 December 09, at 05:09 UT. This event involves a star with a magnitude G = 15.6. More details on this occultation can be found in Lucky Star page. The black lines indicate the Echeclus shadow limits and the red dashed lines indicate the 1σ uncertainty along the shadow path. The black dots are spaced by one minute and the big black dot corresponds to the geocentric closest approach (2023-12-09 05:09:13). The arrow indicates the shadow direction.

We use the 3D model and pole orientation (λ, $\beta = 115.2°$, $21.5°$) for Echeclus from ISAM service and its rotational period (P = 26.785178 ± 10^{-6} h) proposed by Rousselot et al. (2021) to fit the projected limb to the stellar occultation chords. As the 2020 event has two positive chords, we propagate the rotation of Echeclus from the model's reference epoch to the epoch of the occultation. By varying the limb center and scale, we calculate the values for the semi-axes of Echeclus, being: $a = 37.0 \pm 0.6$ km, $b = 28.4 \pm 0.5$ km, and $c = 24.9 \pm 0.4$ km, giving us an area-equivalent radius of 30.0 ± 0.5 km. Using the area of the projected limb and the rotational phase at the occultation epoch, we determine the instantaneous geometric albedo as $p_v = 0.050 \pm 0.003$.

Assuming reasonable densities for Echeclus, we used the method proposed by Holsapple (2001, 2004, 2007), where the relationship between spin, shape, and assumption of certain geological properties was used to constrain the object's internal structure. Echeclus has a triaxial shape with an internal friction angle $8.5° > \phi > 10.5°$. The range of possible densities can be further constrained by assuming further limits for ϕ (Fig. 4). For $\phi = 9°$, Echeclus must have a density of $500 - 1,210$ kg m^{-3}. For $\phi = 10°$, it must have a density superior to 600 kg m^{-3}. Lastly, $8.5° \phi < 10.5°$ must have a density between 500 and 1900 kg m^{-3}. These values indicate that Echeclus comprises ice and silicates, with a low proportion of ice and significant porosity, as rubble-pile or layered-pile (Belton et al. 2007) structures. Based on Rosenberg's study of comet 67P, Rousselot et al. (2021) propose that a layered structure and the internal inhomogeneity of Echeclus may be directly related to the erratic ejections of material observed by this object, with outbursts of different intensity and duration.

We searched for significant flux drops in the stellar occultation light curves, indicating sparsed or confined material around Echeclus. Here, we consider the standard deviation at the 3σ level to be the upper limit for the apparent opacity p′ (on the sky plane), so we can estimate the limits for the actual optical depth τ. In 2019, the best data set gave us an optical depth limit of $\tau = 0.07$, considering structures with a radial width of 2.6 km in the sky plane. In the case of opaque structures, small satellites with a diameter greater than 380 meters would be detectable in the regions probed by the chords.

In 2020, the best light curve allowed structures with a radial width 2.9 km in the sky plane to be detected if they have an optical depth $\tau > 0.15$, or opaque small satellites with a minimum diameter of 800 m. For 2021, structures with a radial width of 1.2 km in the sky plane would be detected with $\tau > 0.16$, or opaque structures with ~370 m in diameter. These values are for the best data sets presented in this work. However, it is clear that the detection limits of opaque structures, such as small satellites, need to be considered individually. Each light curve sweeps a different region of the Echeclus neighbourhoods and is susceptible to detecting a small satellite.

During the detection limit procedure, we observed some points with flux drops greater than the 3σ standard deviation. These notable points were individually analysed against calibration light curves. This eliminates the possibility that these drops were caused by artefacts in the image that were not fully mitigated during the construction of the flux ratio light curve. From this analysis, we noted that these individual points outside 3σ on flux standard deviation are related to passing clouds or seeing degradation. So, if there is scattered material around Echeclus, it does not have enough optical depth to be detected in the light curves of stellar occultations obtained so far.

Finally, observations of new stellar occultations by Echeclus are needed so that the 3D model can be improved. Therefore, multichord stellar occultations are essential. Indeed, a promising event should occur on 2023 December 9, involving a star with magnitude G = 15.8, with the shadow passing over southern Brazil, northern Argentina, and La Serena region in Chile (Fig. 4).

ACKNOWLEDGEMENTS

DATA AVAILABILITY

Data available on request.

REFERENCES

Archinal B. A. et al., 2018, Celest. Mech. Dyn. Astron., 130, 22

Assafin M. et al., 2011, Proccedings Gaia Follow-up Network for Solar System Objects, p. 85.

Astropy Collaboration, 2013, A&A, 558, A33

Bartczak P., Dudziński G., 2018, MNRAS, 473, 5050

Barucci M. A., Doressoundiram A., Cruikshank D. P., 2004, in Festou M. C., Keller H. U., Weaver H. A., eds, Comets II. Univ. Arizona Press, Tuscon, p. 647

Bauer J. M., Choi Y.-J., Weissman P. R., Stansberry J. A., Fernández Y. R., Roe H. G., Buratti B. J., Sung H.-I., 2008, PASP, 120, 393

Bauer J. M. et al., 2013, ApJ, 773, 22

van Belle G. T., 1999, PASP, 111, 1515

Belton M. J. et al., 2007, Icarus, 191, 573

Bérard D. et al., 2017, AJ, 154, 144

Boissel Y. et al., 2014, A&A, 561, A144

Braga-Ribas F. et al., 2013, ApJ, 773, 26

Braga-Ribas F. et al., 2023, A&A, 676, A72

Butcher H., Stevens R., 1981, Kitt Peak Natl. Obs. Newsl., 16, 6

Choi Y. J., Weissman P. R., Polishook D., 2006a, Cent. Bur. Electron. Telegrams, 355, 1

Choi Y. J., Weissman P., Chesley S., Bauer J., Stansberry J., Tegler S., Romanishin W., Consolmagno G., 2006b, Cent. Bur. Electron. Telegrams, 563, 1

Cuzzi J. N., 1985, Icarus, 63, 312

Delrez L. et al., 2018, in Marshall H. K., Spyromilio J., eds, SPIE Conf. Ser. Vol. 10700, Ground-based and Airborne Telescopes VII. SPIE, Bellingham, p. 107001

Desmars J. et al., 2015, A&A, 584, A96

Duffard R. et al., 2014, A&A, 564, A92

Elliot J. L. et al., 1995, Nature, 373, 46

Fernández Y. R., 2009, Planet. Space Sci., 57, 1218

Gaia Collaboration, 2018, A&A, 616, A1

Gaia Collaboration et al., 2022, A&A, 674, 22

Gomes-Júnior A. R. et al., 2022, MNRAS

Holsapple K. A., 2001, Icarus, 154, 432

Holsapple K. A., 2004, Icarus, 172, 272

Holsapple K. A., 2007, Icarus, 187, 500

Jaeger M., Prosperi E., Vollmann W., Sato H., Sostero G., Guido E., 2011, IAU Circ., 9213, 2

James N. D., 2018, J. Br. Astron. Assoc., 128, 51

Jehin E. et al., 2011, The Messenger, 145, 2

Jehin E. et al., 2018, The Messenger, 174, 2

Jewitt D., 2009, AJ, 137, 4296

Kaasalainen M., Torppa J., Muinonen K., 2001, Icarus, 153, 37

Kareta T., Sharkey B., Noonan J., Volk K., Reddy V., Harris W., Miles R., 2019, AJ, 158, 255

Lellouch E. et al., 2017, A&A, 608, A45

Lindegren L. et al., 2018, A&A, 616, A2

Miles R., 2016, CBET, 4313

Morales R. et al., 2022, European Planetary Science Congress, 16, EPSC2022–652

Morgado B. E. et al., 2021, A&A, 652, A141

Morgado B. E. et al., 2023, Nature, 614, 239

Ortiz J. L. et al., 2015, A&A, 576, A18

Ortiz J. L. et al., 2017, Nature, 550, 219

Ortiz J. L. et al., 2023, A&A, 676, L12

Pereira C. L. et al., 2023, A&A, 673, L4

Rousselot P., Korsun P. P., Kulyk I., Guilbert-Lepoutre A., Petit J. M., 2016, MNRAS, 462, S432

Rousselot P. et al., 2021, MNRAS, 507, 3444

Ruprecht J. D., Bosh A. S., Person M. J., Bianco F. B., Fulton B. J., Gulbis A. a. A. S., Bus S. J., Zangari A. M., 2015, Icarus, 252, 271

Sarid G., Volk K., Steckloff J. K., Harris W., Womack M., Woodney L. M., 2019, ApJ, 883, L25

Senay M. C., Jewitt D., 1994, Nature, 371, 229

Shchuko O. B., Shchuko S. D., Kartashov D. V., Orosei R., 2014, Planet. Space Sci., 104, 147

Sicardy B. et al., 2011, Nature, 478, 493

Sickafoose A. A. et al., 2020, MNRAS, 491, 3643

Souami D. et al., 2020, A&A, 643, A125

Stansberry J., Grundy W., Brown M., Cruikshank D., Spencer J., Trilling D., Margot J.-L., 2007, The Solar System Beyond Neptune. Univ. Arizona Press, Tucson, p. 161

Tanga P. et al., 2023, A&A, 674, A12

Tiscareno M. S., Malhotra R., 2003, AJ, 126, 3122

Weissman P. R., Chesley S. R., Choi Y. J., Bauer J. M., Tegler S. C., Romanishin W. J., Consolmagno G., Stansberry J. A., 2006, in AAS/Division for Planetary Sciences Meeting Abstracts #38. p. 37.06

Wierzchos K., Womack M., 2020, AJ, 159, 136

Yasui M., Arakawa M., 2009, J. Geophys. Res. (Planets), 114, E09004

APPENDIX A: ASTROMETRIC POSITIONS

The astrometric positions obtained for Echeclus for the geocentric closest approach instant in each stellar occultation event are presented in A1.

Table A1. Astrometric positions of Echeclus based on the 3D model centre for the geocentric closest approach epoch.

Epoch (UT)	RA	Dec.
2020-01-22 01:44:49.9	$04^h\ 51^m\ 35^s.9201947 \pm 0.146$ mas	$17°\ 48^m\ 18^s.024343 \pm 0.171$ mas
2021-01-19 09:10:44.3	$05^h\ 43^m\ 05^s.0114595 \pm 0.063$ mas	$18°\ 40^m\ 37^s.397107 \pm 0.093$ mas

APPENDIX B: OBSERVATIONAL CIRCUMSTANCES

The observational circumstances for each site involved in the stellar occultation campaigns presented in this work are listed in Table B1.

In total, we have three positive light curves, fourteen negatives, and nine sites with no data provided due to technical problems or a cloudy sky.

Table B1. Observational circumstances for the occultation campaigns between 2019 and 2021. It presents the site name, geographic coordinates, telescope aperture, the detector configuration (filter, exposure time, and cycle), and the observer names.

Site	Latitude (N) Longitude (E) Altitude (m)	Telescope aperture (m) Detector Filter	Exposure time Cycle (s)	Observers	$\sigma_{\rm flux}$ Status
2019 October 29 – South America					
SOAR	−30°14′16.7″	4.1	0.4	J. Camargo	0.035
Cerro Pachón	−70°44′01.0″	Raptor/Merlin127	0.4	A.R. Gomes-Jr	Negative
Chile	2,738	Clear		F. Rommel	
TRAPPIST-South	−29° 15′16.6″	0.6	1.5	E. Jehin	0.020
La Silla	−70° 44′21.8″	FLI PL3041-BB	2.2	E. Ducrot	Negative
Chile	2,337	Clear			
SPECULOOS – South (SSO)	−24° 36′57.9″	1.0	1.0		0.010
Cerro Paranal	−70° 23′26.0″	Andor Tech	2.2	E. Jehin	Negative
Chile	2,479.2	Clear			
Celestial Explorations Observatory	−22° 57′09.8″	0.4	3.0	A. Maury	0.035
San Pedro de Atacama	−68° 10′48.7″	FLI PL16803	4.7	J. Fabrega	Negative
Chile	2,396.9	Clear			
NTT	−29° 15′32.1″	3.58	0.2		0.045
La Silla	−70° 44′01.5″	SofI	0.2	B. Sicardy	Negative
Chile	2,375	H			
ASH2	−22° 57′09.8″	0.4	–		
San Pedro de Atacama	−68° 10′48.7″	STL 11000	–	N. Morales	No data
Chile	2,396.9	Clear			
2020 January 22 – South America					
SOAR	−30°14′16.7″	4.1	0.25	J. Camargo	0.063
Cerro Pachón	−70°44′01.0″	Raptor/Merlin127	0.25	A.R. Gomes-Jr	Positive
Chile	2,738	Clear		F. Rommel	
La Canellila	−30° 32′01″	0.520	0.3		0.152
Limarí	−70° 47′46″	ZWO ASI1600 MM	0.3	M. Meunier	Positive
Chile	1,570	Clear			
Geminis Austral Obs.	−32° 59′3.84″	0.4	2.0		0.152
Rosario	−60° 39′29.28″	ZWO ASI1600 MM	2.0	J. L. Sanchez	Negative
Argentina	22	Clear			
CTIO	−30° 10′03.7″	1.0	0.5		0.031
Cerro Tololo	−70° 48′19.3″	?	1.8	J. Pollock	Negative
Chile	2,286	Clear			
PROMPT P5	−30° 10′03.7″	0.4	0.5		0.115
Cerro Tololo	−70° 48′19.3″	U47-MB	1.2	J. Pollock	Negative
Chile	2,286	Clear			
Santa Martina	−33° 16′09.0″	0.4	1.5	L. Vanzi	0.076
Santiago	−70° 32′04.0″	Raptor/Merlin127	1.5	C. M. Sierralta	Negative
Chile	1,450	Clear			
Córdoba Ast. Obs.	−31° 25′12.2″	0.4	–		No data
Córdoba	−64° 11′55.1″	QHY6	–	R. Artola	Technical
Argentina	427	Clear			Problems
ASH2	−22° 57′09.8″	0.4	–		
San Pedro de Atacama	−68° 10′48.7″	STL 11000	–	N. Morales	No data
Chile	2,396.9	Clear			
Information about all sites					
TRAPPIST-South	−29° 15′16.6″	0.6	–		No data
La Silla	−70° 44′21.8″	FLI PL3041-BB	–	E. Jehin	Overcast
Chile	2,337	Clear			
El Gato Gris Observatory	−31° 21′24.58″	0.35	–		No data
Tanti	−64° 35′34.41″	QHY 174M	–	C. Colazo	Overcast

Table B1 – *continued*

Site	Latitude (N) Longitude (E) Altitude (m)	Telescope aperture (m) Detector Filter	Exposure time Cycle (s)	Observers	σ_{flux} Status
Argentina	864	Clear			
CASLEO (Jorge Sahade Telescope)	−31° 47′54.7″	2.15	–	L. A. Mammana	No data
San Juan	−69° 17′44.1″	Roper Versarray 2048B	–	M. Melita	Overcast
Argentina	2,552.0	Clear			
CASLEO (HSH Telescope)	−31° 47′54.7″	0.6	–	L. A. Mammana	No data
San Juan	−69° 17′44.1″	SBIG STL-1001E	–	M. Melita	Overcast
Argentina	2,552.0	Clear			
NTT	−29° 15′32.1″	3.58	–		No data
La Silla	−70° 44′01.5″	SofI	–	None	Technical Problems/
Chile	2,375.0				Overcast
		2021 January 19 – Japan			
Anan Science Center	33°56′56.2″	0.254	0.0276		0.225
Tokushima	134°40′23.0″	ZWO ASI290MM	0.0278	T. Gondou	Positive
Japan	15.3	Clear			
Hamamatsu	34°43′07.0″	0.250	0.269		0.57
Shizuoka	137°44′23.0″	WAT-120N +	0.300	M. Owada	Negative
Japan	17	Clear			
Toyohashi	34°49′40.2″	0.2	0.246		4.13
Aichi	137°26′09.0″	ZWO ASI290MM	0.246	H. Yamamura	Negative
Japan	8	Clear			
Okazaki	34°56′06.0″	0.2	0.071		0.086
Aichi	137°08′33.2″	ZWO ASI290MM	0.071	M. Ida	Negative
Japan	20	Clear			
Inabe	35°10′14.7″	0.355	0.048		
Mie	136°31′24.7″	ZWO ASI290MM	0.048	A. Asai	Negative
Japan	187	Clear			
Inabe	35°07′10.2″	0.130	0.33		
Mie	136°33′33.9″	WAT-120N	0.33	H. Watanabe	Negative
Japan	92	Clear			
Musashino	35°42′36.9″	0.4	0.013		0.156
Tokyo	139°33′41.3″	ZWO ASI290MC	0.013	K. Kitazaki	Negative
Japan	66	Clear			
Kashiwa	35°52′08.44″	0.250	0.033		0.114
Chiba	139°58′50.67″	WAT-910HX	0.033	S. Uchiyama	Negative
Japan	20	Clear			
Chichibu	35°58′04.5″	0.4	visual		
Saitama	139°01′59.6″	No cam	visual	A. Hashimoto	Negative
Japan	355	No filter			
National Museum of Nature and Science	36°06′05.1″	0.5	0.033		
Ibaraki	140°06′40.7″	WAT-910HX	0.033	T. Horaguchi	Negative
Japan	40	Clear			
Toshima-ku	35°44′14.2″	0.3	–		
Tokyo	139°44′35.8″	WAT-910HX	–	N. Sasanuma	No data
Japan	31	Clear			

APPENDIX C: DETECTION LIMITS

Table C1 presents the results from detection limits determination calculated as explained in Section 5. W stands for width in the sky plane (δ_r for original resolution light curves), $\tau = \tau'/2$ is the optical depth, obtained from $\tau' = -\ln(1 - p'(3\sigma))$, and E'_p is the apparent equivalent width. The sky cover is not necessarily centered in the body's position.

Table C1. Detection limits calculated for all light curves provided in this work for original spatial resolution and resampled data.

Date	Site	Original resolution			Re-sampled data		Sky cover (km)
		δ_r (km)	τ	E'_p (km)	W (km)	τ	
	SOAR	5.3	0.06	0.65	94.8	0.02	12,397
	San Pedro de Atacama	39.6	0.06	4.47	79.1	0.04	30,970
2019-10-29	TRAPPIST-South	19.8	0.03	1.28	98.8	0.02	9,385
	SPECULOOS-South Obs. (SSO) – Io	13.2	0.02	0.44	92.3	0.01	9,851
	NTT	2.6	0.07	0.38	97.5	0.01	7,122
	CTIO	5.7	0.05	0.59	92.8	0.01	14,210
	PROMPT-P5	5.7	0.21	2.21	97.8	0.05	9,930
2020-01-22	SOAR	2.9	0.15	0.80	97.8	0.04	13,809
	Santa Martina	17.2	0.13	4.38	86.2	0.06	13,782
	La Canelilla	3.4	0.28	1.79	96.7	0.06	1,723
	Anan Sci. Center	0.5	0.39	0.32	99.7	0.02	576
	Hamamatsu	2.6	0.11	0.54	96.5	0.02	2,031
	Toyohashi	4.2	0.08	0.69	96.5	0.02	9,207
2021-01-19	Okazaki	1.2	0.16	0.37	99.4	0.02	9,614
	Kashiwa	0.6	0.24	0.24	99.9	0.09	3,093
	Musashino	2.2	0.14	0.59	99.0	0.02	14,359
	Inabe	4.6	0.14	1.24	96.0	0.04	3,498
	National Museum of Nat. and Sci.	0.6	0.16	0.17	99.4	0.02	3,718

APPENDIX D: LIGHT CURVES

We present the light curves of the radial distance from Echeclus center versus flux (Figs D1, D2, and D3) with all data sets provided by observers, be positive or negative detections. These light curves are organized in these plots from north to south. Data recording at some sites was interrupted just before the local closest approach, for this reason, they are not shown in this graph. Also, we remove the data points within the ingress and egress interval to better view the flux standard deviation at 3σ level (detection limits for apparent opacity).
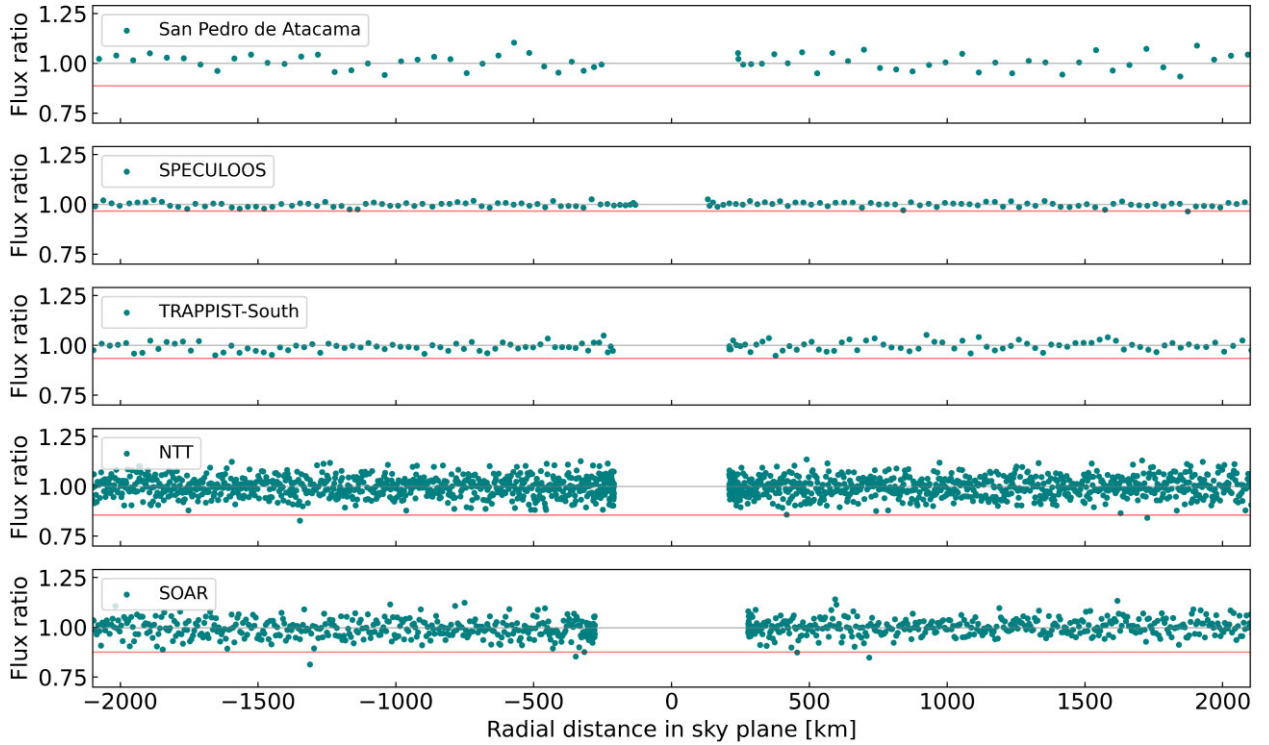
Figure D1. Light curves obtained on 2019 Echeclus appulse, with normalized flux plotted against radial distance in the sky plane. The grey horizontal line indicates the mean flux and the red horizontal line presents the depth of an occultation caused by a structure with apparent opacity p'(3σ).
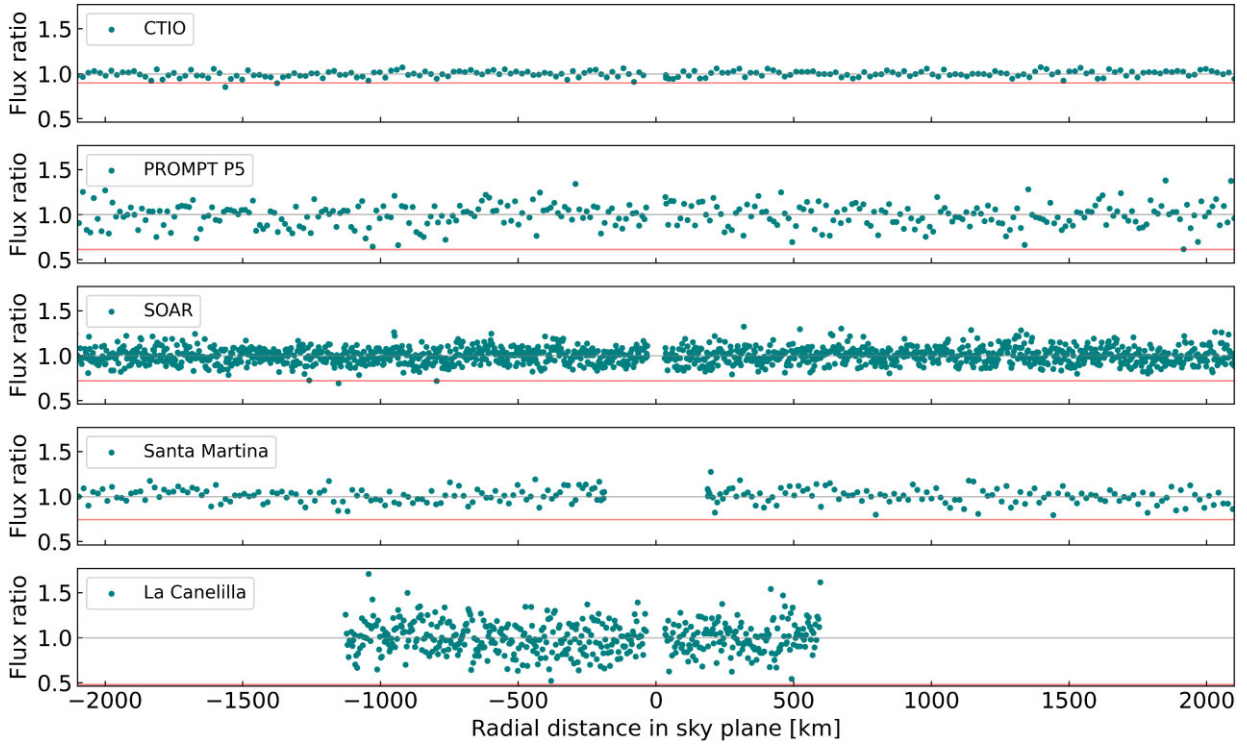
Figure D2. Light curves obtained on 2020 occultation event, with normalized flux plotted against radial distance in the sky plane. The grey horizontal line indicates the mean flux, and the red horizontal line presents the depth of an occultation caused by a structure with apparent opacity p'(3σ). The detection of the main body in the SOAR and La Canelilla light curve was omitted in this analysis.
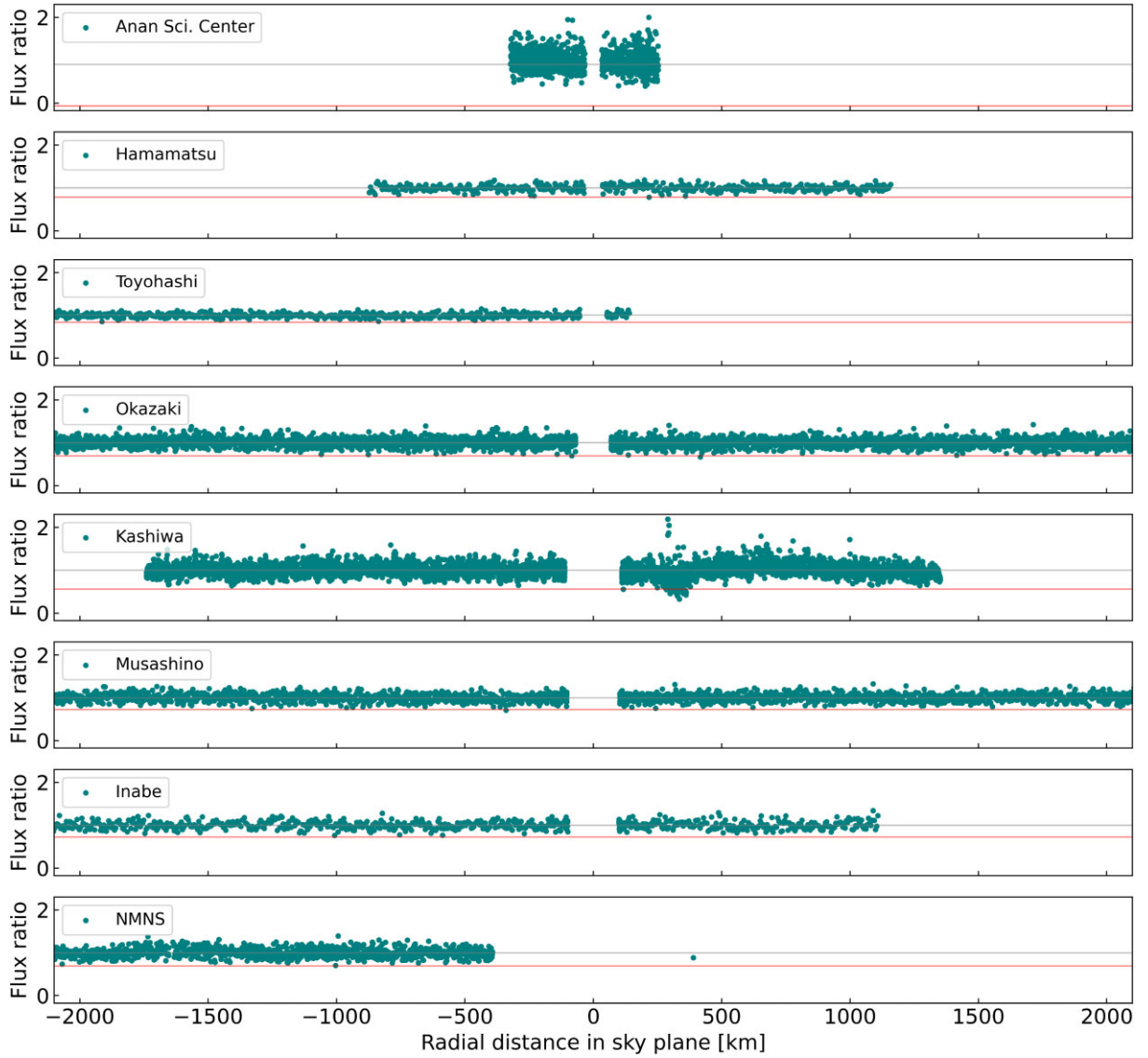
Figure D3. Light curves obtained on 2021 stellar occultation, with normalized flux plotted against radial distance in the sky plane. The grey horizontal line indicates the mean flux, and the red horizontal line presents the depth of an occultation caused by a structure with apparent opacity p′(3σ). The detection of the main body at the Anan Science Center light curve was omitted in this analysis. The Toyohashi acquisition ended just after the closest approach, hence the lack of data in the graph. The same occurred with the National Museum of Nature and Science data, with the acquisition about 400 km outside the expected closest approach position.

APPENDIX E: MODELED LIGHT CURVES

Positive light curves were modeled with the Fresnel scale, exposure time, star apparent diameter, and square-well model to determine the instants of ingress and egress (Table 3). Fig. E1 presents these modeled light curves in more detail.
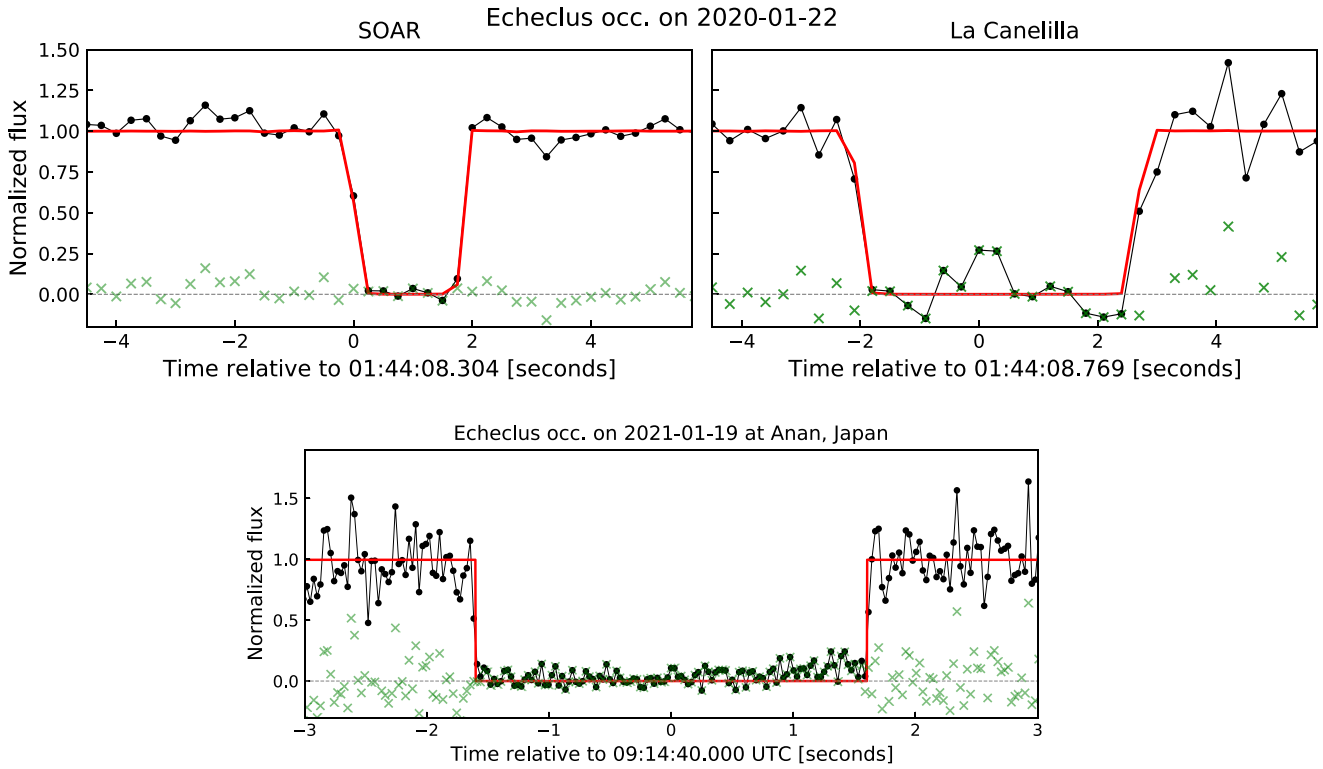
Figure E1. Modelled light curves for 2020 (top) and 2021 (bottom) stellar occultations. The black curve represents the data, and the red curve is the modelled light curve. The green markers represent the residuals. The zero instant in graphs is the closest approach in each site.

APPENDIX F: OCCULTATION MAPS

The Figs F1, F2, and F3 contain the maps of 2019, 2020, and 2021 occultations, showing the shadow's path and the geographical position of all the sites involved in observations.
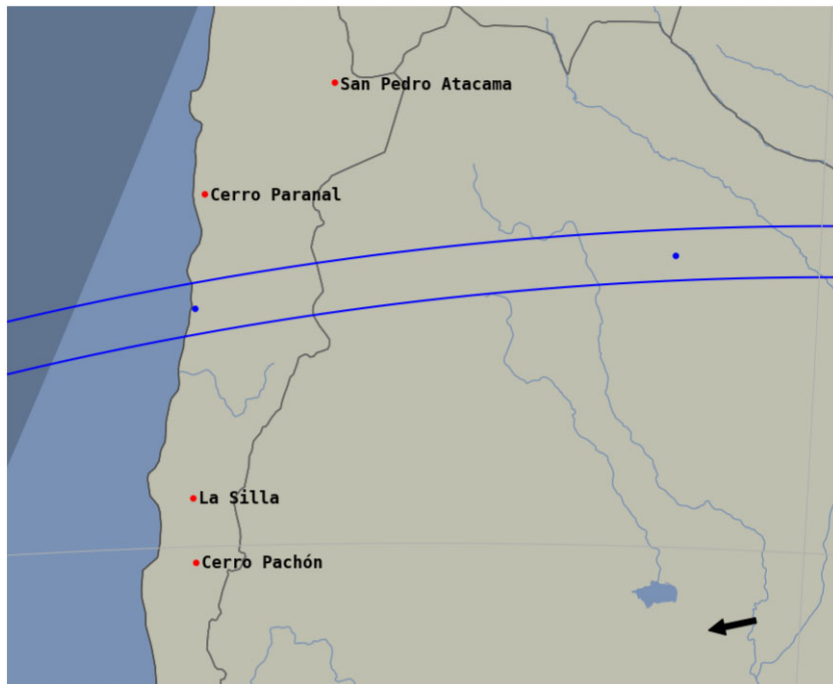
Figure F1. Map with the theoretical shadow's path of the 2019 appulse represented by the blue lines. The sites that participated of this observational campaign are indicated by the red markers.

Figure F2. Map of the event observed on 2020 January 22. The green dots represent the sites that successfully observe the occultation. The sites which not detect this event are represented in red (observed, but no event was seen), white (overcast), and yellow (technical problems). The blue lines represent the Echeclus shadow path, and the arrow shows the direction of shadow movement.
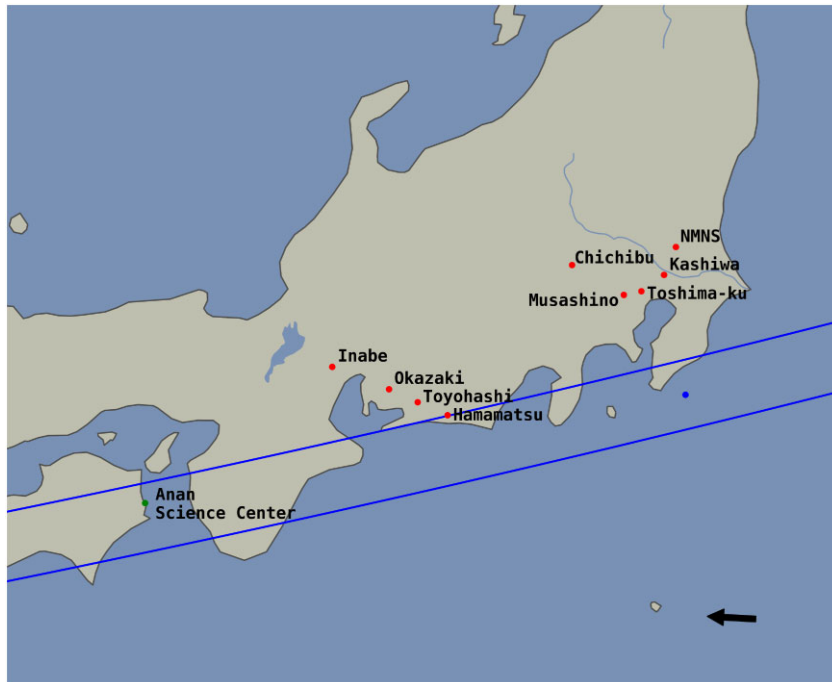
Figure F3. Map of the event observed on 2021 January 19. The green dot represents the site that successfully observes the occultation. The sites not detecting this event are represented by red dots (observed, but no event was seen). The blue lines represent the Echeclus shadow path, and the arrow shows the direction of shadow movement.

[1] *Observatório Nacional/MCTI, R. General José Cristino 77, CEP 20921-400 Rio de Janeiro - RJ, Brazil*

[2] *Laboratório Interinstitucional de e-Astronomia - LIneA, Av. Pastor Martin Luther King Jr 126, CEP: 20765-000 Rio de Janeiro, RJ, Brazil*

[3] *Federal University of Technology - Paraná (UTFPR-Curitiba), Rua Sete de Setembro, 3165, CEP 80230-901, Curitiba, PR, Brazil*

[4] *LESIA, Observatoire de Paris, Université PSL, Sorbonne Université, Université de Paris, CNRS, 92190 Meudon, France*

[5]*Institute of Physics, Federal University of Uberlândia, Av. Joao Naves de Avila, CEP 38408-100, Uberlândia-MG, Brazil*

[6]*UNESP - São Paulo State University, Grupo de Dinâmica Orbital e Planetologia, CEP 12516-410, Guaratinguetá, SP, Brazil*

[7]*Instituto de Astrofísica de Andalucía - Consejo Superior de Investigaciones Científicas, Glorieta de la Astronomía S/N, E-18008, Granada, Spain*

[8]*Space Science and Technology Centre, Curtin University, Kent Street, Bentley, Perth, Western Australia 6102, Australia*

[9]*Universidade Federal do Rio de Janeiro - Observatório do Valongo, Ladeira Pedro Antônio 43, CEP 20.080-090, Rio de Janeiro - RJ, Brazil*

[10]*Institut Polytechnique des Sciences Avancées IPSA, 63 boulevard de Brandebourg, 94200 Ivry-sur-Seine, France*

[11]*Institut de Mécanique Céleste et de Calcul des Éphémérides, IMCCE, Observatoire de Paris, PSL Research University, CNRS, Sorbonne Universités, UPMC Univ Paris 06, Univ. Lille, France*

[12]*Universidade Estadual de Ponta Grossa, Av. General Carlos Cavalcanti - Uvaranas CEP 84030-000, O.A. - DEGEO, Ponta Grossa (PR), Brazil*

[13]*Japan Occultation Information Network (JOIN), Japan*

[14]*International Occultation Timing Association - East Asia, 281, Kasadashinden, Inabe, Mie, 511-0205 , Japan*

[15]*STAR Institute, University of Liège, Allée du 6 avril, 19C, B-4000 Liège, Belgium*

[16]*Obs. Ast. Córdoba, Universidad Nacional de Córdoba-CONICET Laprida 854, X5000 BGR, Córdoba, Argentina*

[17]*Observatorio Astronómico El Gato Gris, San Luis CPA X5155DXA, Tanti - Valle de Punilla - Córdoba - Argentina*

[18]*AIM, CEA, CNRS, Université Paris-Saclay, Université de Paris, 91191 Gif-sur-Yvette, France*

[19]*Panamanian Observatory in San Pedro de Atacama - OPSPA, San Pedro de Atacama, Chile*

[20]*Florida Space Institute, UCF, 12354 Research Parkway, Partnership 1 building, Room 211, Orlando, USA*

[21]*Astrobiology Research Unit, Université de Liège, Allée du 6 Août 19C, B-4000 Liège, Belgium*

[22]*National Museum of Nature and Science, 4-1-1 Amakubo, Tsukuba, Ibaraki 305-0005, Japan*

[23]*Complejo Astronómico El Leoncito (CASLEO), Av. España 1512 Sur J5402DSP, San Juan, Argentina*

[24]*San Pedro de Atacama Celestial Explorations - SPACE, Solor, San Pedro de Atacama, Chile, Chile*

[25]*Instituto de Astronomía y Fiísica del Espacio, (CONICET-UBA), Intendente Güiraldes S/N, CABA, C1428ZAA, Argentina*

[26]*Facultad de Ciencias Astronómicas y Geofiísicas, Universidad Nacional de La Plata, Paseo del Bosque S/N, La Plata, B1900FWA, Argentina*

[27]*Instiuto de Tecnologia e Ingeneria, UNAHUR, Vergara 2222, Hurlingham, Prov. de Buenos Aires, Argentina*

[28]*Instituto de Astrofísica, Facultad de Física, Pontificia Universidad Católica de Chile, Av. Vicuña Mackenna 4860, Santiago, Chile*

[29]*Physics and Astronomy Department, Appalachian State University, Boone, NC 28608, USA*

[30]*Estación Astrofísica Bosque Alegre, Córdoba, Argentina*

[31]*School of Physics & Astronomy, University of Birmingham, Edgbaston, Birmingham B15 2TT, UK*

[32]*Department of Electrical Engineering and Center of Astro Engineering, Pontificia Universidad Católica de Chile, Av. Vicuña Mackenna 4860, Santiago, Chile*

This paper has been typeset from a TEX/LATEX file prepared by the author.

Appendix C

Centaur 29P/Schwassmann-Wachmann 1 and its near-nucleus environment from a stellar occultation

Research

CrossMark
click for updates

Author for correspondence:

Chrystian Luciano Pereira

e-mail: chrystianpereira@on.br

Centaur 29P/Schwassmann-Wachmann 1 and its near-nucleus environment from a stellar occultation

C. L. Pereira[1,2], F. Braga-Ribas[3,2], B. Sicardy[4], B. E. Morgado[5,2], J. L. Ortiz[6], M. Assafin[5,2] R. Miles[7], J. Desmars[8,9], J. I. B. Camargo[1,2], G. Benedetti-Rossi[10,2], M. Kretlow[6], R. Vieira-Martins[1,2]

[1] Observatório Nacional/MCTI, Rio de Janeiro, RJ, Brazil; [2] Laboratório Interinstitucional de e-Astronomia - LIneA, Rio de Janeiro, RJ, Brazil; [3] Federal University of Technology - Paraná (PPGFA/UTFPR), Curitiba, PR, Brazil; [4] LESIA, Observatoire de Paris, Université PSL, Sorbonne Université, Université de Paris, CNRS, 92190 Meudon, France; [5] Universidade Federal do Rio de Janeiro - Observatório do Valongo, Rio de Janeiro, RJ, Brazil; [6] Instituto de Astrofísica de Andalucía – Consejo Superior de Investigaciones Científicas, Granada, Spain; [7] British Astronomical Association, United Kingdom; [8] Institut Polytechnique des Sciences Avancées IPSA, 94200 Ivry-sur-Seine, France; [9] Institut de Mécanique Céleste et de Calcul des Éphémérides, IMCCE, Observatoire de Paris, PSL Research University, CNRS, Sorbonne Universités, UPMC Univ Paris 06, Univ. Lille, France; [10] UNESP - Sao Paulo State University, Grupo de Dinamica Orbital e Planetologia, Guaratinguetá, SP, Brazil;

Comets offer valuable insights into the early Solar System's conditions and processes. Stellar occultations enables detailed study of cometary nuclei typically hidden by their coma. Observing the star's light passing through the coma helps infer dust's optical depth near the nucleus and determine dust opacity detection limits. 29P/Schwassmann-Wachmann 1, a Centaur with a diameter of approximately 60 km, lies in a region transitioning from Centaurs to Jupiter-Family comets. Our study presents the first-ever occultation by 29P, refining its orbit and predicting future occultations more precisely. We identified features around 1,700 km from the nucleus in the sky plane for which upper limits on apparent opacity and equivalent width were determined. Gradual dimming within 23 km of the nucleus during ingress only is interpreted as a localised dust cloud above the surface, with an optical depth of approximately $\tau = 0.18$.

THE ROYAL SOCIETY
PUBLISHING

1. Introduction

Comets, as remnants from the early Solar System, provide invaluable insights into the conditions and processes that shaped our celestial neighbourhood. They are typically classified into two categories based on their orbital characteristics: long-period comets (LPC), which have orbits lasting thousands to millions of years and come from the Oort Cloud, a region of icy bodies at the edge of the Solar System, and short-period comets, as the Jupiter-Family Comets (JFC, comets that are dynamically affected by Jupiter), which have orbits of less than 200 years and originate from the Kuiper Belt region. During the inward drift of a Kuiper Belt Object (KBO) to become a JFC, these bodies can be trapped in chaotic orbits between Jupiter and Neptune, being part of the Centaur class (1).

The object designated 29P/Schwassmann-Wachmann 1 (hereafter 29P) has captivated astronomers' attention due to its intriguing behaviour and dynamic nature. It was discovered in 1927 at Hamburg Observatory, Germany, by Arnold Schwassmann and Arno Arthur Wachmann while active and was then classified as a comet. The estimated diameter of 29P varies according to different sources: (2) provide a value of 40 ± 5 km based on thermal measurements; (3) estimate it to be 54 ± 10 km; (4) from WISE measurements estimate it to be 46 ± 13 km, and (5) estimate a diameter of $D = 60.4^{+7.4}_{-5.8}$ km. It orbits the Sun in a quasi-circular orbit with a semi-major axis of $a = 5.98$ au, and low inclination $i = 9.4°$, with an orbital period of approximately 14 years (JPL K192/80). So, disregarding the frequent material ejections by the nucleus, we find the 29P in the Centaur classification. More precisely, this object lies in a region called "Gateway" - where the objects are transitioning from Centaurs to the JFC (6).

Stellar occultations, the passage of a Small Solar System Body in front of a star, offer a unique opportunity to study the cometary nuclei in detail, usually hidden beneath their coma. By observing the star's light as it passes through the cometary coma, astronomers can infer the optical depth of the dust close to the nucleus or determine detection limits for the dust opacity (7). As an active comet presents an extensive coma, the photo centre of the object can not be retrieved accurately. This implies low precision in the comet astrometric position and significant errors in the stellar occultation predictions. This problem is overcome when occultation by the cometary nucleus is detected.

This work presents the results of the first-ever occultation by 29P, which results in determining the astrometric position with accuracy never achieved for this body. This allows the orbit refinement and more precise stellar occultation predictions to be made. We also searched for additional material in the object's vicinity, identifying some features at distances of about 1,700 km from the nucleus. The gradual dimming of the star during the ingress was interpreted as a dust cloud close to the nucleus extending at least 23 km above the surface, with an optical depth $\tau' = 0.18 \pm 0.02$. We also determine upper detection limits on apparent opacity and apparent equivalent width.

2. Prediction and observation

The stellar occultation investigated in this work was predicted by the Lucky Star project using Numerical Integration of the Motion of an Asteroid (NIMAv2, based on 559 Earth-based direct observations) ephemeris[1] (8) and Gaia Data Release 3 (Gaia DR3) sources (9). The shadow path was predicted to cross the central regions of Chile and Argentina on December 05, 2022, at 08:14:19 UTC, as presented in Figure 1. The star (Gaia DR3 888441442906065536 source) has a magnitude G = 16.9. This source's Re-normalised Unit Weight Error (RUWE)[2] equals 1.027, and there is a false flag for duplicity. At the time of the event, the apparent motion of the comet projected on the sky plane was 0.24"/min in p.a. 274°, which equates to a geocentric velocity of 14.8 km/s, giving an expected maximum duration for the centrality of 4.1 seconds for a body diameter of 60 km (5). The star's equatorial coordinates were propagated to the event epoch using the proper motion and parallax (11), resulting in the geocentric position:

---

[1]https://lesia.obspm.fr/lucky-star/obj.php?p=997
[2]The Renormalised Unit Weight Error (RUWE) is a measure of the reliability of a single-star model derived from observations. A value close to 1 is typically expected. Values exceeding 1.4 could indicate that the source is not a single star or that there are problems with the astrometric solution (10).)
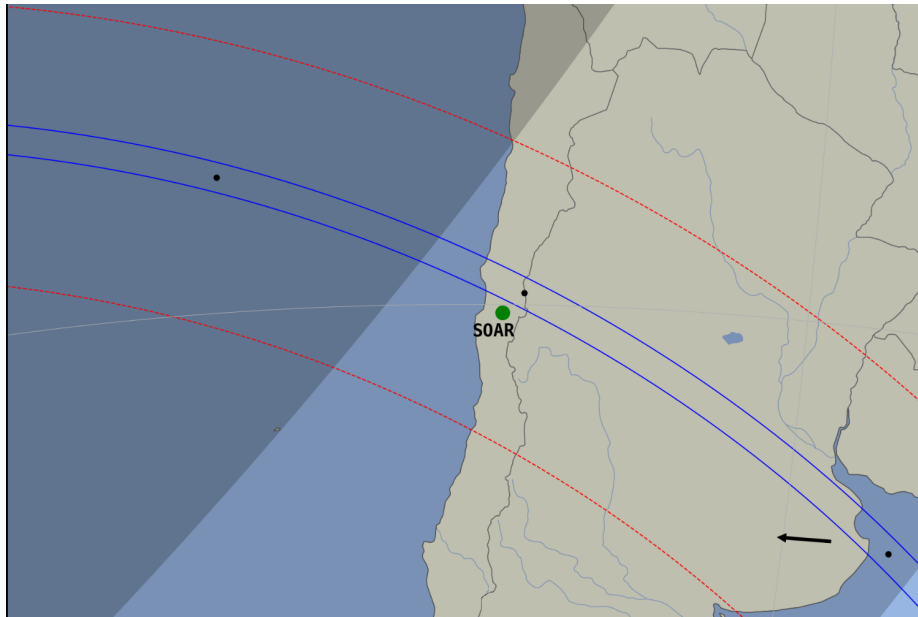
Figure 1. Prediction map with the shadow path considering the estimated radius (blue continuous lines). The black dots are separated by 60 seconds from each other. The dashed red line limits the 1σ uncertainty in the path. The arrow indicates the shadow direction of movement. The first version of this prediction was published on the Lucky Star web page.

$$\text{RA}: 6^h\,50^m\,43.88513^s \pm 0.4939\,mas,$$
$$\text{DEC}: +29°\,23'\,47.8773'' \pm 0.4999\,mas.$$

Before the event, the nucleus of 29P exhibited its three strongest outbursts of 2022, namely on 2022 Nov 21.95 ± 0.30, 2022 Nov 27.69 ± 0.15, and on 2022 Nov 29.15 ± 0.03, the latter just 6.2 days before the predicted occultation (data from MISSION 29P[3]). This enhanced activity increased the likelihood that residual ejecta remained in a temporary orbit close to the nucleus.

The observation occurred at the Southern Astrophysical Research Telescope (hereafter SOAR), located at Cerro Pachón, Chile. This telescope has a diameter of 4.1-meter and Ritchey-Chrétien f/16 optics. The images were acquired in Flexible Image Transport System (FITS) format using the SOAR visitor instrument Raptor 247 Merlin camera with a field-of-view of approximately 1.2'x0.9' and with GPS as a time source. The data set contains 2,998 science images with 0.5 seconds of exposure time and about 100 calibration images to correct biases and pixel-to-pixel sensitivity variations. The dead time of the Raptor camera is negligible.

3. Data Analysis and instants determination

The initial data set undergoes meticulous calibration through the classical correction by flat and bias frames using the Image Reduction and Analysis Facility (IRAF, 12). This procedure ensures the reduction of artefacts and inaccuracies introduced during image acquisition. Photometric analysis is then conducted on these calibrated frames using the Package for the Reduction of Astronomical Images Automatically photometric task (PRAIA, 13).We detect contamination from the cometary coma during the aperture photometry performed on the target star. To effectively eliminate this contamination and obtain a light curve without significant interference from the scattered light of the coma entering the photometric aperture, we process each image in the data set individually.

[3]https://britastro.org/section_information_/comet-section-overview/mission-29p-2

The x and y positional data obtained from the photometric analysis are employed to align the stars within the images precisely. These aligned frames isolate the relative motion of the moving body, thereby facilitating a focused analysis of their behaviour against the fixed stellar background. Assuming that the object's trajectory appears as a straight line within the observed field, we can fit a first-degree polynomial to obtain theoretical positions in each frame, enhancing the precision of subsequent analysis. Using these theoretical positions, a composite frame is generated using median stacking, offering a clear representation of the cometary coma. The last step is subtracting this stacked frame from each frame, as exemplified in Figure 2.
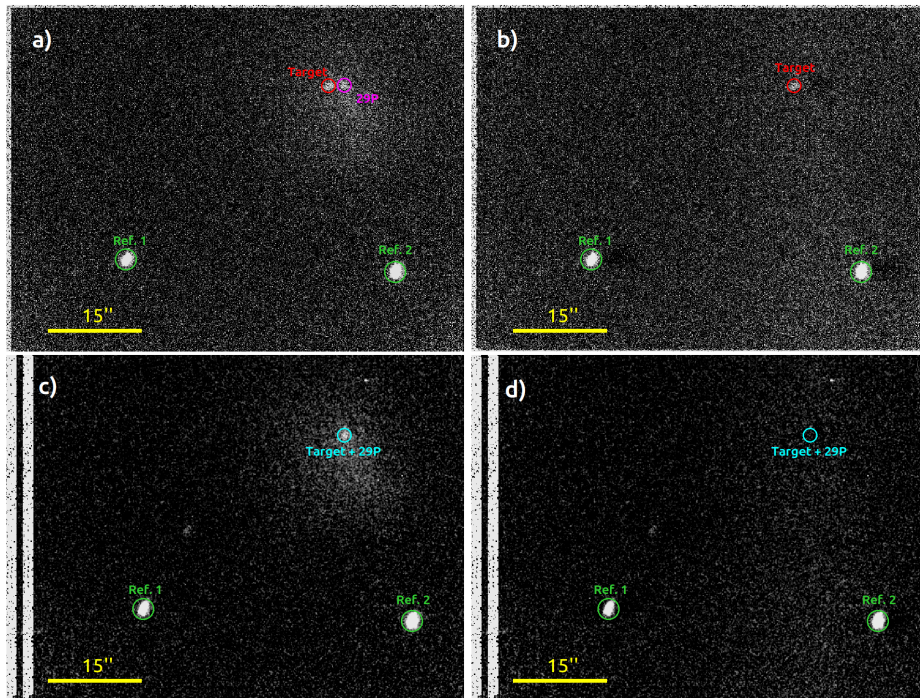
Figure 2. Elimination of the contamination from the cometary coma. First frame of the data set before (a) and after (b) the coma removal process. The frames c and d are in the central instant for the occultation, before and after the coma removal process, respectively. The red circle indicates the target star separated from the occulting body (magenta region). The cyan regions show the target star plus occulting body flux. The green regions indicate the reference stars used during the differential aperture photometry. Each frame has a field of view (FOV) of $\sim 1.2' \times 0.9'$.

Finally, we can perform the differential aperture photometry using the coma-eliminated frames. The target star flux was measured with a circular aperture, and the other two stars in the field were used as calibrators to mitigate the sky's fluctuations. To normalise the light curve, we follow these steps: i) From photometry, we obtain the target and the calibrators' fluxes (ADU), both corrected from the sky background; ii) These fluxes were normalised by dividing them by their respective medians, thus not affected by the outliers. We call this light curve un-detrended; iii) Using the Savitzky-Golay (SG) digital filter, we calculated the trend of these systematic flux variations using windows of 135 seconds ($\sim 1,000$ km, for an average spatial resolution of 7.4 km) in the outer regions of the occultation. Subsequently, we interpolated the region within the occultation using a polynomial function; iv) By diving the un-detrended light curve by the SG resampled light curve, we obtained the detrended light curve, where the systematic low-frequency flux variations were removed. A similar approach was used to decrease the systematic variations in transit light curves, improving the detection of exoplanets (14). The results of the coma removal and normalisation processes are presented in Figure 3. The current methodology excludes diffuse and broader structures. This intentional decision corrects slow variations in

the light curve, although it may not consider the presence of diffuse material around the body extinguishing the stellar flux.
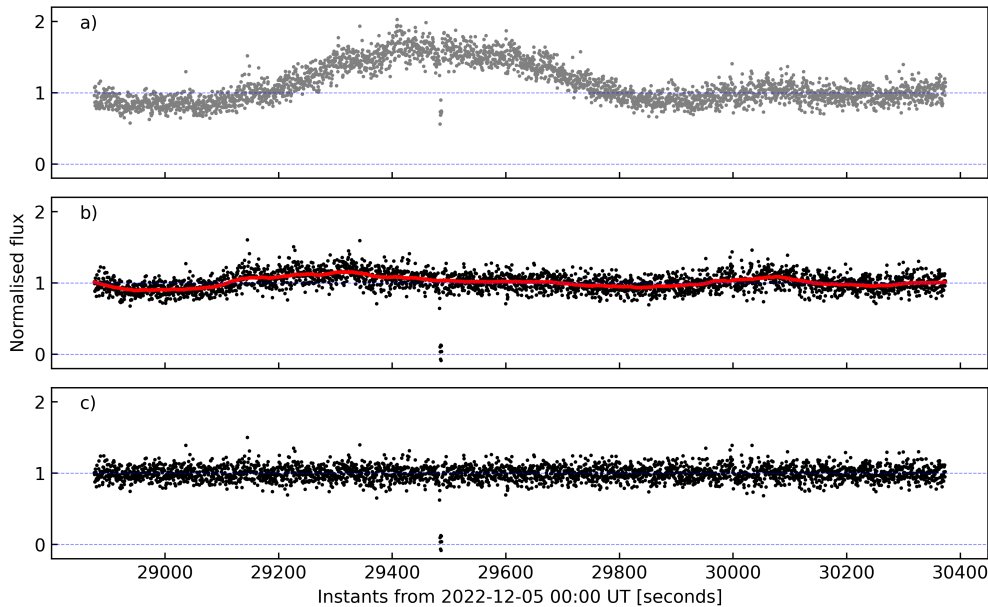
Figure 3. Light curves obtained from the aperture photometry. a) light curve obtained from images before the cometary coma is removed. b) Un-detrended light curve (black dots) obtained from differential photometry in the frames corrected from cometary coma plotted over the resampled light curve obtained with the Savitzky-Golay (SG) digital filter (red). c) Normalised light curve after the detrending process.

We can now obtain the ingress and egress instants of the star behind the nucleus from the normalised light curve using the algorithms built using the Stellar Occultation Reduction and Analysis (SORA, 11) package. A synthetic light curve is built considering an occultation by a sharp edge box convolved with the Fresnel diffraction, the apparent star diameter, observation wavelength, and the exposure time. Thus, we generate 100,000 models and fit them to the observed light curve using the χ^2 statistics, resulting in the best model and their uncertainties. The ingress and egress instants are 08:11:23.00 $\pm$ 0.06 UT and 08:11:26.64 $\pm$ 0.07 UT, with an occultation duration of 3.65 $\pm$ 0.05 seconds and length of 54.0 $\pm$ 1.5 km. The minimum chi-square per degree of freedom is $\chi^2_{pdf} = 0.902$. The instrumental response dominates this light curve (0.5 seconds or 7.42 km). The calculated value for the Fresnel scale effect is 0.035 seconds or 0.52 km, and the star diameter effect is 0.013 km (for a star apparent diameter from (15)). The best-fitted model is presented in Figure 4.

4. Event geometry

Each chord extremity represents the intersection between the star position from an observer's point-of-view and the occulting body's silhouette. We can fit a circle to the chord extremities with only a single positive detection by varying the centre. For that we use the equivalent radius of $R_{equiv} = 30.2^{+3.7}_{-2.9}$ km obtained with *Spitzer* (5). Two possible solutions for the circle's centre position (f_0, g_0) are possible: the north (resp. south) solution, with the centre located on the north (resp. south) side of the chord. The best-fitted circles are presented in Figure 5. The purple circle (south solution) has centre position $f_0 = -6.5 \pm 0.8$ km and $g_0 = -67.1 \pm 1.7$ km, and the black circle (north solution) has centre positions $f_0 = -4.8 \pm 0.7$ km and $g_0 = -43.1 \pm 1.7$ km. As north and south solutions are possible, both should be used as astrometric positions of 29P for orbit fit
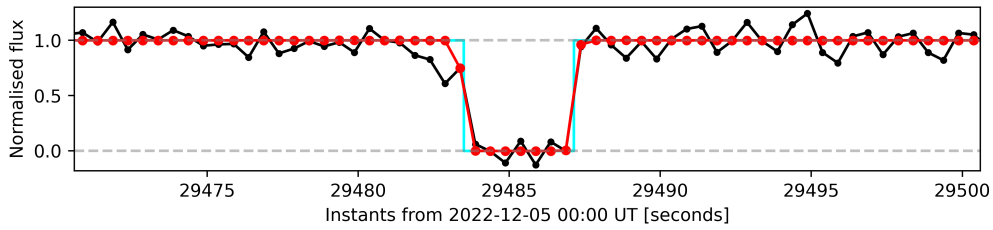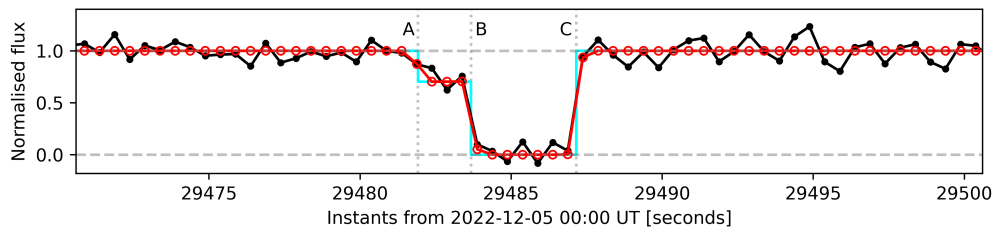
Figure 4. Modelled light curve (red) that best fits the observed data (black). The cyan curve represents the square-well model. Note the gradual drop in flux in the ingress region, explained in Section 5.
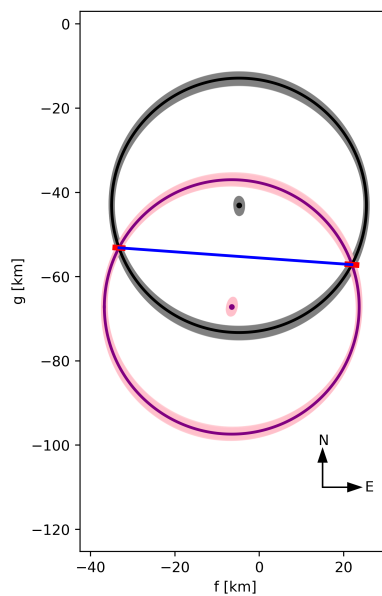
Figure 5. Two circles fitted to the SOAR chords showing the possible solutions for the 29P centre at event epoch. The south (resp. north) solution is in purple (resp. black), with the 1σ uncertainty in light purple (resp. grey) for the centre and the circular limb.

(16), before further observations can show that one is preferable. Note that the difference between the two positions is only 6 mas; therefore, they represent a better position than those we can have from ground observation. The astrometric geocentric positions of 29P on 2022 December 05, at 08:14:19.9 UT, are presented in Table 1.

5. Gradual star dimming at ingress

We observe a gradual decline in flux during the ingress of the star behind the nucleus that appears absent at egress. This can be interpreted as 1) the star gradually occulted by the opaque body, revealing topographic features on the limb, or 2) a dense dust cloud close to the nucleus that partially blocks the stellar flux.

Considering that the SOAR chord is close diametrical, a semi-transparent structure of ∼23 km over the limb of a ∼60 km would be needed. Therefore, we analyse this feature as a semi-transparent screen representing a dust cloud over the surface. A topography hypothesis seems

Solution	Right ascension (h m s) Declination (° ′ ″)	Astrometric uncertainty (mas)
North	6 50 43.8769153	±0.523
	+29 23 46.530272	±0.659
South	6 50 43.8768801	±0.530
	+29 23 46.523902	±0.652

Table 1. Astrometric positions for the two solution of 29P centre for the geocentric closest approach epoch 2022 December 05 08:14:19.9 UT.

unlikely because we do not know the exact event geometry. Figure 6 presents the step-wise model fitted to the semi-transparent structures plus opaque nucleus.

Figure 6. Modelled light curve (red) that best fits the observed data (black). The cyan curve represents the step-wise model for the semi-transparent screen blocking the stellar flux (segment A to B) right before the occultation by the nucleus (B to C).

This modelling is analogous to the procedure described in Section 3, but besides the times of ingress and egress, we vary the box's opacity for the gradual dimming. The best synthetic light curve was obtained by χ^2 statistics comparing the 100,000 generated models with the observed light curve, with the 1σ marginal error bar determined by the interval of $\chi^2_{min} + 1$. The fitted semi-transparent box can be interpreted as a cloud of dust at a height of 23.4 km from the nucleus limb with an optical depth $\tau = 0.18 \pm 0.02$ (this optical depth takes into account the Airy diffraction (see 17)). Note that the occultation by the nucleus (segment BC) presents a slightly smaller chord length (∼51.7 km) when compared with the previous fit, disregarding the gradual flux variation (Sec. 3), which is not significant for the astrometric position.

6. Detection limits on additional material

Equivalent width was employed to determine detection limits for additional material in light curves with arc detections (18) during Neptune's stellar occultations (1983-1989). A similar approach was used to establish upper limits for structures around Pluto (19), Chariklo (20; 21), Quaoar (22; 23), Chiron (24), and Echeclus (25). The equivalent width is defined as the width of an opaque strip that blocks the same amount of stellar light that a semi-transparent structure with width W_r. This quantity does not depend on the stellar apparent diameter or diffraction since both effects conserve energy (18).

The upper limit on apparent equivalent width (apparent because we do not have a pole orientation for 29P, thus calculated on the sky's plane) is calculated by transforming the flux versus time light curve to apparent equivalent width $E'(i)$ versus the radial distance in the sky plane using

$$E'(i) = [1 - \phi(i)]\Delta r(i), \tag{6.1}$$

where $\phi(i)$ is the normalised flux, $\Delta r(i)$ is the radial distance between consecutive points projected in the sky plane, and i is the number of frames. Then, the 3σ average deviation is

calculated in the regions outside the main body occultation. The resulting curve is presented in Figure 7, depicting $E'(i)$ against radial distance. Similarly, we calculated the 3σ average deviation of the stellar flux $\phi(i)$ to determine the upper limits on apparent opacity. The 3σ upper limit on apparent equivalent width and apparent opacity is $E'(i) \sim 2.3$ km and $p' \sim 0.3$, covering a radial distance in the sky plane of 16,000 km (or 4.3 arc-seconds) centred in the 29P. This implies that any structure with intermediate solutions between these two extreme cases would be detectable: an opaque structure with a width of about 2.3 km or a semi-transparent structure with a width of $W_\perp \sim 7.4$ km (light curve mean spatial resolution) and with an apparent opacity $p' \sim 0.3$.
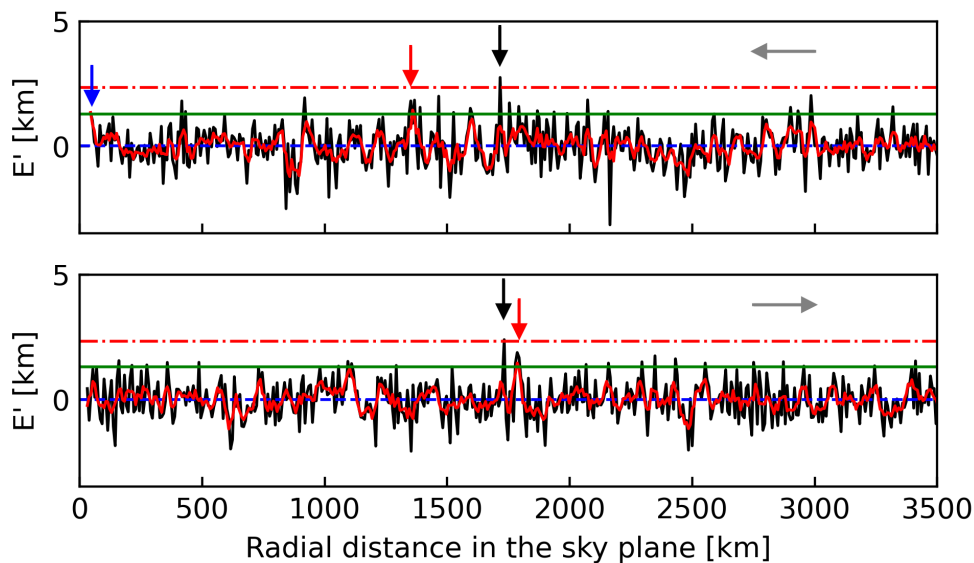
Figure 7. Apparent equivalent width as a function of the radial distance for the regions prior (top panel) and post (bottom panel) closest approach, covering a total of 7,000 km in the sky plane. The grey horizontal arrows indicate the time evolution. The blue-dashed line indicates the mean of the E' distribution, and the red-dot-dashed line presents the 3σ upper limit of E'. The green horizontal line indicates the 3σ upper limit for the 25 km-resampled curve (red). The arrows show the identified features over the upper limits for the full-resolution (black) and resampled (red) curves. We can also see the dust cloud (Section 5) in the 25 km-resampled curve (blue arrow).

We identified features above the 3σ cut at an average distance of 1,730 km from the object's centre, assuming that this centre is the mean value between the two possible circular solutions. At the ingress region (before the main event), the feature has $E' = 2.8$ km (3.6σ) at 1,715 km in the sky plane. The feature in the egress (after the main event) is located 1,730 km in the sky plane, with $E' = 2.4$ km (3σ). This is equivalent to a semi-transparent structure with a width of ~ 7.4 km and apparent opacities of $p' = 0.368$ and $p' = 0.316$, for ingress and egress, respectively. This distance is close to the co-rotational region ($\sim 1,757$ km), obtained considering the nucleus rotational period of 57.7 days (estimated from the periodicity of the outbursts), radius of 30.2 km, and density $\rho = 1,119$ kg m^{-3} (based on estimates from active Centaur Chiron (24)). Using 25 km bins in our search for slightly larger structures, we found beyond our 3σ cut from the mean of the distribution, the dust cloud presented in Section 5 and two more significant features. Unlike the structures previously presented, these have more points inside the flux drop, which increases the significance of these detections, standing at 3.8σ and 3.9σ of the mean for ingress and egress regions, respectively. We applied a square-box fit with variable apparent opacity to determine the properties of these potential detections. Located at $1,352.3 \pm 1.0$ km (resp. $1,796.8 \pm 2.2$ km) from the centre in the sky plane at ingress (resp. egress), these features have an average width

of $W_\perp = 29.4 \pm 2.2$ km and opacity $p = 0.10 \pm 0.03$ (resp. $W_\perp = 28.0 \pm 5.0$ km and opacity $p = 0.12 \pm 0.05$), considering the individual diffraction of particles (17) and errors within 1σ level.

7. Conclusion

This work presents the results of the first-ever stellar occultation by the Centaur 29P, observed with the SOAR telescope on December 5, 2022. The event involved a star with magnitude G = 16.9 while 29P was active and showed an extensive cometary coma. The acquired images were corrected to eliminate the coma contamination, enabling the stellar occultation light curve to be extracted through differential aperture photometry.

Our analysis revealed a gradual dimming of the star during ingress. The nucleus of 29P exhibited three strong outbursts 6 to 13 days before the occultation, on 2022 November 21.95 $\pm$ 0.30, with an amplitude of 3.75 mag, on 2022 November 27.69 $\pm$ 0.15, with an amplitude of 1.65 mag, and on 2022 November 29.15 $\pm$ 0.03 with an amplitude of 0.32 mag. The relative intensities of these three outbursts can be described by the additional light reflected from each new outburst coma. Specifically, the intensities for these three were 164, 96, and 32 nucleus-equivalents, respectively. The absence of equivalent dimming on egress is inconsistent with a shell of material close to the nucleus left over from this period of intense outburst activity. Also, slow-moving material in this region would be expected to fall back under the gravitational influence of the nucleus. Therefore, we attribute the dimming to a localised emission of dust and gas from an area on the nucleus near the morning terminator, solar radiation heating that region and provoking the activity. In this case, the observation would suggest the nucleus spins in a retrograde direction. This behaviour was interpreted as a potential dense dust cloud near the nucleus, extending for a height > 23 km above the surface and with an optical depth of $\tau = 0.18 \pm 0.02$. This single-chord event also allows for a better determination of the 29P's astrometric position, improving the orbit and future stellar occultation predictions.

When analysing the full-resolution light curve, we identify single data point flux drops that correspond to possible structures with apparent equivalent width $E' = 2.8$ km and $E' = 2.4$ km, for the regions prior and after the closest approach, respectively, and localised at an average distance of 1,737 km from the cometary nucleus in the sky plane. The 25 km resampled light curve shows flux variations over the 3σ upper limit: at $1,352.3 \pm 1.0$ km from the nucleus centre in the prior-closest approach region, the feature has a width $W_\perp = 29.4 \pm 2.2$ km and opacity $p = 0.10 \pm 0.03$. After the closest approach, the feature has a width $W_\perp = 28.0 \pm 5.0$ km and opacity $p = 0.12 \pm 0.05$. Despite the low significance of these features, the symmetry concerning the body's centre is noteworthy. While unlikely, these features might suggest a localised accumulation of material ejected by the nucleus, forming a debris envelope or other confined narrow structures.

Overall, our findings contribute to a deeper understanding of 29P/Schwassmann-Wachmann 1 and underscore the importance of stellar occultations in probing the intricate nature of small solar system bodies. Future studies building upon these results could further elucidate the dynamics and evolution of comets in our solar system.

References

1 Horner J, Evans NW, Bailey ME. 2004 Simulations of the population of Centaurs – I. The bulk statistics. Monthly Notices of the Royal Astronomical Society **354**, 798–810. (10.1111/j.1365-2966.2004.08240.x)

2 Cruikshank DP, Brown RH. 1983 The nucleus of comet P/Schwassmann-Wachmann 1. Icarus **56**, 377–380. (10.1016/0019-1035(83)90158-6)

3 Stansberry JA, Van Cleve J, Reach WT, Cruikshank DP, Emery JP, Fernandez YR, Meadows VS, Su KYL, Misselt K, Rieke GH, Young ET, Werner MW, Engelbracht CW, Gordon KD, Hines DC, Kelly DM, Morrison JE, Muzerolle J. 2004 Spitzer Observations of the Dust Coma and Nucleus of 29P/Schwassmann-Wachmann 1. ApJS **154**, 463–468. (10.1086/422473)

4 Bauer JM, Grav T, Blauvelt E, Mainzer AK, Masiero JR, Stevenson R, Kramer E, Fernández YR, Lisse CM, Cutri RM, Weissman PR, Dailey JW, Masci FJ, Walker R, Waszczak A, Nugent CR, Meech KJ, Lucas A, Pearman G, Wilkins A, Watkins J, Kulkarni S, Wright EL, the WISE, Teams P. 2013 The Astrophysical Journal**773**, 22. (10.1088/0004-637X/773/1/22)

5 Schambeau CA, Fernández YR, Lisse CM, Samarasinha N, Woodney LM. 2015 A new analysis of Spitzer observations of Comet 29P/Schwassmann-Wachmann 1. Icarus **260**, 60–72. (10.1016/j.icarus.2015.06.038)

6 Sarid G, Volk K, Steckloff JK, Harris W, Womack M, Woodney LM. 2019 29P/Schwassmann–Wachmann 1, A Centaur in the Gateway to the Jupiter-family Comets. The Astrophysical Journal Letters **883**, L25. (10.3847/2041-8213/ab3fb3)

7 Combes M, Lecacheux J, Encrenaz T, Sicardy B, Zeau Y, Malaise D. 1983 On stellar occultations by comets. Icarus **56**, 229–232. (10.1016/0019-1035(83)90035-0)

8 Desmars J et al.. 2015 Orbit determination of trans-Neptunian objects and Centaurs for the prediction of stellar occultations. A&A **584**, A96. (10.1051/0004-6361/201526498)

9 Gaia Collaboration et al.. 2023 Gaia Data Release 3. Summary of the content and survey properties. A&A **674**, A1. (10.1051/0004-6361/202243940)

10 Lindegren L, Hernández J, Bombrun A, Klioner S, Bastian U, Ramos-Lerate M, de Torres A, Steidelmüller H, Stephenson C, Hobbs D, Lammers U, Biermann M, Geyer R, Hilger T, Michalik D, Stampa U, McMillan PJ, Castañeda J, Clotet M, Comoretto G, Davidson M, Fabricius C, Gracia G, Hambly NC, Hutton A, Mora A, Portell J, van Leeuwen F, Abbas U, Abreu A, Altmann M, Andrei A, Anglada E, Balaguer-Núñez L, Barache C, Becciani U, Bertone S, Bianchi L, Bouquillon S, Bourda G, Brüsemeister T, Bucciarelli B, Busonero D, Buzzi R, Cancelliere R, Carlucci T, Charlot P, Cheek N, Crosta M, Crowley C, de Bruijne J, de Felice F, Drimmel R, Esquej P, Fienga A, Fraile E, Gai M, Garralda N, González-Vidal JJ, Guerra R, Hauser M, Hofmann W, Holl B, Jordan S, Lattanzi MG, Lenhardt H, Liao S, Licata E, Lister T, Löffler W, Marchant J, Martin-Fleitas JM, Messineo R, Mignard F, Morbidelli R, Poggio E, Riva A, Rowell N, Salguero E, Sarasso M, Sciacca E, Siddiqui H, Smart RL, Spagna A, Steele I, Taris F, Torra J, van Elteren A, van Reeven W, Vecchiato A. 2018 Gaia Data Release 2. The astrometric solution. A&A **616**, A2. (10.1051/0004-6361/201832727)

11 Gomes-Júnior AR et al.. 2022 SORA: Stellar Occultation Reduction and Analysis. MNRAS. (10.1093/mnras/stac032)

12 Butcher H, Stevens R. 1981 Image Reduction and Analysis Facility Development. Kitt Peak National Observatory Newsletter **16**, 6.

13 Assafin M. 2023 Differential aperture photometry and digital coronagraphy with PRAIA. Planet. Space Sci. **239**, 105816. (10.1016/j.pss.2023.105816)

14 Boufleur RC, Emilio M, Janot-Pacheco E, Andrade L, Ferraz-Mello S, do Nascimento, José-Dias J, de La Reza R. 2018 A modified CoRoT detrend algorithm and the discovery of a new planetary companion. MNRAS **473**, 710–720. (10.1093/mnras/stx2187)

15 Kervella P, Thévenin F, Di Folco E, Ségransan D. 2004 The angular sizes of dwarf stars and subgiants. Surface brightness relations calibrated by interferometry. A&A **426**, 297–307. (10.1051/0004-6361:20035930)

16 Rommel FL, Braga-Ribas F, Desmars J, Camargo JIB, Ortiz JL, Sicardy B, Vieira-Martins R, Assafin M, Santos-Sanz P, Duffard R, Fernández-Valenzuela E, Lecacheux J, Morgado BE, Benedetti-Rossi G, Gomes-Júnior AR, Pereira CL, Herald D, Hanna W, Bradshaw J, Morales N, Brimacombe J, Burtovoi A, Carruthers T, de Barros JR, Fiori M, Gilmore A, Hooper D, Hornoch K, Jacques C, Janik T, Kerr S, Kilmartin P, Winkel JM, Naletto G, Nardiello D, Nascimbeni V, Newman J, Ossola A, Pál A, Pimentel E, Pravec P, Sposetti S, Stechina A, Szakáts R, Ueno Y,

11

royalsocietypublishing.org/journal/rsta   Phil. Trans. R. Soc. A 0000000

Zampieri L, Broughton J, Dunham JB, Dunham DW, Gault D, Hayamizu T, Hosoi K, Jehin E, Jones R, Kitazaki K, Komžík R, Marciniak A, Maury A, Mikuž H, Nosworthy P, Fábrega Polleri J, Rahvar S, Sfair R, Siqueira PB, Snodgrass C, Sogorb P, Tomioka H, Tregloan-Reed J, Winter OC. 2020 Stellar occultations enable milliarcsecond astrometry for Trans-Neptunian objects and Centaurs. A&A **644**, A40. (10.1051/0004-6361/202039054)

17 Cuzzi JN. 1985 Rings of Uranus: Not so thick, not so black. Icarus **63**, 312–316. (10.1016/0019-1035(85)90014-4)

18 Sicardy B, Roques F, Brahic A. 1991 Neptune's rings, 1983-1989: Ground-based stellar occultation observations I. Ring-like arc detections. Icarus **89**, 220–243. (10.1016/0019-1035(91)90175-S)

19 Boissel Y, Sicardy B, Roques F, Gaulme P, Doressoundiram A, Widemann T, Ivanov VD, Marco O, Mason E, Ageorges N, Mousis O, Rousselot P, Dhillon VS, Littlefair SP, Marsh TR, Assafin M, Braga Ribas F, da Silva Neto D, Camargo JIB, Andrei A, Vieira Martins R, Behrend R, Kretlow M. 2014 An exploration of Pluto's environment through stellar occultations. A&A **561**, A144. (10.1051/0004-6361/201321836)

20 Bérard D, Sicardy B, Camargo JIB, Desmars J, Braga-Ribas F, Ortiz JL, Duffard R, Morales N, Meza E, Leiva R, Benedetti-Rossi G, Vieira-Martins R, Gomes Júnior AR, Assafin M, Colas F, Dauvergne JL, Kervella P, Lecacheux J, Maquet L, Vachier F, Renner S, Monard B, Sickafoose AA, Breytenbach H, Genade A, Beisker W, Bath KL, Bode HJ, Backes M, Ivanov VD, Jehin E, Gillon M, Manfroid J, Pollock J, Tancredi G, Roland S, Salvo R, Vanzi L, Herald D, Gault D, Kerr S, Pavlov H, Hill KM, Bradshaw J, Barry MA, Cool A, Lade B, Cole A, Broughton J, Newman J, Horvat R, Maybour D, Giles D, Davis L, Paton RA, Loader B, Pennell A, Jaquiery PD, Brillant S, Selman F, Dumas C, Herrera C, Carraro G, Monaco L, Maury A, Peyrot A, Teng-Chuen-Yu JP, Richichi A, Irawati P, De Witt C, Schoenau P, Prager R, Colazo C, Melia R, Spagnotto J, Blain A, Alonso S, Román A, Santos-Sanz P, Rizos JL, Maestre JL, Dunham D. 2017 The Structure of Chariklo's Rings from Stellar Occultations. AJ **154**, 144. (10.3847/1538-3881/aa830d)

21 Morgado BE, Sicardy B, Braga-Ribas F, Desmars J, Gomes-Júnior AR, Bérard D, Leiva R, Ortiz JL, Vieira-Martins R, Benedetti-Rossi G, Santos-Sanz P, Camargo JIB, Duffard R, Rommel FL, Assafin M, Boufleur RC, Colas F, Kretlow M, Beisker W, Sfair R, Snodgrass C, Morales N, Fernández-Valenzuela E, Amaral LS, Amarante A, Artola RA, Backes M, Bath KL, Bouley S, Buie MW, Cacella P, Colazo CA, Colque JP, Dauvergne JL, Dominik M, Emilio M, Erickson C, Evans R, Fabrega-Polleri J, Garcia-Lambas D, Giacchini BL, Hanna W, Herald D, Hesler G, Hinse TC, Jacques C, Jehin E, Jørgensen UG, Kerr S, Kouprianov V, Levine SE, Linder T, Maley PD, Machado DI, Maquet L, Maury A, Melia R, Meza E, Mondon B, Moura T, Newman J, Payet T, Pereira CL, Pollock J, Poltronieri RC, Quispe-Huaynasi F, Reichart D, de Santana T, Schneiter EM, Sieyra MV, Skottfelt J, Soulier JF, Starck M, Thierry P, Torres PJ, Trabuco LL, Unda-Sanzana E, Yamashita TAR, Winter OC, Zapata A, Zuluaga CA. 2021 Refined physical parameters for Chariklo's body and rings from stellar occultations observed between 2013 and 2020. A&A **652**, A141. (10.1051/0004-6361/202141543)

22 Morgado BE, Sicardy B, Braga-Ribas F, Ortiz JL, Salo H, Vachier F, Desmars J, Pereira CL, Santos-Sanz P, Sfair R, de Santana T, Assafin M, Vieira-Martins R, Gomes-Júnior AR, Margoti G, Dhillon VS, Fernández-Valenzuela E, Broughton J, Bradshaw J, Langersek R, Benedetti-Rossi G, Souami D, Holler BJ, Kretlow M, Boufleur RC, Camargo JIB, Duffard R, Beisker W, Morales N, Lecacheux J, Rommel FL, Herald D, Benz W, Jehin E, Jankowsky F, Marsh TR, Littlefair SP, Bruno G, Pagano I, Brandeker A, Collier-Cameron A, Florén HG, Hara N, Olofsson G, Wilson TG, Benkhaldoun Z, Busuttil R, Burdanov A, Ferrais M, Gault D, Gillon M, Hanna W, Kerr S, Kolb U, Nosworthy P, Sebastian D, Snodgrass C, Teng JP, de Wit J. 2023 A dense ring of the trans-Neptunian object Quaoar outside its Roche limit. Nature **614**, 239–243. (10.1038/s41586-022-05629-6)

23 Pereira CL, Sicardy B, Morgado BE, Braga-Ribas F, Fernández-Valenzuela E, Souami D, Holler BJ, Boufleur RC, Margoti G, Assafin M, Ortiz JL, Santos-Sanz P, Epinat B, Kervella P, Desmars J, Vieira-Martins R, Kilic Y, Gomes Júnior AR, Camargo JIB, Emilio M, Vara-Lubiano M, Kretlow M, Albert L, Alcock C, Ball JG, Bender K, Buie MW, Butterfield K, Camarca M, Castro-Chacón JH, Dunford R, Fisher RS, Gamble D, Geary JC, Gnilka CL, Green KD, Hartman ZD, Huang CK, Januszewski H, Johnston J, Kagitani M, Kamin R, Kavelaars JJ, Keller JM, de Kleer KR, Lehner MJ, Luken A, Marchis F, Marlin T, McGregor K, Nikitin V, Nolthenius R, Patrick C, Redfield S, Rengstorf AW, Reyes-Ruiz M, Seccull T, Skrutskie MF, Smith AB, Sproul M, Stephens AW, Szentgyorgyi A, Sánchez-Sanjuán S, Tatsumi E, Verbiscer A, Wang

SY, Yoshida F, Young R, Zhang ZW. 2023 The two rings of (50000) Quaoar. A&A **673**, L4. (10.1051/0004-6361/202346365)

24 Braga-Ribas F, Pereira CL, Sicardy B, Ortiz JL, Desmars J, Sickafoose A, Emilio M, Morgado B, Margoti G, Rommel FL, Camargo JIB, Assafin M, Vieira-Martins R, Gomes-Júnior AR, Santos-Sanz P, Morales N, Kretlow M, Lecacheux J, Colas F, Boninsegna R, Schreurs O, Dauvergne JL, Fernandez E, van Heerden HJ, González H, Bihel D, Jankowsky F. 2023 Constraints on (2060) Chiron's size, shape, and surrounding material from the November 2018 and September 2019 stellar occultations. A&A **676**, A72. (10.1051/0004-6361/202346749)

25 Pereira CL, Braga-Ribas F, Sicardy B, Gomes-Júnior AR, Ortiz JL, Branco HC, Camargo JIB, Morgado BE, Vieira-Martins R, Assafin M, Benedetti-Rossi G, Desmars J, Emilio M, Morales R, Rommel FL, Hayamizu T, Gondou T, Jehin E, Artola RA, Asai A, Colazo C, Ducrot E, Duffard R, Fabrega J, Fernandez-Valenzuela E, Gillon M, Horaguchi T, Ida M, Kitazaki K, Mammana LA, Maury A, Melita M, Morales N, Moya-Sierralta C, Owada M, Pollock J, Sanchez JL, Santos-Sanz P, Sasanuma N, Sebastian D, Triaud A, Uchiyama S, Vanzi L, Watanabe H, Yamamura H. 2024 Physical properties of Centaur (60558) 174P/Echeclus from stellar occultations. MNRAS **527**, 3624–3638. (10.1093/mnras/stad3318)

12

royalsocietypublishing.org/journal/rsta Phil. Trans. R. Soc. A 0000000

Appendix D

Proposal SOAR - Chiron's rotational light curve for 3D shape characterization

LABORATÓRIO NACIONAL DE ASTROFÍSICA

SOAR TELESCOPE - Brazilian National Office
Observing Time Application Form (Ver. 3.0.1)
Semester: *2023B* (Aug/2023 - Jan/2024)

A.M.(<=)	1.8	Moon P.	Gray
Image Quality		Seeing < 1.3 "	
Cloudy Cover		Photometric	

Title of Proposal: *Chiron's rotation light curve for 3D shape characterization*

Observing Mode: Remote/Classical mode

Principal Investigator: Chrystian Luciano Pereira

PI Affiliation: ON

PI Email: chrystianpereira@on.br

PI Phone: 42999360056

Co-authors

Name	Affiliation	E-mail
Felipe Braga-Ribas	UTFPR/DAFIS	felipebribas@gmail.com
Marcelo Assafin	OV/UFRJ	massaf@ov.ufrj.br
Gustavo Benedetti-Rossi	FEG/UNESP	gugabrossi@gmail.com
Altair Ramos Gomes-Junior	UFU	altairgomesjr@gmail.com
Roberto Vieira-Martins	ON	rvm@on.br
Bruno Eduardo Morgado	OV/UFRJ	morgado.fis@gmail.com
Flavia Luane Rommel	UTFPR/DAFIS	flaviarommel@on.br
Bruno Sicardy	Observatoire de Paris	bruno.sicardy@obspm.fr
Jose Luis Ortiz	IAA	ortiz@iaa.es
Giuliano Margoti	UTFPR/DAFIS	giulianomargoti@alunos.utfpr.edu.br
Viviane Figueiredo Peixoto	UFRJ	vivianepeixoto989@gmail.com
Feliphe de Souza Ferreira	ON	felipheferreira@on.br

Is there a thesis or dissertation that will benefit from the data?: YES

Student	Degree
Chrystian Luciano Pereira	PhD student
Giuliano Margoti	MsC student

Abstract:

We propose observing the centaur object Chiron to determine its rotational phase a few days before a stellar occultation, thus allowing the characterization of its full 3D shape. Chiron is the second largest centaur object, with an estimated diameter of 210 km. This centaur has shown cometary activity on different occasions since its discovery. From stellar occultations observed in the 1990s, 2011, and 2022, the presence of additional material in the body's vicinity was detected, indicating the presence of a structure, such as rings or shells, which is not yet fully understood. Our goal is to obtain a rotational light curve close in time to a stellar occultation that will take place on September 10, 2023. These observations and other older lightcurves observed at different times and orientations will allow us to derive its full three-dimensional shape.

Time requested: 19 hours.

Minimum time accepted: 13 hours.

Instruments:

Instrument	Camera
Goodman (Imaging)	Red Camera

Instrument	Filter	Grating	Slit
Goodman (Imaging)			
	R		
	iÂ´		
	rÂ´		

Optimal dates:

11/SEP/2023, 12/SEP/2023, 13/SEP/2023.

Impossible dates:

09/SEP/2023, 10/SEP/2023. After 24/SEP/2023.

Previous missions of this proposal with the SOAR Telescope:

This proposal has not been submitted before.

Previous missions of other proposals with the SOAR Telescope:

- SO2015A-015: we got 5 hours as payback which were used to obtain a new Chariklo light curve (using SOI) in a different epoch from previous observations and is published [1].

- 2019B: Data acquired for Chariklo's rotation light curve and 3D shape characterization, but high seeing and pointing limitations prevented attaining the proposal objectively. Two stellar occultations by the Centaur Echeclus were observed in SOAR: the first was a close negative in October 2019. The second event, in January 2020, had two **positive** detections of this centaur, allowing the determination of upper limits in the dimensions of the body. These events, together with a more recent one observed from Japan in 2021, were analyzed and will appear in a paper in advanced preparation relative to the central body and their surroundings by Chrystian Luciano Pereira. Indeed, these results were presented at the Europlanet Science Congress (EPSC) 2022 (Granada, Spain).

- 2021B: Rotation light curve for the high-inclination TNO 2004XR190 ("Buffy") were obtained. Stellar occultations are also proposed, where the ice in the dome prevents observing the 2004 PF115 event. The other event proposed were successfully observed: 2002 GZ32, where the light curve indicates a negative event.

- 2022B: Stellar occultation events by the comet 29P/Schwassmann-Wachmann (positive detection) and by the Transneptunian Object Salacia (negative on SOAR). The single chord event by 29P was the first detection of an occultation by this object, allowing an orbit refinement and leading to a multi-chord detection a few weeks later from the USA.

- 2023A: Stellar occultation events by the Transneptunian Objects Varda, 2007 JJ43 and Ixion. The event by Varda was not observed due to the ice in the dome. The events by 2003 JJ43 and Ixion are later this year.

Previous results in the field by the Principal Investigator:

- Braga-Ribas, F., et al., Database on detected stellar occultations by small outer Solar System objects. Journal of Physics. Conference Series (PRINT), v. 1365, p. 012024, 2019. doi: 10.1088/1742-6596/1365/1/012024

- Pereira, C. L., Tamanho e forma do Centauro (2060) Chiron e a busca por estruturas em seu entorno a partir de ocultações estelares. 2020. Dissertação (Mestrado em Física e Astronomia) - Universidade Tecnológica Federal do Paraná, Curitiba, 2020. http://repositorio.utfpr.edu.br/jspui/handle/1/5272

- Souami, D., et al., A multi-chord stellar occultation by the large trans-Neptunian object (174567) Varda. Astronomy & Astrophysics, v. 643, p. A125, 2020. doi: 10.1051/0004-6361/202038526

- Rommel, F. L., et al., Stellar occultations enable milliarcsecond astrometry for Trans-Neptunian objects and Centaurs. Astronomy & Astrophysics, v. 644, p. A40, 2020. doi: 10.1051/0004-6361/202039054

- Morgado, B. E., et al., Refined physical parameters for Chariklo's body and rings from stellar occultations observed between 2013 and 2020. Astronomy & Astrophysics, v. 652, p. A141, 2021. doi: 10.1051/0004-6361/202141543

- Marques Oliveira, J. et al., Constraints on the structure and seasonal variations of Triton's atmosphere from the 5 October 2017 stellar occultation and previous observations. Astronomy & Astrophysics, v. 659, p. A136, 2022. doi: 10.1051/0004-6361/202141443

- Morgado, B. E., et al., Milliarcsecond Astrometry for the Galilean Moons Using Stellar Occultations. The Astronomical Journal, v. 163, p. 240, 2022. doi: 10.3847/1538-3881/ac6108

- Vara-Lubiano, M., et al., The multichord stellar occultation on 2019 October 22 by the trans-Neptunian Object (84922) 2003 VS2. Astronomy & Astrophysics. v.663, p.A121 - , 2022. doi: 10.1051/0004-6361/202141842

- Santos-Sanz, P., et al., Physical properties of the trans-Neptunian object (38628) Huya from a multi-chord stellar occultation. Astronomy & Astrophysics. v.664, p.A130 - , 2022. doi: 10.1051/0004-6361/202141546

- Morgado, B. E., et al., A stellar occultation by the transneptunian object (50000) Quaoar observed by CHEOPS. Astronomy & Astrophysics. v.664, p.L15 - , 2022. doi: 10.1051/0004-6361/202244221

- Pereira, C. L., et al., Recent results of stellar occultations by (60558) Echeclus 2022, European Planetary Science Congress. doi:10.5194/epsc2022-557

- Fernández-Valenzuela, E., et al., The multichord stellar occultation by the centaur Bienor on January 11, 2019. Astronomy & Astrophysics. v.669, p.A112 - , 2023. doi: 10.1051/0004-6361/202243214

- Morgado, B. E., et al., A dense ring of the trans-Neptunian object Quaoar outside its Roche limit. Nature. v.614, p.239 - 243, 2023. doi: 10.1038/s41586-022-05629-6

Publications:

Not related to this proposal since it is its first submission. Nevertheless, they are relevant for this proposal, as they use data obtained with SOAR and have the PI or at least one of the co-author's participation.

- "The first observed stellar occultations by the irregular satellite Phoebe (Saturn IX) and improved rotational period", Gomes-Júnior, A. R.; Assafin, M.; Braga-Ribas, F.; Benedetti-Rossi, G.; Morgado, B. E. et al. (2020), Monthly Notices of the Royal Astronomical Society, DOI: 10.1093/mnras/stz3463

- "Size and shape of Chariklo from multi-epoch stellar occultation", Leiva, R., Sicardy, B., Camargo, J. I. B., et al. (2017), AJ, DOI:10.3847/1538-3881/aa8956

- "A ring system detected around the Centaur (10199) Chariklo", Braga-Ribas,et al. (2014), Nature, 508, 72.

Scientific Case

Centaurs are small Solar System bodies that orbit the Sun between the orbits of Jupiter and Neptune and not in 1:1 mean-motion resonance with any planet [3]. These bodies are believed to be the main source of Jupiter family comets (JFC) and are notable due to cometary-like activity, which is observed in ~13% of known centaurs.

The first centaur observed was (2060) Chiron in November 1977 [4]. Photographic plates present precovery observations in 1895 and 1941 from Boyden Observatory in South Africa Being the second largest object in this class (Chariklo is the larger Centaur), the Chiron's diameter was estimated using different techniques, with more recent values obtained with the Herschel Space Telescope [5] as 218 ± 20 km, and using Atacama Large Millimeter Array (ALMA) estimated on 210 ± 10 km. Since the discovery, Chiron has shown brightness variations. From the 1988 and 1989 observations, it was hypothesized that Chiron had a cometary coma, when the object received the designation of comet 95P/Chiron [6,7,8,9]. More recently, on February 2021, a large brightness increase was observed in Chiron, being observed until mid-June 2021 [11].

Stellar occultations observed in the 90's [10,12] showed characteristics of the presence of dust inside the coma, interpreted as jets of material expelled by the nucleus. In 2011, another stellar occultation revealed the presence of symmetrical structures around Chiron [13,14], similar to the rings observed in Chariklo [15]. Using these observations of stellar occultations, a possible orientation for Chiron's pole was determined [16]. Recently, other three events by Chiron were observed by our group: November 2018, when we obtained only one positive chord for the main body and searched for additional material in the surroundings; September 2019, where the main body was detected by four small telescopes, allowing size and shape constraints (Figure 1). The results of these observations were part of the PI's master's thesis and will be presented in a paper to be submitted soon, with shape, density, and mass estimations. Finally, last December we detected another stellar occultation by Chiron and those data are under analysis.

Since we know the Chiron rotational period of $P = 5.917813 \pm 0.000007$ hours [18], obtaining the rotational light curve at a time close to stellar occultation allows us to determine whether the event occurred close to the minimum or maximum projected area, in other words, it give us the rotational phase at the time of occultation. Once we know the rotational phase in which the occultation occurred, we can relate the observed area and the amplitude of the light curve thus obtaining the axes ratio from $\Delta m = 2.5\log(a/b)$ and therefore a possible 3D model for the body. Initial estimates based on the true light curve amplitude ($m_0 = 0.16 \pm 0.03$ [19]), the assumption that Chiron is in hydrostatic equilibrium (Jacobi ellipsoid), and the area observed during the 2019 stellar occultation, suggest semi-axes $a = 126 \pm 22$ km, $b = 109 \pm 19$ km, and $c = 68 \pm 12$ km for the Chiron's 3D shape (Figure 1) [20].

Scientific Impact

As stated above, stellar occultations are useful not only to estimate the body's size and two-dimensional shape but to determine the three-dimensional shape using multi-epoch stellar occultations together with rotational light curves. In this context, this proposal intends to determine the rotational phase of the object during a stellar occultation campaign predicted to be observed in September 2023 for various sites (including SOAR), which, together with previous events, can help us in this interpretation.

Considering that Chiron has good estimates for the pole orientation and a well-determined rotational period of 5.917813 hours, we can constrain the possible solutions for the projected ellipses by determining the object's rotational phase at the instant of occultation. Determining the object's shape and size is important to constrain its density and mass. Also, to explain the formation and location of the proposed rings around Chiron since the shape can cause strong resonances and these are closely linked with ring confinement.
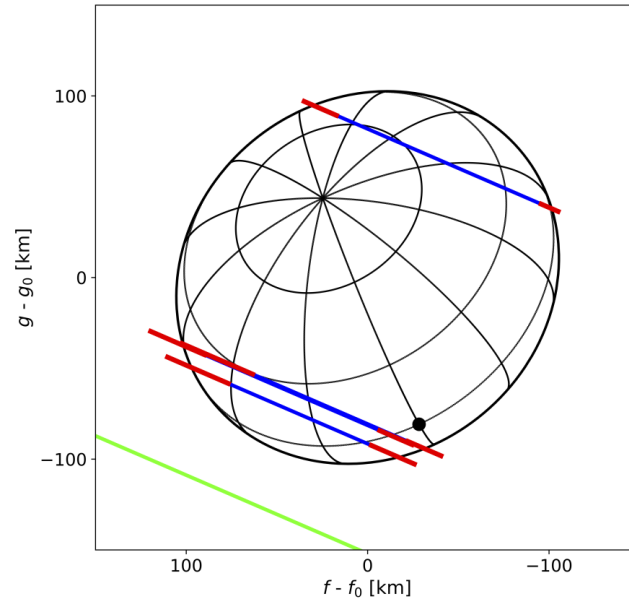
Figure 1: Best fit of the Chiron three-dimensional shape compared with the positive chords from 2019 stellar occultation observed in Europe.

References

1. Leiva, R., Sicardy, B., Camargo, J. I. B., et al. (2017), AJ.

2. Gomes-Júnior, A. R.; Assafin, M.; Braga-Ribas, F.; Benedetti-Rossi, G.; Morgado, B. E. et al. (2020), Monthly Notices of the Royal Astronomical Society.

3. Jewitt, D. The Astronomical Journal, 137 4296, 2009.

4. Kowal, C. T.; Liller, W.; Marsden, B. G. In: Duncombe, R. L. (Ed.). Dynamics of the Solar System. [S.l.: s.n.], 1979. (IAU Symposium, v. 81), p. 245.

5. Fornasier, S. et al. Astronomy & Astrophysics, v. 555, p. A15, jul. 2013.

6. Luu, J. X.; Jewitt, D. C. The Astronomical Journal, v. 100, p. 913, Sep 1990.

7. Tholen D. J., Hartmann W. K., Cruikshank D. P., Lilly S., Bowell E., Hewitt A. 1988, IAU Circ.4554, 2

8. Meech, K. J.; Belton, M. J. S. The Atmosphere of 2060 Chiron. The Astronomical Journal, v. 100, p. 1323, out. 1990.

9. Hartmann, W. K. et al. 2060 Chiron: Colorimetry and cometary behavior. Icarus, v. 83, n. 1, p. 1–15, jan. 1990.

10. Bus, S. J. et al. Science, v. 251, n. 4995, p. 774–777, fev. 1991.

11. Dobson, M. M., Schwamb, M. E., Fitzsimmons, A., et al. 2021, Research Notes of the American Astronomical Society, 5, 211

12. Elliot, J. L., Olkin, C. B., Dunham, E. W., et al.: 1995, Nature, 373, 46.

13. Ruprecht. J. D., Bosh, A. S., Person, M. J., et al.: 2015, Icarus, 252, 271-276.

14. Sickafoose, A.A., Bosh, A.S., Levine, S.E., et al.: 2019, Icarus, 319, 657.

15. Braga-Ribas, F. et al. (2014), Nature, 508, 72.

16. Ortiz, J. L., Duffard, R., Pinilla-Alonso, N., et al.: 2015, Astronomy & Astrophysics, 576, A18.

17. Ortiz, J.L., et al. (2017), Nature, DOI:10.1038/nature24051

18. Marcialis, R. L., Buratti, B. J.: 1993, Icarus, 104, 234–243.

19. Groussin, O., Lamy, P. and Jorda L.: 2004, A&A, 1163-1175, 413, 3.

20. Braga-Ribas, F., Pereira, C. L., Sicardy, B., *in prep.*

Technical Justification

We request three half nights (18 hours on target plus 1 hour of overheads with Goodman RED (imaging), to measure the rotational light curve of (2060) Chiron on nights close to the stellar occultation that will occur on September 10. The minimum acceptable time is 13 hours, divided into two half nights. Average Chiron's rotational period is around 6 hours, and therefore, the required observation time allows the entire rotational phase space of the object to be covered in each night. To have such a precise light curve we need a clear and gray night.

The nights prior to September 10th, i.e. prior to the occultation event, **should not** be scheduled for observation due to the Moon and a close star (at September 9th). On the night of the occultation (2022-09-10 05:07 UT) we would have a 4 hour gap for observation, but **should not** be scheduled since the proximity to the bright star involved in the occultation (mag G=13.3, against the magnitude V = 18.6 of Chiron) makes the observation unfeasible. Nights prior to September 24th are acceptable. Nights after that date show contamination of the Moon, in addition to the propagation of error in Chiron's rotational period will not allow the rotational phase to be accurately recovered for the occultation date.

Chiron's apparent V magnitude in September 2023 will be ∼18.6, and the expected short therm brightness variation (rotation light curve) is 0.04 for an aspect angle of 39 degrees. We plan to use exposures of 110 seconds to achieve an SNR > 200, although larger exposures may be used if needed, or co-adding images during the analysis may also be used to increase the signal-to-noise ratio and achieve a magnitude precision of 0.005. We choose the R filter as it gives a good compromise between flux and image quality. Chiron's position at 03:00 UT for September 11th, 12th and 13th, when observable conditions are favorable, are presented in object list.

Data analysis starts with the traditional flat and dark calibrations. We then extract object flux and comparison stars via differential aperture photometry, since this technique already accounts for common variations that affect all objects on the image.

After traditional flat and dark calibrations, to build the light curve and to measure the rotation period, we will use differential photometry to measure the fluxes once the technique already accounts for common variations that affect all objects on the image, we do not need photometric conditions. With the obtained light curve, we search for periodic signatures using standard time series analysis techniques. As Chiron's rotational period is well known, we will fold the data to increase the number of points during one rotation period and fit the period to determine the phase and amplitude of the rotation lightcurve.

Special Instruments Requirements

There is no need for calibration fields.
Observations **should *not* be scheduled** for September 9th and 10th, 2023 because the object will be too close to background bright stars.
Optimal dates for observations: September 11th, 12th, and 13th, 2023.
Acceptable dates for observations: prior to September 24th 2023.

Objects List.

Object	A.R.(h,m)	Dec.(deg)	Mag.	Band	Comments
Chiron	01:06:22.84	+08:43:54.07	18.48	R	2023-Sep-11 03:00 UT
Chiron	01:06:14.43	+08:43:00.82	18.48	R	2023-Sep-12 03:00 UT
Chiron	01:06:05.91	+08:42:06.79	18.47	R	2023-Sep-13 03:00 UT
Chiron	01:05:57.28	+08:41:12.00	18.47	R	2023-Sep-14 03:00 UT
Chiron	01:05:48.55	+08:40:16.47	18.46	R	2023-Sep-15 03:00 UT
Chiron	01:05:39.72	+08:39:20.22	18.46	R	2023-Sep-16 03:00 UT
Chiron	01:05:30.79	+08:38:23.27	18.45	R	2023-Sep-17 03:00 UT
Chiron	01:05:21.77	+08:37:25.64	18.45	R	2023-Sep-18 03:00 UT
Chiron	01:05:12.66	+08:36:27.35	18.44	R	2023-Sep-19 03:00 UT
Chiron	01:05:03.47	+08:35:28.44	18.44	R	2023-Sep-20 03:00 UT
Chiron	01:04:54.19	+08:34:28.91	18.43	R	2023-Sep-21 03:00 UT
Chiron	01:04:44.84	+08:33:28.80	18.42	R	2023-Sep-22 03:00 UT
Chiron	01:04:35.42	+08:32:28.13	18.42	R	2023-Sep-23 03:00 UT

Appendix E

Co-authorship on articles within the Lucky Star collaboration

Here, I present the first page of the published works I co-authored during my PhD project. My main contribution to most of them was the photometric analysis and the acquisition of occultation light curves, modeling them to determine the instants of occultation and obtain the elliptical fitting. I highlight the articles ORTIZ *et al.* (2023), BRAGA-RIBAS *et al.* (2023), and MORGADO *et al.* (2023), where in addition to data analysis, I also contributed to the manuscript writing.

Astronomy & Astrophysics

Refined physical parameters for Chariklo's body and rings from stellar occultations observed between 2013 and 2020[*]

B. E. Morgado[1,2,3], B. Sicardy[1], F. Braga-Ribas[4,3,2,1], J. Desmars[5,6,1], A. R. Gomes-Júnior[7,2], D. Bérard[1],
R. Leiva[8,9,1], J. L. Ortiz[10], R. Vieira-Martins[3,2,11], G. Benedetti-Rossi[1,2,7], P. Santos-Sanz[10],
J. I. B. Camargo[3,2], R. Duffard[10], F. L. Rommel[3,2,4], M. Assafin[11,2], R. C. Boufleur[2,3], F. Colas[6],
M. Kretlow[12,10,13], W. Beisker[12,13], R. Sfair[7], C. Snodgrass[14], N. Morales[10], E. Fernández-Valenzuela[15],
L. S. Amaral[16], A. Amarante[17], R. A. Artola[18], M. Backes[19,20], K.-L. Bath[12,13], S. Bouley[21], M. W. Buie[22],
P. Cacella[23], C. A. Colazo[24], J. P. Colque[25], J.-L. Dauvergne[26], M. Dominik[27], M. Emilio[28,3], C. Erickson[29],
R. Evans[19], J. Fabrega-Polleri[30], D. Garcia-Lambas[18], B. L. Giacchini[31,32], W. Hanna[33], D. Herald[12,33],
G. Hesler[34], T. C. Hinse[35,36], C. Jacques[37], E. Jehin[38], U. G. Jørgensen[39], S. Kerr[33,40], V. Kouprianov[41,42],
S. E. Levine[43,44], T. Linder[45], P. D. Maley[46,47], D. I. Machado[48,49], L. Maquet[6], A. Maury[50], R. Melia[18],
E. Meza[1,51,52], B. Mondon[34], T. Moura[7], J. Newman[33], T. Payet[34], C. L. Pereira[4,3,2], J. Pollock[53],
R. C. Poltronieri[54,16], F. Quispe-Huaynasi[3], D. Reichart[41], T. de Santana[1,7], E. M. Schneiter[18], M. V. Sieyra[55],
J. Skottfelt[56], J. F. Soulier[57], M. Starck[58], P. Thierry[59], P. J. Torres[60,61], L. L. Trabuco[49], E. Unda-Sanzana[25],
T. A. R. Yamashita[7], O. C. Winter[7], A. Zapata[62,63], and C. A. Zuluaga[44]

(Affiliations can be found after the references)

ABSTRACT

Context. The Centaur (10199) Chariklo has the first ring system discovered around a small object. It was first observed using stellar occultation in 2013. Stellar occultations allow sizes and shapes to be determined with kilometre accuracy, and provide the characteristics of the occulting object and its vicinity.

Aims. Using stellar occultations observed between 2017 and 2020, our aim is to constrain the physical parameters of Chariklo and its rings. We also determine the structure of the rings, and obtain precise astrometrical positions of Chariklo.

Methods. We predicted and organised several observational campaigns of stellar occultations by Chariklo. Occultation light curves were measured from the datasets, from which ingress and egress times, and the ring widths and opacity values were obtained. These measurements, combined with results from previous works, allow us to obtain significant constraints on Chariklo's shape and ring structure.

Results. We characterise Chariklo's ring system (C1R and C2R), and obtain radii and pole orientations that are consistent with, but more accurate than, results from previous occultations. We confirm the detection of W-shaped structures within C1R and an evident variation in radial width. The observed width ranges between 4.8 and 9.1 km with a mean value of 6.5 km. One dual observation (visible and red) does not reveal any differences in the C1R opacity profiles, indicating a ring particle size larger than a few microns. The C1R ring eccentricity is found to be smaller than 0.022 (3σ), and its width variations may indicate an eccentricity higher than ~0.005. We fit a tri-axial shape to Chariklo's detections over 11 occultations, and determine that Chariklo is consistent with an ellipsoid with semi-axes of $143.8^{+1.4}_{-1.5}$, $135.2^{+1.4}_{-2.8}$, and $99.1^{+5.4}_{-2.7}$ km. Ultimately, we provided seven astrometric positions at a milliarcsecond accuracy level, based on *Gaia* EDR3, and use it to improve Chariklo's ephemeris.

Key words. occultations – methods: observational – methods: data analysis – minor planets, asteroids: individual: Chariklo – planets and satellites: rings

1. Introduction

The Centaur (10199) Chariklo is a small object in our Solar System moving on an elliptical orbit between Saturn and Uranus, at heliocentric distances varying from 13.1 to 18.9 au. It was discovered in 1997 (Ticha et al. 1997), and is the largest Centaur known to date. From thermal infrared observations, its surface equivalent radius ranges between 109 and 151 km (Jewitt & Kalas 1998; Altenhoff et al. 2001; Campins & Fernández 2002; Sekiguchi et al. 2012; Bauer et al. 2013; Fornasier et al.

2013, 2014; Lellouch et al. 2017); the most recent solution of 121 ± 4 km (Lellouch et al. 2017) was obtained with the Atacama Large Millimeter/submillimeter Array (ALMA[1]).

From a stellar occultation observed in 2013, Braga-Ribas et al. (2014) reported the discovery of two dense and narrow rings (2013C1R and 2013C2R, hereafter C1R and C2R) surrounding Chariklo at 390 and 405 km from the body centre, respectively. This was the first time that rings had been observed elsewhere than around giant planets. Being narrow and dense, they bear some resemblance to some of Uranus' rings (Elliot et al. 1984; French et al. 1991). More on Chariklo's rings properties (orbital

---

[1] https://www.almaobservatory.org/en/home/

Astronomy & Astrophysics

Constraints on the structure and seasonal variations of Triton's atmosphere from the 5 October 2017 stellar occultation and previous observations[⋆]

J. Marques Oliveira[1], B. Sicardy[1], A. R. Gomes-Júnior[2,3], J. L. Ortiz[4], D. F. Strobel[5], T. Bertrand[1,6],
F. Forget[7], E. Lellouch[1], J. Desmars[8,9], D. Bérard[1], A. Doressoundiram[1], J. Lecacheux[1], R. Leiva[10,11],
E. Meza[12,13], F. Roques[1], D. Souami[1,14], T. Widemann[1], P. Santos-Sanz[4], N. Morales[4], R. Duffard[4],
E. Fernández-Valenzuela[15,4], A. J. Castro-Tirado[4], F. Braga-Ribas[16,1,17,3], B. E. Morgado[17,1,3], M. Assafin[18,3],
J. I. B. Camargo[17,3], R. Vieira-Martins[17,3,9], G. Benedetti-Rossi[1,3,2], S. Santos-Filho[18,3], M. V. Banda-Huarca[17,3],
F. Quispe-Huaynasi[17], C. L. Pereira[17,3], F. L. Rommel[17,3], G. Margoti[16], A. Dias-Oliveira[19], F. Colas[9],
J. Berthier[9], S. Renner[9,20], R. Hueso[21], S. Pérez-Hoyos[21], A. Sánchez-Lavega[21], J. F. Rojas[21], W. Beisker[22,23],
M. Kretlow[4,22,23], D. Herald[24,25], D. Gault[24], K.-L. Bath[22,23], H.-J. Bode[22,23,†], E. Bredner[23,26,27,28], K. Guhl[29,23],
T. V. Haymes[30,23], E. Hummel[23], B. Kattentidt[23], O. Klös[23], A. Pratt[23,30], B. Thome[23], C. Avdellidou[31], K. Gazeas[32],
E. Karampotsiou[32], L. Tzouganatos[32], E. Kardasis[33], A. A. Christou[34], E. M. Xilouris[35], I. Alikakos[35],
A. Gourzelas[35], A. Liakos[35], V. Charmandaris[36,37], M. Jelínek[38], J. Štrobl[38], A. Eberle[39], K. Rapp[39], B. Gährken[40],
B. Klemt[41], S. Kowollik[42], R. Bitzer[42], M. Miller[43], G. Herzogenrath[43], D. Frangenberg[43], L. Brandis[43], I. Pütz[43],
V. Perdelwitz[44,45], G. M. Piehler[46], P. Riepe[26,47], K. von Poschinger[48], P. Baruffetti[49], D. Cenadelli[50],
J.-M. Christille[50], F. Ciabattari[51], R. Di Luca[52], D. Alboresi[52], G. Leto[53], R. Zanmar Sanchez[53], P. Bruno[53],
G. Occhipinti[53], L. Morrone[54], L. Cupolino[55], A. Noschese[56], A. Vecchione[56], C. Scalia[57,58,53], R. Lo Savio[57],
G. Giardina[57], S. Kamoun[59], R. Barbosa[60], R. Behrend[61], M. Spano[62], E. Bouchet[63], M. Cottier[63], L. Falco[64],
S. Gallego[65], L. Tortorelli[66], S. Sposetti[67], J. Sussenbach[68], F. Van Den Abbeel[69], P. André[70], M. Llibre[70],
F. Pailler[70], J. Ardissone[71], M. Boutet[72], J. Sanchez[72], M. Bretton[73], A. Cailleau[74], V. Pic[74], L. Granier[74],
R. Chauvet[75], M. Conjat[76], J. L. Dauvergne[77], O. Dechambre[78], P. Delay[79,80], M. Delcroix[81], L. Rousselot[81],
J. Ferreira[82,10], P. Machado[82], P. Tanga[10], J.-P. Rivet[10], E. Frappa[83], M. Irzyk[84], F. Jabet[85], M. Kaschinski[86],
A. Klotz[87], Y. Rieugnie[88], A. N. Klotz[89,90], O. Labrevoir[91], D. Lavandier[92], D. Walliang[92], A. Leroy[93], S. Bouley[94],
S. Lisciandra[95,†], J.-F. Coliac[95,96], F. Metz[97], D. Erpelding[97], P. Nougayrède[97], T. Midavaine[27], M. Miniou[98],
S. Moindrot[99], P. Morel[100,101], B. Reginato[102], E. Reginato[103,104], J. Rudelle[105], B. Tregon[106], R. Tanguy[107],
J. David[107], W. Thuillot[9], D. Hestroffer[9], G. Vaudescal[108], D. Baba Aissa[109], Z. Grigahcene[109], D. Briggs[110,30],
S. Broadbent[110,30,111], P. Denyer[30], N. J. Haigh[30], N. Quinn[30], G. Thurston[30,112], S. J. Fossey[113], C. Arena[113],
M. Jennings[114], J. Talbot[115], S. Alonso[116], A. Román Reche[117], V. Casanova[4], E. Briggs[118], R. Iglesias-Marzoa[119,120],
J. Abril Ibáñez[119], M. C. Díaz Martín[119], H. González[121], J. L. Maestre García[122], J. Marchant[123],
I. Ordonez-Etxeberria[124], P. Martorell[124], J. Salamero[124], F. Organero[125], L. Ana[125], F. Fonseca[125], V. Peris[126],
O. Brevia[126], A. Selva[127], C. Perello[127], V. Cabedo[128,129], R. Gonçalves[130], M. Ferreira[131], F. Marques Dias[132],
A. Daassou[133,134], K. Barkaoui[134,135], Z. Benkhaldoun[134], M. Guennoun[136], J. Chouqar[134], E. Jehin[137], C. Rinner[138],
J. Lloyd[139], M. El Moutamid[140], C. Lamarche[141], J. T. Pollock[142], D. B. Caton[142], V. Kouprianov[143,144],
B. W. Timerson[25,†], G. Blanchard[145], B. Payet[146], A. Peyrot[146], J.-P. Teng-Chuen-Yu[146], J. Françoise[147],
B. Mondon[147], T. Payet[147], C. Boissel[148], M. Castets[149], W. B. Hubbard[150], R. Hill[150], H. J. Reitsema[151],
O. Mousis[152], L. Ball[153], G. Neilsen[153], S. Hutcheon[153], K. Lay[153,†], P. Anderson[153], M. Moy[153,†], M. Jonsen[154],
I. Pink[154], R. Walters[154,†], and, B. Downs[155]

(Affiliations can be found after the references)

[⋆] Light curves are only available at the CDS via anonymous ftp to cdsarc.u-strasbg.fr (130.79.128.5) or via http://cdsarc.u-strasbg.fr/viz-bin/cat/J/A+A/659/A136

[†] Deceased.

Milliarcsecond Astrometry for the Galilean Moons Using Stellar Occultations

B. E. Morgado[1,2,3,6], A. R. Gomes-Júnior[2,4], F. Braga-Ribas[1,2,3,5], R. Vieira-Martins[1,2,6], J. Desmars[7,8], V. Lainey[8], E. D'aversa[9], D. Dunham[10], J. Moore[10], K. Baillié[8], D. Herald[11,12], M. Assafin[2,6], B. Sicardy[3], S. Aoki[13], J. Bardecker[10], J. Barton[10], T. Blank[10], D. Bruns[10], N. Carlson[10], R. W. Carlson[14], K. Cobble[10], J. Dunham[10], D. Eisfeldt[10], M. Emilio[15], C. Jacques[16], T. C. Hinse[17,18], Y. Kim[19,20], M. Malacarne[21], P. D. Maley[10,22], A. Maury[23], E. Meza[24,25], F. Oliva[9], G. S. Orton[14], C. L. Pereira[1,2,5], M. Person[26], C. Plainaki[27], R. Sfair[4,28], G. Sindoni[27], M. Smith[10], E. Sussenbach[29], P. Stuart[10], J. Vrolijk[30], and O. C. Winter[4]

[1] Observatório Nacional/MCTI, R. General José Cristino 77, CEP 20921-400 Rio de Janeiro—RJ, Brazil; morgado.fis@gmail.com
[2] Laboratório Interinstitucional de e-Astronomia—LIneA, Rua Gal. José Cristino 77, Rio de Janeiro, RJ 20921-400, Brazil
[3] LESIA, Observatoire de Paris, Université PSL, CNRS, Sorbonne Université, Université Paris Diderot, Sorbonne Paris Cité, 5 Place Jules Janssen, F-92195 Meudon, France
[4] UNESP—São Paulo State University, Grupo de Dinâmica Orbital e Planetologia, CEP 12516-410, Guaratinguetá, SP, Brazil
[5] Federal University of Technology—Paraná (UTFPR/DAFIS), Rua Sete de Setembro, 3165, CEP 80230-901, Curitiba, PR, Brazil
[6] Universidade Federal do Rio de Janeiro—Observatório do Valongo, Ladeira Pedro Antônio 43, CEP 20.080-090 Rio de Janeiro—RJ, Brazil
[7] Institut Polytechnique des Sciences Avancées IPSA, 63 Boulevard de Brandebourg, F-94200 Ivry-sur-Seine, France
[8] IMCCE, Observatoire de Paris, PSL University, CNRS, Sorbonne Université, Université Lille, 77 Av. Denfert-Rochereau, F-75014 Paris, France
[9] Istituto Nazionale di Astrofisica-Istituto di Astrofisica e Planetologia Spaziali, INAF-IAPS, Rome, Italy
[10] International Occultation Timing Association (IOTA), PO Box 20313, Fountain Hills, AZ 85269, USA
[11] International Occultation Timing Association/European Section, Am Brombeerhag 13, D-30459 Hannover, Germany
[12] Trans-Tasman Occultation Alliance (TTOA), Wellington PO Box 3181, New Zealand
[13] Japan Aerospace Exploration Agency, JAXA, Japan
[14] Jet Propulsion Laboratory, California Institute of Technology, Pasadena, CA, USA
[15] Universidade Estadual de Ponta Grossa (UEPG), Ponta Grossa, Brazil
[16] Observatório SONEAR, Brazil
[17] Institute of Astronomy, Faculty of Physics, Astronomy and Informatics, Nicolaus Copernicus University, Grudziadzka 5, 87-100, Torun, Poland
[18] Chungnam National University, Department of Astronomy and Space Science, 34134, Daejeon, Republic of Korea
[19] Department of Astronomy and Space Science, Chungbuk National University, 28644 Cheongju, Republic of Korea
[20] Chungbuk National University Observatory, Chungbuk National University, 28644 Cheongju, Republic of Korea
[21] Universidade Federal do Espírito Santo, Av. Fernando Ferrari 514, Vitória, ES, 29075-910, Brazil
[22] NASA Johnson Space Center Astronomical Society, Houston, TX, USA
[23] San Pedro de Atacama Celestial Explorations—SPACE, Chile
[24] Comisión Nacional de Investigación y Desarrollo Aeroespacial del Perú - CONIDA, Peru
[25] Observatorio Astronómico de Moquegua—MPC Code W73, Peru
[26] MIT, Cambridge, MA, USA
[27] Agenzia Spaziale Italiana, ASI, Rome, Italy
[28] Institut für Astronomie und Astrophysik, Eberhard Karls Universität Tübingen, Auf der Morgenstelle 10, D-72076 Tübingen, Germany
[29] Pletterijweg Oost, Willemstad, Curaçao, The Netherlands
[30] Space and Nature Aruba Foundation, Aruba, The Netherlands

Abstract

A stellar occultation occurs when a Solar System object passes in front of a star for an observer. This technique allows the sizes and shapes of the occulting body to be determined with kilometer precision. In addition, this technique constrains the occulting body's positions, albedos, densities, and so on. In the context of the Galilean moons, these events can provide their best ground-based astrometry, with uncertainties in the order of 1 mas (∼3 km at Jupiter's distance during opposition). We organized campaigns and successfully observed a stellar occultation by Io (JI) in 2021, one by Ganymede (JIII) in 2020, and one by Europa (JII) in 2019, with stations in North and South America. We also re-analyzed two previously published events: one by Europa in 2016 and another by Ganymede in 2017. We then fit the known 3D shape of the occulting satellite and determine its center of figure. This resulted in astrometric positions with uncertainties in the milliarcsecond level. The positions obtained from these stellar occultations can be used together with dynamical models to ensure highly accurate orbits of the Galilean moons. These orbits can help when planning future space probes aiming at the Jovian system, such as JUICE by ESA and Europa Clipper by NASA. They also allow more efficient planning of flyby maneuvers.

Unified Astronomy Thesaurus concepts: Occultation (1148); Galilean satellites (627); Astrometry (80)

1. Introduction

The progress in the astrometry and modeling of the orbits of planetary satellites in the last decade has enabled the accurate

estimation of tidal effects in natural satellites and their primaries (Lainey et al. 2009, 2012, 2017). However, these studies need accurate observations that are spread over a significant period of time to provide essential constraints on short and long-term dynamics, up to formation processes (Charnoz et al. 2011; Crida & Charnoz 2012).

Accurate orbits also help in the preparation of space missions targeting these systems (Dirkx et al. 2016, 2017). ESA's JUICE

LETTER TO THE EDITOR

A stellar occultation by the transneptunian object (50000) Quaoar observed by CHEOPS[*]

B. E. Morgado[1,2,3], G. Bruno[4], A. R. Gomes-Júnior[5,6,3], I. Pagano[4], B. Sicardy[7], A. Fortier[8,9], J. Desmars[10,11], P. F. L. Maxted[12], F. Braga-Ribas[13,2,3], D. Queloz[14,15], S. G. Sousa[16], J. L. Ortiz[17], A. Brandeker[18], A. Collier Cameron[19], C. L. Pereira[2,3], H. G. Florén[18], N. Hara[20], D. Souami[21,7,22], K. G. Isaak[23], G. Olofsson[18], P. Santos-Sanz[17], T. G. Wilson[19], J. Broughton[24,25], Y. Alibert[8], R. Alonso[26,27], G. Anglada[28,29], T. Bárczy[30], D. Barrado[31], S. C. C. Barros[16,32], W. Baumjohann[33], M. Beck[20], T. Beck[8], W. Benz[8,9], N. Billot[20], X. Bonfils[34], C. Broeg[8,9], J. Cabrera[35], S. Charnoz[36], S. Csizmadia[35], M. B. Davies[37], M. Deleuil[38], L. Delrez[39,40], O. D. S. Demangeon[16,32], B. O. Demory[9], D. Ehrenreich[20], A. Erikson[35], L. Fossati[33], M. Fridlund[41,42], D. Gandolfi[43], M. Gillon[39], M. Güdel[44], K. Heng[9,45], S. Hoyer[38], L. L. Kiss[46,47], J. Laskar[48], A. Lecavelier des Etangs[49], M. Lendl[20], C. Lovis[20], D. Magrin[50], L. Marafatto[50], V. Nascimbeni[50], R. Ottensamer[51], E. Pallé[26], G. Peter[52], D. Piazza[8], G. Piotto[50,53], D. Pollacco[45], R. Ragazzoni[50,53], N. Rando[54], F. Ratti[54], H. Rauer[35,55,56], C. Reimers[51], I. Ribas[28,29], N. C. Santos[16,32], G. Scandariato[4], D. Ségransan[20], A. E. Simon[8], A. M. S. Smith[35], M. Steller[33], G. M. Szabó[57,58], N. Thomas[8], S. Udry[20], V. Van Grootel[40], N. A. Walton[59], and K. Westerdorff[52]

(Affiliations can be found after the references)

ABSTRACT

Context. Stellar occultation is a powerful technique that allows the determination of some physical parameters of the occulting object. The result depends on the photometric accuracy, the temporal resolution, and the number of chords obtained. Space telescopes can achieve high photometric accuracy as they are not affected by atmospheric scintillation.

Aims. Using ESA's CHEOPS space telescope, we observed a stellar occultation by the transneptunian object (50000) Quaoar. We compare the obtained chord with previous occultations by this object and determine its astrometry with sub-milliarcsecond precision. Also, we determine upper limits to the presence of a global methane atmosphere on the occulting body.

Methods. We predicted and observed a stellar occultation by Quaoar using the CHEOPS space telescope. We measured the occultation light curve from this dataset and determined the dis- and reappearance of the star behind the occulting body. Furthermore, a ground-based telescope in Australia was used to constrain Quaoar's limb. Combined with results from previous works, these measurements allowed us to obtain a precise position of Quaoar at the occultation time.

Results. We present the results obtained from the first stellar occultation by a transneptunian object (TNO) using a space telescope orbiting Earth; it was the occultation by Quaoar observed on 2020 June 11. We used the CHEOPS light curve to obtain a surface pressure upper limit of 85 nbar for the detection of a global methane atmosphere. Also, combining this observation with a ground-based observation, we fitted Quaoar's limb to determine its astrometric position with an uncertainty below 1.0 mas.

Conclusions. This observation is the first of its kind, and it shall be considered as a proof of concept of stellar occultation observations of transneptunian objects with space telescopes orbiting Earth. Moreover, it shows significant prospects for the James Webb Space Telescope.

Key words. Methods: observational – Techniques: photometry – Occultations – Minor planets, asteroids: individual: Quaoar

1. Introduction

Stellar occultations happen when a body passes in front of a star as viewed by an observer. The detection of these events allow the determination of 2D apparent sizes and shapes with kilometre uncertainties (Sicardy et al. 2011). Also, with these events, we can probe the vicinity of the occulting object in search for material, such as rings (Braga-Ribas et al. 2014; Ortiz et al. 2017), and even detect, characterise, or determine limits to atmospheres (Marques Oliveira et al. 2022; Meza et al. 2019; Arimatsu et al. 2019; Ortiz et al. 2012). From an astrometric point of view, these events can provide highly accurate positions of the occulting

object, with uncertainties of the order of a few milliarcseconds (mas, Rommel et al. 2020).

This Letter details the analysis of the stellar occultation by the large transneptunian object (TNO; 50000) Quaoar on 2020 June 11. Quaoar belongs to the dynamical class of Cubewanos. It has a semi-major axis of 43.51 au, an orbital eccentricity of 0.035, and an inclination of 7.98 degrees. Quaoar was discovered in 2002 by Brown & Trujillo (2004). These authors estimated Quaoar's diameter to be about 1260 ± 190 km based on Hubble Space Telescope (HST) images. From previous stellar occultations, Braga-Ribas et al. (2013) obtained an area equivalent diameter of 1110 ± 5.0 km under the assumption that Quaoar is a Maclaurin spheroid. Also, thermal models based on Herschel

---

[*] This article uses data from CHEOPS programme CH_PR100021.

Astronomy & Astrophysics

Physical properties of the trans-Neptunian object (38628) Huya from a multi-chord stellar occultation

P. Santos-Sanz[1], J. L. Ortiz[1], B. Sicardy[2], M. Popescu[3,4], G. Benedetti-Rossi[2,5,6], N. Morales[1],
M. Vara-Lubiano[1], J. I. B. Camargo[7,5], C. L. Pereira[7,5], F. L. Rommel[7,5], M. Assafin[8,5], J. Desmars[9,10],
F. Braga-Ribas[11,2,5,7], R. Duffard[1], J. Marques Oliveira[2], R. Vieira-Martins[5,7], E. Fernández-Valenzuela[12],
B. E. Morgado[2,5,7], M. Acar[13,14], S. Anghel[3,10,15], E. Atalay[16], A. Ateş[13], H. Bakış[17], V. Bakış[17], Z. Eker[17],
O. Erece[17,18], S. Kaspi[19], C. Kayhan[13,20], S. E. Kilic[18], Y. Kilic[17,18], I. Manulis[21], D. A. Nedelcu[3],
M. S. Niaei[16], G. Nir[21], E. Ofek[21], T. Ozisik[18], E. Petrescu[22], O. Satir[16], A. Solmaz[23,24], A. Sonka[3], M. Tekes[23],
O. Unsalan[25], C. Yesilyaprak[16,26], R. Anghel[27], D. Berteşteanu[28], L. Curelaru[29], C. Danescu[30], V. Dumitrescu[31],
R. Gherase[28,32], L. Hudin[33], A-M. Stoian[34], J. O. Tercu[34,35], R. Truta[36], V. Turcu[37], C. Vantdevara[38], I. Belskaya[39],
T. O. Dementiev[40], K. Gazeas[41], S. Karampotsiou[41], V. Kashuba[42], Cs. Kiss[43,44], N. Koshkin[42],
O. M. Kozhukhov[40], Y. Krugly[39], J. Lecacheux[2], A. Pal[43], Ç. Püsküllü[45,46], R. Szakats[43], V. Zhukov[42],
D. Bamberger[47], B. Mondon[48], C. Perelló[49,50], A. Pratt[51,50], C. Schnabel[49,50], A. Selva[49,50], J. P. Teng[52],
K. Tigani[53], V. Tsamis[53], C. Weber[50], G. Wells[47], S. Kalkan[54], V. Kudak[55], A. Marciniak[56], W. Ogłoza[57],
T. Özdemir[58], E. Pakštienė[59], V. Perig[55], and M. Żejmo[60]

(Affiliations can be found after the references)

ABSTRACT

Context. As part of our international program aimed at obtaining accurate physical properties of trans-Neptunian objects (TNOs), we predicted a stellar occultation by the TNO (38628) Huya of the star *Gaia* DR2 4352760586390566400 (m_G = 11.5 mag) on March 18, 2019. After an extensive observational campaign geared at obtaining the astrometric data, we updated the prediction and found it favorable to central Europe. Therefore, we mobilized half a hundred of professional and amateur astronomers in this region and the occultation was finally detected by 21 telescopes located at 18 sites in Europe and Asia. This places the Huya event among the best ever observed stellar occultation by a TNO in terms of the number of chords.
Aims. The aim of our work is to determine an accurate size, shape, and geometric albedo for the TNO (38628) Huya by using the observations obtained from a multi-chord stellar occultation. We also aim to provide constraints on the density and other internal properties of this TNO.
Methods. The 21 positive detections of the occultation by Huya allowed us to obtain well-separated chords which permitted us to fit an ellipse for the limb of the body at the moment of the occultation (i.e., the instantaneous limb) with kilometric accuracy.
Results. The projected semi-major and minor axes of the best ellipse fit obtained using the occultation data are (a', b') = (217.6 ± 3.5 km, 194.1 ± 6.1 km) with a position angle for the minor axis of P' = 55.2° ± 9.1. From this fit, the projected area-equivalent diameter is 411.0 ± 7.3 km. This diameter is compatible with the equivalent diameter for Huya obtained from radiometric techniques (D = 406 ± 16 km). From this instantaneous limb, we obtained the geometric albedo for Huya (p_V = 0.079 ± 0.004) and we explored possible three-dimensional shapes and constraints to the mass density for this TNO. We did not detect the satellite of Huya through this occultation, but the presence of rings or debris around Huya was constrained using the occultation data. We also derived an upper limit for a putative Pluto-like global atmosphere of about p_{surf} = 10 nbar.

Key words. Kuiper belt objects: individual: Huya – methods: observational – techniques: photometric

1. Introduction

The stellar occultation technique is a very direct way to obtain highly accurate sizes and to derive albedos, as well as, in some cases, even the densities and 3D shapes for trans-Neptunian objects (TNOs, e.g., Sicardy et al. 2011; Ortiz et al. 2012, 2017). Atmospheres and satellites can also be detected and characterized via stellar occultations (Sicardy et al. 2006; Meza et al. 2019). Minute details that are otherwise undetectable by any other ground-based technique may also be detected using stellar occultations, such as the rings detected around the centaurs Chariklo (Braga-Ribas et al. 2014) and Chiron (Ortiz et al. 2015;

Ruprecht et al. 2015) and around the dwarf planet Haumea (Ortiz et al. 2017). These discoveries have opened a new way of research within the planetary sciences of the distant solar system bodies (Sicardy et al. 2019, 2020). All of the above demonstrates how the stellar occultation technique serves as a powerful means of obtaining information on the physical properties of TNOs.

From October 2009 onwards, when the first stellar occultation by a TNO (apart from Pluto) was recorded (Elliot et al. 2010), to date, about 77 stellar occultations produced by 33 different TNOs, excluding the one presented here, have been detected. About 50 of these occultations have been detected from only one or two different locations, which was not sufficient to

Astronomy & Astrophysics

The multichord stellar occultation on 2019 October 22 by the trans-Neptunian object (84922) 2003 VS2[*]

M. Vara-Lubiano[1], G. Benedetti-Rossi[2,3,4], P. Santos-Sanz[1], J. L. Ortiz[1], B. Sicardy[2], M. Popescu[5,6],
N. Morales[1], F. L. Rommel[7,3], B. Morgado[2,3,7], C. L. Pereira[7,3], A. Álvarez-Candal[1,7],
E. Fernández-Valenzuela[8], D. Souami[2,9], D. Ilic[10,11], O. Vince[12], R. Bachev[13], E. Semkov[13], D. A. Nedelcu[5],
A. Şonka[5], L. Hudin[14], M. Boaca[14,†], V. Inceu[14], L. Curelaru[15], R. Gherase[16,17], V. Turcu[18], D. Moldovan[18],
L. Mircea[18], M. Predatu[19], M. Teodorescu[20], L. Stoian[21], A. Juravle[21], F. Braga-Ribas[22,2,7,3], J. Desmars[23,24],
R. Duffard[1], J. Lecacheux[2], J. I. B. Camargo[7,3], M. Assafin[25,3], R. Vieira-Martins[7,3,24], T. Pribulla[26], M. Husárik[26],
P. Sivanič[26], A. Pal[27], R. Szakats[27], C. Kiss[27], J. Alonso-Santiago[28], A. Frasca[28], G. M. Szabó[29,30], A. Derekas[29,30],
L. Szigeti[29], M. Drozdz[31], W. Ogloza[31], J. Skvarč[32], F. Ciabattari[33], P. Delincak[34], P. Di Marcantonio[35], G. Iafrate[35],
I. Coretti[35], V. Baldini[35], P. Baruffetti[36], O. Klös[37], V. Dumitrescu[38], H. Mikuž[39,40], and A. Mohar[41]

(Affiliations can be found after the references)

ABSTRACT

Context. Stellar occultations have become one of the best techniques to gather information about the physical properties of trans-Neptunian objects (TNOs), which are critical objects for understanding the origin and evolution of our Solar System.
Aims. The purpose of this work is to determine, with better accuracy, the physical characteristics of the TNO (84922) 2003 VS2 through the analysis of the multichord stellar occultation on 2019 October 22 and photometric data collected afterward.
Methods. We predicted, observed, and analyzed the multichord stellar occultation of the Second *Gaia* Data Release (*Gaia* DR2) source 3449076721168026624 ($m_v = 14.1$ mag) by the plutino object 2003 VS2 on 2019 October 22. We performed aperture photometry on the images collected and derived the times when the star disappeared and reappeared from the observing sites that reported a positive detection. We fit the extremities of such positive chords to an ellipse using a Monte Carlo method. We also carried out photometric observations to derive the rotational light curve amplitude and rotational phase of 2003 VS2 during the stellar occultation. Combining the results and assuming a triaxial shape, we derived the 3D shape of 2003 VS2.
Results. Out of the 39 observatories involved in the observational campaign, 12 sites, located in Bulgaria (one), Romania (ten), and Serbia (one), reported a positive detection; this makes it one of the best observed stellar occultations by a TNO so far. Considering the rotational phase of 2003 VS2 during the stellar occultation and the rotational light curve amplitude derived ($\Delta m = 0.264 \pm 0.017$ mag), we obtained a mean area-equivalent diameter of $D_{\mathrm{Aeq}} = 545 \pm 13$ km and a geometric albedo of 0.134 ± 0.010. By combining the rotational light curve information with the stellar occultation results, we derived the best triaxial shape for 2003 VS2, which has semiaxes $a = 339 \pm 5$ km, $b = 235 \pm 6$ km, and $c = 226 \pm 8$ km. The derived aspect angle of 2003 VS2 is $\theta = 59° \pm 2°$ or its supplementary $\theta = 121° \pm 2°$, depending on the north-pole position of the TNO. The spherical-volume equivalent diameter is $D_{\mathrm{Veq}} = 524 \pm 7$ km. If we consider large albedo patches on its surface, the semi-major axis of the ellipsoid could be ~ 10 km smaller. These results are compatible with the previous ones determined from the single-chord 2013 and four-chord 2014 stellar occultations and with the effective diameter and albedo derived from *Herschel* and *Spitzer* data. They provide evidence that 2003 VS2's 3D shape is not compatible with a homogeneous triaxial body in hydrostatic equilibrium, but it might be a differentiated body and/or might be sustaining some stress. No secondary features related to rings or material orbiting around 2003 VS2 were detected.

Key words. Kuiper belt objects: individual: 2003 VS2 – methods: observational – techniques: photometric

1. Introduction

Trans-Neptunian objects (TNOs) offer a unique opportunity to better understand the origins and the chemical, dynamical, and collisional evolution of the outer Solar System. Possibly dispatched to further distances from the Sun than that of Neptune due to gravitational perturbations after their formation (Gomes et al. 2005; Levison et al. 2008), their global composition has

been virtually unaffected by solar irradiation, keeping it very similar to that of the primitive nebula (Morbidelli et al. 2008).

In the last decade, stellar occultations by TNOs have proved to be one of the best techniques to determine the size and shape of these objects, to show features such as satellites (Sickafoose et al. 2019) or rings (Braga-Ribas et al. 2014; Ortiz et al. 2015, 2017), and to reveal possible atmospheres (Hubbard et al. 1988; Stern & Trafton 2008; Meza et al. 2019). If we combine this technique with light-reflection measurements, we can also derive their geometric albedo. Furthermore, we can calculate their density if we assume hydrostatic equilibrium or if the body is part of a binary system or has a satellite, in which case we can obtain its mass.

---

[*] The photometric data used to obtain the rotational light curve of (84922) 2003 VS2 are only available at the CDS via anonymous ftp to cdsarc.u-strasbg.fr (130.79.128.5) or via http://cdsarc.u-strasbg.fr/viz-bin/cat/J/A+A/663/A121

[†] Deceased.

Astronomy & Astrophysics

Constraints on (2060) Chiron's size, shape, and surrounding material from the November 2018 and September 2019 stellar occultations

F. Braga-Ribas[1,2,3], C. L. Pereira[4,3,1], B. Sicardy[2], J. L. Ortiz[5], J. Desmars[6,7], A. Sickafoose[8], M. Emilio[9], B. Morgado[10,3], G. Margoti[1,3], F. L. Rommel[1,3], J. I. B. Camargo[4,3], M. Assafin[10,3], R. Vieira-Martins[4,3], A. R. Gomes-Júnior[11,3], P. Santos-Sanz[5], N. Morales[5], M. Kretlow[5,12], J. Lecacheux[2], F. Colas[7], R. Boninsegna[12], O. Schreurs[13,14], J. L. Dauvergne[15], E. Fernandez[13,14], H. J. van Heerden[16], H. González[17], D. Bihel[18], and F. Jankowsky[19]

(Affiliations can be found after the references)

ABSTRACT

Context. After the discovery of rings around the largest known Centaur object, (10199) Chariklo, we carried out observation campaigns of stellar occultations produced by the second-largest known Centaur object, (2060) Chiron, to better characterize its physical properties and presence of material on its surroundings.

Aims. We aim to provide constraints on (2060) Chiron's shape for the first time using stellar occultations. We investigate the detectability of material previously observed in its vicinity using the 2018 occultation data obtained from South Africa Astronomical Observatory (SAAO).

Methods. We predicted and successfully observed two stellar occultations by Chiron. These observations were used to constrain its size and shape by fitting elliptical limbs with equivalent surface radii in agreement with radiometric measurements. We also obtained the properties of the material observed in 2011 with the same technique used to derive Chariklo's ring properties in our previous works, used to obtain limits on the detection of secondary events in our 2018 observation.

Results. Constraints on the (2060) Chiron shape are reported for the first time. Assuming an equivalent radius of $R_{\text{equiv}} = 105^{+6}_{-7}$ km, we obtained a semi-major axis of $a = 126 \pm 22$ km. Considering Chiron's true rotational light curve amplitude and assuming it has a Jacobi equilibrium shape, we were able to derive a 3D shape with a semi-axis of $a = 126 \pm 22$ km, $b = 109 \pm 19$ km, and $c = 68 \pm 13$ km, implying in a volume-equivalent radius of $R_{\text{vol}} = 98 \pm 17$ km. We determined the physical properties of the 2011 secondary events around Chiron, which may then be directly compared with those of Chariklo rings, as the same method was used. Data obtained from SAAO in 2018 do not show unambiguous evidence of the proposed rings, mainly due to the large sampling time. Meanwhile, we discarded the possible presence of a permanent ring similar to (10199) Chariklo's C1R in optical depth and extension.

Conclusions. Using the first multi-chord stellar occultation by (2060) Chiron and considering it to have a Jacobi equilibrium shape, we derived its 3D shape, implying a density of 1119 ± 4 kg m^{-3}. New observations of a stellar occultation by (2060) Chiron are needed to further investigate the material's properties around Chiron, such as the occultation predicted for September 10, 2023.

Key words. comets: individual: (2060) Chiron – minor planets, asteroids: general – planets and satellites: rings – Kuiper belt: general

1. Introduction

After discovering rings around the Centaur object (10199) Chariklo, it was proposed that this feature may be common among distant small Solar System objects (Braga-Ribas et al. 2014). The centaur object (2060) Chiron is the second largest object of its kind. It has an equivalent diameter of 210^{+11}_{-14} km (model dependent), measured using data from the space telescopes *Spitzer* and *Herschel*, as well as from the Atacama Large Millimeter Array (ALMA; Lellouch et al. 2017).

Fundamental properties such as size and shape for objects of this kind can be obtained from Earth-based observations using stellar occultations (Ortiz et al. 2020)[1]. High-cadence observations in terms of time and high signal-to-noise ratio (S/N) allow

for detecting or setting upper limits to the presence of material around the occulting body, for instance, on dust shells, jets, or rings (Elliot et al. 1995; Ortiz et al. 2020).

Secondary events on previous stellar occultation by (2060) Chiron have been reported for events in 1993, 1994, and 2011 (Bus et al. 1996; Elliot et al. 1995; Ruprecht et al. 2015). They were all interpreted as dust or jets coming from Chiron's surface, as it has presented periods of cometary activity (Tholen et al. 1988; Belskaya et al. 2010). In 1989, Meech & Belton (1989) were the first to detect a comma around Chiron. Later, Luu & Jewitt (1990) analyzed 1988–1990 data, further investigating Chiron's activity. As far as we know, no non-gravitational acceleration has been detected so far.

The November 29, 2011 occultation was observed using the Infrared Telescope Facility (IRTF), which detected the main body event, and from Faulkes Telescope North (FTN), which had a much higher cadence and S/N, but with no detection of the main body (Ruprecht et al. 2015). The latter data presented two

---

[1] An updated list of the detected stellar occultations by outer Solar System objects that we are aware of can be found at http://occultations.ct.utfpr.edu.br/results (Braga-Ribas et al. 2019).

Astronomy & Astrophysics

The multichord stellar occultation by the centaur Bienor on January 11, 2019

E. Fernández-Valenzuela[1,2], N. Morales[2], M. Vara-Lubiano[2], J. L. Ortiz[2], G. Benedetti-Rossi[3,4,5], B. Sicardy[5],
M. Kretlow[2], P. Santos-Sanz[2], B. Morgado[4,5,7], D. Souami[5,6], F. Organero[8], L. Ana[8], F. Fonseca[8], A. Román[9],
S. Alonso[10], R. Gonçalves[11], M. Ferreira[12], R. Iglesias-Marzoa[13], J. L. Lamadrid[13], A. Alvarez-Candal[2,7,14],
M. Assafin[4,15], F. Braga-Ribas[4,7,16], J. I. B. Camargo[4,7], F. Colas[3], J. Desmars[17,18], R. Duffard[2], J. Lecacheux[5],
A. R. Gomes-Júnior[3,4], F. L. Rommel[4,7], R. Vieira-Martins[4,5,7], C. L. Pereira[4,7], V. Casanova[2], A. Selva[19,20],
C. Perelló[19,20], S. Mottola[21], S. Hellmich[21], J. L. Maestre[22], A. J. Castro-Tirado[2], A. Pal[23], J. M. Trigo-Rodriguez[24,25],
W. Beisker[20], A. Laporta[26,27], M. Garcés[26,27], L. Escaned[26,27], and M. Bretton[28]

(Affiliations can be found after the references)

ABSTRACT

Within our program of physical characterization of trans-Neptunian objects and centaurs, we predicted a stellar occultation by the centaur (54598) Bienor to occur on January 11, 2019, with good observability potential. We obtained high accuracy astrometric data to refine the prediction, resulting in a shadow path favorable for the Iberian Peninsula. This encouraged us to carry out an occultation observation campaign that resulted in five positive detections from four observing sites. This is the fourth centaur for which a multichord (more than two chords) stellar occultation has been observed so far, the other three being (2060) Chiron, (10199) Chariklo, and (95626) 2002 GZ$_{32}$. From the analysis of the occultation chords, combined with the rotational light curve obtained shortly after the occultation, we determined that Bienor has an area-equivalent diameter of 150 ± 20 km. This diameter is ~30 km smaller than the one obtained from thermal measurements. The position angle of the short axis of the best fitting ellipse obtained through the analysis of the stellar occultation does not match that of the spin axis derived from long-term photometric models. We also detected a strong irregularity in one of the minima of the rotational light curve that is present no matter the aspect angle at which the observations were done. We present different scenarios to reconcile the results from the different techniques. We did not detect secondary drops related to potential rings or satellites. Nonetheless, similar rings in size to that of Chariklo's cannot be discarded due to low data accuracy.

Key words. Kuiper belt: general – minor planets, asteroids: individual: Bienor – planets and satellites: composition – planets and satellites: formation

1. Introduction

Centaurs are objects that orbit the Sun with orbital semi-major axes between those of Jupiter and Neptune. Dynamical evolution models show that these objects originated in the trans-Neptunian region, but they have been injected into inner parts of the Solar System as a result of planetary encounters, mostly with Neptune. Dynamical simulations also estimate that the mean half-life of the entire sample of 32 well-known centaurs is 2.7 Myr (Horner et al. 2004), which means they have spent most of their lifetime in the trans-Neptunian region. Therefore, centaurs present an excellent opportunity to study smaller trans-Neptunian objects (TNOs) much closer to the Earth, providing a better characterization of their physical properties. Due to their short lifetime in their current region, centaurs have suffered less chemical or radiolytic processes than other bodies (e.g., asteroids and comets). Hence, the study of the physical properties of this population provides important information to help reconstruct the history of the Solar System formation and evolution.

During the last years, there has been a growing interest in the centaur population due to the discovery of a ring system around (10199) Chariklo (Braga-Ribas et al. 2014). Also, the data of several stellar occultations by (2060) Chiron reveal features similar to those found for Chariklo; although, there is still an open debate on whether these features are attributed to rings

(Ortiz et al. 2015; Ruprecht et al. 2015; Sickafoose et al. 2020). The discovery of ring systems has opened a new branch of research to understand how these rings are formed and how they survive around these small bodies. Collisions and rotational disruptions seem to be plausible scenarios for their formation (see, Braga-Ribas et al. 2014; Ortiz et al. 2015; Sicardy et al. 2019, and references therein). Additionally, the discovery of another ring system around the dwarf planet Haumea (Ortiz et al. 2017) raises the question of whether rings are formed in the trans-Neptunian region surviving through the planetary encounters (which does not seem to be very unlikely, Araujo et al. 2016). Another proposed scenario is by tidal disruption of a satellite when encountering the giant planets (Hyodo et al. 2017); although, the probability of such an event seems to be very small (e.g., Melita et al. 2017). Moreover, this would not explain Haumea's system (which includes the only known dynamical family of objects in the trans-Neptunian region, Brown et al. 2007; Ortiz et al. 2012, 2020a; Proudfoot & Ragozzine 2019). Regardless, these three objects, Chariklo, Chiron, and Haumea, share some physical properties; for instance, they all have highly elongated ellipsoidal shapes, rotate relatively fast, and present water ice in their unresolved spectra, (i.e., main body plus rings, see, e.g., Barucci et al. 2011; Braga-Ribas et al. 2014; Duffard et al. 2014b; Ortiz et al. 2017; Cikota et al. 2018; Sicardy et al. 2019; Morgado et al. 2021, and references therein), and most

Article

A dense ring of the trans-Neptunian object Quaoar outside its Roche limit

B. E. Morgado[1,2,3 ✉], B. Sicardy[4], F. Braga-Ribas[5], J. L. Ortiz[6], H. Salo[7], F. Vachier[8], J. Desmars[8,9], C. L. Pereira[2,3], P. Santos-Sanz[6], R. Sfair[10,11], T. de Santana[4,11], M. Assafin[1,3], R. Vieira-Martins[2,3], A. R. Gomes-Júnior[3,11,12], G. Margoti[5], V. S. Dhillon[13,14], E. Fernández-Valenzuela[15], J. Broughton[16,17], J. Bradshaw[18], R. Langersek[19], G. Benedetti-Rossi[3,11], D. Souami[4,20,21], B. J. Holler[22], M. Kretlow[6,23,24], R. C. Boufleur[2,3], J. I. B. Camargo[2,3], R. Duffard[6], W. Beisker[23,24], N. Morales[6], J. Lecacheux[4], F. L. Rommel[2,3], D. Herald[17], W. Benz[25,26], E. Jehin[27], F. Jankowsky[28], T. R. Marsh[29,43], S. P. Littlefair[13], G. Bruno[30], I. Pagano[30], A. Brandeker[31], A. Collier-Cameron[32], H. G. Florén[31], N. Hara[33], G. Olofsson[31], T. G. Wilson[32], Z. Benkhaldoun[34], R. Busuttil[35], A. Burdanov[36], M. Ferrais[37], D. Gault[17], M. Gillon[38], W. Hanna[17], S. Kerr[17,39], U. Kolb[35], P. Nosworthy[17], D. Sebastian[40], C. Snodgrass[41], J. P. Teng[42] & J. de Wit[36]

Planetary rings are observed not only around giant planets[1], but also around small bodies such as the Centaur Chariklo[2] and the dwarf planet Haumea[3]. Up to now, all known dense rings were located close enough to their parent bodies, being inside the Roche limit, where tidal forces prevent material with reasonable densities from aggregating into a satellite. Here we report observations of an inhomogeneous ring around the trans-Neptunian body (50000) Quaoar. This trans-Neptunian object has an estimated radius[4] of 555 km and possesses a roughly 80-km satellite[5] (Weywot) that orbits at 24 Quaoar radii[6,7]. The detected ring orbits at 7.4 radii from the central body, which is well outside Quaoar's classical Roche limit, thus indicating that this limit does not always determine where ring material can survive. Our local collisional simulations show that elastic collisions, based on laboratory experiments[8], can maintain a ring far away from the body. Moreover, Quaoar's ring orbits close to the 1/3 spin–orbit resonance[9] with Quaoar, a property shared by Chariklo's[2,10,11] and Haumea's[3] rings, suggesting that this resonance plays a key role in ring confinement for small bodies.

In our efforts to characterize Quaoar's shape and search for putative material around it, we have predicted and observed several stellar occultations by this body. Following a report from Australia of a Neptune-like ring detected during a 2021 occultation and independently suspected in 2019, we have identified secondary events in previous occultations observed between 2018 and 2020 (Fig. 1, details in Extended Data Table 1, Supplementary Table 1 and Supplementary Fig. 1). They are consistent with a circular ring centred on the body, with two possible mirror solutions for the ring orientation (Methods and Fig. 2). Both solutions have radii close to 4,100 km, or roughly 7.4 Quaoar radii. One solution has a ring pole that presents a large mismatch with Weywot's orbital pole[7], whereas the other solution is consistent with a ring coplanar with Weywot's orbit (details in Table 1). This is our preferred solution, as a primordial collisional system surrounding Quaoar is expected to settle in a disc that subsequently forms both the ring and Weywot.

[1]Federal University of Rio de Janeiro - Observatory of Valongo, Rio de Janeiro, Brazil. [2]National Observatory/MCTI, Rio de Janeiro, Brazil. [3]Interinstitutional e-Astronomy Laboratory (LIneA), Rio de Janeiro, Brazil. [4]LESIA, Observatory of Paris, University PSL, CNRS, UPMC, Sorbonne University, University of Paris Diderot, Sorbonne Paris City, Meudon, France. [5]Federal University of Technology, Paraná (UTFPR/DAFIS), Curitiba, Brazil. [6]Institute of Astrophysics at Andalucía, IAA-CSIC, Granada, Spain. [7]Space Physics and Astronomy Research unit, University of Oulu, Oulu, Finland. [8]The Institute of Celestial Mechanics and Ephemeris Calculation (IMCCE), Observatory of Paris, PSL Research University, CNRS, Sorbonne University, University of Paris, University of Lille, Lille, France. [9]Polytechnic Institute of Advanced Sciences (IPSA), Ivry-sur-Seine, France. [10]Institute for Astronomy and Astrophysics, Eberhard Karls University of Tübingen, Tübingen, Germany. [11]Orbital Dynamics and Planetology Group, UNESP - São Paulo State University, Guaratinguetá, Brazil. [12]Institute of Physics, Federal University of Uberlândia, Uberlândia, Brazil. [13]Department of Physics and Astronomy, University of Sheffield, Sheffield, UK. [14]Institute of Astrophysics of The Canary Islands, La Laguna, Spain. [15]Florida Space Institute, University of Central Florida, Orlando, FL, USA. [16]Reedy Creek Observatory, Gold Coast, Queensland, Australia. [17]Trans-Tasman Occultation Alliance (TTOA), Wellington, New Zealand. [18]Samford Valley Observatory (Q79), Brisbane, Queensland, Australia. [19]Algester Astronomical Observatory, Brisbane, Queensland, Australia. [20]Observatory of the Côte d'Azur, Lagrange Laboratory UMR7293 CNRS, Nice, France. [21]naXys, University of Namur, Namur, Belgium. [22]Space Telescope Science Institute, Baltimore, MD, USA. [23]International Occultation Timing Association / European Section, Hannover, Germany. [24]International Amateur Observatory e.V. (IAS), Mittenwalde, Germany. [25]Institute of Physics, University of Bern, Bern, Switzerland. [26]Center for Space and Habitability, University of Bern, Bern, Switzerland. [27]STAR Institute, University of Liège, Liège, Belgium. [28]Heidelberg-Königstuhl State Observatory, Heidelberg, Germany. [29]Department of Physics, University of Warwick, Coventry, UK. [30]INAF, Catania Astrophysical Observatory, Catania, Italy. [31]Department of Astronomy, Stockholm University, AlbaNova University Center, Stockholm, Sweden. [32]Centre for Exoplanet Science, SUPA School of Physics and Astronomy, University of St Andrews, North Haugh, St Andrews, UK. [33]Astronomical Observatory at the University of Geneva, Versoix, Switzerland. [34]Oukaimeden Observatory, High Energy Physics and Astrophysics Laboratory, FSSM, Cadi Ayyad University, Marrakech, Morocco. [35]School of Physical Sciences, The Open University, Walton Hall, Milton Keynes, UK. [36]Department of Earth, Atmospheric and Planetary Sciences, MIT, Cambridge, MA, USA. [37]Laboratory of Astrophysics of Marseille, University of Aix Marseille, CNRS, CNES, Marseille, France. [38]Astrobiology Research Unit, University of Liège, Liège, Belgium. [39]Astronomical Association of Queensland, Pimpama, Queensland, Australia. [40]School of Physics and Astronomy, University of Birmingham, Birmingham, UK. [41]Institute for Astronomy, University of Edinburgh, Royal Observatory, Edinburgh, UK. [42]AGORA Observatory of Makes, AGORA, La Rivière, France. [43]Deceased: T. R. Marsh. ✉e-mail: bmorgado@ov.ufrj.br

Astronomy
&
Astrophysics

LETTER TO THE EDITOR

Changing material around (2060) Chiron revealed by an occultation on December 15, 2022

J. L. Ortiz[1] , C. L. Pereira[2,3], B. Sicardy[4], F. Braga-Ribas[5,2,3], A. Takey[6], A. M. Fouad[6], A. A. Shaker[6], S. Kaspi[7],
N. Brosch[7], M. Kretlow[1,8], R. Leiva[1], J. Desmars[9,10], B. E. Morgado[11,2,3], N. Morales[1], M. Vara-Lubiano[1],
P. Santos-Sanz[1], E. Fernández-Valenzuela[12,1], D. Souami[4,13,14], R. Duffard[1], F. L. Rommel[5,2,3], Y. Kilic[15,16],
O. Erece[16], D. Koseoglu[16], E. Ege[17], R. Morales[1], A. Alvarez-Candal[1,18], J. L. Rizos[1], J. M. Gómez-Limón[1],
M. Assafin[11,3], R. Vieira-Martins[2,3], A. R. Gomes-Júnior[19,20,3], J. I. B. Camargo[2,3], and J. Lecacheux[4]

(Affiliations can be found after the references)

Received 26 May 2023 / Accepted 21 July 2023

ABSTRACT

We were able to accurately predict the shadow path and successfully observe an occultation of a bright star by Chiron on December 15, 2022. The Kottamia Astronomical Observatory in Egypt did not detect the occultation by the solid body, but we found three extinction features in the light curve that had symmetrical counterparts with respect to the central time of the occultation. One of the features is broad and shallow, whereas the other two features are sharper, with a maximum extinction of ~25% at the achieved spatial resolution of 19 km per data point. From the Wise Observatory in Israel, we detected the occultation caused by the main body and several extinction features surrounding the body. When all the secondary features are plotted in the sky plane, we find that they can be caused by a broad ~580 km disk with concentrations at radii of 325 ± 16 km and 423 ± 11 km surrounding Chiron. At least one of these structures appears to be outside the Roche limit. The ecliptic coordinates of the pole of the disk are $\lambda = 151° \pm 8°$ and $\beta = 18° \pm 11°$, in agreement with previous results. We also reveal our long-term photometry results, indicating that Chiron had suffered a brightness outburst of at least 0.6 mag between March and September 2021 and that Chiron was still somewhat brighter at the occultation date than at its nominal pre-outburst phase. The outermost extinction features might be consistent with a bound or temporarily bound structure associated with the brightness increase. However, the nature of the brightness outburst is unclear, and it is also unclear whether the dust or ice released in the outburst could be feeding a putative ring structure or whether it is emanating from it.

Key words. occultations – Kuiper belt: general – comets: general – minor planets, asteroids: individual: Chiron

1. Introduction

Soon after the unexpected discovery of a dense double ring separated by a small gap in the centaur (10199) Chariklo from a well-observed stellar occultation (Braga-Ribas et al. 2014), a natural question arose as to whether that ring structure is something unique to Chariklo or whether there could be similar structures present in other centaurs or related bodies in the outer Solar System. In that context, the claim that the centaur (2060) Chiron might also have a ring system (Ortiz et al. 2015), based on a few observed stellar occultations reported in the literature (Elliot et al. 1995; Ruprecht et al. 2015; Bus et al. 1996; Sickafoose et al. 2020) in combination with photometric and spectroscopic hints, has not been as convincing as the Chariklo case; this is mainly because Chariklo's observations were obtained from several locations, not just two sites. A particularly intriguing detail is that some extinction features have not been seen at all longitudes around Chiron, meaning that the putative ring system would be incomplete or highly inhomogeneous and quite different from Chariklo's ring system. In addition, previous claims have asserted that extinction events on an occultation by Chiron might be due to cometary-like jets (Elliot et al. 1995).

Another ring system was then unambiguously detected, this time around the large trans-Neptunian object (TNO) and dwarf planet Haumea (Ortiz et al. 2017). In addition, yet another ring system has just been reported around the large TNO Quaoar

(Morgado et al. 2023; Pereira et al. 2023). This time, the ring is outside Quaoar's Roche limit, with at least a very dense arc and tenuous material coexisting in the ring structure, meaning that such a ring is highly inhomogeneous in longitude. In this new context, the inhomogeneity of the potential ring around Chiron would not be that surprising.

Predicting and observing new stellar occultations was very relevant to characterize the material around Chiron properly. Within the Lucky Star collaboration[1], a promising event was identified for 2022 December 15, successfully observed, and the preliminary results are reported here.

2. Observations of the occultation

Observations were obtained with the 1.88 m telescope at Kottamia Astronomical Observatory (KAO) in Egypt (Azzam et al. 2010), equipped with the Kottamia Faint Imaging Spectro-Polarimeter, KFISP (Azzam et al. 2022). We used the imaging mode in binning 4×4 to decrease the readout time as much as possible. The Sloan Digital Sky Survey SDSS *g*-band filter was used, the integration time was 3 s, and the average readout time was around 1.5 s, meaning that the full cycle of consecutive observations typically took 4.5 s. Given that the speed of Chiron with respect to the observer was 4.24 km s⁻¹, the achieved spatial resolution was 19 km. The observing sequence started at

---

[1] https://lesia.obspm.fr/lucky-star

A study of centaur (54598) Bienor from multiple stellar occultations and rotational light curves

J. L. Rizos[1], E. Fernández-Valenzuela[2,1], J. L. Ortiz[1], F. L. Rommel[3,2,4], B. Sicardy[5], N. Morales[1], P. Santos-Sanz[1], R. Leiva[1], M. Vara-Lubiano[1], R. Morales[1], M. Kretlow[1], A. Alvarez-Candal[1,6], B. J. Holler[7], R. Duffard[1], J. M. Gómez-Limón[1], J. Desmars[8,9], D. Souami[5,10], M. Assafin[4,11], G. Benedetti-Rossi[4,5,12], F. Braga-Ribas[3,4,13], J. I. B. Camargo[4,13], F. Colas[12], J. Lecacheux[5], A. R. Gomes-Júnior[4,12], R. Vieira-Martins[4,5,13], C. L. Pereira[4,13], B. Morgado[4,5,13], Y. Kilic[14], S. Redfield[15], C. Soloff[15], K. McGregor[15], K. Green[16,17], T. Midavaine[18], O. Schreurs[19,20], M. Lecossois[20], R. Boninsegna[21], M. Ida[22], P. Le Cam[23], K. Isobe[24], Hayato Watanabe[25], S. Yuasa[25], Hikaru Watanabe[25], and S. Kidd[26]

(Affiliations can be found after the references)

Received May 22, 2024

ABSTRACT

Context. Centaurs, distinguished by their volatile-rich compositions, play a pivotal role in understanding the formation and evolution of the early solar system, as they represent remnants of the primordial material that populated the outer regions. Stellar occultations offer a means to investigate their physical properties, including shape, rotational state, or the potential presence of satellites and rings.
Aims. This work aims to conduct a detailed study of the centaur (54598) Bienor through stellar occultations and rotational light curves from photometric data collected during recent years.
Methods. We successfully predicted three stellar occultations by Bienor, which were observed from Japan, Western Europe, and the USA. In addition, we organized observational campaigns from Spain to obtain rotational light curves. At the same time, we develop software to generate synthetic light curves from three-dimensional shape models, enabling us to validate the outcomes through computer simulations.
Results. We resolve Bienor's projected ellipse for December 26, 2022, determine a prograde sense of rotation, and confirm an asymmetric rotational light curve. We also retrieve the axes of its triaxial ellipsoid shape as a = (127 ± 5) km, b = (55 ± 4) km, and c = (45 ± 4) km. Moreover, we refine the rotation period to 9.1736 ± 0.0002 hours and determine a geometric albedo of (6.5 ± 0.5) %, higher than previously determined by other methods. Finally, by comparing our findings with previous results and simulated rotational light curves, we analyze whether an irregular or contact-binary shape, the presence of an additional element such as a satellite, or significant albedo variations on Bienor's surface, may be present.

Key words. Stellar occultation – Light curve – Trans-Neptunian Object – Centaurs – (54598) Bienor

1. Introduction

Among the small bodies of the solar system, there exists the so-called centaurs, some of them characterized by their combination of cometary and asteroidal features. It is theorized that centaurs are originally trans-Neptunian objects expelled due to gravitational scattering by Neptune (Holman & Wisdom 1993; Duncan et al. 1995; Duncan & Levison 1997). These objects, transient in nature, have an average lifespan of only a few million years (Horner et al. 2004), primarily because of their gravitational interactions with the giant planets that lead to their eventual expulsion from the region. Therefore, centaurs present a unique opportunity to study trans-Neptunian objects, providing a better characterization of their physical properties.

The first centaur discovered was Chiron in 1977, although its cometary properties were not identified until a decade later —to date, comet activity has been confirmed in ~13 % of cases (Bauer et al. 2008). Since the discovery of a second object in 1992, (5145) Pholus, hundreds[1] of them have been discovered, although the number depends on the criteria used for their definition. There is not a universally accepted definition of centaurs. Several criteria can be found in the literature, such as having a

semi-major axis between 5 and 30 au or those presenting a Tisserand parameter larger than 3 and a semi-major axis larger than the semi-major axis of Jupiter. Some estimations suggest that there are > 40,000 centaurs larger than 1 km in diameter, although other authors have estimated > 100 million (Di Sisto & Brunini 2007).

In a study by Lacerda et al. (2014), more than 100 TNOs and centaurs were examined for their color-albedo distribution. The study identified two clusters: one characterized by dark-neutral objects with a geometric albedo (p_V) of approximately ~5%, and another composed of bright red objects with geometric albedos exceeding > 6%. This division based on color-albedo has been particularly pronounced among centaurs (Bauer et al. 2013; Duffard et al. 2014b; Tegler et al. 2016) with median albedos of approximately ~5% for the dark-neutral group and ~8.4% for the bright red group (Müller et al. 2020).

Due to the large geocentric distances of these small bodies and the consequent challenges in their study, we have only a limited understanding of the physical properties of these objects thus far. To date, through the technique of stellar occultations, we have gathered data on the shape and spatial orientation of the centaur Chariklo (Leiva et al. 2017; Morgado et al. 2021). Moreover, a three-dimensional morphology has been postulated for the centaur Chiron under the assumption of hydrostatic equilib-

---

[1] At the time of writing this article, 761 centaurs are listed at https://ssd.jpl.nasa.gov/